

THÈSE

Présentée à

L'UNIVERSITÉ BORDEAUX 1

École doctorale des sciences chimiques

par

IE-RANG JEON

Pour obtenir le grade de

DOCTEUR

SPÉCIALITÉ : Physico-Chimie de la Matière Condensée

Organisation par chimie de coordination de molécules-aimants : vers une nouvelle génération de matériaux magnétiques et photomagnétiques

Soutenue le 13 Novembre 2012

En attente de l'avis de:

M. Jesper BENDIX

Rapporteur

M. Andreas HAUSER

Rapporteur

Devant la commission d'examen formée de :

M. Jesper BENDIX

Professeur, University of Copenhagen

Rapporteur

M. Andreas HAUSER

Professeur, Université de Genève

M. Rodolphe CLÉRAC

Chargé de Recherche, CNRS

Examinateur

M^{me}. Corine MATHONIERE

Professeur, Université Bordeaux 1

M. Philippe RICHETTI

Directeur de Recherche, CNRS

M. Philippe SAINCTAVIT

Directeur de Recherche, CNRS

M. Claude COULON

Professeur, Université Bordeaux 1

Membre invité

The day came when the risk to remain tight in a bud was more painful than the risk it took to blossom

- Anais Nin

To my parents

After three years of PhD, I'm on the final line of my doctoral journey. Getting to the end of a PhD is not a personal achievement, many people provided support and I doubt I will be able to acknowledge them as they deserve. I may forget to mention some people as there are so many to thank for every little helps, but know your contribution was appreciated.

Firstly thank to Dr. Philippe Richetti and Dr. Claude Delmas for welcoming me at the Centre de Recherche Paul Pascal (CRPP) and the Institute de Chimie de la Matière Condensée de Bordeaux (ICMCB) as a PhD scholar. I acknowledge the generous support and the great working environment of both laboratories. I also thank Prof. Jean Etourneau for his support in scientific research and funding since my master FAME. I am grateful to Prof. Jesper Bendix, Prof. Andreas Hauser, Dr. Philippe Saintavit, Dr. Philippe Richetti, Prof. Claude Coulon for dedicating their precious time to evaluate this thesis. I must also thank Prof. Jin-Ho Choy for all his support since when I was in master course in Korea. He encouraged me to go abroad to study and introduced me the FAME master program: he is one of the biggest reasons I am here.

I would like to express my sincere gratitude to my supervisors, Rodolphe Clérac and Corine Mathonière for their invaluable support, guidance, inspiration, encouragement, and confidence on me. I very much appreciate everything they have done in the course of the supervision of this thesis. They also allowed me a great freedom on my research to be independent by myself, with knowing to give good advices at the right moment. Especially, Rodolphe has convinced me to carry on a PhD when I hesitated a lot at the end of my master: it's only because of him I could open my eyes and my mind to the world of research in molecular magnetism. His dynamic attitude and his passion on research were always good model for me. I am grateful to Corine for her warm cares during my thesis. Her optimistic attitude, good mood, and patience were always helpful for both scientific and non-scientific discussion. I will keep in mind their advices and comments for all along my scientific career.

I must express many thanks to Claude Coulon for his immense contribution to this thesis. He dedicated his precious time to teach me all physical matters not only for the thesis but also for my general scientific knowledge, with his exceptional pedagogic way. Without him, my thesis would never have been same as it is.

I thank Wolfgang Wernsdorfer for welcoming me in his laboratory to perform the micro-SQUID measurements and to treat the data. It was such a great opportunity to work and discuss with him. I appreciate Pierre Dechambenoit, Philippe Guionneau, Stanislav Péchev, Yangguang Li for their help and discussion on all scientific and technical problems to collect, solve, and refine my crystal structures.

I also thank all people who participated on my thesis project: Lollita Lecren for the initiation of one of my projects, Sergiu Calancea, Anangamohan Panja, Dalice M. Piñero Cruz for the preparation of precursors, Olivier Roubeau and Patrick Rosa for scientific discussion, Alain Wattiaux for Mössbauer, Fabien Durola and Wilfrid Neri for NMR, Nicolas Mano for electrochemistry, Gilles Sigaud for DSC, Mathieu Rouzières for SQUID and glove box, Béatrice Agricole for FT-IR. Without their help, I could not accomplish my work promptly and properly.

I would like to thank my previous office mates and laboratory colleagues for offering me such a nice environment and helping me in many senses: Elizabeth Hillard, Rodica ababei, Diana Siretanu, Oleg Palamarciuc, Céline Pichon, Vivien Pianet, Indrani Bhowmick, Dmitri Mitcov, Mihail Secu, Marguerite Kalisz, Kasper Steen Pedersen, and Evangelia Koumoussi. I wish bright careers with them. I also thank an internship student who worked with me, Soraya Bourdin, for her cheers till the end of my thesis.

I express my gratitude to the people from all departments of CRPP and ICMCB: cellules chimie, service gestion, informatique, instrumentation, bâtiment, bibliothèque, especially Stephane Gineste, Mbolotiana Rajaoarivelo, Anne Facq and Jean-Luc Laborde for their hands whenever I need.

Now my thanks are oriented to the people who shared one of the important parts of everyday laboratory life: I have met many friends including the most important in my life. I especially appreciate Olivier Merchier, Clémence Tallet, Ludivine Malassis, Hélène Fay, Christophe Coutant, Kévin Ehhardt, Paula Aldeanueava, and Veronica Castillo for sharing lunch and coffee time and also for the evening going out and sports time to time. I thank also Ahmed Bentaleb with “Club de Running des Petites Poulettes” and Mbolotiana Rajaoarivelo for my sportive life during these three years.

Away from the laboratory, thanks to Paula, Deniz, Ren Wei, Hongfeng, Basak, Oyku, Andreas and Julien for sharing joyful moments at the beginning of Bordeaux life. Especially thousands of thanks to Julien for his immense support, help, and encouragement, especially during all my PhD. Then, I met Katerina, Olivier, Dalice, Rémi, Diego, Alessandro, Melissa, and Victoria. Many thanks to them for sharing great brunches, evenings, cookings, parties, and trips. Also thanks to only one Korean friend in Bordeaux, Eun-Jung, for her presence and help, and all my friends in Korea for their cheers.

Last but not least, I would like to thank my parents and my family for their encouragement and eternal support throughout my life.

November, 2012

Ie-Rang Jeon



Table of Contents

General introduction	1
I. Theoretical aspects	3
I.1 Single-molecule magnets (SMMs)	5
I.1.1 Slow relaxation of the magnetization	6
I.1.2 Quantum tunneling of the magnetization (QTM)	10
I.2 Single-chain magnets (SCMs)	12
I.2.1 Static properties	13
I.2.2 Dynamic properties	16
I.3 Spin crossover (SC) and electron transfer (ET) systems	17
I.3.1 Ideal solution model: conversion	20
I.3.2 Regular solution model: from conversion to transition	22
I.4 Conclusion	24
I.5 Supporting information	26
References	33
II. State of the art and contexts	36
II.1 SMM-based coordination networks.....	36
II.1.1 Dinuclear SMMs.....	37
II.1.1.1 [Mn ₂] SMMs.....	37
II.1.1.2 [Dy ₂] SMMs	40
II.1.1.3 [CuTb] and [NiDy] SMMs	41
II.1.2 Trinuclear SMMs.....	43
II.1.2.1 [Mn ₃] SMMs	43
II.1.2.2 [Mn ₂ Ni] and [Mn ₂ Fe] SMMs.....	46
II.1.3 Tetranuclear SMMs	46
II.1.3.1 [Mn ₄] SMMs.....	46
II.1.3.2 [Co ₄] SMMs.....	50
II.1.4 Higher nuclearity SMMs	52
II.1.4.1 [Mn ₁₇] SMMs.....	52
II.1.5 Concluding remarks.....	53
II.2 Photoactive cyanido-based bimetallic materials.....	54
II.2.1 3D to 1D molecule-based systems.....	54
II.2.2 Toward molecular complexes.....	57
II.2.3 Concluding remarks.....	60

II.3 Conclusion and motivation	60
References	62
III. Coordination assemblies based on [Mn₄] SMMs	68
III.1 1D assemblies with diamagnetic chlorido ligands	68
III.1.1 Syntheses and general structural comments	68
III.1.2 Structural description of 1	69
III.1.3 Structural description of 2	71
III.1.4 Static magnetic properties of 1 and 2	75
III.1.5 Dynamic magnetic properties of 1 and 2	80
III.1.6 Concluding remarks for 1 and 2	84
III.2 1D and 2D assemblies with paramagnetic metal(II) picolinate	85
III.2.1 Synthetic approach	85
III.2.2 Crystallographic characterizations	86
III.2.3 Magnetic properties of 3	90
III.2.4 Magnetic properties of 4	93
III.2.5 Magnetic properties of 5	101
III.2.6 Concluding remarks for 3 – 5	103
III.3 Conclusion and perspectives	104
III.4 Supporting information	107
III.4.1 Experimental section	107
III.4.2 Supporting figures	110
III.4.3 Theoretical model: chain of alternating Ising and isotropic spins	112
References	123
IV. Heterometallic molecular systems based on [Fe(BBP)(CN)₃]²⁻ building block	128
IV.1 Dinuclear [FeCo] system	128
IV.1.1 Synthetic approach, compounds 6, 7 and 8	128
IV.1.2 Structures and magnetic properties of precursor complexes, 6 and 7	129
IV.1.3 Solid-state properties	132
IV.1.4 Solution properties	137
IV.1.5 Model of the protonation mechanism	142
IV.1.6 Concluding remark	146
IV.2 Trinuclear [Mn ₂ Fe] system	147
IV.2.1 Synthetic approach	147
IV.2.2 Structural description	148
IV.2.3 Magnetic properties	150

IV.2.4 Concluding remark.....	154
IV.3 Conclusion and perspectives.....	154
IV.4 Preliminary results	156
IV.4.1 Dinuclear [(bbp)Fe(CN) ₃ Co(PY5R ₂)] systems (R = Me, H, OH)	156
IV.4.2 Dinuclear [(Tp)Fe(CN) ₃ Co(PY5Me ₂)] ⁺ system	159
IV.4.3 Heterometallic [MnFe] systems	172
IV.5 Supporting information	174
IV.5.1 Experimental section.....	174
IV.5.2 Supporting figures.....	178
References	181
General conclusion and perspectives	183
Abbreviations and physical constants	187
List of publications	189

General introduction

The rational design of molecule-based materials is currently a subject of worldwide research activity, largely driven by the rapid development of modern technology that requires better performance from existing materials (Bradshaw et al. 2005; Bruce et al. 2010; Yen et al. 2012). This line of research is extremely active thanks to the development of coordination chemistry and molecular engineering. They offer a molecular approach to select the properties of the precursors and linkers to obtain materials with desired architectures and physical properties (Dinolfo et al. 2001; Lehn 1995; Öhrström et al. 2005).

This tremendously growing field also offers different alternatives to produce magnetic materials that are indispensable in our present life. Classical magnets, such as iron, cobalt, chromium oxide, or alloys of rare-earth metals are rigid and require energy-intensive and high temperature metallurgical methods (Buschow 1986; Robinson 1984). The aforementioned features prompted researchers to develop novel type of magnets, namely molecule-based magnets, which are magnetic materials designed and constructed using a molecular approach (Miller et al. 2001; Miller et al. 2011). It is worth noting that one of the breakthroughs in this field is the synthesis of the first molecule-based ferrimagnet in a premeditated manner (Kahn et al. 1988).

In general, molecule-based magnets can be prepared at room temperature allowing the possibility of subtle modifications comparable to organic syntheses. Thus, magnetic materials with solubility in organic solvents, transparency, and low density can be obtained. In these systems, the magnetic interactions between building units and consequently the final properties of the material can be also controlled in a rational manner by changing the linkers that mediate exchange interactions. Moreover, linkers with useful functionalities can be combined to the original magnetic building blocks. Incorporating both of them in a network may induce synergistic effects between co-existing properties, and eventually lead to high-performance magnets for electronic, magnetic, photonic devices, with potential uses ranging from medical imaging to sensor and data storage, etc.

One of the most conspicuous achievements in the field of molecule-based magnets is the synthesis of high-temperature magnets based on various molecular precursors. In 1991, the first room temperature molecule-based magnet, $V(\text{TCNE})_2$, was discovered (Manriquez et al. 1991), and later in 1995 the Prussian blue analogue $[V^{II}_{0.42}V^{III}_{0.58}(\text{Cr}(\text{CN})_6)_{0.86}] \cdot 2\text{H}_2\text{O}$ was reported to order at 315 K (Ferlay et al. 1995). Following these seminal works, numerous compounds based on hexacyanidometalates ($M = \text{Cr}, \text{V}$) (Entley and Girolami 1995; Ferlay et al. 1995; Hatlevik et al. 1999; Holmes et al. 1999), heptacyanidometallates ($M = \text{Mo}$) (Larionova et al. 1998; Milon et al. 2007; Tanase et al. 2003; Tomono et al. 2010), and octacyanidometallates ($M = \text{Mo}, \text{Nb}, \text{W}$) (Imoto et al. 2012) were reported with a critical temperature up to 376 K. In addition, building units possessing metal-to-metal electron transfer and, more recently, spin crossover properties were introduced in Prussian blue analogues to generate multi-functional magnets (Arimoto et al. 2003; Ohkoshi et al. 2011; Tokoro et al. 2008). Under the external stimuli such as temperature or light irradiation, these additional phenomena result in changes of electronic spin state of one or more metal ions inside the network, and consequently induce magnetic ordering.

As shown above, numerous researchers have tried to achieve high temperature magnets through designing three-dimensional metal complexes with cyanido bridges. This line of research was

partially fuelled by the potential applications in information storage devices working at room temperature. On the other hand, a considerable research effort has been also devoted to the synthesis of systems at the nanometer scale in order to reduce the size of the magnetic units for the storage of information, and therefore the size of devices. Different approaches have been used to obtain mono-domain magnetic particles, but the early 90s was marked by the discovery of the single-molecule magnets (SMMs) (Boyd et al. 1988; Caneschi et al. 1991; Sessoli et al. 1993). These paramagnetic complexes have generated great expectations to code information on single molecules of this type and thus dramatically reduce the size of magnetic storage units. Therefore, it is becoming of strategic importance to dedicate a part of our research to the organization of molecules in order to achieve devices for applications. Many groups in the world have considered this research strategy in top priority.

In the group “Magnetic Molecular Materials” (M^3) in Centre de Recherche Paul Pascal (CRPP), we are interested in the organization of SMMs into coordination networks. During the thesis of L. Lecren (2002 – 2006), she has shown the possibility to organize SMMs through diamagnetic linkers such as dicyanamide, azide, acetate. She developed new SMMs based on $[Mn_4]$ core (Lecren et al. 2005a; Lecren et al. 2005c), and also 1D networks in which $[Mn_4]$ SMMs are antiferromagnetically coupled (Lecren et al. 2008; Lecren et al. 2005b). Then, the thesis work of R. Ababei (2007 – 2011) was dedicated to the organization of $[Mn_2(SB)_2]^{2+}$ (SB = Schiff base) SMMs with tunable magnetic linkers, in order to create switchable SMM-based systems. She mainly focused on the Fe^{II} spin crossover complex as a coordinating linker, leading isolated bimetallic complexes and chains (Ababei 2011). In these complexes, Mn^{III}_{HS} ($S = 2$) and Fe^{II}_{HS} ($S = 2$) are antiferromagnetically coupled, and therefore a compensation of magnetic moments is observed.

To continue the foregoing works, we propose two different approaches to answer some of the questions facing in the group and in the field of molecular magnetism. The first one is to utilize paramagnetic linkers that may favor strong magnetic interactions and an effective ferromagnetic arrangement of the SMM units, finally to enhance the characteristics and the performance of these SMM-based systems. The second one is to develop new photo-responsive electron transfer complexes and SMMs with an ultimate goal of assembling them, finally to realize photo-switchable magnet. This second part of work is conducted in collaboration with group VI in Institut de Chimie de la Matière Condensée de Bordeaux (ICMCB). Chapter I contains the theoretical backgrounds and characteristics in the four important classes of magnetic coordination complexes that are considered in this thesis: single-molecule magnets, single-chain magnets, spin crossover, and electron transfer systems. This chapter will help the readers from different domains to follow the subsequent chapters. Chapter II provides a general view of the state of the art in the frame of this thesis project. Concerning the two different parts of thesis, we highlight both (i) organization of SMMs in coordination networks and (ii) photoactive cyanido-based bimetallic materials. Chapter III presents the organization of $[Mn_4]$ SMMs *via* diamagnetic and paramagnetic linkers, emphasizing syntheses and extensive discussion on crystallography and magnetic properties. Chapter IV is devoted to the novel cyanido-bridged SMM and multifunctional complexes that are characterized by extensive chemical and physical methods. Finally, we will provide a conclusion to this work with emphasizing perspectives to enrich the field of molecule-based magnetism.

- Ababei R (2011) PhD Thesis. Bordeaux 1 University.
- Arimoto Y, Ohkoshi S, Zhong ZJ, Seino H, Mizobe Y, Hashimoto K (2003) *J. Am. Chem. Soc.* 125, 9240.
- Boyd PDW, Li Q, Vincent JB, Folting K, Chang HR, Streib, WE, Huffman JC, Christou G, Hendrickson DN (1988) *J. Am. Chem. Soc.* 110, 8537.
- Bradshaw D, Claridge JB, Cussen EJ, Prior TJ, Rosseinsky MJ (2005) *Acc. Chem. Res.* 38, 273.
- Bruce DW, O'Hare D, Walton R (2010) *Molecular Materials*. John Wiley & Sons, UK.
- Buschow KHJ (1986) *Materials Science Reports* 1, 1.
- Caneschi A, Gatteschi D, Sessoli R, Barra AL, Brunel LC, Guillot M (1991) *J. Am. Chem. Soc.* 113, 5873.
- Dinolfo PH, Hupp JT (2001) *Chem. Mater.* 13, 3113.
- Entley WR, Girolami GS (1995) *Science* 268, 397.
- Ferlay S, Mallah T, Ouahes R, Veillet P, Verdaguer M (1995) *Nature* 378, 701.
- Hatlevik Ø, Buschmann WE, Zhang J, Manson JL, Miller JS (1999) *Adv. Mater.* 11, 914.
- Holmes SM, Girolami GS (1999) *J. Am. Chem. Soc.* 121, 5593.
- Imoto K, Takemura M, Tokoro H, Ohkoshi S (2012) *Eur. J. Inorg. Chem.* 2649.
- Kahn O, Pei Y, Verdaguer M, Renard JP, Sletten J (1988) *J. Am. Chem. Soc.* 110, 782.
- Larionova J, Clérac R, Sanchiz J, Kahn O, Golhen S, Ouahab L (1998) *J. Am. Chem. Soc.* 120, 1388.
- Lecren L, Li Y-G, Wernsdorfer W, Roubeau O, Miyasaka H, Clérac R (2005a) *Inorg. Chem. Commun.* 8, 626.
- Lecren L, Roubeau O, Coulon C, Li Y-G, Le Goff XF, Wernsdorfer W, Miyasaka H, Clérac R (2005b) *J. Am. Chem. Soc.* 127, 17353.
- Lecren L, Roubeau O, Li Y-G, Le Goff XF, Miyasaka H, Richard F, Wernsdorfer W, Coulon C, Clérac R (2008) *Dalton Trans.* 755.
- Lecren L, Wernsdorfer W, Li Y, Roubeau O, Miyasaka H, Clérac R (2005c) *J. Am. Chem. Soc.* 127, 11311.
- Lehn J-M (1996) *Supramolecular Chemistry*, John Wiley & Sons.
- Manriquez JM, Yee GT, Mclean RS, Epstein AJ, Miller JS (1991) *Science* 252, 1415.
- Miller JS, Drillon M (2001) *Magnetism: Molecules to Materials I – V*. John Wiley & Sons.
- Miller JS, Gatteschi D (2011) *Themed issue: Molecule-based magnets. Chem. Soc. Rev.* 40, 3053.
- Milon J, Daniel M-C, Kaiba A, Guionneau P, Brandès S, Sutter J-P (2007) *J. Am. Chem. Soc.* 129, 13872.
- Ohkoshi S, Imoto K, Tsunobuchi Y, Takano S, Tokoro H (2011) *Nature Chem.* 3, 564.
- Robinson AL (1984) *Science* 223, 920.
- Sessoli R, Tsai HL, Schake AR, Wang S, Vincent JB, Folting K, Gatteschi D, Christou G, Hendrickson DN (1993) *J. Am. Chem. Soc.* 115, 1804.
- Tanase S, Tuna F, Guionneau P, Maris T, Rombaut G, Mathonière C, Andruh M, Kahn O, Sutter J-P (2003) *Inorg. Chem.* 42, 1625.
- Tokoro H, Matsuda T, Nuida T, Moritomo Y, Ohoyama K, Dangui EDL, Boukheddaden K, Ohkoshi S (2008) *Chem. Mater.* 20, 423.
- Tomono K, Tsunobuchi Y, Nakabayashi K, Ohkoshi S (2010) *Inorg. Chem.* 49, 1298.
- Yen Y-S, Chou H-H, Chen Y-C, Hsu C-Y, Lin JT (2012) *J. Mater. Chem.* 22, 8734.
- Öhrström L, Larsson K (2005) *Molecule-based materials*. Elsevier Science, Amsterdam

I. Theoretical aspects

I.1 Single-molecule magnets (SMMs)	5
I.1.1 Slow relaxation of the magnetization	6
I.1.2 Quantum tunneling of the magnetization (QTM)	10
I.2 Single-chain magnets (SCMs)	12
I.2.1 Static properties	13
I.2.2 Dynamic properties	16
I.3 Spin crossover (SC) and electron transfer (ET) systems	17
I.3.1 Ideal solution model: conversion	20
I.3.2 Regular solution model: from conversion to transition	22
I.4 Conclusion	24
I.5 Supporting information	26
References	33

The field of molecular magnetism has rapidly expanded with remarkable improvements, thanks to the possible interdisciplinary research between chemistry and physics. Materials in this field are built through the bottom-up approach that allows a judicious choice of building blocks (metals and ligands, or the coordination complexes). In this way, we can predict and control not only the structural dimensionalities and geometries but also the related magnetic properties. Especially, the advantage of the molecular materials is that molecules are all identical to each other, therefore allowing relatively easy experiments on large assemblies of them, while still being able to monitor, for example, quantum effects. This means that we can relate the macroscopic properties and the microscopic ones through studying the simple quantum mechanics and thermodynamics. Therefore, an understanding of the underlying physics of the system is important for chemists in order to construct a delicate strategy to design magnetic materials with desired and enhanced properties. In this regard, we will discuss the theoretical tools in this chapter.

Even though all details of physical concepts concerning molecular magnetic materials cannot be covered in this chapter, the basic and essential concepts that will be useful to help the readers in the following chapters are summarized here. This thesis is focused on the organization of single-molecule magnets through different types of linkers. Our objective is to develop magnetic materials with enhanced properties and photomagnetic materials. Therefore, the work along this thesis will cover following four topics: single-molecule magnets, single-chain magnets, spin crossover, and electron transfer systems.

I.1 Single-molecule magnets (SMMs)

Over the last couple of decades, a considerable research effort has been devoted to the synthesis of systems at the nanometer scale in order to reduce the size of the magnetic units for information storage, and therefore the size of devices. Different approaches have been used to obtain mono-

domain magnetic particles, but the early 90s was marked by the discovery of the single-molecule magnets (SMMs) that gave the hope to store one bit of information on a single molecule (Boyd et al. 1988; Caneschi et al. 1991; Leuenberger et al. 2001; Sessoli et al. 1993). A SMM molecule becomes a tiny magnet, in the sense that if magnetized by an applied field it retains the magnetization below the so-called blocking temperature,¹ giving rise to M vs H hysteresis loops (Christou et al. 2000; Gatteschi et al. 2003; Sessoli et al. 1993). Meanwhile, its well-defined structure with well-characterized spin ground state and magnetic anisotropy make the observation of quantum phenomena possible. Especially, a crystal contains sets of symmetry-wise identical SMM molecules in a same orientation, which allow direct access to single molecule properties by macroscopic measurements. Thus, this led to the first observation of quantum tunneling of the magnetization (Aubin et al. 1998; Sangregorio et al. 1997; Thomas et al. 1996) and quantum phase interference effects (Lecren et al. 2005; Wernsdorfer et al. 2005; Wernsdorfer et al. 2002b; Wernsdorfer et al. 2000; Wernsdorfer et al. 1999) in magnets. At the same time, a large community of chemists has been also working on the improvement of SMM characteristics and extraordinary advances have been made over the last two decades resulting in a huge number of new SMMs in scientific literatures. Remarkable results were reported recently, such as the slow relaxation of the magnetization in mononuclear complexes including lanthanides (AlDamen et al. 2008; Ishikawa et al. 2003), actinides (Rinehart et al. 2009), and even in 3d transition metals (Freedman et al. 2010; Harman et al. 2010; Jurca et al. 2011; Lin et al. 2011). In parallel, dysprosium-containing molecules present notably large energy barriers as high as 530 K (Blagg et al. 2011), and show magnetic hysteresis up to 8.3 K at a sweep rate of 0.08 T s^{-1} (Rinehart et al. 2011). In the following paragraphs, basic physics of SMMs are described to understand how these complexes are capable to show not only the classical magnet-like behavior but also the quantum properties.

I.1.1 Slow relaxation of the magnetization

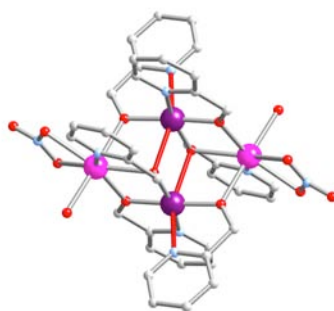


Figure I.1 View of the $[\text{Mn}_4]$ core in $[\text{Mn}_4(\text{hmp})_6(\text{NO}_3)_2(\text{H}_2\text{O})_2](\text{NO}_3)_2 \cdot 2.5\text{H}_2\text{O}$ (**1**) (Lecren et al. 2005). The JT axes on Mn(III) ions are highlighted in red. Mn(III) violet, Mn(II) purple, C grey, O red, N light blue. The hydrogen atoms have been omitted for clarity.

The $[\text{Mn}_4]$ SMM molecule, $[\text{Mn}_4(\text{hmp})_6(\text{NO}_3)_2(\text{H}_2\text{O})_2](\text{NO}_3)_2 \cdot 2.5\text{H}_2\text{O}$ (**1**) (Lecren 2006; Lecren et al. 2005),² that is used as building blocks along this thesis work is chosen to illustrate SMM properties in this section. It has a mixed-valence $[\text{Mn}^{\text{III}}_2\text{Mn}^{\text{II}}_2]$ core with manganese ions arranged in a double-cuboidal fashion (**Figure I.1**). In most cases, all manganese ions (Mn^{III} , $S = 2$; Mn^{II} , $S = 5/2$) are ferromagnetically coupled to give an $S_{\text{T}} = 9$ spin ground state (Lecren et al. 2005; Yoo et al. 2001).

¹ A blocking temperature can be defined only with the given frequency.

² The experimental data from these references will be used in this section, to describe details of SMM properties.

The central Mn^{III} ions exhibit a Jahn-Teller (JT) distortion (Jahn 1938; Jahn and Teller 1937) that induces a magnetic anisotropy on $[\text{Mn}_4]$ molecule. Therefore, the direction of two JT axes that are parallel in a molecule can be considered as an easy direction of the magnetization for these complexes.

Let's consider now the above SMM as a macro-spin S_T with the three directions of the magnetization (x , hard; y , intermediate; z , easy). A spin quantum number S_T possesses $2S_T + 1$ sub levels, each characterized by a spin projection quantum number m_S , where $-S_T \leq m_S \leq S_T$. The simple way to describe a SMM in the presence of a magnetic field is given by the following Hamiltonian (H_{tot}):

$$H_{\text{tot}} = DS_{T,z}^2 + E(S_{T,x}^2 - S_{T,y}^2) - g\mu_B \vec{S}_T \cdot \vec{H} \quad \text{Eq I.1}$$

where S_T is the total spin ground state, $S_{T,x}^2$, $S_{T,y}^2$, $S_{T,z}^2$ spin operators along the three principal directions of magnetization, D and E are easy axis and transverse anisotropy parameters (that arise due to geometrical deviations from perfect uniaxial symmetry), g is the Landé factor and μ_B is the Bohr magneton. The last term is the Zeeman effect contribution that characterizes the interaction of spin with external magnetic field. In the presence of a strong uniaxial anisotropy (D is negative and $|D| \gg E$), the E parameter can be neglected resulting the simplified Hamiltonian (H_D) as below:

$$H_D = DS_{T,z}^2 - g\mu_B \vec{S}_T \cdot \vec{H} \quad \text{Eq I.2}$$

The energies of the spin sublevels corresponding to H_D are in fact easy to calculate when H is along the easy direction:

$$E_{m_S} = Dm_S^2 - g\mu_B m_S H_Z \quad \text{Eq I.3}$$

The level energies given by Eq I.3 can be plotted as shown in upper part of **Figure I.2**. When no external field is applied, the levels form degenerate pairs except for $m_S = 0$. With applying a longitudinal field (along z), the sublevels with positive m_S values become energetically stabilized while sublevels with negative m_S values are destabilized. Therefore, energy levels of positive and negative quantum numbers cross at certain fields $H_Z^{(n)}$:

$$H_Z^{(n)} = nD / g\mu_B. \quad \text{Eq I.4}$$

with $n = 1, 2, 3, \dots$. The strong enough field leads to a preferred population of the $m_S = +9$ sublevel corresponding to a favored orientation of the microscopic magnetic moments in the direction of the external field. The induced effect is a magnetization of the macroscopic sample.

An alternative representation of the energy distribution of m_S states is given on bottom part of **Figure I.2**. The population that was equal at zero field (**Figure I.2**, bottom left) will be in $m_S = +9$ states at high enough H_Z (**Figure I.2**, bottom middle) and low enough temperature. On the removal of the external field, the system must go back to thermal equilibrium, meaning that half of molecules return to $m_S = -9$, in order for the magnetization to go back to zero. This relaxation process occurs through the coupling of the spin system with the environment. If there is sufficient thermal energy ($k_B T$) then the molecule can absorb heat from the vibrational modes of the lattice (phonons). Due to the selection rules of spin-phonon interaction, the only allowed paths are $\Delta m_S = \pm 1$ and ± 2 . Thus, in order to relax to the equilibrium state, the system must successively absorb phonons until it reaches $m_S = 0$, then it can reach $m_S = -9$ through phonon emission (**Figure I.2**, bottom right). This is the origin of the thermal energy barrier to the slow relaxation of the magnetization in SMMs.

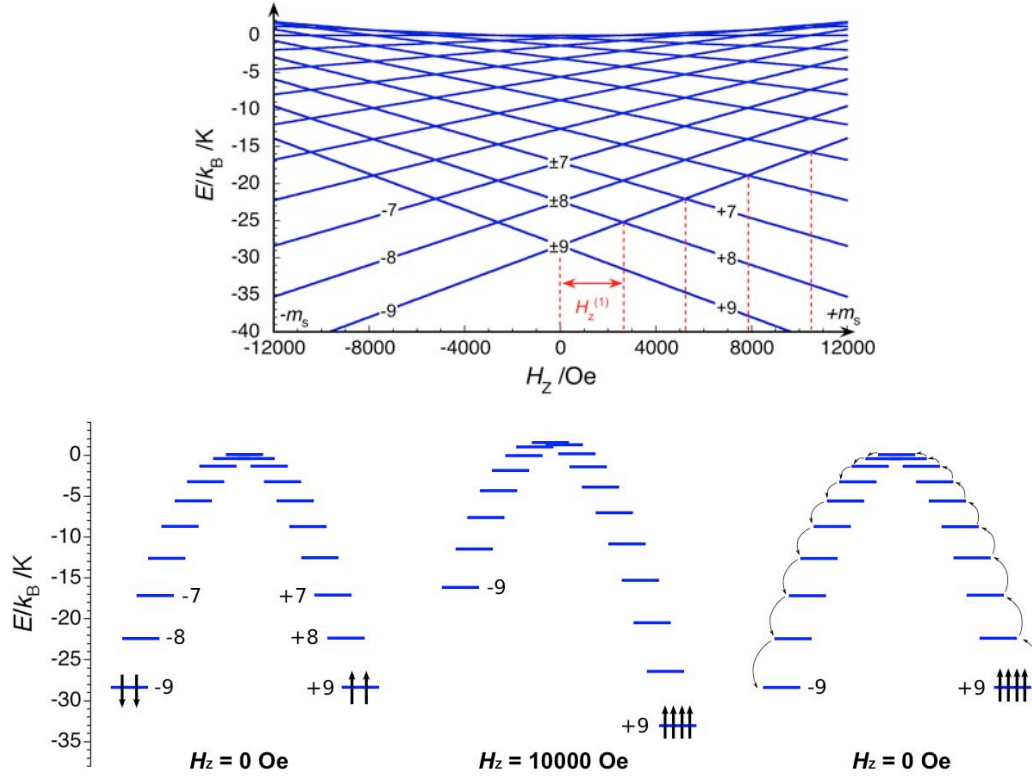


Figure I.2 Top: Zeeman diagram for $S_T = 9$ with $D/k_B = -0.35$ K and a magnetic field applied along the z axis. The transverse anisotropy term is neglected. Bottom: Energy distribution of the m_S states for $S_T = 9$ with $D/k_B = -0.35$ K in zero (left) and 10000 Oe (middle) applied field along the z axis, and after removing the field (right) assuming only the lowest states are populated. Each black arrow indicates one macrospin, S_T . The curled arrows indicate the path to relaxation *via* absorption and then emission of thermal energy from/to lattice.

The relaxation can be monitored by measuring the time decay of the magnetization, $M(t)$. In a simple case, the magnetization decreases exponentially with the time at fixed temperature:

$$M(t) = M_0 \exp(-t / \tau) \quad \text{Eq I.5}$$

where $M_0 = M_S(t = 0)$ is the saturation magnetization, $M(t)$ is the magnetization at a given time t and τ is the relaxation time. By calculating the transition probabilities between different m_S states as a function of temperature from Eq I.5 (Villain et al. 1994), it can be demonstrated that the relaxation of the magnetization is temperature dependent and follows the Arrhenius law:

$$\tau = \tau_0 \exp(\Delta_A / k_B T) \quad \text{Eq I.6}$$

where Δ_A is the energy barrier, k_B is the boltzmann constant, and τ_0 is the pre-exponential factor, a constant that can be experimentally determined and depends on the nature of SMM and its environment. The energy barrier is equal to $\Delta_A = |D|S_{T,z}^2$ for integer spins and $\Delta_A = |D|(S_{T,z}^2 - 1/4)$ for half-integer spins.

The most common experimental method that yields information about magnetization dynamics of SMMs is the alternating current (ac) magnetic measurements. The ac magnetic susceptibility produces two quantities: an in-phase (real) component χ' and an out-of-phase (imaginary) component χ'' as:³

³ The alternating field with a frequency ν ($\omega = 2\pi\nu$) and a amplitude H ($H_{ac}(\omega) = H \exp(i\omega t)$) induces the time-dependent magnetic moment in a sample: $M_{ac}(\omega) = M(\omega) \exp(i(\omega t + \phi(\omega)))$ and therefore, $\chi_{ac}(\omega) = (M/H) \exp(i\phi(\omega))$. Hence, real and

$$\chi_{ac} = \chi' + i\chi'' \quad \text{Eq I.7}$$

When the relaxation time τ of the compound is shorter than the characteristic experimental time τ_{exp} ($\tau_{\text{exp}} = (2\pi\nu_{\text{exp}})^{-1}$), the magnetization vector oscillates with the ac field, and only a static behavior is observed (only the real component χ'). However, when τ is longer than τ_{exp} , a dynamic behavior is perceived and the magnetization vector is dephased (non-zero imaginary component χ''). Experimentally, we can measure the χ'' vs T at a given frequency and the χ'' vs ν at fixed temperature (**Figure I.3**). The temperature or frequency where χ'' reaches its maximum value corresponds to the so-called blocking temperature (T_B), or blocking frequency (ν_B), respectively. The relaxation time can be deduced from the maxima of the $\chi''(T)$ and/or $\chi''(\nu)$ curves at T_B and ν_B . By plotting τ vs T^{-1} in semi-logarithm scale, we can see the linear variation of $\ln(\tau)$ depending on T^{-1} that indicates the thermally-activated relaxation of the magnetization (inset of **Figure I.4**). The slope of this curve gives the estimation of the energy barrier based on Eq I.6.

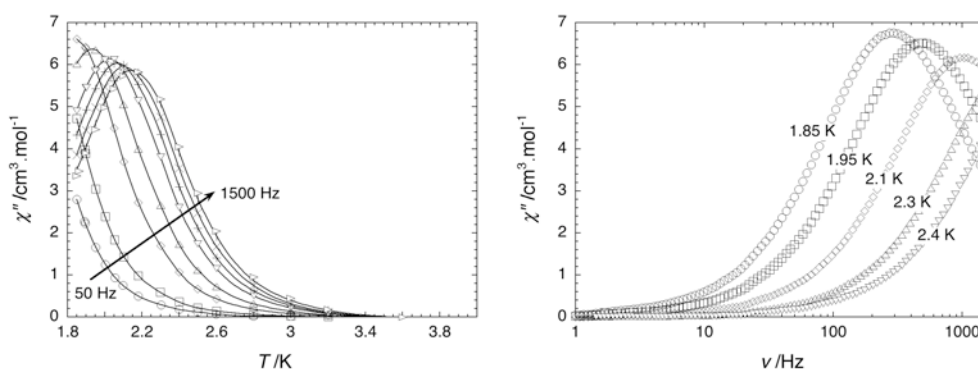


Figure I.3 Temperature (left) and frequency (right) dependence of out-of-phase susceptibility, χ'' , for **1** at different frequencies and temperatures as indicated, respectively, in zero dc field (Lecren 2006).

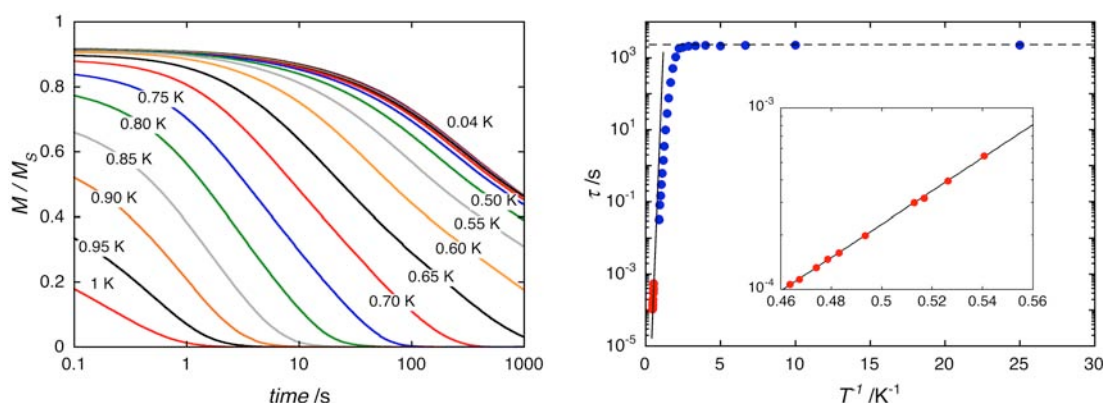


Figure I.4 Relaxation of the magnetization for **1** at different temperatures (left). τ vs T^{-1} plot of **1** determined by dc (blue dots) and ac (red dots) techniques. Inset: τ vs T^{-1} plot using ac data with Arrhenius fit in black solid line (Lecren 2006).

To complete the ac data and to ensure an accurate analysis over a wide range of temperature, time decay of direct current (dc) magnetization can be also measured (**Figure I.4**, left). First strong dc field is applied to the sample at a fixed temperature to saturate its magnetization in the easy direction. When the field is switched off, the magnetization is measured as a function of time. The experiment

imaginary components of ac susceptibility are given by: $\chi_{ac}(\omega) = \chi'(\omega) + i\chi''(\omega)$ with $\chi'(\omega) = \chi_0(\omega)\cos(\varphi(\omega))$ and $\chi''(\omega) = \chi_0(\omega)\sin(\varphi(\omega))$.

should be performed at different temperatures. Assuming the decay of the magnetization is an exponential function of time, the relaxation time τ is extracted at each temperature by taking $\tau = t$ when the M/M_S reaches $1/e$ based on Eq I.5. As shown in **Figure I.4**, the relaxation of compound **1** is thermally activated with $\Delta_{\text{eff}}/k_B = 20.9$ K and $\tau_0 = 6.7 \times 10^{-9}$ s between 1.8 and 2.4 K. Note that the experimentally found Δ_{eff}/k_B is lower than the expected barrier: $\Delta_A/k_B = \Delta_A = |D|S_{Tz}^2 = 28.4$ K (with $D/k_B = -0.35$ K determined from M vs H measurements. This result will be discussed in the following section). It can be explained by competition between two relaxation processes (thermal and quantum) that makes short-cut of the thermal barrier (thermally assisted quantum tunneling of the magnetization). Moreover, relaxation time below 1 K does not follow an Arrhenius law and saturates (**Figure I.4**, right), indicating the presence of quantum tunneling of the magnetization (QTM). Now the obvious question has to be asked: what is QTM and related phenomena in SMMs?

I.1.2 Quantum tunneling of the magnetization (QTM)

In the previous section I.1.1, we have assumed the strong uni-axial anisotropy of SMMs that can be described in Hamiltonian H_D (Eq I.2). As long as this Hamiltonian is valid the two $\pm m_S$ states are orthogonal to each other, and there is no mixing. Upon the scanning of external magnetic field, they simply cross over each other and the mechanism for tunneling does not exist (**Figure I.2**, top). In reality, however, there is always a transverse contribution, and therefore, the contribution of the following Hamiltonian H_E cannot be neglected:

$$H_E = E(S_{T,x}^2 - S_{T,y}^2) \quad \text{Eq I.8}$$

The transverse term containing $S_{T,x}$ or $S_{T,y}$ spin operators mixes two different m_S states and creates a gap (Δ , tunnel splitting) at the crossing of m_S levels (**Figure I.5**). The spin S is “in resonance” between two states when the local longitudinal field is close to this avoided level crossing. Thus QTM is allowed to take place with the probability (P) being related to the magnitude of the tunnel splitting.

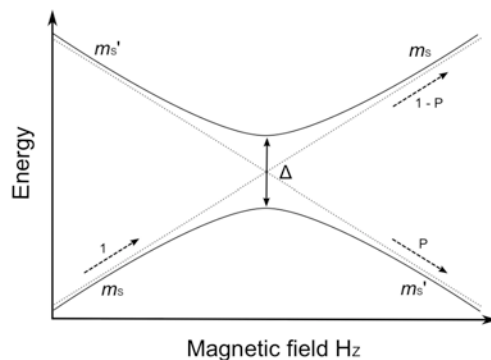


Figure I.5 Detail of the energy level diagram near an avoided level crossing. m_S and $m_{S'}$ are the quantum numbers of the energy level. Δ is the tunnel splitting and P is the tunneling probability when sweeping the applied field from the left to the right over the crossing point.

At low enough temperature where phonons are insufficient to promote population to $m_S = +8$, the temperature-independent quantum regime can be experimentally observed, as it becomes faster than the thermally activated relaxation. In zero field, states with $m_S = \pm 9$ quantum numbers having the same energy, and then, QTM between these pairs of levels is possible. In other words, this quantum

mechanism allows individual nanomagnets to reverse their spin and therefore the magnetization of the material to relax to zero. It is worth to note that there is an intermediate temperature regime where both thermally activated relaxation and QTM are important. This is easily understood from **Figure I.6**: at zero field $m_S = \pm 8, \pm 7$, and so on are in resonance in addition to $m_S = \pm 9$. Hence, spins can be thermally promoted to, for example, $+7$ by phonon absorption and then tunnel to -9 . This is “thermally assisted QTM” and it results in a short-cut through the thermal barrier. When a longitudinal field is applied, the probability of QTM for $\pm m_S$ states significantly decreases except for particular magnetic fields as defined in Eq I.4. At this field, “resonant quantum tunneling” is observed when two m_S states of opposite signs are raised at the same energy (**Figure I.6**). When sweeping the longitudinal dc field, the tunnel rate of relaxation becomes periodically faster than the thermal pathway creating steps on M vs H_Z curve at each particular value of H_Z . With this technique, the axial anisotropy, D , can be easily estimated. The experimental data of **1** shows regular steps of the loops correspond to resonant tunneling transitions between $m_S = -9$ and $m_S = +9$ (at -200 Oe), $m_S = +8$ (at 2400 Oe), $m_S = +7$ (at 5000 Oe) (**Figure I.6**, top) (Lecren et al. 2005). From the field separation between steps (~ 2600 Oe) and Eq I.4, D/k_B is estimated at -0.35 K. The small shift of the $m_S = \pm 9$ transition from zero field is due to the presence of very weak inter-SMM AF interactions.

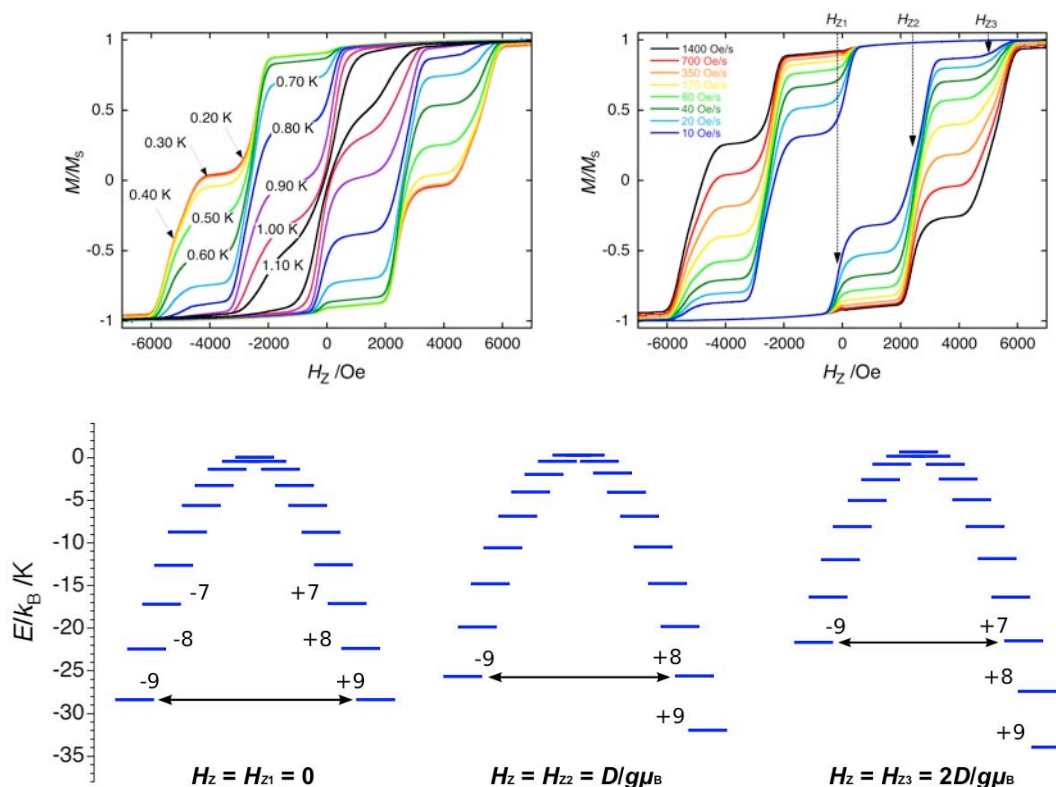


Figure I.6 Top: M vs H hysteresis loops in the average easy axis of monocrystal of **1**, in the temperature range of $1.10 - 0.04$ K at a 700 Oe/s sweep rate (left) and in the sweep rate range of $1400 - 10$ Oe/s at 0.04 K (Lecren 2006). Bottom: Resonant quantum tunneling between m_S levels on opposite sides of the barrier at specific applied fields, H_Z .

The tunnel splitting (Δ) can be qualitatively estimated indeed by measuring the tunneling probability, P .⁴ With a large negative magnetic field, H_Z , at very low temperature, all molecules are in

⁴ The tunneling probability P when sweeping the longitudinal field H_Z at a constant rate over an avoided energy level crossing (**Figure I.5**) is given by $P = 1 - \exp\{-\pi\Delta^2/[2\hbar g\mu_B|m_S - m_S'| \mu_0(dH_Z/dt)]\}$. (Wernsdorfer et al. 1999)

the $m_S = -9$ ground state (**Figure I.2**). Then, the longitudinal field, H_Z , is swept over the avoided crossing of a sample and the fraction of molecules that relaxes is measured. This fraction depends on the sweeping rate; that is, the slower sweeping rate induces the larger value of P . This is clearly shown in the M vs H hysteresis loop measurements showing larger steps for slower sweeping rate (**Figure I.6**, top). Using this method, a fascinating effect was observed with applying a transverse field, H_{tr} , in the xy plane:⁵ Δ oscillates with a characteristic period on increasing H_{tr} , rather than increasing monotonically. It has been interpreted as a “quantum phase interference” effect: constructive or destructive interference of quantum spin phases of two tunnel paths to give a maxima and minima in Δ depending on the strength of H_{tr} and the azimuth angle between H_{tr} and x .⁶ For $[\text{Mn}_4]$ SMM (**1**), the oscillation period, that is in good accord with the calculated value, was estimated at 0.40 kOe, leading to $E/k_B = +0.083$ K (Lecren et al. 2005).

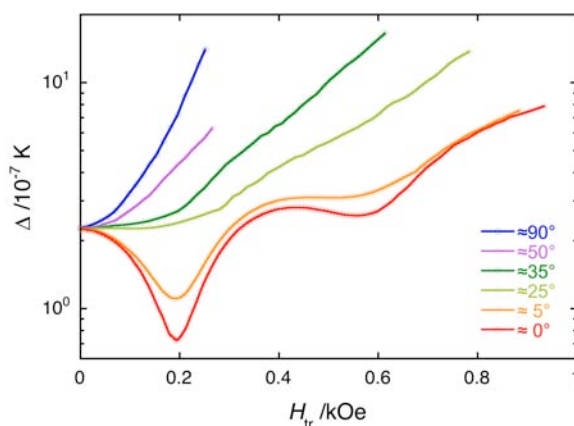


Figure I.7 Tunnel splitting (Δ) in **1** as a function of the transverse field rotated in the xy plane of the crystal (average hard direction: 0° ; average intermediate direction: 90°) for the $m_S = \pm 9$ quantum transition at 40 mK and a field sweep rate of 0.28 kOe/s (Lecren et al. 2005).

In this section, the physical background to understand SMM characteristics and associated experimental techniques was introduced based on $[\text{Mn}_4]$ SMM (**1**), that was used as a precursor to design high dimensional SMM networks described in Chapter III. It is worth noting that the explained quantum behaviors had long been predicted for quantum magnets but only became observable with the advent of SMMs. Other external effects on QTM in SMMs have also been investigated, including exchange coupling with another molecule (Wernsdorfer et al. 2002a) and excitation with electromagnetic radiation (Sorace et al. 2003). Now let us move into single-chain magnet (SCM) that is also one of the interesting molecule-based nanomagnets.

I.2 Single-chain magnets (SCMs)

Since the discovery of SMM offered an important step in the miniaturization process of future memory devices, much effort has focused on increasing the thermal energy barrier of this system to have a long enough relaxation time. This active research on molecular nanomagnets has also led to design of one-dimensional coordination systems with uncompensated magnetic moments that show

⁵ A second applied field in another direction is possible in micro-SQUID apparatus. (Wernsdorfer 2001)

⁶ The period of oscillation is given by: $\Delta H = 2k_B[2E(E + |D|)]^{1/2}/(g\mu_B)$.

slow relaxation of the magnetization (Caneschi et al. 2001). This type of magnet was called single-chain magnets (SCMs) by analogy to single-molecule magnets (Clérac et al. 2002). A purely 1D system does not exhibit any long-range order at a finite temperature, and therefore remains in paramagnetic state. Nevertheless, the combination of a large uni-axial anisotropy and intrachain magnetic interactions between high-spin magnetic units of the 1D arrangement promotes frozen situation of the magnetization at a finite temperature in the absence of an applied field. The relaxation of the magnetization becomes so slow at low temperature that these systems can then be considered as real magnet. As this situation is metastable, one of the important things is to understand slow dynamics to return to the equilibrium state. However, the description of the thermodynamic state is also a key point in the analysis of SCM properties. Especially an accurate understanding of SCM behavior is achieved only when both dynamic and thermodynamic data are consistently described. Thus, the following first two parts of this section will deal successively with simple thermodynamic description and then magnetic relaxation. Both parts are essentially devoted to a chain of ferromagnetically coupled Ising spins that gives the simplest approach for SCMs. However, some remarks will be given for the “Ising-like” systems that are closer to the real materials. Meanwhile, the experimental techniques to observe dynamics of SCMs can be consulted in the previous section for SMMs, as the resulted macroscopic dynamic behaviors in both SMM and SCM are superparamagnetic-like properties.

I.2.1 Static properties

As SCMs are composed of magnetically isolated chains, the magnetic measurements obtained for these systems essentially reveal the intrinsic behavior of a 1D system. To describe the magnetic chains, we can consider three different limits that can be described in a simple way: the classic-spin Heisenberg chain, the anisotropic Heisenberg chain, and the Ising chain (Coulon et al. 2006). For the Ising chain model, an exact solution can be obtained, in which the spins are assumed to be aligned along a given z easy axis. In this case, the spins possess an infinite uni-axial magnetic anisotropy. The corresponding Hamiltonian is given by:

$$H = -2J \sum_{i=-\infty}^{\infty} S_{i,z} S_{i+1,z} = -2JS^2 \sum_{i=-\infty}^{\infty} \sigma_i \sigma_{i+1} \quad \text{Eq I.9}$$

For any classical and Ising 1D models, the zero field susceptibility can be obtained according to the fluctuation-dissipation theorem:⁷

$$\frac{\chi T}{C} = \sum_{n=-\infty}^{n=+\infty} \langle \sigma_i \sigma_{i+n} \rangle \quad \text{Eq I.10}$$

with $\langle \sigma_i \sigma_{i+n} \rangle = u^n$ and $u = \langle \sigma_i \sigma_{i+1} \rangle$ being the nearest neighbors correlation function ($\langle \rangle$ means average on the chain), and C is the Curie constant ($C = g^2 \mu_B^2 S^2 / k_B$ for Ising model⁸) normalized per site. In practice $\langle \sigma_i \sigma_{i+n} \rangle$ indicates the probability that, if the spin i has +1 value, the spin $i+n$ also has +1 value. And this quantity decays exponentially with the characteristic length defined as the correlation length, ζ :

⁷ See supporting information.

⁸ In general, the Curie constant for Heisenberg model or quantum model is defined as $C = g^2 \mu_B^2 S(S+1) / 3k_B$.

$$u^n = \langle \sigma_i \sigma_{i+n} \rangle = \exp\left(-n \frac{a}{\xi}\right) \quad \text{Eq I.11}$$

with a being the cell parameter of chain. For Ising model with ferromagnetic interactions, u is given by (Marsh 1966):⁷

$$u = \tanh(2\beta JS^2) \quad \text{Eq I.12}$$

where $\beta = 1/k_B T$. At low temperature, the correlation function can be approximated by:

$$u \approx 1 - 2\exp(-4\beta JS^2) \quad \text{Eq I.13}$$

that approaches to 1. It means majority of spins is oriented in parallel fashion creating large magnetic domains of average size, 2ξ , separated by sharp domain walls.⁹ Following the Hamiltonian (Eq I.9), the energy necessary to create one of these domains (Δ_ξ) is:

$$\Delta_\xi = 4|J|S^2 \quad \text{Eq I.14}$$

Now, turning back to the susceptibility, Eq I.10 can be simplified as below:

$$\frac{\chi T}{C} = \sum_{n=-\infty}^{n=+\infty} \langle \sigma_i \sigma_{i+n} \rangle = \sum_{n=-\infty}^{n=+\infty} u^n = \left(2 \sum_{n=0}^{n=+\infty} u^n \right) - 1 = \frac{2}{1-u} - 1 = \frac{1+u}{1-u} \quad \text{Eq I.15}$$

which means that, the susceptibility can be directly obtained from the nearest neighbors spin-spin correlation function, u . Therefore, it leads the magnetic susceptibility as:

$$\frac{\chi T}{C} = \exp(4\beta JS^2) = \exp\left(\frac{\Delta_\xi}{k_B T}\right) \quad \text{Eq I.16}$$

For the anisotropic Heisenberg chain,¹⁰ Eq I.16 is also valid at low temperature when a system has large anisotropy (so-called “Ising-like” for $|D/J| \gg 4/3$). And a low temperature expansion yields:

$$\frac{\chi T}{C} \approx \frac{2\xi}{a} \quad \text{Eq I.17}$$

It is worth to note that in this low temperature limit, χT directly measures the magnetic correlation length that is indeed very general for all classical magnetic chains. As indicated in Eq I.16, a plot of $\ln(\chi T)$ vs T^{-1} will give a straight line in the Ising or anisotropic Heisenberg model, and the energy to create a domain wall (Δ_ξ) can be estimated from the slope.

For Ising model (Eq I.9), a compact expression of the field-dependence of the magnetization can be also obtained using the transfer matrix method:⁷

$$m = \frac{\sinh(g\mu_B S\beta H)}{\sqrt{\sinh^2(g\mu_B S\beta H) + \exp(-8\beta JS^2)}} \quad \text{Eq I.18}$$

⁹ Domain wall here is used to indicate two anti-parallel spins at the interface between two domains with opposite orientation. The fluctuation of infinite chain results in the creation of domains.

¹⁰ When the single-ion anisotropy is relevant, a finite magnetic anisotropy has to be considered. In this case, the corresponding Hamiltonian is $H = -2J \sum_{i=-\infty}^{\infty} \vec{S}_i \vec{S}_{i+1} + D \sum_{i=-\infty}^{\infty} \vec{S}_{iz}^2$. As long as $|D/J| \gg 4/3$, sharp domain walls are present with a creation energy still given by $\Delta_\xi = 4|J|S^2$ like in Ising model. This model is, thus, classified as “Ising-like”.

where m is the normalized magnetization per site: $m = M/M_S$. This expression indicates the magnetization at zero field is zero, implying the absence of the magnetic order at finite temperature. Thus, a phase diagram shows a critical point at $T = 0$ and $H = 0$, in the case of 1D Ising model.

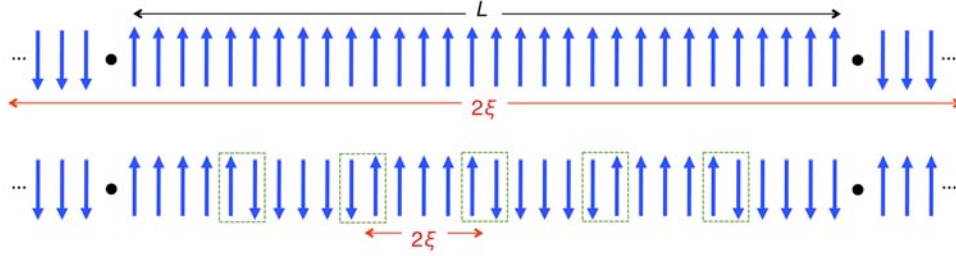


Figure I.8 Schematic view of a magnetic Ising chain (or Heisenberg anisotropic chain with $|D/J| \gg 4/3$)¹⁰ with oriented domains of a length of 2ξ separated by sharp domain walls (indicated in dashed green line), highlighting two different regimes: finite-size (top, $T < T^*$) and infinite-size one (bottom, $T > T^*$). The defects are depicted as black dots.

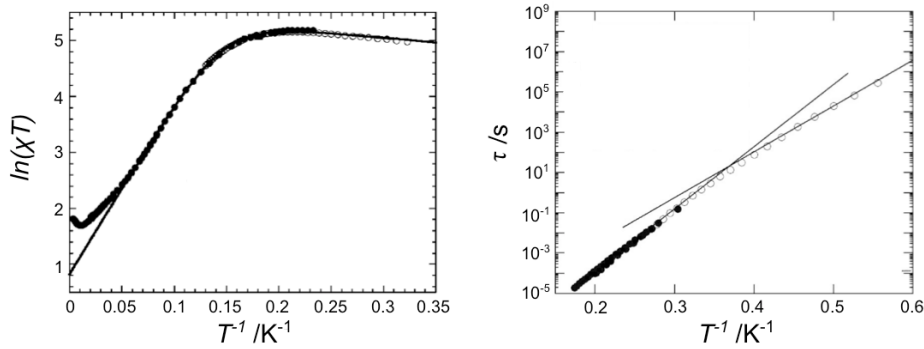


Figure I.9 Semilog plot of χT vs T^{-1} of a SCM, $[\text{Mn}_2(\text{saltmen})_2\text{Ni}(\text{pao})_2(\text{py})_2](\text{ClO}_4)_2$ (**2**) (Cl rac et al. 2002): solid line represents a fit using equation in footnote 11 (left). Semilog plot of τ vs T^{-1} of **2**: the corresponding straight lines give the energy gaps, $\Delta_{\tau 1}/k_B$ (74 K) and $\Delta_{\tau 2}/k_B$ (55 K) (right). The full and open dots were obtained from ac and dc measurements, respectively (Coulon et al. 2004).¹¹

It is worth to note that the aforementioned discussion concerns the chain size as infinite. In real systems, however, the chain length is limited by naturally occurring defects, like non-magnetic impurities, lattice dislocations, etc... At a given temperature, if $2\xi \ll L$ (L being the size of chain segments separated by defects) the system can be considered as infinite (infinite size regime, **Figure I.8** bottom). At very low temperatures, the creation of domain walls will cost too much energy, and therefore, the correlation length becomes longer than the distance between two defects in a chain ($2\xi \gg L$, finite size regime, **Figure I.8** top). In this regime, the system behaves like a collection of finite segments with an effective spin of size nS ,¹² showing Curie-like behavior ($\chi T/C \approx n$). This will be observed in $\ln(\chi T)$ vs T^{-1} plot as a saturation at low temperatures (**Figure I.9**, left). The temperature separating these two different regimes is called a crossover temperature (T^*). This finite size regime

¹¹ The difference of crossover temperature on the susceptibility and the relaxation time is due to the effects of poly-dispersity and weak inter-chain interactions (Coulon et al. 2006).

¹² We consider only mono-dispersed case. Considering an open uniform chain of n sites, the magnetic susceptibility per site can be calculated (Coulon et al. 2006):

$$\frac{\chi_n T}{C} = \exp(4\beta J S^2) \left(1 - \frac{2u(1-u^n)}{n(1-u^2)} \right)$$

The poly-dispersed model can be consulted in the reference (Coulon et al. 2006).

induced by the presence of defects plays also an important role in dynamics of the chain that are outlined in the following paragraph.

I.2.2 Dynamic properties

A remanent magnetization in the absence of an applied field can appear in SCMs as the result of slow dynamics and metastability. This phenomenon is associated, like in the case of SMMs, with an energy barrier to be overcome in order for the chain to reach the true equilibrium state. In order to describe this dynamics in which one microscopic state of the chain passes to the other, we indeed need a time-dependent Hamiltonian that is too complicated for a chain. However, we can consider the time-dependent probability from one microscopic state to the other state to describe the dynamics, as firstly proposed by Glauber (Glauber 1963). The interacting spins are represented by functions of time, $\sigma_i(t)$, in contact with a large thermal bath that induces spontaneous spin-flips. Glauber's model assumes only single-spin flips, and this transition probability per unit time that the i^{th} spin flips from σ_i to $-\sigma_i$ depends on the neighboring spins. This approach leads to an exponential decay of the magnetization with a single characteristic time (τ):⁷

$$\tau = \frac{\tau_0}{1 - \tanh(4\beta JS^2)} \quad \text{Eq I.19}$$

In the low temperature limit and for ferromagnetic interactions along the chain, Eq I.19 can be simplified as:

$$\tau = \frac{\tau_0}{2} \exp(8\beta JS^2) = \frac{\tau_0}{2} \exp(2\Delta_\xi / k_B T) \quad \text{Eq I.20}$$

The relaxation time can be expressed also by the correlation length, ξ :

$$\tau = 2\tau_0 \left(\frac{\xi}{a} \right)^2 \quad \text{Eq I.21}$$

Knowing that the correlation length diverges exponentially at low temperature, the relaxation time also evolves in the same sense.

In order to compare the above description of the dynamic properties with experimental data, the temperature dependence of the characteristic time, τ_0 , should be considered. As seen in the previous paragraph, τ_0 describes the time necessary for an isolated spin to flip. Concerning an anisotropic spin ($|D/J| \gg 4/3$),¹⁰ the spin experiences an energy barrier:

$$\Delta_A = DS^2 \quad \text{Eq I.22}$$

during its flip. Thus, τ_0 follows an Arrhenius law:

$$\tau_0(T) = \tau_i \exp(\Delta_A / k_B T) \quad \text{Eq I.23}$$

where the pre-factor τ_i describes the intrinsic dynamics of the spin in contact with the thermal bath, in the absence of an energy barrier. When Eq I.23 is substituted in Eq I.20, the relaxation time of a SCM becomes:

$$\tau(T) = \frac{\tau_i}{2} \exp[(2\Delta_\xi + \Delta_A) / k_B T] \quad \text{Eq I.24}$$

with an associated energy gap (Δ_T):

$$\Delta_{\tau 1} = 2\Delta_{\xi} + \Delta_A \quad \text{Eq I.25}$$

This result is indeed very general because it depends only on the thermal dependence of the magnetic correlations.

However, the presence of small number of defects, which has been shortly discussed in the previous paragraph, also plays an important role on the dynamic properties of SCMs as well as static properties. For $T > T^*$, the dynamics of a segment of n Ising spins is same as that for the infinite chain, and therefore Eq I.24 is still valid. In the low temperature regime, $T < T^*$, the flipping probability is much higher from the ends of the segment because these terminal spins are linked to only one neighbor and they have to overcome only one interaction to reverse. Hence, in this finite size regime, the magnetic correlation still gives a contribution that can be expressed as:

$$\tau(T) = \frac{\tau_i}{2} \exp[(\Delta_{\xi} + \Delta_A) / k_B T] \quad \text{Eq I.26}$$

with an activated gap ($\Delta_{\tau 2}$):

$$\Delta_{\tau 2} = \Delta_{\xi} + \Delta_A \quad \text{Eq I.27}$$

As a consequence, the temperature dependence of the relaxation time of a SCM can exhibit a crossover between two activated regimes (**Figure I.9**, right).

In this theoretical part dedicated to the SCM behavior, both static and dynamic properties were discussed, mostly based on the simplest Ising model. In order to analyze SCMs without an ambiguity, it is evident now that both thermodynamic and dynamic properties should be simultaneously compared. The key points of SCM properties can be summarized to the following general equations: Eq I.16, Eq I.24, and Eq I.26. Especially in the case of sharp domain walls and single-ion anisotropy (Ising-like), Δ_{ξ} and Δ_A are simple functions of S , D , and J (Eq I.14 and Eq I.22), but in all other cases, analytical expressions are rarely available at the moment.

Up to now, we have seen the molecular magnets, SMMs and SCMs, whose slow dynamics, induced by the presence of an energy gap, promotes the magnet behavior of the system. As shown in two preceding parts, a lot of fruitful theories have been developed and proved by experimental results, which finally will offer better synthetic strategies to chemists.

At the same time, molecular magnetic systems that can alter their magnetic state under external stimuli have also received a great attention in the field of magnetism. The most pronounced examples are spin crossover and electron-transfer complexes, that show experimentally the inter-conversion between two different states, or eventually bistability. The following part is to understand the mechanism of their bistability based on a simple thermodynamic model: the binary solution model.

I.3 Spin crossover (SC) and electron transfer (ET) systems

Molecule-based systems showing a reversible change in their physical properties as a function of external stimuli (temperature, electric or magnetic fields, light, pressure, etc.) have attracted a great deal of attention during recent years. Among them, the most studied examples in the community of magnetism are the systems exhibiting spin crossover (SC) (Gütlich and Goodwin 2004) and electron transfer (ET) (Sato et al. 2007). The observed phenomena in both systems are associated with the

change of the electronic configuration of metal centers in the material that results in the concomitant major changes in their magnetic and optical properties.

Spin crossover (SC). In perfect octahedral symmetry, the d orbitals of a transition metal ion are split into t_{2g} and e_g orbitals, with the energy splitting (Δ) between the two orbitals. In such situations, d^4 to d^7 configurations may stabilize either high-spin (HS) or low-spin (LS) ground states (**Figure I.10**). The magnitude of the ligand field along with the spin pairing energy (Π) of the complex determines whether LS or HS configuration is stabilized (Hauser 2004): (i) if $\Pi > \Delta$, the electrons fill the orbitals according to Hund's rule, populating the higher lying orbitals rather than pairing electrons in the lower lying orbitals, to stabilize HS state. (ii) if $\Pi < \Delta$, a substantial amount of energy is required for the electrons to overcome the energy gap (Δ) to comply with Hund's rule. Thus, electrons will fill the low energy orbitals rather than populating high energy ones, stabilizing the LS state. (iii) if $\Pi \approx \Delta$, the system can exist in both states. Therefore, the latter situation can lead to an observation of the spin configuration changes ($LS \leftrightarrow HS$), the so-called SC.

The ligand field strength (Δ) indeed depends considerably on the combinations of ligands and a metal ion as $1/r^n$ with r being the metal-ligand distances and $n = 5 - 6$ (Fleisch et al. 1977). For example, metal ligand bond lengths of HS Fe^{II} are considerably larger than those of LS Fe^{II} complexes ($\Delta r_{HL} \sim 0.2 \text{ \AA}$). This is due to the fact that two of six electrons reside in the anti-bonding e_g orbitals in HS state, whereas all six electrons occupy the non-bonding t_{2g} orbitals in LS state. When a complex goes from the LS to HS state, the significant change in the metal-ligand distances also leads to an abrupt change in Δ as $\Delta_{LS}/\Delta_{HS} = (r_{HS}/r_{LS})^n$. This ratio for Fe^{II} SC complex is estimated to be 1.75. Given the fact that Π hardly changes during the SC, we have the following relations for the SC complexes, $\Delta_{HS} < \Pi < \Delta_{LS}$.

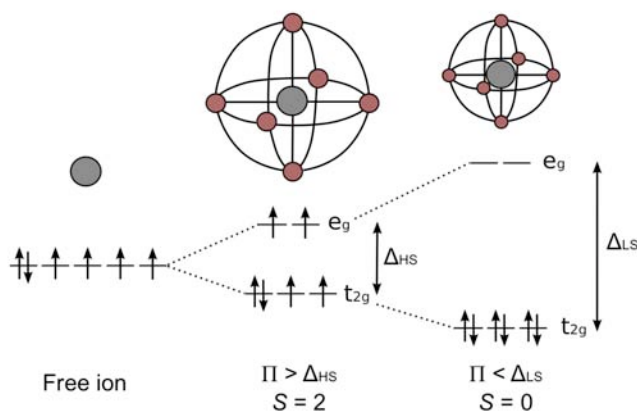


Figure I.10 Schematic view of the splitting of d-orbitals in an octahedral field for Fe^{II} (d^6) ion.

Since the first discovery of this phenomenon in iron(III) complex in 1931 (Cambi et al. 1931), it has been observed in many complexes of Fe^{II} (Gütlich and Goodwin 2004), Fe^{III} (van Koningsbruggen et al. 2004), Co^{II} (Goodwin 2004; Hayami et al. 2011; Krivokapic et al. 2007), Co^{III} (Eberspach et al. 1982; Gütlich et al. 1980; Kläui et al. 1987), Cr^{II} (Halepoto et al. 1989), Mn^{II} (Ammeter et al. 1974; Switzer et al. 1974), Mn^{III} (Kaustov et al. 1997; Sim et al. 1981), and Mo^{II} (Chisholm et al. 1985). The majority of SC complexes known today are octahedral iron(II) with a d^6

configuration, showing a crossover between the diamagnetic LS state ($S = 0$, t_{2g}^6) and the paramagnetic HS state ($S = 2$, $t_{2g}^4 e_g^2$) (**Figure I.10**).

Electron-transfer (ET). An ET is a redox process between two units, one being the donor and the other being the acceptor. The first generally accepted theory of ET was developed by Marcus in 1956 (Marcus 1956). It was mainly addressed to outer-sphere (intermolecular) electron transfer reactions and was based on a transition state theory approach. Hush extended this theory to the problem of inner sphere (intramolecular) electron transfer reactions (Hush 1985). Different other models have been developed to complete existing ones, one of which is vibronic coupling model (PKS model) to calculate absorption profiles of the electron transfer systems (Piepho et al. 1978). Since ET process is one of the most fundamental processes in physics, chemistry, and biology, the field of research concerning this phenomenon is very broad (Prassides 1991). A metal-to-metal electron transfer is firstly observed in the mixed valence Creutz-Taube ion, $[(H_3N)_5Ru^{II}(pyr)Ru^{III}(NH_3)_5]^{5+}$ (pyr = μ -pyrazine) in 1969 (Creutz et al. 1969). The discovery of ET in Co/Fe Prussian blue analogue, $K_{0.2}Co_{1.4}[Fe(CN)_6] \cdot 6.9 H_2O$ (Sato et al. 1996), has drawn a big attraction of the scientists in the field of magnetism. This compound contains $\{Fe(\mu-CN)Co\}$ motifs that exhibit a reversible metal-to-metal electron transfer converting diamagnetic $\{Fe^{II}_{LS}(\mu-CN)Co^{III}_{LS}\}$ (Fe^{II} , t_{2g}^6 , $S = 0$; Co^{III} , t_{2g}^6 , $S = 0$) into paramagnetic $\{Fe^{III}_{LS}(\mu-CN)Co^{II}_{HS}\}$ (Fe^{III} , t_{2g}^5 , $S = 1/2$; Co^{II} , $t_{2g}^5 e_g^2$, $S = 3/2$) pairs (**Figure I.11**).

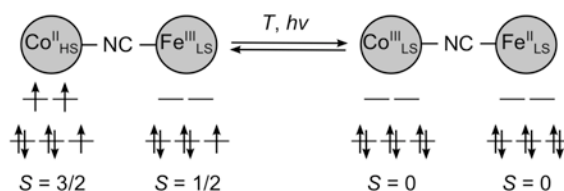


Figure I.11 Schematic representation of metal-to-metal electron transfer induced by external stimuli (T , $h\nu$) in the example of $\{Fe^{III}_{LS}(\mu-CN)Co^{II}_{HS}\}$ and $\{Fe^{II}_{LS}(\mu-CN)Co^{III}_{LS}\}$ pairs.

Given the fact that the SC and the ET process occurs on one metal center and a pair of metals, respectively, we will consider a metal ion or a pair that are isolated in the following, to describe the basic process underlain. Both thermal SC and ET phenomena involve two states (A and B) that are energetically close and therefore, in an equilibrium state. The different two states can be easily distinguished by measuring the temperature dependence of the χT product, as each state is expected to be diamagnetic or paramagnetic that follows, for the latter, a Curie law. Thus, the χT product corresponds to the Curie constants (C) of each state ($C = 0$ for a diamagnetic species) and is related to their molar fraction, x , according to the following equation:

$$\chi T = x_A(\chi T)_A + x_B(\chi T)_B \quad \text{Eq I.28}$$

where A and B represent high and low temperature fractions of a given system. Assuming that $x_A = x$, then Eq I.28 becomes:

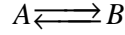
$$\chi T = x(\chi T)_A + (1-x)(\chi T)_B \quad \text{Eq I.29}$$

The $(\chi T)_A$ and the $(\chi T)_B$ products are in most cases temperature independent. Therefore, studying $\chi T = f(T)$ gives a direct access to $x = f(T)$. This common point makes us to describe both SC and ET systems

together by a simple thermodynamic model for binary solutions. Experimentally, SC and ET are observed either as a conversion or as a transition. In the following, we will describe the temperature variation of x by both ideal and regular solution model to understand the difference between a conversion and a transition, and finally to construct a phase diagram.

I.3.1 Ideal solution model: conversion

The low and high temperature fractions of SC or ET can be described as equilibrium between two states:



with a Gibbs energy change:

$$\Delta G = \Delta H - T\Delta S \quad \text{Eq I.30}$$

where $\Delta G = G_A - G_B = \Delta H - T\Delta S = (H_A - H_B) - T(S_A - S_B)$. The energy is positive below a temperature named T^* and negative above it. When $T = T^*$ ($\Delta G = 0$), the following relationship is verified:

$$\Delta H = T^* \Delta S \quad \text{Eq I.31}$$

In the ideal solution model, we assume A and B states are mixed without interaction. If N is total number of motifs responsible for the SC or the ET phenomenon in a material, $N_A = x_A N = xN$ is the number of motifs in A state, and $N_B = x_B N = (1-x)N$ is the number of motifs in B state. In statistical thermodynamics, the Gibbs energy of the system can be written:

$$G = N_A G_A + N_B G_B + G_{\text{mix}} \quad \text{Eq I.32}$$

where G_A and G_B are the molar Gibbs energy for A and B motifs, respectively, and G_{mix} is the energy of the mixture:

$$G_{\text{mix}} = -TS_{\text{mix}} = Nk_B T [x \ln x + (1-x) \ln(1-x)] \quad \text{Eq I.33}$$

hence ($S_A = k_B \ln g_A$):

$$G = xN(H_A - k_B T \ln g_A) + (1-x)N(H_B - k_B T \ln g_B) + Nk_B T [x \ln x + (1-x) \ln(1-x)] \quad \text{Eq I.34}$$

The relationship allows describing the Gibbs energy for each motif, g_N , as following:

$$g_N = \frac{G}{N} = x \left[\Delta H - k_B T \ln \frac{g_A}{g_B} \right] + k_B T [x \ln x + (1-x) \ln(1-x)] + G_B \quad \text{Eq I.35}$$

Introducing the ratio of degeneracies, $a = \ln(g_A/g_B)$:

$$g_N = \frac{G}{N} = x [\Delta H - k_B T a] + k_B T [x \ln x + (1-x) \ln(1-x)] + G_B = g'_N(x) + G_B \quad \text{Eq I.36}$$

The condition for equilibrium requires:

$$\left(\frac{\partial g'_N}{\partial x} \right)_{T,N} = 0 \quad \text{Eq I.37}$$

as G_B is a constant. So we get:

$$\left(\frac{\partial g'_N}{\partial x} \right)_{T,N} = \Delta H - k_B T a + k_B T \ln \frac{x_{\min}}{1 - x_{\min}} = 0 \quad \text{Eq I.38}$$

The equation can be rearranged in the form of:

$$x_{\min} = \left[1 + \exp \left(\frac{\Delta H}{k_B T} - a \right) \right]^{-1} \quad \text{Eq I.39}$$

For $T = T^*$, $x_A = x_B = x_{\min} = 0.5$ and therefore $\ln[x_{\min}/(1 - x_{\min})] = 0$ and $a = \Delta H_{AB}/(k_B T^*)$. Then, the Eq I.39 becomes:

$$x_{\min} = \left[1 + \exp \left(\frac{\Delta H}{k_B} \left(\frac{1}{T} - \frac{1}{T^*} \right) \right) \right]^{-1} = \left[1 + \exp \left(a \left(\frac{T^*}{T} - 1 \right) \right) \right]^{-1} \quad \text{Eq I.40}$$

or

$$\frac{T}{T^*} = a \left[a + \ln \frac{1 - x_{\min}}{x_{\min}} \right]^{-1} \quad \text{Eq I.41}$$

This equation allows the drawing of $x_{\min} = f(T/T^*)$ plot (**Figure I.12**), where $T^* = \Delta H/(k_B a)$.

Whatever is the value of a , the function x_{\min} increases when T/T^* increases. This model predicts that at low temperature ($T/T^* \ll 1$), the system is in B state, so $x_{\min} = 0$. We can observe that all curves pass through a common point, $T/T^* = 1$, and $x_{\min} = 0.5$. So we can conclude that T^* is a characteristic temperature of the system. At this point, the system contains 50% of A and 50% of B motifs. Note that in the literature, T^* is often noted as $T_{1/2}$ to reflect the composition of the system.

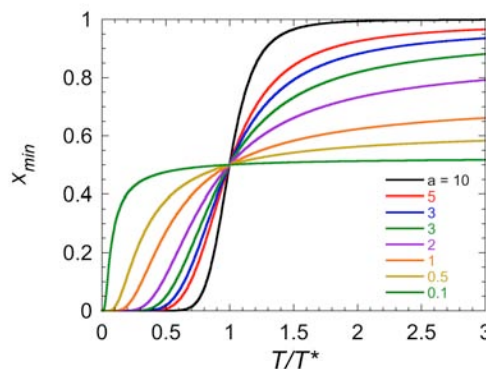


Figure I.12 Temperature dependence of HS molar fraction x_{\min} for different values of degeneracy, a , in ideal solution model.

Now let us consider a real case, for example a Fe^{II} octahedral SC system. The A state (HS) corresponds to the $^5\text{T}_{2g}$ spectroscopic term, so the spin degeneracy is 5 and the orbital degeneracy ($2L_{\text{HS}} + 1$) is 3. The B state (LS) corresponds to the $^1\text{A}_{1g}$ spectroscopic term for which the spin degeneracy is 1 and the orbital degeneracy is 1. So $g_{\text{HS}} = 5 \times 3$ and $g_{\text{LS}} = 1 \times 1$, which gives $a = \ln 15 = 2.71$. The most similar case in **Figure I.12** is the simulation with $a = 3$ in which x_{\min} tends to 0.85 at high temperature ($T/T^* > 2$), while x_{\min} is very close to 1 in real systems. Indeed, the entropy change of the Fe^{II} system can be experimentally measured by calorimetric methods, giving the estimation of a value between 4.2 and 9.6 (Boča 1999; König 1991). This shows that in real complexes not only the

electronic contributions to the degeneracy are present, but also the vibrational contributions for HS and LS states that are different, due to different geometry in both states.

I.3.2 Regular solution model: from conversion to transition

When we study the solid phase of the SC and ET systems, the inter-conversion phenomenon is strongly influenced by inter-motif interactions (mostly of elastic origin) in crystalline phase. They play an important role in the macroscopic properties of the systems. Therefore, we can assume the interaction energy that is responsible for the cooperative effects based on the regular solution model. Hence, the Gibbs energy of the system can be written as:

$$G = N_A G_A + N_B G_B + G_{mix} + I \quad \text{Eq I.42}$$

where the interaction energy term (I) is given by the formula:

$$I(x) = Wx(1-x) \quad \text{Eq I.43}$$

with W being the intermolecular interaction parameter (in units of energy) that is independent of temperature. Note that $I(x)$ is a simple exchange term in the mean-field approximation: $Wx(1-x) = Wx_Ax_B$. Insertion of this term in the molar Gibbs energy gives:

$$\begin{aligned} G = & xN(H_A - k_B T \ln g_A) + (1-x)N(H_B - k_B T \ln g_B) \\ & + Nk_B T[x \ln x + (1-x) \ln(1-x)] + Wx(1-x) \end{aligned} \quad \text{Eq I.44}$$

then:

$$g'_N = x[\Delta H - k_B Ta] + k_B T[x \ln x + (1-x) \ln(1-x)] + Wx(1-x) \quad \text{Eq I.45}$$

and from the condition of equilibrium (Eq I.37):

$$\Delta H - k_B Ta + k_B T \ln \frac{x_{\min}}{1-x_{\min}} + W(1-2x_{\min}) = 0 \quad \text{Eq I.46}$$

or:

$$k_B T = \left[\Delta H + W(1-2x_{\min}) \right] \left[a + \ln \left(\frac{1-x_{\min}}{x_{\min}} \right) \right]^{-1} \quad \text{Eq I.47}$$

For given values of a , $x_{\min} = f(T/T^*)$ can be plotted (**Figure I.13**, left) and the function is defined by:

$$\frac{T}{T^*} = \left[a + \frac{W}{k_B T^*} (1-2x_{\min}) \right] \left[a + \ln \left(\frac{1-x_{\min}}{x_{\min}} \right) \right]^{-1} \quad \text{Eq I.48}$$

As shown in **Figure I.13** (left), the inter-motif interaction (W) plays an important role to define the stable state depending on the temperature. Here, three cases can be discussed: (i) $W/k_B T^* = 2$, there is a vertical jump of x_{\min} at $T/T^* = 1$. This gives a first order transition at a critical intra-motif interaction, $W_C = 2k_B T^*$. (ii) $W < W_C$ ($W/k_B T^* < 2$). x_{\min} is increasing when T/T^* increases, and the corresponding curves are more and more steep for higher values of W , but possess the same inflection point given by $T/T^* = 1$ and $x_{\min} = 0.5$. This phenomenon is a conversion. (iii) $W > W_C$ ($W/k_B T^* > 2$), the curve has a S-shape, and for $T/T^* = 1$, not only the $x_{\min} = 0.5$ solution is possible, but Gibbs energy

adopts two other local minimum values. In this case, a first order transition is associated with thermal hysteresis depending on the experimental scanning rate of the temperature (**Figure I.13**, right). As shown in **Figure I.13** (right), it is noteworthy to mention that T^* is not at the center of thermal hysteresis.

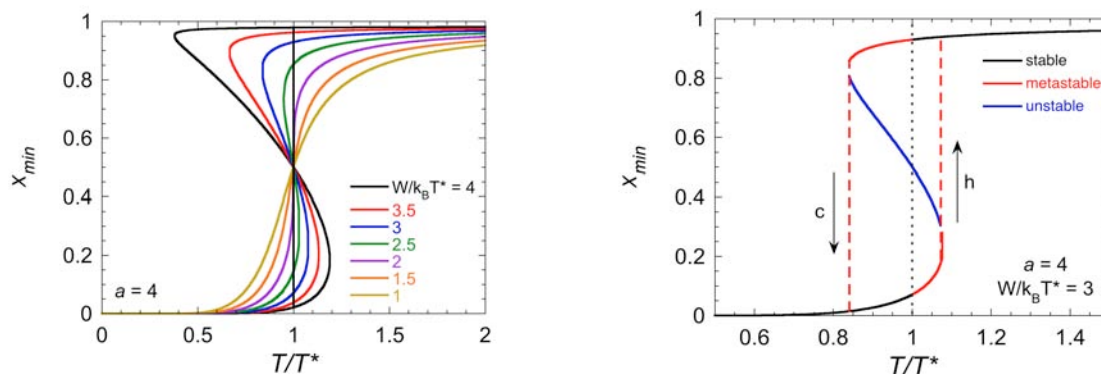


Figure I.13 Temperature dependence of HS molar fraction x_{\min} for different values of $W/k_B T^*$ at fixed $a = 4$, in regular solution model (left). Thermal hysteresis when $a = 4$ and $W/k_B T^* = 3$ with c – cooling mode and h – heating mode (right).

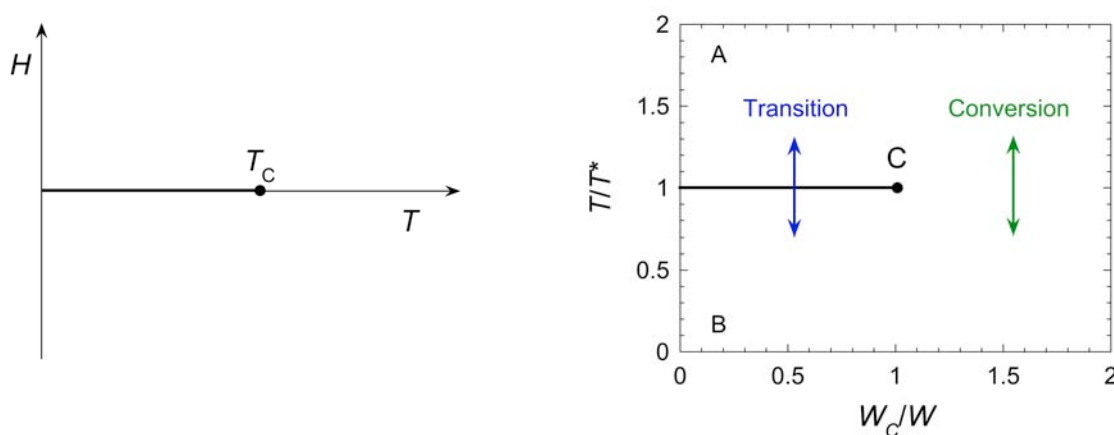


Figure I.14 Phase diagram of Ising model ($W = \text{constant}$) (left). Phase diagram for the regular solution model with $W > 0$ in the plane $(T/T^*, W_C/W)$ (right).

The above Eq I.45 is indeed equivalent to the mean field solution of Ising model in which the Hamiltonian is given by:

$$H = -W \sum_{i,j} \sigma_i \sigma_j - \sum_i \sigma_i H \quad \text{Eq I.49}$$

with $\sigma_i = \pm 1$ that correspond to A and B motifs. The first and the second terms in the above equation respectively indicate interaction (W) between motifs and the effect of the external field ($H = -\Delta H + k_B T a$). For a given W , the phase diagram of Ising model is universal as shown in **Figure I.14** (left) and the most general phase diagram would be a 3D representation. In a SC system, however, the external field term is a function of temperature but depends on ΔH and a ($H = -\Delta H + k_B T a$). Therefore, the real phase diagram for a SC system has four variables: T , W , ΔH , and a . In order to present a two-dimensional representation, one should consider a projection of the real phase diagram taking two variables. Given the fact that one of the variables that can be controlled for chemists is inter-motif

interaction, W , we decided to discuss SC behavior with W and T variables, and consequently to present a $(W_C/W, T/T^*)$ phase diagram in the following (ΔH_{AB} and a were considered as constants). We can construct a phase diagram that describes the system at any temperature and any value of W (**Figure I.14**, right). The phase diagram consists in a line of first order phase transition at $T/T^* = 1$ that ends with a critical point, C ($W_C = 2k_B T^*$). From this phase diagram, we can predict if an experimental system will present a conversion or a transition. If $W \geq W_C$, the system crosses the transition line and a transition is observed, otherwise if $W < W_C$, the system is beyond the critical point and a conversion is observed.

In this section, the thermal SC and ET behaviors could be described by the binary solution model. This simple approach tells us that the interactions between the motifs responsible for the inter-conversion phenomena are crucial to exhibit a transition, and therefore to display bistability.

I.4 Conclusion

Throughout this chapter, the basic concepts of molecular magnetic materials were presented, concerning single-molecule magnets (SMMs), single-chain magnets (SCMs), spin crossover (SC), and electron transfer (ET) systems. These basic theories will help to follow Chapters III and IV that present the main results of this thesis. In addition, an advanced theory will be developed in Chapter III based on this chapter.

The first types of two molecular nanomagnets, SMMs and SCMs, show a frozen dynamics at low temperature due to the presence of an energy barrier. We have seen that this energy gap is induced by the large anisotropy and the high spin ground state for SMMs, and the 1D correlations in addition to aforementioned two factors in the case of SCMs. Therefore, slow relaxation of the magnetization is observed, and can be proven by M vs H hysteresis curves (depending on the field sweeping rate) and temperature and/or frequency dependent ac susceptibility measurements. Beside the presence of slow dynamics, another fascinating behavior is the quantum properties of SMMs and SCMs. These two systems, indeed, made possible to prove experimentally the quantum behaviors of nanomagnets that had been predicted before. A short discussion on the quantum properties of SMMs was discussed in this chapter. All these unique magnetic properties of the SMM and SCM systems open perspectives for their application in high-density information storage devices (Leuenberger et al. 2001).

Beside SMM and SCM, other class of molecular magnetic materials, such as SC and ET complexes, presents also continuous interest in this field. The core interest in these systems can be found in their tunable magnetic and/or optical properties that are induced by external stimuli such as temperature and light irradiation. Therefore, such materials may approach the realization of energy efficient molecule-based electronics (Sato et al. 2007). Herein we have discussed, through thermodynamic description the key role of the intermolecular (or inter-motifs) interactions in crystalline state to achieve a coexistence of the two different states, and therefore the bistability.

Thanks to the development of the foregoing theoretical tools discussed in this chapter, many new compounds have been indeed reported with fascinating properties. In the field of SMM, for example, the slow relaxation of the magnetization was observed in mononuclear complexes including lanthanides (AlDamen et al. 2008; Ishikawa et al. 2003), actinides (Rinehart and Long 2009), and even 3d transition metals (Freedman et al. 2010; Harman et al. 2010; Jurca et al. 2011; Lin et al. 2011). In

parallel, dysprosium-containing molecules present notably large energy barriers as high as 530 K (Blagg et al. 2011), and show magnetic hysteresis up to 8.3 K at a sweep rate of 0.08 T s^{-1} (Rinehart et al. 2011). However, it is becoming of strategic importance to dedicate a part of our research to the organization of these molecules in order to achieve information storage devices for applications. One of the strategies generally applied is to associate them through coordinating linkers, finally to construct networks in higher dimension. In this thesis work, we have chosen this strategy to develop novel SMM networks displaying enhanced magnetic and photomagnetic behaviors. Therefore, let us now provide the general view and the current status considering “the organization of SMMs into coordination networks” in Chapter II. As possible coordinating linkers between SMMs, a photomagnetic complex bearing cyanide groups is one of our targets. In this regard, we will also summarize the state of the art in the cyanido-based photoactive bimetallic materials showing metal-to-metal electron transfer.

I.5 Supporting information

1D Ising model and the transfer matrix

Bulk properties in the thermodynamic limit are insensitive to boundary conditions. Calculations are most easily carried out in a model in which lattice sites lie on a circle with sites 1 and N connected. Therefore, let us consider a closed chain (a periodic boundary condition) of N Ising spins in the presence of the applied field, H . The corresponding Hamiltonian is given by:

$$H = -2JS^2 \sum_{i=1}^N \sigma_i \sigma_{i+1} - g\mu_B SH \sum_{i=1}^N \sigma_i \quad \text{Eq I.50}$$

By introducing variables $K = 2\beta JS^2$ (with $\beta = 1/(k_B T)$) and $h = \beta g\mu_B SH$, Eq I.50 becomes:

$$-\beta H = K \sum_{i=1}^N \sigma_i \sigma_{i+1} + h \sum_{i=1}^N \sigma_i \quad \text{Eq I.51}$$

$$\begin{aligned} &= K \sum_{i=1}^N \sigma_i \sigma_{i+1} + \frac{h}{2} \sum_{i=1}^N (\sigma_i + \sigma_{i+1}) \\ &= M(\sigma_i, \sigma_{i+1}) \end{aligned} \quad \text{Eq I.52}$$

The partition function for this model can be calculated exactly using transfer matrices. The exponential of $M(\sigma, \sigma')$ is a two-by-two matrix in the variable σ and σ' with entries:

$$e^{T(\sigma, \sigma')} = \begin{pmatrix} e^{K+h} & e^{-K} \\ e^{-K} & e^{K-h} \end{pmatrix} \equiv T(K, h) \quad \text{Eq I.53}$$

Hence, the partition function is given by:

$$\begin{aligned} Z &= \sum_{\sigma_1=\pm 1} \sum_{\sigma_2=\pm 1} \cdots \sum_{\sigma_N=\pm 1} \exp(-\beta H) \\ &= \sum_{\sigma_1, \dots, \sigma_N} \prod_{i=1}^N \exp\left(K\sigma_i \sigma_{i+1} + \frac{h}{2}(\sigma_i + \sigma_{i+1})\right) \end{aligned} \quad \text{Eq I.54}$$

$$= \sum_{\sigma_1, \dots, \sigma_N} e^{M(\sigma_1, \sigma_2)} e^{M(\sigma_2, \sigma_3)} \cdots e^{M(\sigma_N, \sigma_1)} \quad \text{Eq I.55}$$

The following relation makes possible to express the partition function as a trace of a product of transfer matrices:

$$\begin{aligned} \sum_{\sigma_j=\pm 1} e^{M(\sigma_i, \sigma_j)} e^{M(\sigma_j, \sigma_k)} &= (e^{M(\sigma_i, \sigma_k)})^2 \\ Z &= \text{Tr}[T^N] \end{aligned} \quad \text{Eq I.56}$$

The matrix T is diagonalizable, giving a diagonal matrix λ with eigenvalues λ_+ and λ_- :

$$\lambda = S^{-1}TS = \begin{pmatrix} \cos \alpha & \sin \alpha \\ -\sin \alpha & \cos \alpha \end{pmatrix} \begin{pmatrix} e^{K+h} & e^{-K} \\ e^{-K} & e^{K-h} \end{pmatrix} \begin{pmatrix} \cos \alpha & -\sin \alpha \\ \sin \alpha & \cos \alpha \end{pmatrix} = \begin{pmatrix} \lambda_+ & 0 \\ 0 & \lambda_- \end{pmatrix} \quad \text{Eq I.57}$$

where:

$$\cos(2\alpha) = \frac{\sinh h}{\sqrt{\sinh^2 h + e^{-4K}}}, \quad \sin(2\alpha) = \frac{e^{-2K}}{\sqrt{\sinh^2 h + e^{-4K}}} \quad \text{Eq I.58}$$

$$\text{and } \lambda_{\pm} = e^K \left[\cosh h \pm \sqrt{\sinh^2 h + e^{-4K}} \right] \quad \text{Eq I.59}$$

Therefore, Eq I.56 can be expressed:

$$Z = \lambda_+^N + \lambda_-^N = \lambda_+^N \left(1 + \frac{\lambda_-}{\lambda_+} \right)^N \quad \text{Eq I.60}$$

In the limit of large N ($N \rightarrow \infty$), Eq I.56 can be simplified as:

$$Z \approx \lambda_+^N \quad \text{Eq I.61}$$

Normalized magnetization, $m = M/M_S$, can be obtained from the following relation:¹³

$$m = \langle \sigma_i \rangle = \frac{1}{Z} \sum_{\sigma_1, \dots, \sigma_N} \sigma_i \exp(-\beta H) \quad \text{Eq I.62}$$

$$= \frac{1}{Z} \text{Tr} [T^N \hat{\sigma}] \quad \text{Eq I.63}$$

with

$$\hat{\sigma} = \begin{pmatrix} 1 & 0 \\ 0 & -1 \end{pmatrix}$$

If we now let $\Sigma = S \hat{\sigma} S^{-1}$, where S is the same matrix that diagonalizes M , then Eq I.63 becomes (with large N) (Marsh 1966):

$$m = \langle \sigma_i \rangle = \frac{1}{\lambda_+^N} \text{Tr} [\lambda^N \Sigma] = \Sigma_{++} + \Sigma_{--} \left(\frac{\lambda_-}{\lambda_+} \right)^N = \Sigma_{++} \quad \text{Eq I.64}$$

where:

¹³ The normalized magnetization can be also calculated by following method:

$$m = \langle \sigma_i \rangle = \frac{1}{N} \frac{\partial \ln Z}{\partial h} = \frac{\partial \ln \lambda_+}{\partial h}$$

since:

$$\frac{\partial Z}{\partial h} = \sum_{\sigma_1, \sigma_2, \dots, \sigma_N} \left(\sum_{i=1}^N \sigma_i \right) \exp \left(K \sum_{i=1}^N \sigma_i \sigma_{i+1} + h \sum_{i=1}^N \sigma_i \right)$$

and dividing by Z:

$$\frac{1}{Z} \frac{\partial Z}{\partial h} = \langle \sum_{i=1}^N \sigma_i \rangle = N \langle \sigma_i \rangle = \frac{\partial \ln Z}{\partial h}$$

$$\Sigma = \begin{pmatrix} \Sigma_{++} & \Sigma_{+-} \\ \Sigma_{-+} & \Sigma_{--} \end{pmatrix} = \begin{pmatrix} \cos 2\alpha & -\sin 2\alpha \\ -\sin 2\alpha & -\cos 2\alpha \end{pmatrix}$$

Therefore, m is given by:

$$m = \frac{\sinh(h)}{\sqrt{\sinh^2(h) + e^{-4K}}} \quad \text{Eq I.65}$$

Replacing h and K in the above equation by $\beta g \mu_B S H$ and $2\beta J S^2$, respectively, Eq I.18 in the main text is obtained.

Correlation functions are also easily calculated in the 1D Ising model. At the limit of small field ($h \rightarrow 0$), the spontaneous magnetization at finite temperature is zero. Magnetic interaction (J) between spins induces a parallel arrangement of them but thermal fluctuation results in the average magnetization, $\langle \sigma_i \rangle$, being zero. Nevertheless, it is interesting to know how spins on different sites, σ_i and σ_{i+n} are correlated, $\langle \sigma_i \sigma_{i+n} \rangle$. Any two spin correlation function (u^n) can be written:

$$\begin{aligned} u^n = \langle \sigma_i \sigma_{i+n} \rangle &= \frac{1}{Z} \sum_{\sigma_1, \dots, \sigma_N} \sigma_i \sigma_{i+n} \exp(-\beta H) \\ &= \frac{1}{Z} \sum_{\sigma_1, \dots, \sigma_N} e^{M(\sigma_1, \sigma_2)} \dots e^{M(\sigma_{i-1}, \sigma_i)} \sigma_i e^{M(\sigma_i, \sigma_{i+1})} \dots e^{M(\sigma_{i+n-1}, \sigma_{i+n})} \sigma_{i+n} e^{M(\sigma_{i+n}, \sigma_{i+n+1})} \dots e^{M(\sigma_N, \sigma_1)} \\ &= \frac{1}{Z} \sum_{\sigma_i, \sigma_{i+n}} e^{(i-1)M(\sigma_i, \sigma_{i-1})} \sigma_i e^{nM(\sigma_i, \sigma_{i+n-1})} \sigma_{i+n} e^{(N-i-n+1)M(\sigma_{i+n}, \sigma_1)} \end{aligned} \quad \text{Eq I.66}$$

Then, we can write Eq I.66 in matrices (Marsh 1966):

$$\langle \sigma_i \sigma_{i+n} \rangle = \frac{1}{\lambda_+^N} \text{Tr}(\lambda^{N-n} \Sigma \lambda^n \Sigma) = \Sigma_{++}^2 + \Sigma_{+-}^2 \left(\frac{\lambda_-}{\lambda_+} \right)^n = \cos^2 2\alpha + \sin^2 2\alpha \left(\frac{\lambda_-}{\lambda_+} \right)^n \quad \text{Eq I.67}$$

When there is no external field ($H = 0$), u^n is given by (by introducing Eq I.58):

$$u^n = \langle \sigma_i \sigma_{i+n} \rangle_{H=0} = \left(\frac{\lambda_-}{\lambda_+} \right)^n = [\tanh(K)]^n \quad \text{Eq I.68}$$

The above equation is given in Eq I.12 by replacing $K = 2\beta J S^2$. Furthermore, this correlation function is directly related to the zero field susceptibility as seen in the following fluctuation-dissipation theorem.

Fluctuation-dissipation theorem

In the fluctuation dissipation theorem, the response of a system in thermodynamic equilibrium to a small applied force is assumed to be same as its response to a spontaneous fluctuation. It is worth to note that the following description works only for classical model in which H_0 and H_Z communicate. Under the perturbation of the field, the total Hamiltonian is the sum of the Hamiltonian at zero field (H_0) and the Hamiltonian under the field (H_Z):

$$H = H_0 + H_Z \quad \text{Eq I.69}$$

where ($\mu_j = g\mu_B S_j$)

$$H_Z = -\sum_j \mu_j H \quad \text{Eq I.70}$$

When the field is small, we have following relation at the first order expansion:

$$\exp(-\beta H_Z) \approx 1 - \beta H_Z \quad \text{Eq I.71}$$

Hence we can write the magnetization per spin as below:

$$\langle \mu_i \rangle_{H \neq 0} = \frac{\sum_{\{\mu_j\}} \mu_i e^{-\beta H_0} (1 + \beta H \sum_j \mu_j)}{\sum_{\{\mu_j\}} e^{-\beta H_0} (1 + \beta H \sum_j \mu_j)} \quad \text{Eq I.72}$$

Where $\sum_{\{\mu_j\}}$ is the sum over all spin configurations (there are 2^N spin configurations if we have chain of N spins) whereas \sum_j is the sum over all sites.

When $H = 0$, the first order term in μ should be zero, as there should be no spontaneous magnetization. Thus, Eq I.72 can be simplified as below:

$$\langle \mu_i \rangle_{H \neq 0} = \frac{\sum_{\{\mu_j\}} \beta H_Z \sum_j \mu_i \mu_j e^{-\beta H_0}}{\sum_{\{\mu_j\}} e^{-\beta H_0}} \quad \text{Eq I.73}$$

Thus,

$$\langle \mu_i \rangle_{H \neq 0} = \beta H_Z \sum_j \langle \mu_i \mu_j \rangle_{H=0} \quad \text{Eq I.74}$$

Hence,

$$\chi = \frac{\langle \mu_i \rangle}{H} = \beta \sum_j \langle \mu_i \mu_j \rangle_{H=0} \quad \text{Eq I.75}$$

and

$$\frac{\chi T}{C} = \sum_j \langle \sigma_i \sigma_j \rangle_{H=0} \quad \text{Eq I.76}$$

As j is the arbitrary spin in any distance from i , Eq I.76 can be written as:

$$\frac{\chi T}{C} = \sum_n \langle \sigma_i \sigma_{i+n} \rangle_{H=0} \quad \text{Eq I.77}$$

with $\langle \sigma_i \sigma_{i+n} \rangle = u^n$, and $u = \langle \sigma_i \sigma_{i+1} \rangle$ being the nearest neighbors correlation function ($\langle \rangle$ means average on the chain). The above equation is given in Eq I.10 in the main text.

Glauber's stochastic model to describe relaxation of the magnetization for a chain at zero field

Glauber's model assumes only single-spin flips, for example, the spin configurations in a chain from $(\sigma_1, \dots, \sigma_i, \dots, \sigma_N)$ to $(\sigma_1, \dots, -\sigma_i, \dots, \sigma_N)$. The spin-flips from σ_i to $-\sigma_i$ is associated to the transition probability per unit time, $W_i(\sigma_i)$, while the inverse spin-flips can be expressed as $W_i(-\sigma_i)$. Then, we can write a master equation, the probability to have the configuration $(\sigma_1, \dots, \sigma_i, \dots, \sigma_N)$ at an instant time t , as below:

$$\frac{d}{dt} P(\sigma_1, \dots, \sigma_i, \dots, \sigma_N)_t = \sum_i -W_i(\sigma_i) P(\sigma_1, \dots, \sigma_i, \dots, \sigma_N)_t + W_i(-\sigma_i) P(\sigma_1, \dots, -\sigma_i, \dots, \sigma_N)_t \quad \text{Eq I.78}$$

At the equilibrium, $dP_{(\sigma_1, \dots, \sigma_i, \dots, \sigma_N)}/dt$ is 0, and therefore, it gives the detailed balance relation:

$$\frac{W_i(\sigma_i)}{W_i(-\sigma_i)} = \frac{P(\sigma_1, \dots, -\sigma_i, \dots, \sigma_N)_{eq}}{P(\sigma_1, \dots, \sigma_i, \dots, \sigma_N)_{eq}} = \frac{e^{-\beta E_i \sigma_i}}{e^{\beta E_i \sigma_i}} \quad \text{Eq I.79}$$

where E_i is the local field (in energy unit) seen by spin σ_i that is defined as ($H = -\sigma_i E_i$; E_i is defined like the external field in Zeeman term of the Hamiltonian):

$$E_i = 2JS^2(\sigma_{i-1} + \sigma_{i+1}) \quad \text{Eq I.80}$$

Therefore, Eq I.79 can be written as:

$$\frac{W_i(\sigma_i)}{W_i(-\sigma_i)} = \frac{e^{-\beta E_i \sigma_i}}{e^{\beta E_i \sigma_i}} = \frac{e^{-2\beta JS^2 \sigma_i (\sigma_{i-1} + \sigma_{i+1})}}{e^{2\beta JS^2 \sigma_i (\sigma_{i-1} + \sigma_{i+1})}} = \frac{e^{-x_i \sigma_i}}{e^{x_i \sigma_i}} \quad \text{Eq I.81}$$

with $x_i = 2\beta JS^2(\sigma_{i-1} + \sigma_{i+1})$. Then we can transform this equation as below:

$$\frac{W_i(\sigma_i)}{W_i(-\sigma_i)} = \frac{e^{-x_i \sigma_i}}{e^{x_i \sigma_i}} = \frac{\cosh(x_i) - \sigma_i \sinh(x_i)}{\cosh(x_i) + \sigma_i \sinh(x_i)} = \frac{1 - \sigma_i \tanh(x_i)}{1 + \sigma_i \tanh(x_i)} \quad \text{Eq I.82}$$

since $\sigma_i = \pm 1$. Indeed, Eq I.82 has infinite number of solutions, and Glauber's choice was:

$$W_i(\sigma_i) = \frac{1}{2\tau_0} [1 - \sigma_i \tanh(x_i)] \quad \text{Eq I.83}$$

where τ_0 represents the characteristic time that describes the flip of a given spin in the absence of interaction. Since all possible values of $\tanh(x)$ is $\tanh(\pm 4\beta JS^2)$ or 0, we can express:

$$\tanh(\beta E_i) = \tanh(2\beta JS^2(\sigma_{i-1} + \sigma_{i+1})) \equiv \frac{\tanh 4\beta JS^2}{2} (\sigma_{i-1} + \sigma_{i+1}) \quad \text{Eq I.84}$$

Therefore, Eq I.83 becomes ($\gamma = \tanh(4\beta JS^2)$):

$$W_i(\sigma_i) = \frac{1}{2\tau_0} \left[1 - \frac{\gamma}{2} \sigma_i (\sigma_{i-1} + \sigma_{i+1}) \right] \quad \text{Eq I.85}$$

Now, let's think about the average value of σ_i , $\langle \sigma_i \rangle$, that can be expressed as:

$$\langle \sigma_i \rangle = \sum_{\{\sigma\}} \sigma_i P(\sigma_1, \dots, \sigma_i, \dots, \sigma_N)_t \quad \text{Eq I.86}$$

where $\{\sigma\}$ means that we make a sum for all configurations $(\sigma_1, \dots, \sigma_N)$. Then, we want to calculate the time-dependent derivative of this $\langle \sigma_i \rangle$:

$$\frac{d\langle\sigma_i\rangle}{dt} = \sum_{\{\sigma\}} \sigma_i \frac{dP(\sigma_1, \dots, \sigma_i, \dots, \sigma_N)_t}{dt} \quad \text{Eq I.87}$$

Thanks to the master equation (Eq I.78), we can write above equation as:

$$\frac{d\langle\sigma_i\rangle}{dt} = -\sum_j \sum_{\{\sigma\}} \sigma_i W_j(\sigma_j) P(\sigma_1, \dots, \sigma_j, \dots, \sigma_N)_t + \sum_j \sum_{\{\sigma\}} \sigma_i W_j(-\sigma_j) P(\sigma_1, \dots, -\sigma_j, \dots, \sigma_N)_t \quad \text{Eq I.88}$$

For $i \neq j$, $\{\sigma\}$ becomes only for $\pm\sigma_j$, and therefore, all terms can be canceled. For $i = j$, $\{\sigma\}$ is $\pm\sigma_i$, giving:

$$\frac{d\langle\sigma_i\rangle}{dt} = -2 \sum_{\{\sigma\}} \sigma_i W_i(\sigma_i) P(\sigma_1, \dots, \sigma_i, \dots, \sigma_N)_t \quad \text{Eq I.89}$$

If we write in average, it becomes:

$$\frac{d\langle\sigma_i\rangle}{dt} = -2 \langle \sigma_i W_i(\sigma_i) \rangle \quad \text{Eq I.90}$$

By introducing Eq I.85 into Eq I.90, we have (knowing Eq I.84):

$$\tau_0 \frac{d\langle\sigma_i\rangle}{dt} + \langle\sigma_i\rangle = \frac{\gamma}{2} \langle \sigma_{i-1} + \sigma_{i+1} \rangle \equiv \langle \tanh(\beta E_i) \rangle \quad \text{Eq I.91}$$

For infinite chains, the average value is independent on i , and therefore, $\langle \sigma_{i-1} + \sigma_{i+1} \rangle = 2\langle \sigma_i \rangle$. Hence, Eq I.84 and Eq I.91 give:

$$\gamma \langle \sigma_i \rangle \equiv \langle \tanh(\beta E_i) \rangle \quad \text{Eq I.92}$$

Then, the dynamic equation (Eq I.91) can be simplified to:

$$\tau_0 \frac{d\langle\sigma_i\rangle}{dt} + \langle\sigma_i\rangle (i - \gamma) = 0 \quad \text{Eq I.93}$$

This equation implies that the magnetization relaxes exponentially, with a single characteristic time (τ):

$$\tau = \frac{\tau_0}{1 - \tanh(4\beta JS^2)} \quad \text{Eq I.94}$$

The above equation is given in Eq I.19 in the main text.

References

- AlDamen MA, Clemente-Juan JM, Coronado E, Martí-Gastaldo C, Gaita-Ariño A (2008) *J. Am. Chem. Soc.* 130, 8874.
- Ammeter JH, Bucher R, Oswald N (1974) *J. Am. Chem. Soc.* 96, 7833.
- Aubin SMJ, Dilley NR, Wemple MW, Maple MB, Christou G, Hendrickson DN (1998) *J. Am. Chem. Soc.* **7863**, 839.
- Blagg RJ, Muryn CA, McInnes EJJ, Tuna F, Winpenny REP (2011) *Angew. Chem. Int. Ed.* 50, 6530.
- Boyd PDW, Li Q, Vincent JB, Folting K, Chang HR, Streib, WE, Huffman JC, Christou G, Hendrickson DN (1988) *J. Am. Chem. Soc.* 110, 8537.
- Boča R (1999). *Theoretical Foundations of Molecular Magnetism*, Elsevier.
- Cambi L, Szegő L (1931) *Ber. Dtsch. Chem. Ges.* 64, 2591.
- Caneschi A, Gatteschi D, Lalioti N, Sangregorio C, Sessoli R, Venturi G, Vindigni A, Rettori A, Pini MG, Novak MA (2001) *Angew. Chem. Int. Ed.* 40, 1760.
- Caneschi A, Gatteschi D, Sessoli R, Barra AL, Brunel LC, Guillot M (1991) *J. Am. Chem. Soc.* 113, 5873.
- Chisholm MH, Kober EM, Ironmonger DJ, Thornton P (1985) *Polyhedron* 4, 1869.
- Christou G, Gatteschi D, Hendrickson DN, Sessoli R (2000) *MRS Bulletin* 25, 66.
- Clérac R, Miyasaka H, Yamashita M, Coulon C (2002) *J. Am. Chem. Soc.* 124, 12837.
- Coulon C, Clérac R, Lecren L, Wernsdorfer W, Miyasaka H (2004) *Phys. Rev. B.* 69, 132408.
- Coulon C, Miyasaka H, Clérac R (2006) *Struct. Bond.* 122, 163.
- Creutz C, Taube H (1969) *J. Am. Chem. Soc.* 91, 3988.
- Eberspach W, Murr NE, Kläui W (1982) *Angew. Chem. Int. Ed.* 21, 915.
- Fleisch J, Guetlich P, Hasselbach KM (1977) *Inorg. Chem.* 16, 1979.
- Freedman DE, Harman WH, Harris TD, Long GJ, Chang CJ, Long JR (2010) *J. Am. Chem. Soc.* 132, 1224.
- Gatteschi D, Sessoli R (2003) *Angew. Chem. Int. Ed.* 42, 268.
- Glauber RJ (1963) *J. Math. Phys.* 4, 294.
- Goodwin HA (2004). *Top. Curr. Chem.* 234, 23.
- Gütlich P, Goodwin HA (2004) *Spin Crossover in Transition Metal Compounds I-III*. Springer, Heidelberg.
- Gütlich P, McGarvey BR, Kläui W (1980). *Inorg. Chem.* 19, 3704.
- Halepoto DM, Holt DGL, Larkworthy LF, Leigh GJ, Povey DC, Smith GW (1989) *Chem. Commun.* 1322.
- Harman WH, Harris TD, Freedman DE, Fong H, Chang A, Rinehart JD, Ozarowski A, Sougrati MT, Grandjean F, Long GJ, Long JR, Chang CJ (2010) *J. Am. Chem. Soc.* 132, 18115.
- Hauser A (2004) *Top. Curr. Chem.* 233, 49.
- Hayami S, Komatsu Y, Shimizu T, Kamihata H, Lee YH (2011). *Coord. Chem. Rev.* 255, 1981.
- Hush NS (1985) *Coord. Chem. Rev.* 64, 135.
- Ishikawa N, Sugita M, Ishikawa T, Koshihara, S-y, Kaizu Y (2003) *J. Am. Chem. Soc.* 125, 8694.
- Jahn HA (1938) *Proc. Royal Soc. A* 164, 117.
- Jahn HA, Teller E (1937) *Proc. Royal Soc. A* 161, 220.
- Jurca T, Farghal A, Lin P-H, Korobkov I, Murugesu M, Richeson DS (2011) *J. Am. Chem. Soc.* 133, 15814.
- Kaustov L, Tal ME, Shames AI, Gross Z (1997). *Inorg. Chem.* 36, 3503.
- Kläui W, Eberspach W, Guetlich P (1987) *Inorg. Chem.* 26, 3977.
- Krivokapic I, Zerara M, Daku ML, Vargas A, Enachescu C, Ambrus C, Tregenna-Piggott P, Amstutz N, Krausz E, Hauser A (2007) *Coord. Chem. Rev.* 251, 364.
- König E (1991) *Struc. Bond.* 76, 51.
- Lecren L (2006) PhD Thesis, Bordeaux University.
- Lecren L, Wernsdorfer W, Li Y, Roubeau O, Miyasaka H, Clérac R (2005) *J. Am. Chem. Soc.* 127, 11311.
- Leuenberger MN, Loss D (2001) *Nature* 410, 789.
- Lin P-H, Smythe NC, Gorelsky SI, Maguire S, Henson NJ, Korobkov I, Scott BL, Gordon JC, Baker RT, Murugesu M (2011) *J. Am. Chem. Soc.* 133, 15806.
- Marcus RA (1956) *J. Chem. Phys.* 24, 966.
- Marsh JS (1966) *Phys. Rev.* 145, 251.
- Piepho SB, Krausz ER, Schatz PN (1978) *J. Am. Chem. Soc.* 100, 2996.
- Prassides K (1991) *Mixed Valency Systems: Applications in Chemistry, Physics and Biology*, Kluwer Academic Publishers, Dordrecht.
- Rinehart JD, Fang M, Evans WJ, Long JR (2011) *Nature Chem.* 22, 538.

- Rinehart JD, Long JR (2009) *Slow J. Am. Chem. Soc.* 131, 12558.
- Sangregorio C, Ohm T, Paulsen C, Sessoli R, Gatteschi D (1997) *Phys. Rev. Lett.* 78, 4645.
- Sato O, Iyoda T, Fujishima A, Hashimoto K (1996) *Science* 272, 704.
- Sato O, Tao J, Zhang Y-Z (2007) *Angew. Chem. Int. Ed.* 46, 2152.
- Sessoli R, Gatteschi D, Caneschi A, Novak MA (1993) *Nature* 365, 141.
- Sim PG, Sinn E (1981) *J. Am. Chem. Soc.* 103, 241.
- Sorace L, Wernsdorfer W, Thirion C, Barra A-L, Pacchioni M, Mailly D, Barbara B (2003) *Phys. Rev. B* 68, 220407.
- Switzer ME, Wang R, Rettig MF, Maki AH (1974) *J. Am. Chem. Soc.* 96, 7669.
- Thomas L, Lioni F, Ballou R, Gatteschi D, Sessoli R, Barbara B (1996) *Nature* 383, 145.
- van Koningsbruggen PJ, Maeda Y, Oshio H (2004) *Top. Curr. Chem.* 233, 259.
- Villain J, Hartman-Boutron F, Sessoli R, Rettori A (1994) *Europhysics Lett.* 27, 159.
- Wernsdorfer W, Aliaga-Alcalde N, Hendrickson DN, Christou G (2002a) *Nature* 416, 406.
- Wernsdorfer W, Chakov NE, Christou G (2005) *Phys. Rev. Lett.* 95, 037203.
- Wernsdorfer W, Sessoli R (1999) *Science* 284, 133.
- Wernsdorfer W, Sessoli R, Caneschi A, Gatteschi D, Cornia A, Mailly D (2000) *J. Appl. Phys.* 87, 5481.
- Wernsdorfer W, Soler M, Christou G, Hendrickson DN (2002b) *J. Appl. Phys.* 91, 362.
- Yoo J, Yamaguchi A, Nakano M, Krzystek J, Streib WE, Brunel L-C, Ishimoto H, Christou G, Hendrickson DN, (2001) *Inorg. Chem.* 40, 4604.

II. State of the art and contexts

II.1 SMM-based coordination networks	36
II.1.1 Dinuclear SMMs.....	37
II.1.1.1 [Mn ₂] SMMs.....	37
II.1.1.2 [Dy ₂] SMMs	40
II.1.1.3 [CuTb] and [NiDy] SMMs	41
II.1.2 Trinuclear SMMs.....	43
II.1.2.1 [Mn ₃] SMMs.....	43
II.1.2.2 [Mn ₂ Ni] and [Mn ₂ Fe] SMMs.....	46
II.1.3 Tetranuclear SMMs	46
II.1.3.1 [Mn ₄] SMMs.....	46
II.1.3.2 [Co ₄] SMMs.....	50
II.1.4 Higher nuclearity SMMs	52
II.1.4.1 [Mn ₁₇] SMMs.....	52
II.1.5 Concluding remarks.....	53
II.2 Photoactive cyanido-based bimetallic materials	54
II.2.1 3D to 1D molecule-based systems.....	54
II.2.2 Toward molecular complexes.....	57
II.2.3 Concluding remarks.....	60
II.3 Conclusion and motivation.....	60
References	62

The unique magnetic properties of the SMM molecules, that are discussed in Chapter I, have opened perspectives for their application in high-density information storage devices (Leuenberger and Loss 2001). Therefore their controlled arrangement in different dimensions has become a major challenge in this research field. In this respect, several strategies have been developed and the most promising results involve their deposition on surfaces (Cornia et al. 2011; Domingo et al. 2011; Gatteschi et al. 2009; Mannini et al. 2010; Mannini et al. 2009; Saywell et al. 2010) and their association in extended coordination networks. This thesis focuses on the latter one: **organization of SMMs by coordinating linkers** such as (i) **diamagnetic anions** and (ii) **paramagnetic metal complexes**. In this context, we here offer an opportunity to become familiarized with the tremendously growing database of interesting coordination compounds based on single-molecule magnets (SMMs). Our aim in highlighting numerous recent examples of SMM-based networks is to underscore the intriguing features induced by the interactions between SMM building blocks through the coordination linkers.

At the same time, one of the greatest challenges in this area is to design multi-functional SMMs, SCMs or magnets in which two or more co-existing properties interplay. This realization may be achieved by introducing functional linkers such as photomagnetic, spin crossover, electron-transfer molecular complexes (Sato et al. 2007), into the coordination network of SMMs. Among known switchable functional molecule-based systems, tunable optical and magnetic properties have been

reported in several cyanido-based materials such as Prussian blue analogues (Tokoro et al. 2011; Verdaguer et al. 1999). The associated switching phenomenon is mostly from either spin crossover or metal-to-metal electron transfer that can be thermally and/or photo-induced. During the thesis of Ababei (CRPP, 2007 – 1011), she has focused on known spin crossover linkers to organize SMMs. In this thesis, we are interested in **(iii) photomagnetic linkers** that display a metal-to-metal electron transfer that can further coordinate to SMMs. Especially, we have limited our investigations to complexes containing cyanide groups for several aspects (Beltran et al. 2005; Shatruck et al. 2009; Tanase et al. 2006): short diatomic bridge mediates efficient magnetic couplings; its linearity allows easy prediction of final geometry and nature of magnetic coupling; the metal-to-metal electron transfer is well known through the cyanido bridges. In this regard, we briefly review the current status of such photoactive electron transfer systems based on cyanido coordination compounds, in the second part of this chapter. This area consists of materials from 3D Prussian blue analogues to 0D molecular complexes.

In the following, we provide the history and state of the art in the aforementioned two streams of research in this field. The first part is dedicated to the controlled organization of SMMs especially in coordination networks, and followed by the second part devoted to the photoactive cyanido-based bimetallic materials. Based on the literature reviewed throughout this chapter, the motivation and the objectives of this thesis work will be detailed in conclusion.

II.1 SMM-based coordination networks

SMMs are promising molecular building blocks to organize in an extended coordination network, in order to enhance the original SMM properties, and eventually to generate magnets working at high temperature. As shown by Wernsdorfer and co-workers, weak interactions between SMMs such as hydrogen bonds, that generate 0D to 3D supramolecular arrangements, indeed modify the intrinsic SMM properties and provide new magnetic behaviors: each SMM has an exchange interaction with its neighbors, shifting in field the quantum tunneling resonances observed for the individual SMM (Tiron et al. 2003a; Tiron et al. 2003b; Wernsdorfer et al. 2002a). These supramolecular intermolecular interactions were strong enough to modify the SMM quantum properties, however, they were too weak to transform spin network into a classical magnetic material. Thus the magnetic interactions through coordinating linking units between SMMs in well-designed architectures provide a unique opportunity to investigate new behaviors at the frontier between SMMs and classical ordered magnets.

In this section, the SMM assemblies in coordination networks, from one-dimensional to three-dimensional are reviewed with an emphasis on the synthetic strategies and magnetic properties. The following discussion will be divided relative to the degree of the nuclearity of the SMM units. The synthetic construction of coordination polymers relies upon many different parameters to form a desirable network, and the magnetic interactions can be strongly influenced by a small variation in the coordination environments. In this respect, even materials in which the metallic core loses its magnet-like property after the formation of the network will be shortly reviewed.

II.1.1 Dinuclear SMMs

II.1.1.1 [Mn₂] SMMs

Dinuclear complexes of Mn^{III} salen-type tetradentate Schiff-bases (SB) (salen = *N,N'*-ethylene-bis(salicylideneimine)) have been widely used to design magnetic networks. This great interest is motivated by the available *trans* coordinating sites along their Jahn-Teller (JT) axis corresponding to their local magnetic anisotropy easy axis. The self-assembled [Mn₂] unit has parallel JT axes and, in most of the cases, exhibits intramolecular ferromagnetic interactions between Mn^{III} ions to generate an $S_T = 4$ ground state and SMM properties (Lecren et al. 2007; Lu et al. 2006; Miyasaka et al. 2004a).

Isolated SMMs. The first report on SMM behavior of a dinuclear species was published in 2004 for [Mn₂(saltmen)₂(ReO₄)₂] (saltmen = *N,N'*-(1,1,2,2-tetramethylene)bis(salicylideneimine)) (**1**) that is shown in **Figure II.1** (Miyasaka et al. 2004a). The relaxation of the magnetization above 1.9 K follows an Arrhenius law with an effective energy gap, Δ_{eff}/k_B , of 16 K and a pre-exponential factor, τ_0 , of 8×10^{-9} s. Because of QTM (see section I.1.2 in Chapter I), the energy barrier was reduced from the expected value of 26 K. Similar magnetic properties have been reported in related dinuclear complexes: [Mn₂(saltmen)₂(X)₂] ($X^- = \text{CH}_3\text{COO}^-$ (**2**), N_3^- (**3**)), [Mn₂(salen)₂(NCO)₂] (**4**) and [Mn₂(3,5-Brsalen)₂(3,5-Brsalicylaldehyde)₂] (**5**) (3,5-Brsalen = *N,N'*-ethylene-bis(3,5-dibromosalicylideneimine)) (Lu et al. 2006). Moreover, [Mn₂(salpn)₂(H₂O)₂](ClO₄)₂ (**6**) (salpn = *N,N'*-propane-bis(salicylideneimine)) displayed an intermediate behavior between SMM and SCM thanks to the magnetic interaction through 1D hydrogen bonded supramolecular organization of dinuclear SMM units (Lecren et al. 2007).

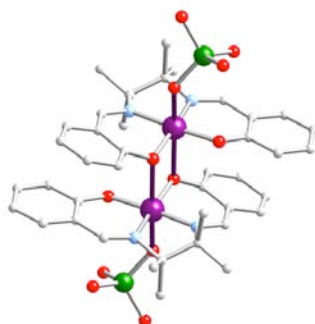


Figure II.1 View of the molecular structure of **1**. The JT axes on the Mn(III) ions are highlighted in violet. Color codes used throughout this chapter: Mn(III) violet, Re(VII) green, C grey, O red, and N light blue. The hydrogen atoms have been omitted for clarity (Miyasaka et al. 2004a).

Networks. In most cases, 2D architectures based on out-of-plane dinuclear [Mn₂(SB)₂]²⁺ units and paramagnetic linkers exhibit 3D order at low temperature. For example, [{Mn(saltmen)}₄-{Fe(CN)₆}] (ClO₄) (**7**) has been obtained by reacting [Mn₂(saltmen)₂(ClO₄)₂] with K₃[Fe(CN)₆] in a water/methanol mixture (Miyasaka et al. 1996). This network was reported to be a ferromagnet below 4.5 K (T_C). Two ferromagnetic exchange interactions, one between Mn^{III} and Fe^{III} through the cyanide bridge and the other in the out-of-plane [Mn^{III}₂] dinuclear core, induced an overall 3D order. A similar behavior was observed with another Mn-Fe system, [{Mn(saltmen)}₄{Fe(CN)₅(1-CH₃im)}](ClO₄)₂ (**8**) (1-CH₃im = 1-methylimidazole) that is shown in **Figure II.2** (Ni et al. 2007a). The Mn...Fe and Mn...Mn interactions were also found to be ferromagnetic and T_C was estimated at 4.8 K. In addition, structurally similar Mn-Cr systems were also reported: [{Mn(saltmen)}₄{Cr^I(CN)₅(NO)}](ClO₄) (**9**)

and $[\{\text{Mn}(\text{saltmen})\}_4\{\text{Cr}^{\text{III}}(\text{CN})_6\}](\text{ClO}_4)$ (**10**) (Liu et al. 2008b; Ni et al. 2007b). While the ferromagnetic interaction inside the dinuclear $[\text{Mn}^{\text{III}}_2]$ core is preserved, the coupling between Mn^{III} and $\text{Cr}^{\text{I}}/\text{Cr}^{\text{III}}$ through the cyanide bridge is antiferromagnetic for both of them, leading to a ferrimagnetic ground state below 6.4 K and 5 K, respectively. The diamagnetic $[\text{Fe}(\text{CN})_5(\text{NO})]^{2-}$ building block was also connected to the $[\text{Mn}_2(\text{saltmen})_2]^{2+}$ moiety to obtain a 2D compound: $[\{\text{Mn}(\text{saltmen})\}_4\{\text{Fe}(\text{CN})_5(\text{NO})\}](\text{ClO}_4)_2$ (**11**) (Ababei et al. 2009). The interaction between $[\text{Mn}_2]$ units was found to be very weakly antiferromagnetic through the Fe^{II} diamagnetic linker. As a result, the dynamics of magnetization are almost identical to the isolated $[\text{Mn}_2]$ SMMs, suggesting a negligible influence of inter-SMM coupling. It is worth noting here that all these 2D networks were produced with saltmen as a ligand and perchlorate as a counter anion. This reveals the key role played by the designed building blocks in the supramolecular interactions and that the architecture of a given system is not just simply controlled by the stoichiometry of the precursors.

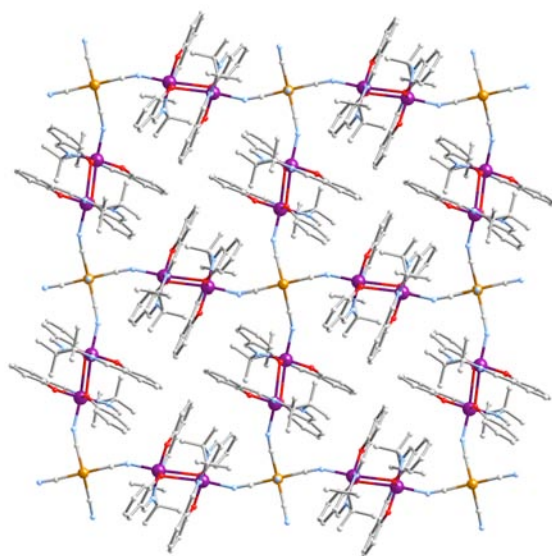
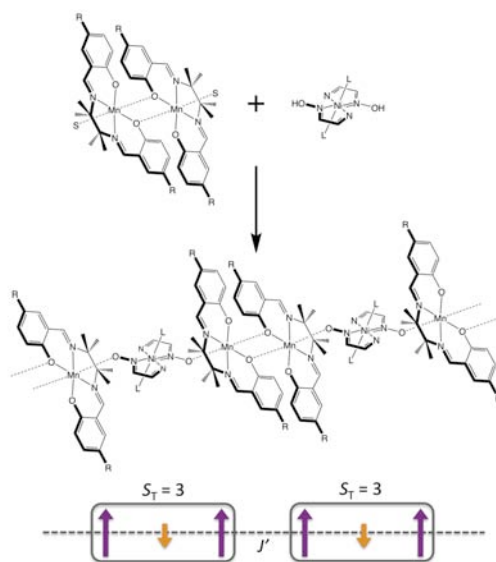


Figure II.2 View of the 2D network of **8**. Fe(III) is in yellow and the hydrogen atoms have been omitted for clarity (Ni et al. 2007a).

The 1D systems containing $[\text{Mn}_2]$ units are among the most studied single-chain magnets (SCMs) (see section I.2 in Chapter I). Based on the idea of connecting Ising-type spins in one dimension in order to generate slow dynamics of the magnetization, Miyasaka and our group have designed several series of uni-dimensional materials containing $[\text{Mn}_2]$ units connected with $\text{Ni}(\text{II})/\text{oxime}$ ligand complexes. The general formula of these materials is $[\text{Mn}_2(5\text{-Rsaltmen})_2\text{Ni}(\text{oxime})_2(\text{L})_x]\text{A}_2$ ($\text{R} = \text{H}$ and MeO ; oxime = pyridine-2-aldoxime (pao), 1-methylimidazole-2-aldoximate (miao), and 1-ethylimidazole-2-aldoximate (eiao); $\text{L} = \text{pyridine}$, 4-picoline, 4-tert-butylpyridine, and N -methylimidazole with $x = 2$ or 2,2'-bipyridine and 1,10-phenanthroline with $x = 1$; $\text{A} = \text{ClO}_4^-$, BF_4^- , PF_6^- , ReO_4^- , and BPh_4^-) (**Scheme II.1**) (Clérac et al. 2002; Miyasaka et al. 2009; Miyasaka et al. 2008; Miyasaka et al. 2003; Saitoh et al. 2007). All reactions were done between two pre-formed building blocks: the $[\text{Mn}_2]$ complex as a coordinating acceptor and Ni^{II} -oxime complex as a coordinating donor. The crystals were produced either by slow evaporation of the final methanol/water mixed solution of the two metal precursors, or by the slow diffusion of two methanol solutions of each metal ion precursor in a thin tube. From a synthetic point of view, the chains can be considered as a 1D network of $[\text{Mn}_2]$ SMMs linked by paramagnetic Ni^{II} oximate

building blocks (**Scheme II.1**). The experimental susceptibility, however, was reproduced well by the Heisenberg $[\text{Mn}^{\text{III}}\text{-Ni}^{\text{II}}\text{-Mn}^{\text{III}}]$ trinuclear model ($H = -2J\{S_{\text{Mn1}}S_{\text{Ni}} + S_{\text{Mn2}}S_{\text{Ni}}\}$, $S_{\text{T}} = S_{\text{Mn1}} + S_{\text{Ni}} + S_{\text{Mn2}}$) with Mn...Mn inter-trinuclear interactions treated in the mean-field approximation. The result showed a relatively strong antiferromagnetic interaction between Mn^{III} and Ni^{II} through the oximato bridge ($-24 \text{ K} < J/k_{\text{B}} < -19 \text{ K}$), compared to the small ferromagnetic interaction inside the $[\text{Mn}_2]$ core ($+0.2 \text{ K} < J'/k_{\text{B}} < +0.9 \text{ K}$). Thus, the repeating magnetic unit constituting the final complex is an $S_{\text{T}} = 3$ $[\text{Mn}^{\text{III}}\text{-Ni}^{\text{II}}\text{-Mn}^{\text{III}}]$ trinuclear unit as shown in **Scheme II.1** (Miyasaka et al. 2005a), and each trinuclear unit is ferromagnetically coupled along the chain *via* the bis-phenoxido bridge. In the low temperature region, most of these 1D systems exhibit slow relaxation of their magnetization with energy gaps between 50 to 73 K and τ_0 on the order of 10^{-10} s. These energy gap values are much higher than that of the repeating $[\text{Mn}^{\text{III}}\text{-Ni}^{\text{II}}\text{-Mn}^{\text{III}}]$ SMM unit, that is 18 K with $\tau_0 \approx 1 \times 10^{-7}$ s (see section II.1.2.2). The dynamics of these 1D coordination polymers are in a good agreement with SCM behavior, except for two systems: $[\text{Mn}_2(\text{saltmen})_2\text{Ni}(\text{pao})_2(\text{L})](\text{PF}_6)_2$ ($\text{L} = 2,2'\text{-bpy}$ (**12**) and phen (**13**)) (Miyasaka et al. 2009). In these two complexes, the NO-*cis*-coordination mode of the $[\text{Ni}(\text{pao})_2(\text{L})]$ moiety made the $[\text{Mn-Ni-Mn}]$ trinuclear unit bent instead of linear as in the other materials. This geometry reduces the magnetic anisotropy, and thus, no SCM behavior was observed.



Scheme II.1

Another example of a $[\text{Mn}_2]$ -based chain is $(\text{Et}_4\text{N})[\text{Mn}_2(5\text{-MeOsalen})_2\text{Fe}(\text{CN})_6]$ (**14**) (5-MeOsalen = *N,N'*-ethylene-bis(5-methoxysalicylideneimine)), in which each dinuclear $[\text{Mn}_2]$ moiety is coordinated to mononuclear $[\text{Fe}^{\text{III}}(\text{CN})_6]^{3-}$ units to make a heterometallic 1D assembly (Ferbinteanu et al. 2005). The compound has been obtained by reacting $[\text{Mn}(5\text{-MeOsalen})(\text{H}_2\text{O})](\text{PF}_6)$ with $(\text{Et}_4\text{N})_3[\text{Fe}(\text{CN})_6]$ in methanol. The final chain stabilizes the dimerization of the Mn^{III} -precursor that is in its monomeric form in the solid state before the reaction. This complex has two types of bridges, a cyanido bridge ($\text{Mn}\cdots\text{Fe}$, $J_{\text{Mn-Fe}}$) and a double phenoxido bridge ($\text{Mn}\cdots\text{Mn}$, J'), that both mediate ferromagnetic interactions ($J_{\text{Mn-Fe}}/k_{\text{B}} = +6.5 \text{ K}$, $J'/k_{\text{B}} = +0.07 \text{ K}$ with $H = -2J_{\text{Mn-Fe}}\{S_{\text{Mn1}}S_{\text{Fe}} + S_{\text{Mn2}}S_{\text{Fe}}\}$, $S_{\text{T}} = S_{\text{Mn1}} + S_{\text{Fe}} + S_{\text{Mn2}}$). Considering $J_{\text{Mn-Fe}} \gg J'$, this system can be viewed as a chain of ferromagnetically coupled $[\text{Mn}^{\text{III}}\text{-Fe}^{\text{III}}\text{-Mn}^{\text{III}}]$ units ($S_{\text{T}} = 9/2$) at low temperature (Ferbinteanu et al. 2005; Miyasaka et al. 1998). The relaxation time showed a crossover between two activated relaxation regimes as a manifestation of the finite-size effects (see section I.2.2): $\Delta_1/k_{\text{B}} = 31 \text{ K}$ with $\tau_0 = 3.7 \times 10^{-}$

10 s above 1.4 K and $\Delta_2/k_B = 25$ K with $\tau_0 = 3 \times 10^{-8}$ s below 1.4 K. In both regimes, the energy gap of the relaxation time has been clearly enhanced by the intra-chain magnetic interactions in comparison to the repeating $[\text{Mn}^{\text{III}}\text{--Fe}^{\text{III}}\text{--Mn}^{\text{III}}]$ SMM unit ($\Delta_{\text{eff}}/k_B = 14$ K and $\tau_0 = 2.5 \times 10^{-7}$ s).

As mentioned above, these 1D systems containing $[\text{Mn}^{\text{III}}_2]$ units can be alternatively seen as chains of $[\text{Mn}^{\text{III}}\text{--M--Mn}^{\text{III}}]$ units ($\text{M} = \text{Ni}^{\text{II}}, \text{Fe}^{\text{III}}$) that are indeed trinuclear SMMs. The readers are invited to see section II.1.2.2 for more details.

Recently, three one-dimensional compounds, $[\text{Mn}(\text{5-Brsaltmen})(\text{H}_2\text{O})(\text{acetone})]_2[\{\text{Mn}_2(\text{5-Brsaltmen})_2\}(\text{SiW}_{12}\text{O}_{40})]$ (**15**), $[\text{Mn}_2(\text{naphtmen})_2(\text{L})] \cdot (\text{ClO}_4)_2 \cdot 2\text{Et}_2\text{O} \cdot 2\text{MeOH} \cdot \text{H}_2\text{O}$ (**16**), and $[\text{Mn}_2(\text{naphtmen})_2(\text{HL})](\text{ClO}_4)_2 \cdot \text{MeOH}$ (**17**) ($\text{naphtmen}^{2-} = \text{N,N}'\text{-(1,1,2,2-tetra-methylethylene)bis(naphthylideneiminato) dianion}$, $\text{HL} = 6\text{-amino-9-}\beta\text{-carboxyethylpurine}$) were reported (Sawada et al. 2012; Zhang et al. 2012). In **15**, the $[\text{Mn}_2(\text{5-Brsaltmen})_2]^{2+}$ units are bridged by large diamagnetic polyoxometalate complexes that behave as spacers between the SMM units. Thus, SMM properties similar to the $[\text{Mn}_2]$ precursor are observed instead of a SCM behavior. For **16** and **17**, inter-chain H-bonds created between nucleoside ligands isolate the chains and prevent the stabilization of a three-dimension long-range order. As a consequence, both **16** and **17** behave as SCMs due to the canting of the anisotropic $S_T = 4$ $[\text{Mn}_2]$ units along the chain.

II.1.1.2 $[\text{Dy}_2]$ SMMs

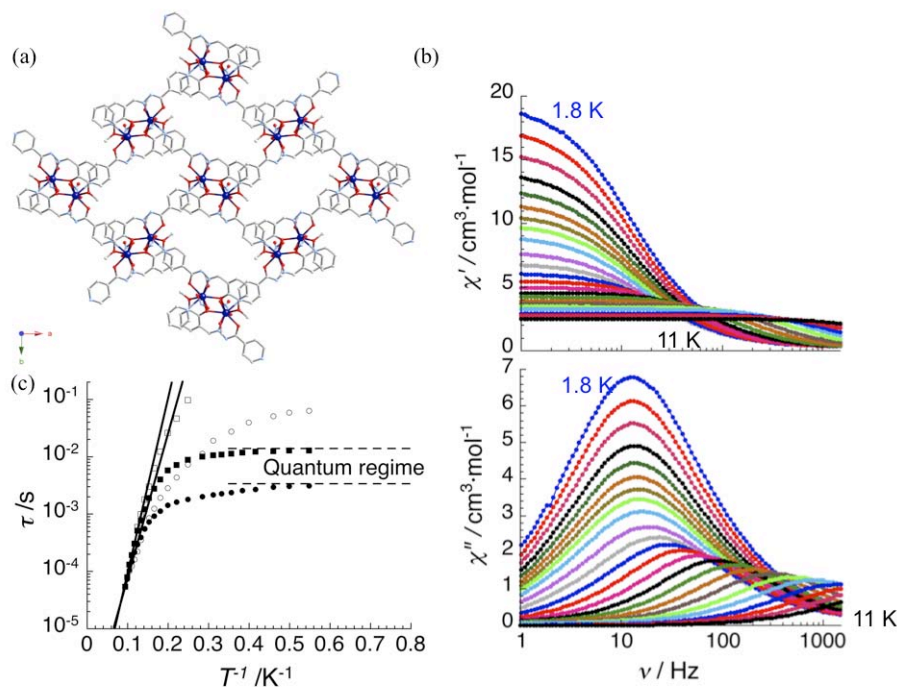


Figure II.3 (a) View of the 2D network of complex **19** along the c -axis. Dy(III) is in dark blue and hydrogen atoms have been omitted for clarity. (b) Frequency dependence of the in-phase (χ') and out-of-phase (χ'') ac susceptibility from 1.8 to 3.2 K at an interval of 0.2 K and from 3.5 to 11 K at an interval of 0.5 K under zero dc field for **19**. (c) Magnetization relaxation time (τ) vs. T^{-1} plot for **18** and **19** under zero dc field (\bullet and \blacksquare respectively) and under the optimum dc fields (\circ and \square , at 800 and 700 Oe for **18** and **19**, respectively). The solid lines correspond to the Arrhenius laws (Lin et al. 2008).

Besides transition metal-SMMs, research interests on pure lanthanide-based systems increased enormously in the past few years. The introduction of lanthanides in SMMs has attracted great attention due to their large intrinsic magnetic anisotropy that might induce a large energy barrier

(Rinehart and Long 2011). Indeed, an only lanthanide-based SMM (a $[\text{Dy}_5]$ complex) holds the record value of the energy barrier at 530 K (Blagg et al. 2011), which surpasses the relaxation barrier previously achieved by 3d transition-metal systems. $[\text{Dy}_2(\text{hmi})_2(\text{NO}_3)_2(\text{MeOH})_2]$ (**18**) and $[\text{Dy}_2(\text{hmi})_2(\text{NO}_3)_2(\text{MeOH})_2]\cdot\text{MeCN}$ (**19**) have similar dinuclear dysprosium(III) cores in which the metal centres are bridged by the phenoxido groups of two hmi ligands with Dy-O-Dy angles of 106.41° and 107.68° for **18** and **19** respectively ($\text{H}_2\text{hmi} = (2\text{-hydroxy-3-methoxyphenyl})\text{-methylene(isonicotino)hydrazine}$) (Lin et al. 2008). **18** is a discrete complex, and **19** forms a 2D network of $[\text{Dy}_2]$ units due to the pyridyl N atoms that further coordinate to the dysprosium atom of the neighboring complexes (**Figure II.3**). Both were synthesized from $\text{Dy}(\text{NO}_3)_3$ and H_2hmi in presence of Et_3N (**18**) or pyridine (**19**). Although their crystallographic structures are different, their magnetic properties are similar. The shape and frequency dependence of the ac susceptibility signal reveal their SMM properties, with a quantum regime of relaxation below 2 K under zero magnetic field. Above 8 K, the relaxation time is thermally activated (**Figure II.3**). The 2D coordination network of $[\text{Dy}_2]$ units, **19**, possesses a slightly enhanced energy barrier, $\Delta_{\text{eff}}/k_{\text{B}} = 71$ K (with $\tau_0 = 7 \times 10^{-8}$ s), in comparison to **18** ($\Delta_{\text{eff}}/k_{\text{B}} = 56$ K with $\tau_0 = 3 \times 10^{-7}$ s). This effect is not the result of the negligible inter- $[\text{Dy}_2]$ interactions through the diamagnetic hmi ligand in **19** but likely the consequence of a geometrical distortion of the Dy^{III} coordination sphere, that optimize the intra-complex ferromagnetic Dy...Dy interaction and/or the anisotropy of the $[\text{Dy}_2]$ units.

II.1.1.3 $[\text{CuTb}]$ and $[\text{NiDy}]$ SMMs

The large magnetic anisotropy of the lanthanide ions motivates researchers to design SMMs incorporating both 3d and 4f metal ions. Indeed, many heterometallic 3d/4f SMMs have been reported in the past few years. Among them, some dinuclear $[\text{Cu}^{\text{II}}\text{Tb}^{\text{III}}]$ and $[\text{Ni}^{\text{II}}\text{Dy}^{\text{III}}]$ complexes based on compartmental Schiff-base ligands display SMM properties and are suitable building units to design coordination networks.

The first $[\text{Cu}^{\text{II}}\text{Tb}^{\text{III}}]$ SMM, $[\text{LCu}(\text{O}_2\text{COME})\text{Tb}(\text{thd})_2]$ (**20**) ($\text{L}^{2-} = \text{N,N}'\text{-2,2-dimethylpropylenedi(3-methoxysalicylideneiminato)}$, thd = tetramethylheptanedionato), was reported in 2006 (Costes et al. 2006b). The Cu^{II} ion adopts a square pyramidal coordination mode with the equatorial plane occupied by N_2O_2 donor atoms provided by the L compartmental ligand, while the axial position is occupied by a μ -bridging CO_2 group from the monomethylcarbonate anion. In this complex, the Tb ion is surrounded by nine coordinating oxygen atoms: two phenoxido, two from the OMe side arms, four from the two bidentate thd ligands, and one from the bridging carbonate anion that complete the coordination sphere. Compound **20** shows slow dynamics of the magnetization with a thermally activated relaxation time ($\Delta_{\text{eff}}/k_{\text{B}} = 13.8$ K and $\tau_0 = 3 \times 10^{-7}$ s). More recently, similar dinuclear $[\text{Cu}^{\text{II}}\text{Tb}^{\text{III}}]$ complexes displaying SMM properties were also reported (Kajiwarra et al. 2011; Kajiwarra et al. 2009; Kajiwarra et al. 2008).

The analogous $[\text{Ni}^{\text{II}}\text{Dy}^{\text{III}}]$ complex, $[\text{Ni}(\text{CH}_3\text{CN})(\text{H}_2\text{O})(\text{valpn})\text{Dy}(\text{NO}_3)_3(\text{H}_2\text{O})_2]\cdot 2\text{NO}_3\cdot\text{CH}_3\text{CN}\cdot\text{H}_2\text{O}$ (valpn = 1,3-propanediyl-bis(2-iminomethylene-6-methoxy-phenol)) (**21**) was also reported to exhibit SMM behavior (Pasatoiu et al. 2011). While the Dy^{III} coordination sphere in **21** is similar to the Tb^{III} one in **20**, the Ni^{II} metal ion adopts an octahedral geometry. Although no maximum was observed in the out-of-phase ac susceptibility down to 2 K in zero field, slow dynamics were clearly observed under 1000 Oe without being able to estimate the relaxation time energy barrier.

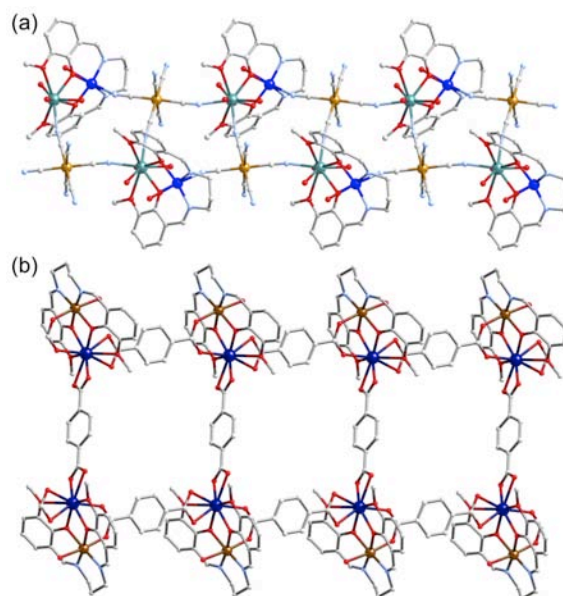


Figure II.4 Views of the ladder-type 1D structures of **22** (a) and **24** (b). Cu(II) is in blue, Tb(III) is in green and Ni(II) is in brown. The hydrogen atoms have been omitted for clarity (Pasatoiu et al. 2010; Shiga et al. 2011).

Both dinuclear $[\text{Cu}^{\text{II}}\text{Tb}^{\text{III}}]$ and $[\text{Ni}^{\text{II}}\text{Dy}^{\text{III}}]$ units can self-assemble into tetranuclear species, that are also SMMs (Costes et al. 2008; Costes et al. 2006a; Hamamatsu et al. 2007; Osa et al. 2003; Pasatoiu et al. 2010), and into 1D compounds when coordination linkers are used. Two one-dimensional networks based on $[\text{Cu}^{\text{II}}\text{Tb}^{\text{III}}]$ SMMs were obtained using (i) a paramagnetic ferricyanide anion ($[\text{Fe}(\text{CN})_6]^{3-}$) and (ii) a photochromic diarylethene ligand as bridging species: $[\{\text{LCuTb}(\text{H}_2\text{O})_3\} \cdot \{\text{Fe}(\text{CN})_6\}] \cdot 4(\text{H}_2\text{O})$ (**22**, **Figure II.4**) ($\text{L}^{2-} = \text{N,N}'\text{-propylenedi(3-methoxysalicylideneiminato)}$) (Gheorghe et al. 2010) and $[\{\text{LCuTb}(n\text{-BuOH})_{0.5}\}_2(\text{dae-c})_3] \cdot 5(\text{DMF}) \cdot 4(n\text{-BuOH}) \cdot 2(\text{H}_2\text{O})$ (**23**) ($\text{H}_2\text{dae} = 1,2\text{-bis(5-carboxyl-2-methyl-3-thienyl)perfluorocyclopentene}$ and $\text{c} = \text{closed form isomer}$), (Shiga et al. 2011) respectively. Both ladder-type chains were synthesized in a rational stepwise approach. First the mononuclear Cu^{II} complex, $[\text{CuL}]$, was isolated and then reacted with terbium nitrate to form the $[\text{Cu}^{\text{II}}\text{Tb}^{\text{III}}]$ complex. Finally the nitrate groups were substituted by the selected bridging ligands. In a similar way, a one-dimensional system was also obtained employing terephthalate dianions (tfa^{2-}) as the diamagnetic linkers between $[\text{Ni}^{\text{II}}\text{Dy}^{\text{III}}]$ units: $[\text{Ni}_2(\text{valpn})_2\text{Dy}_2(\text{H}_2\text{O})_2(\text{tfa})_3]$ (**24**, **Figure II.4**) (Pasatoiu et al. 2010). In **22**, strongly field sweep rate and temperature dependent M vs H hysteresis loops are observed below 1 K indicating the slow dynamics of the magnetization. It is worth mentioning the absence of a pronounced step at $H = 0$ in the hysteresis loops of **22** while fast ground state quantum tunnelling was observed in **20**. This result experimentally demonstrates that the formation of the coordination network modifies the quantum and dynamic properties of the parent $[\text{Cu}^{\text{II}}\text{Tb}^{\text{III}}]$ units by introducing inter-complex magnetic interactions. In **23**, slow relaxation of the magnetization similar to that observed for **20** was studied, indicating that the $[\text{Cu}^{\text{II}}\text{Tb}^{\text{III}}]$ SMM units in the ladder-type chains are, indeed, well isolated by the bridging diarylethene ligands. The irradiation of **23** with visible light induced the expected photochromic effect and also a slight variation of the slow dynamics attributed to a photo-modification of the intermolecular interaction (Shiga et al. 2011). This well-designed system can thus be considered as a multifunctional material with some degree of synergy between the optical and magnetic properties. In **24**, a pronounced quantum tunneling of the magnetization was observed in the ac susceptibility data at zero-external field below 2 K, leading to a very small energy barrier of ca. 2 K ($\tau_0 = 1.3 \times 10^{-5}$ s). The probability of magnetization relaxation

through QTM was minimized by applying an external field. At 1000 Oe, the temperature dependence of the characteristic time in the thermally activated regime of relaxation was measured and the associated energy gap was estimated at 17.4 K ($\tau_0 = 8.0 \times 10^{-7}$ s). Compared to the isolated $[\text{Ni}^{\text{II}}\text{Dy}^{\text{III}}]$ SMM, **21**, the observed dynamics in **24** are significantly slowed down with an enhanced energy barrier (Pasatoiu et al. 2010).

These examples (**22** – **24**) show that both cyanido and carboxylato type ligands can coordinate the $[\text{M}^{\text{II}}\text{Ln}^{\text{III}}]$ cores ($\text{M} = \text{Cu}, \text{Ni}$, $\text{Ln} = \text{Tb}, \text{Dy}$), opening a route towards a broad choice of possible linkers. This diversity will offer synthetic opportunities to design new magnetic systems with, for example, large inter-SMM magnetic interactions and/or multi-functionalities.

II.1.2 Trinuclear SMMs

II.1.2.1 $[\text{Mn}_3]$ SMMs

For decades $\mu_3\text{-O}$ -bridged triangular Mn^{III} complexes were known to exhibit intramolecular antiferromagnetic interactions. However, new $[\text{Mn}_3\text{O}]^{7+}$ systems were discovered recently with intramolecular ferromagnetic interactions and thus an $S_T = 6$ ground state (Stamatatos et al. 2005). This discovery led to active research in coordination chemistry and the field of molecule-based magnetism, to develop new SMMs and their networks with delicate modifications of their structure.

The $[\text{Mn}_3]$ unit is quite flexible and therefore the intra-core ferromagnetic interaction is difficult to maintain when they assemble into networks, (Inglis et al. 2009). It has been also shown that the trinuclear Mn^{III} unit can pair to form $[\text{Mn}_6]$ complexes (**Figure II.5**), and $[\text{Mn}_6]$ themselves can assemble into coordination networks (Inglis et al. 2012). Therefore both $[\text{Mn}_3]$ and $[\text{Mn}_6]$ systems will be discussed in the following sections.

Isolated SMMs. $[\text{Mn}_3\text{O}(\text{O}_2\text{CMe})_3(\text{mpko})_3](\text{ClO}_4) \cdot 3\text{CH}_2\text{Cl}_2$ (Hmpko = methyl 2-pyridyl ketone oxime) (**25**, **Figure II.5**) was the first triangular $[\text{Mn}_3]$ SMM in which the intra-complex magnetic interaction is ferromagnetic resulting in an $S_T = 6$ spin ground state (Stamatatos et al. 2005). Instead of using a one-pot synthesis, this SMM was synthesized from the preformed $[\text{Mn}_3\text{O}(\text{O}_2\text{CMe})_6(\text{py})_3](\text{ClO}_4)$ complex. Even though **25** does not show a large energy barrier ($\Delta_{\text{eff}}/k_B = 10.9$ K, $\tau_0 = 5.7 \times 10^{-8}$ s), this result is an important breakthrough as it was the first evidence that the fine tuning of the Mn-N-O-Mn torsion angle can change the intramolecular magnetic interaction of the core from antiferromagnetic to ferromagnetic.

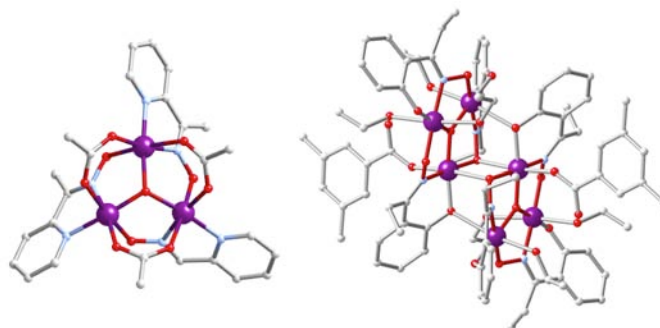


Figure II.5 View of the molecular structures of **25** (left) and **28** (right). The hydrogen atoms have been omitted for clarity (Milios et al. 2007a; Stamatatos et al. 2005).

The first reported pair of $[\text{Mn}_3]$ units, a $[\text{Mn}_6]$ SMM, was $[\text{Mn}_6\text{O}_2(\text{O}_2\text{CR})_2(\text{sao})_6](\text{EtOH})_4 \cdot x\text{EtOH}$ (**26**) ($\text{R} = \text{Me}$ or Ph , $x = 4$ or 1 , H_2sao = salicyl-aldoxime) (Milios et al. 2004). Each

[Mn₃] triangle possesses intramolecular antiferromagnetic interactions, and is further coupled to another triangle through ferromagnetic interactions, to give a spin ground state of 4. An energy barrier of 28 K and the pre-exponential factor of the Arrhenius law (τ_0) of 3.6×10^{-10} s were estimated experimentally.

Finally [Mn₆] complexes with ferromagnetic interactions in the triangular [Mn₃] subunit were also synthesized (Milios et al. 2007a; Milios et al. 2007b): [Mn₆O₂(O₂CPh)₂(Et-sao)₆(EtOH)₆] (**27**) and [Mn₆O₂(O₂CPh(Me)₂)₂(Et-sao)₆(EtOH)₆] (**28**). In **27**, the introduction of an ethyl substituent on the salicylaldoxime ligand induces a severe twisting of the manganese oximate linkage within each [Mn₃] subunit, resulting in the stabilization of an $S_T = 12$ ground state with $\Delta_{\text{eff}}/k_B = 53$ K. Furthermore, the replacement of benzoate in **27** to 3,5-dimethylbenzoate increased the Mn–N–O–Mn torsion angle from 36.5° to 39.1° in **28** (Figure II.5). The bigger puckering of Mn–N–O–Mn torsion angle in a planar [Mn₃] unit brought not only dominant ferromagnetic interactions but also a stronger exchange interaction, resulting in a higher energy barrier: $\Delta_{\text{eff}}/k_B = 86.4$ K (with $\tau_0 = 2 \times 10^{-10}$ s), that is very close to the theoretical value of 89 K expected for this $S_T = 12$ SMM.

Networks. The networks based on [Mn₃]/[Mn₆] units are largely divided into two categories, depending on the capping ligands: pyrazolate and salicylaldoxime-derivatives. Thus, the following discussions are organized based on these ligands.

The one-dimensional structures based on the [Mn^{III}₃O] unit and pyrazolate ligands have the general formula as [Mn^{III}₃O(L)₃(S)_n(OAc)], where L is the capping ligands: ppz, Meppz, or Brppz (H₂ppz = 3-(2-hydroxyphenyl)pyrazole, H₂Meppz = 3-(2-hydroxy-5-methylphenyl)pyrazole, H₂Brppz = 3-(5-bromine-2-phenolate)pyrazolate), S is methanol or ethanol with $n = 3$ or 4 (Bai et al. 2006; Liu et al. 2008a; Liu et al. 2009; Tao et al. 2006). The bridging ligands in all compounds are acetates. The Mn–N–O–Mn torsion angle in the [Mn₃] subunit was not big enough to induce a ferromagnetic interaction, leading to antiferromagnetic interactions inside the triangular core for all compounds. The intrachain magnetic interaction mediated through the *anti-anti* acetato bridge between [Mn₃] subunits was also found to be antiferromagnetic, except for the methanol analogues with ppz and Meppz ligands. In most cases, the methanol analogues result in a long-range ordering, while the ethanol analogues show slow relaxation of the magnetization due to the presence of spin canting.

Instead of using pyrazolate-derivatives as ligands, salicylaldoxime-derivative ligands have been also utilized in [Mn₆] SMMs with the general formula of [Mn₃O(L)₃(L_{br})(CH₃OH)_{4-n}(H₂O)_n] (H₂L = 3,5-di-*tert*-butylsalicylaldoxime or 3-*tert*-butyl-5-methylsalicylaldoxime; L_{br} = formato or azido) (Song et al. 2010; Xu et al. 2007). The magnetic interactions inside the [Mn₃] subunit are found to be antiferromagnetic. However, inter-[Mn₃] interactions along the chain could be modified depending on the bridges: *anti-anti* formato bridges mediated weak antiferromagnetic interactions while azido bridges were found to induce ferromagnetic interactions. All chains exhibit slow relaxation of the magnetization that could be understood considering the non-parallel orientations of the adjacent [Mn₃] units along the chain, i.e. spin-canting. In addition, the $\ln(\chi T)$ vs T^{-1} plot of the compounds with azido bridges showed a linear regime (i.e. exponential increase of the correlation length) as expected for anisotropic 1D systems and thus confirming the 1D nature. As a consequence, they show the enhanced energy barrier compared to the ones with formato bridges.

The networks based on the [Mn₆] unit was obtained that have the formula of [Mn₆O₂(L)₆(S)_x(H₂O)_y(L_{br})], with the capping ligands (L) being sao or Et-sao and the solvents (S) being methanol or ethanol (Jones et al. 2009; Katsenis et al. 2012). As the bridging ligands, bis- or tri-

carboxylates (H_nL = iso-phthalic acid, succinic acid, 1,3,5-benzene-tricarboxylic acid) are used finally to form the 1D and 2D structures depending on the number of carboxylate functionalities on the ligands. However, the magnetic interactions between two adjacent $[Mn_6]$ units are negligible, resulting in quasi-isolated SMM-behaviors. The magnetic interaction between $[Mn_6]$ units was enhanced by replacing carboxylato ligands by azido linkers: $[Mn_6O_2(4-MeO-sao)_6(N_3)_2(MeOH)_4]$ (**29**, **Figure II.6**) (Yang et al. 2010). Compound **29** orders antiferromagnetically below 14 K, but slow relaxation of the magnetization was still observed in the antiferromagnetic phase (**Figure II.6**). This highlights the fact that antiferromagnetic order does not prevent the dynamics of the 1D object as previously demonstrated by Coulon and co-workers (Coulon et al. 2009; Miyasaka et al. 2010).

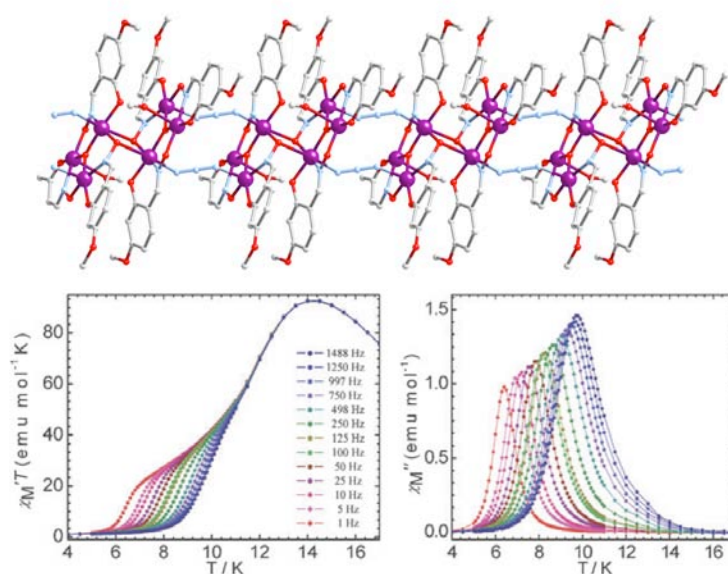


Figure II.6 Top: View of the 1D network in **29**. Hydrogen atoms have been omitted for clarity. Bottom: Temperature dependence of the in-phase susceptibility and temperature product (left) and out-of-phase susceptibility component (right) for **29** under a zero dc field. The data were collected in an ac field oscillating at the indicated frequency (Yang et al. 2010).

An interesting attempt to make a switchable material based on the $[Mn_6]$ unit was also reported, by using the potentially electroactive bithiophenedicarboxylic acid (H_2btda) as a bridging linker (Haryono et al. 2010). In principle, the diamagnetic (in the OFF state) oligothiophene derivatives can be oxidized to a radical that is responsible for the “ON” state. The obtained one-dimensional compound $[Mn_6O_2(Et-sao)(btda)(EtOH)_4(H_2O)_2] \cdot 2EtOH$ (**30**) displays the magnetic behavior of the isolated $S_T = 12$ $[Mn_6]$ SMMs without the switching properties, due to the instability of the radical cation. Nevertheless, **30** proves the possibility of designing hybrid materials with this synthetic strategy.

It is worth noting that most of the synthetic methods to obtain networks based on $[Mn_3]$ or $[Mn_6]$ moieties were direct one-pot methods. In addition, the intramolecular ferromagnetic interactions in the subunits, in order to have a spin ground state of $S_T = 6$ for $[Mn_3]$ or $S_T = 12$ for $[Mn_6]$, were never observed in network systems. In this respect, the rational building block approach might be a promising way to control the important parameters (i.e., the geometry of the capping ligands and bridging ligands) in order to maintain a large enough Mn-N-O-Mn torsion angle to generate intra- $[Mn_3]$ ferromagnetic interactions. Furthermore, all the used linkers were diamagnetic units, and thus sometimes the size of the ligand was too large to create an efficient magnetic interaction between neighboring SMM units. Thus, it would be interesting in the future to introduce suitable paramagnetic

linkers to connect $[\text{Mn}_3]$ and $[\text{Mn}_6]$ SMMs, as shown by Hendrickson and Feng recently (Feng et al. 2010).

II.1.2.2 $[\text{Mn}_2\text{Ni}]$ and $[\text{Mn}_2\text{Fe}]$ SMMs

As explained in the previous section II.1.1.1, some heterometallic 1D materials based on $[\text{Mn}_2]$ SMMs exhibit slow relaxation of the magnetization, also called SCM behavior. In these systems, the repeating magnetic units inside the chain are $[\text{Mn}^{\text{III}}\text{-ON-Ni}^{\text{II}}\text{-NO-Mn}^{\text{III}}]$ and $[\text{Mn}^{\text{III}}\text{-NC-Fe}^{\text{III}}\text{-CN-Mn}^{\text{III}}]$, considered as $S_T = 3$ and $S_T = 9/2$ anisotropic macro-spins at low temperatures. The activation energy of the relaxation time in these one-dimensional objects results from a combined effect of the individual anisotropy of the macro-spin composing the chain and the magnetic correlation along the chain. Thus, this discovery motivated researchers to independently synthesise and analyse the isolated anisotropic trinuclear macro-spins in order to confirm the conclusions obtained on the SCM materials.

Two $[\text{Mn}^{\text{III}}\text{-Ni}^{\text{II}}\text{-Mn}^{\text{III}}]$ trinuclear SMMs were obtained: $[\text{Mn}_2(5\text{-Rsaltmen})_2\text{Ni}(\text{pao})_2(\text{phen})](\text{ClO}_4)_2$ ($R = \text{Cl}$ (**31**), Br (**32**)) (Miyasaka et al. 2005a). In **31** and **32**, the Ni^{II} complex preserved the NO-*trans*-coordination mode to produce a linear molecular structure, which was not the case for the previous 1D network (**13**) (also with phenanthroline as a bidentate ligand on the Ni^{II} ion) (Miyasaka et al. 2009). The exchange interaction between Mn^{III} and Ni^{II} was found to be antiferromagnetic ($J/k_B = -24.3$ K) corresponding well with the value estimated from the chain. The relaxation time of these SMMs shows a thermally activated behavior with $\Delta_{\text{eff}}/k_B \approx 18$ K and $\tau_0 \approx 1 \times 10^{-7}$ s.

The trinuclear complex, $(\text{NEt}_4)[\text{Mn}_2(\text{salmen})_2(\text{MeOH})_2\text{Fe}(\text{CN})_6]$ ($\text{salmen} = \text{rac-N,N'-(1-methylethylene)-bis(salicylideneimine)}$), (**33**) was produced using the salmen ligand for the Mn^{III} precursor instead of 5-MeOsalen like in **14** (Ferbinteanu et al. 2005; Miyasaka et al. 1998). The ferromagnetic interactions between Mn^{III} and Fe^{III} lead to an $S_T = 9/2$ ground state for the complex. This molecular system shows field sweep-rate dependent M vs H hysteresis highlighting the slow relaxation of the magnetization, i.e. SMM properties. The effective energy barrier and the pre-exponential factor were estimated at $\Delta_{\text{eff}}/k_B = 14$ K and $\tau_0 = 2.5 \times 10^{-7}$ s.

These three examples (**31** – **33**), emphasize the importance of the environment in obtaining trinuclear SMMs instead of SCMs. The molecular complexes, **31**, **32**, **33** and their 1D network analogues possess similar intratrinuclear magnetic coupling values. However, the network systems demonstrated that the dynamics can be remarkably slowed down even with the small intertrinuclear interaction along the chains. For more details on the network systems based on these SMMs, the readers are invited to read the previous section II.1.1.1.

II.1.3 Tetranuclear SMMs

II.1.3.1 $[\text{Mn}_4]$ SMMs

One of the most fascinating SMMs used as a building block in order to construct networks in a rationalized way is a tetranuclear $[\text{Mn}_4]$ complex. It has a mixed-valence $[\text{Mn}^{\text{III}}_2\text{Mn}^{\text{II}}_2(\mu_3\text{-O})_2(\mu\text{-O})_4]$ core with manganese ions arranged in a double-cuboidal fashion (**Figure I.1**). The two internal Mn^{III} ions are connected through two μ_3 -oxido bridges and the two external Mn^{II} ions are coordinated with two μ -alkoxido and one μ_3 -oxido atoms. In most cases, all manganese ions are ferromagnetically coupled to give an $S_T = 9$ spin ground state (Lecren et al. 2005b; Yoo et al. 2001). In addition to this large spin ground state, the two Mn^{III} ions have parallel JT axes maximizing of the uniaxial anisotropy

in this complex and thus its SMM behavior. Even though there are some exceptions for which this type of $[\text{Mn}_4]$ complex has an $S_T = 8$ or $S_T = 1$ ground state (Brechtin et al. 1999; Lecren et al. 2005a; Yoo et al. 2000), it is worth noting that the $[\text{Mn}_4]$ core remains quasi-identical in the networks to keep the same $S_T = 9$ spin ground state as in most of the isolated analogues. The available coordination sites on the Mn^{II} ions have been used to construct new magnetic architectures by coordinating appropriate polydentate ligands as illustrated in the following paragraph and in a previous review (Roubeau and Cl  rac 2008).

Isolated SMMs. The first SMMs with this double cuboidal core were $[\text{Mn}_4(\text{Hpdm})_6(\text{MeCO}_2)_2](\text{ClO}_4)_2 \cdot 2\text{MeCN} \cdot 2\text{Et}_2\text{O}$ (H_2pdm = pyridine-2,6-dimethanol) (**34**) and its analogue, $[\text{Mn}_4(\text{Hpdm})_6(\text{MeCO}_2)_2](\text{ClO}_4)_2 \cdot 2.5\text{H}_2\text{O}$ (**34b**), which possess an $S_T = 8$ and $S_T = 9$ spin ground state, respectively (Brechtin et al. 1999). Four of the Hpdm^- have one protonated uncoordinated hydroxymethyl group pointing away from the core, while the deprotonated groups form the four μ -O bridges. The two remaining Hpdm^- ligands have their deprotonated hydroxido oxygen atom in a μ_3 -bridging mode, and the protonated one is coordinated as a terminal ligand to the Mn^{II} ions. Each central Mn^{III} ion is additionally bridged to one of the Mn^{II} ions by an acetato group. The tridentate coordination mode of the Hpdm^- ligands resulted in an efficient chelation to the outer Mn^{II} ions. As all terminal Mn^{II} ions are thus blocked, compound **34** is not a good candidate to build extended assemblies.

In contrast to **34**, $[\text{Mn}_4(\text{hmp})_6\text{Br}_2(\text{H}_2\text{O})_2]\text{Br}_2 \cdot 4\text{H}_2\text{O}$ (Hhmp = 2-hydroxymethylpyridine) (**35**) has Mn^{II} sites with labile coordinating solvents or Br^- anions that can be easily substituted by other bridging ligands (Yoo et al. 2001). This complex was synthesized under aerobic conditions where the Mn^{II} precursor salt is partially oxidized in the presence of the ligand (Hhmp) and base (tetraethylammonium hydroxide). This one-pot synthesis is quite different from the synthetic method of **34** using the preformed $[\text{Mn}_3\text{O}(\text{O}_2\text{CMe})_6(\text{py})_3](\text{ClO}_4)$ complex. The coordinated bromide anions on the terminal Mn^{II} ions interact via a $\text{Br} \cdots \text{Br}$ separation of 4.91   between neighboring $[\text{Mn}_4]$ moieties, resulting in a 1-D supramolecular arrangement of the $[\text{Mn}_4]$ units through these weak contacts. In addition, a 3D hydrogen-bonding network of the $[\text{Mn}_4]$ moieties is observed. Altogether, these intermolecular interactions are at the origin of the magnetic transition observed at 1.33 K to a three-dimensional antiferromagnetic phase. Nevertheless, single-molecule magnet behavior is observed above this temperature ($\Delta_{\text{eff}}/k_B = 15.8$ K and $\tau_0 = 2.9 \times 10^{-8}$ s). This compound was in fact the first $[\text{Mn}_4]$ SMM isolated with the Hhmp ligand.

Since the discovery of **35**, several derivatives that exhibit SMM properties have been reported, including $[\text{Mn}_4(\text{hmp})_6(\text{NO}_3)_2(\text{H}_2\text{O})_2](\text{NO}_3)_2 \cdot 2.5\text{H}_2\text{O}$ (**36**, **Figure I.1**, see section I.1 in Chapter I) (Lecren et al. 2005b). The substitution of terminal Br^- ions by NO_3^- ions prevent the $\text{Br} \cdots \text{Br}$ interactions and π - π interactions observed in **35**. This structural feature allows **36** to be studied in detail down to 0.04 K, since above this temperature no long-range order, as seen in **35**, is detected. The two relaxation modes of the magnetization, thermally activated (above 0.34 K) and through quantum tunneling (below 0.34 K), were studied (**Figure I.4**). In addition, quantum phase interference has been observed and used to estimate the transverse anisotropy parameter ($E/k_B = 0.083$ K) (**Figure I.7**). Remarkably, E in **36** was significantly lower than the estimated value in **35** ($E/k_B = 0.124$ K), resulting in a slowing down of the QTM characteristic relaxation time (τ_{QTM}) and an enhancement of the effective energy barrier (Δ_{eff}) at 20.9 K (with $\tau_0 = 6.7 \times 10^{-9}$ s).

Networks. The very first coordination network of SMMs (with any SMM repeating unit) was reported in 2004: $[\text{Mn}_4(\text{hmp})_4(\text{OH})_2\text{Mn}(\text{dcn})_6] \cdot 2\text{MeCN} \cdot 2\text{THF}$ (dcn^- = dicyanamide) (**37**) (Miyasaka et al. 2004b). This 3D compound was achieved by self-assembly in acetonitrile containing $\text{Mn}(\text{ClO}_4)_2$, Hhmp, and $\text{Na}(\text{dcn})$ in a molar ratio of 1:2:1. It is interesting to note that the introduction of $\text{Mn}(\text{NO}_3)_2$ instead of $\text{Mn}(\text{ClO}_4)_2$, keeping the identical synthetic conditions, does not lead to a 3D network but to a discrete complex, $[\text{Mn}_4(\text{hmp})_6(\text{NO}_3)_2(\text{dcn})_2] \cdot 2\text{MeCN}$ (**38**), due to the strong affinity of NO_3^- anions with the Mn^{II} ions. In **37**, the octahedral sphere of the external Mn^{II} ion is completed by three nitrogen atoms of the dcn^- ligands. Therefore, each dcn^- ligand binds to a Mn^{II} ion, thus forming a $[\text{Mn}^{\text{II}}(\text{dcn})_6]^{4-}$ unit that interconnects the $[\text{Mn}_4(\text{hmp})_4(\mu_3\text{-OH})_2]^{4+}$ cations into the 3D coordination network. At low temperatures, antiferromagnetic interactions mediated by dicyanamido anions between the $[\text{Mn}_4]$ units ($S_T = 9$) and the Mn^{II} ions ($S = 5/2$) stabilize a ferrimagnetic phase below 4.1 K (T_C). T_C allows an estimation of the interaction (J_{3D}/k_B) through the dicyanamido anion of ca. -0.03 K. It is worth emphasizing here that surprisingly small inter- $[\text{Mn}_4]$ exchange interactions of -0.03 K induce the magnet behavior at 4.1 K. Considering that the critical temperature at the mean-field approximation can be estimated using the following relation: $T_C = 2z|J_{3D}|S_T(S_T+1)/3k_B$ (where z is the number of nearest neighbors, J_{3D} is the inter-SMM exchange interaction and S_T is the spin ground state of the SMM), one could achieve a magnet with a high critical temperature by simply promoting an exchange interaction of a few Kelvins with the same spin ground state ($S_T = 9$). This designed 3D magnet (**37**) based on SMM building blocks opened new perspectives to synthesize high temperature anisotropic magnet based on SMMs.

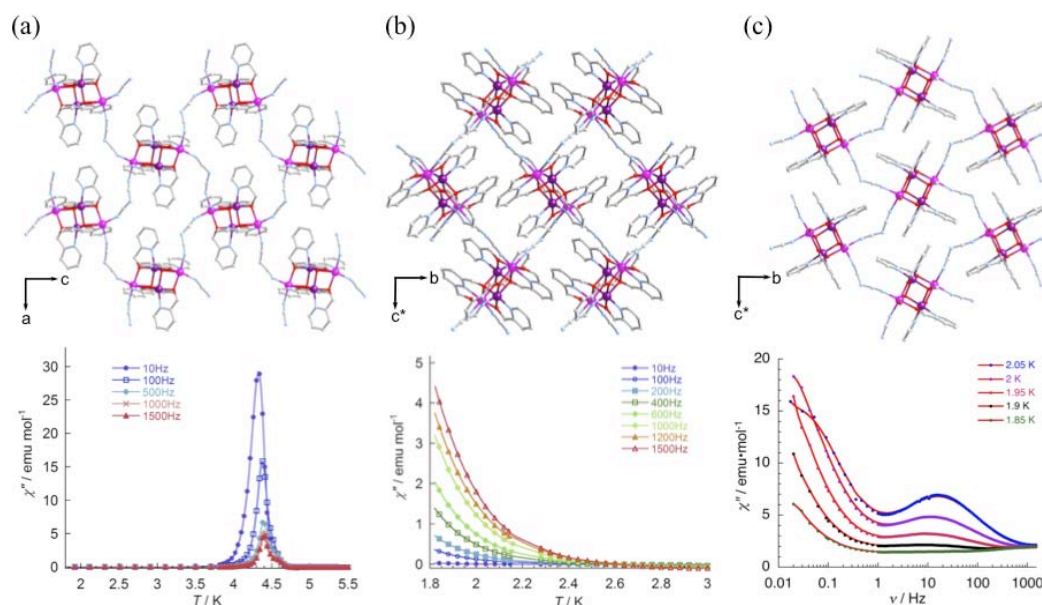


Figure II.7 (a) Packing diagrams projected along the b -axis and temperature dependence of imaginary part of the ac susceptibility for **39**. (b) Packing diagrams projected along the a -axis and temperature dependence of imaginary part of ac susceptibility for **40**. (c) Packing diagrams projected along the a -axis and frequency dependence of imaginary part of ac susceptibility for **41** (Miyasaka et al. 2006).

In order to obtain coordination networks of lower dimensionality, it is obvious that the number of bridging ligand coordinated to the terminal Mn^{II} sites should be decreased. This objective has been achieved in three different ways (Miyasaka et al. 2006): (i) using the same starting reactants as for **37** but in a different ratio of 1:2.5:0.4 for $\text{Mn}(\text{ClO}_4)_2$, Hhmp, and $\text{Na}(\text{dcn})$ respectively, resulting in

$[\text{Mn}_4(\text{hmp})_6(\text{dcn})_2](\text{ClO}_4)_2$ (**39**). The lower amount of dcn^- in the reaction induces the coordination of only four dcn^- anions per $[\text{Mn}_4]$ unit, and thus stabilizes a 2D network. (ii) Another way is to use a co-ligand (H_2pdm) that blocks one more position on the Mn^{II} sites. Using $\text{Mn}(\text{ClO}_4)_2$, Hhmp , H_2pdm and $\text{Na}(\text{dcn})$ in a ratio of 1:2.5:0.5:0.5, a 2D system was also obtained: $[\text{Mn}_4(\text{hmp})_4(\text{Hpdm})_2(\text{dcn})_2](\text{ClO}_4)_2 \cdot 2\text{H}_2\text{O} \cdot 2\text{MeCN}$ (**40**). (iii) The final approach was to make a reaction between the pre-isolated **35** complex and $\text{Na}(\text{dcn})$ in a 1:2 ratio, leading to $[\text{Mn}_4(\text{hmp})_4\text{Br}_2(\text{MeO})_2(\text{dcn})_2] \cdot 0.5\text{H}_2\text{O} \cdot 2\text{THF}$ (**41**), where two terminal water molecules were replaced by dcn^- ligands, and two hmp^- ligands were replaced by methoxy oxygen atoms to form the $\mu_3\text{-O}$ bridges in the core.

Despite similar 2D structures of dicyanamido-bridged $[\text{Mn}_4]$ units, **39**, **40**, and **41** strongly differ in the arrangement of the two crystallographically different $[\text{Mn}_4]$ moieties within the layer. The JT axes of these two units forms an angle (α) of 18, 80, and 63° , respectively (**Figure II.7**). The low-temperature magnetic properties are strongly influenced by this simple structural difference. When α is small, like in **39**, a canted antiferromagnetic order is observed at $T_C = 4.6$ K. For larger angles, the effective magnetic interaction ($J_{\text{eff}} = J \cos \alpha$) between $S_T = 9$ $[\text{Mn}_4]$ moieties is reduced, and the magnetic order is stabilized at lower temperatures, which makes difficult its observation within the timescale of the experiments due to the intrinsic slow dynamics of the $[\text{Mn}_4]$ SMM units. Indeed traditional magnetic measurements reveal that **40** behaves like a typical $[\text{Mn}_4]$ SMM, and in **41**, the magnetic order around 2.1 K is frozen due to the intrinsic SMM properties of the $[\text{Mn}_4]$ units. These three 2D compounds (**39** – **41**) have thus led to new magnetic behaviors resulting from the competition between the intrinsic dynamics of the $[\text{Mn}_4]$ units and the thermodynamic behavior induced by inter-complex magnetic interactions within the coordination networks.

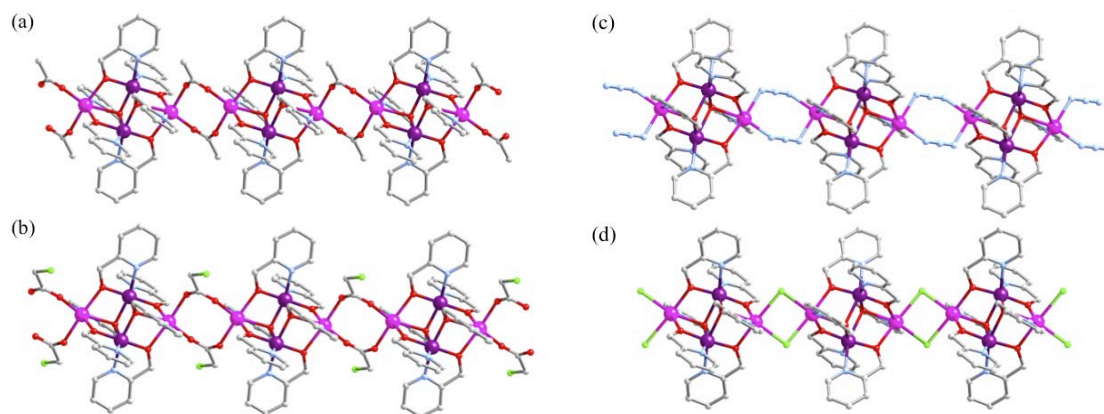


Figure II.8 View of the 1D assemblies of $[\text{Mn}_4]$ units for **42** – **45** ((a) – (d)). Cl is in green and the hydrogen atoms have been omitted for clarity (Lecren 2006).

In order to design 1D assemblies based on $[\text{Mn}_4]$ complexes, it is obvious that the interconnecting ligands should not be too sterically demanding. These considerations were well illustrated by complexes obtained when using acetate, chloroacetate, and trichloroacetate anions as potential bridges. In the latter case with the bulky trichloromethyl group, an isolated $[\text{Mn}_4]$ complex was crystallized, while in the two former cases, chains of $[\text{Mn}_4]$ units connected through double *syn-syn* carboxylato bridges were isolated (**Figure II.8**): $[\text{Mn}_4(\text{hmp})_6(\text{CH}_3\text{CO}_2)_2](\text{ClO}_4)_2 \cdot \text{H}_2\text{O}$ (**42**) and $[\text{Mn}_4(\text{hmp})_6(\text{ClCH}_2\text{CO}_2)_2](\text{ClO}_4)_2 \cdot 2\text{H}_2\text{O}$ (**43**) (Lecren et al. 2008). The use of sufficiently small bridging moieties between $[\text{Mn}_4]$ complexes permitted the design of one-dimensional systems. Indeed using the azido ligand, a similar 1D compound was obtained, namely $[\text{Mn}_4(\text{hmp})_6(\text{N}_3)_2](\text{ClO}_4)_2$ (**44**).

(Lecren et al. 2005a), in which the $[\text{Mn}_4]$ units are linked by double μ -1,3-azido bridges into chains. Moreover, the addition of NaCl or MnCl_2 as a source of chloride afforded another 1D system with di-chlorido bridges: $[\text{Mn}_4(\text{hmp})_6\text{Cl}_2](\text{ClO}_4)_2$ (**45**) (Lecren 2006; Yoo et al. 2005). In these four chain compounds, the $[\text{Mn}_4]$ unit is almost identical to that of the isolated complexes, in which the terminal Mn^{II} ions are hexa-coordinated. The chains are well-isolated in **42** – **45** by perchlorate anions and the interstitial water molecules, allowing no significant interchain interactions. All the anionic bridges mediated weak antiferromagnetic interactions, as expected for such *syn-syn* carboxylato, end-to-end azido, and di-chlorido bridges. The four compounds, therefore, behave as antiferromagnetically coupled chains of $S_{\text{T}} = 9$ $[\text{Mn}_4]$ units. Nevertheless, **42**, **43**, and **44** exhibited slow relaxation of the magnetization following a thermally activated behavior with $\Delta_{\text{T}}/k_{\text{B}} = 37.3, 41.6,$ and 47 K and $\tau_0 = 9.5 \times 10^{-11}, 4.6 \times 10^{-11},$ and 7×10^{-11} s, respectively. The absence of quantum tunnelling down to 1.2 K and the obtained values of the energy barrier indicate that the observed slow relaxation of the magnetization is not the signature of an isolated $[\text{Mn}_4]$ SMM byproduct. Indeed, the slow dynamics in **42** – **44** was explained by the presence of varying amounts of defects in these one-dimensional crystalline materials (or finite size effect) that induces the noncompensation of spins in segments of odd-number units. Thus these defects allow an indirect detection of the slow relaxation of the staggered magnetization in these antiferromagnetically coupled chains. In **45**, $[\text{Mn}_4]$ subunits along the chain are not parallel, and therefore, spin-canting is responsible for the low temperature dynamics.

Interestingly, attempts to make multifunctional magnetic materials were also reported by connecting $[\text{Mn}_4]$ SMMs with functional bridges like photochromic diarylethene ligand (H_2dae) (Morimoto et al. 2009), photo-induced charge transfer complex pentacyanonitrosylferrate(II) ($[\text{Fe}(\text{CN})_5\text{NO}]^{2-}$) (Kushch et al. 2011), and a potentially conducting material, platinum maleonitriledithiolate ($[\text{Pt}(\text{mnt})_2]^{n-}$) (Hiraga et al. 2007). The obtained compounds showed slow relaxation of their magnetization almost identical to the intrinsic $[\text{Mn}_4]$ SMM properties as no direct magnetic interaction between the $[\text{Mn}_4]$ units through the functional bridges was observed. On the other hand, multi-functionality was achieved for the photochromic systems, but the charge-transfer properties or the expected high electrical conductivity were not preserved in the other materials.

II.1.3.2 $[\text{Co}_4]$ SMMs

Polynuclear Co-based SMMs have been much less explored in comparison to the Mn- or lanthanide-based systems (Murrie 2010). Since the first discovery of SMM properties for a Co(II) complex in 2002 with $[\text{Co}_4(\text{hmp})_4(\text{MeOH})_4\text{Cl}_4]$ (**46**) (Yang et al. 2002), several groups have investigated $[\text{Co}_4]$ cubane species, particularly those obtained with citrate ligands.

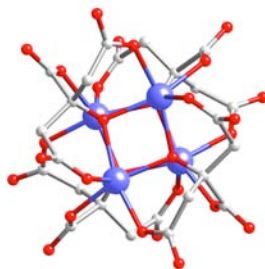


Figure II.9 View of the $[\text{Co}_4]$ core in **47**; Co(II) is in light blue and hydrogen atoms have been omitted for clarity (Galloway et al. 2008).

Isolated SMMs. Two reports on SMM behavior of $[\text{C}(\text{NH}_2)_3]_8[\text{Co}^{\text{II}}_4(\text{cit})_4]$ (**47**, **Figure II.9**) were published in 2008 (Galloway et al. 2008; Moubaraki et al. 2008). Compound **47** was synthesized by an one-pot reaction in the presence of $\text{Co}(\text{NO}_3)_2 \cdot 6\text{H}_2\text{O}$, citric acid, and guanidinium carbonate in water. The main core consists of four Co^{II} ions coordinated by tetradeprotonated citrate ligands. The citrate alkoxido group provides the corner bridging oxygens of the $[\text{Co}_4]$ cubane, with the citrate carboxylato arms capping the cobalt(II) centres. Each Co^{II} site has a twisted trigonal-prismatic geometry due to the short α -carboxylate arms, and the obtained cube has S_4 symmetry. ac susceptibility measurements revealed the presence of a slow relaxation of the magnetization with a thermally activated regime ($\Delta_{\text{eff}}/k_{\text{B}} = 24 \text{ K}$ and $\tau_0 = 3.4 \times 10^{-8} \text{ s}$). The dynamic properties were also confirmed by magnetization hysteresis loops that were temperature and sweep-rate dependent. Very fast QTM, however, resulted in the collapse of M vs H loops at zero field, thus, no coercivity was observed down to 40 mK.

Networks. The large number of dangling carboxylate oxygen atoms around the $[\text{Co}_4(\text{cit})_4]$ cubane provides coordination sites that make this $[\text{Co}_4]$ unit an ideal precursor for coordination networks. An 2D network of $[\text{Co}_4]$ cubane units $\text{A}_4[\mu\{-\text{Co}(\text{glycol})(\text{H}_2\text{O})_2\}\{\text{Co}_4(\text{cit})_4\}]$ (**48**) ($\text{A} = \text{Cs}, \text{Rb}$) was reported (Burzurí et al. 2011). This 2D compound was prepared from the pre-formed $[\text{Co}(\text{H}_2\text{O})_4][\text{Co}_2(\text{Hcit})_2(\text{H}_2\text{O})_4] \cdot 6\text{H}_2\text{O}$ complex under the treatment of CsOH or RbOH , to form isomorphous tetragonal layered structures. In **48**, the $[\text{Co}_4]$ cubane units are connected with paramagnetic $\text{Co}(\text{II})$ ions *via* the *syn-anti* β -carboxylate of the ligand (**Figure II.10**). ac susceptibility measurements showed a transition to the magnetically ordered phase at 0.2 K. As observed in **41** (Miyasaka et al. 2006), the observed critical behavior is nevertheless influenced, *i.e.* “frozen”, by the slow dynamics of the anisotropic $[\text{Co}_4]$ units.

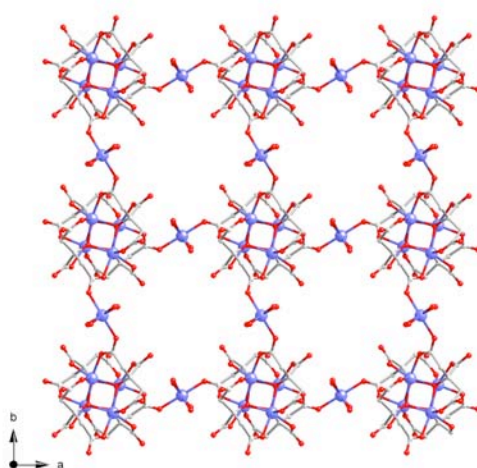


Figure II.10 View of the cationic 2D network of **48**. The hydrogen atoms have been omitted for clarity (Burzurí et al. 2011).

An 3D coordination compound $\{\text{Na}_4\text{Co}_4(\text{cit})_4[\text{Co}(\text{H}_2\text{O})_3]_2(\text{H}_2\text{O})_{15}\} \cdot 3\text{H}_2\text{O}$ (**49**) was also reported recently (Galloway et al. 2010). This system was obtained from the reaction of $\text{CoSO}_4 \cdot 7\text{H}_2\text{O}$ and citric acid in water upon adding $\text{NMe}_4\text{OH} \cdot 5\text{H}_2\text{O}$ to tune the pH to 7.5. It is worth noting that the adjustment of the pH to 7 under identical synthetic conditions led to an isolated complex instead of **49**. Higher pHs help molecular species to stay longer in solution, allowing the crystallization of networks with higher dimensionality. As in **48**, The $[\text{Co}_4(\text{cit})_4]$ units are bonded to paramagnetic $\text{Co}(\text{II})$ centres *via syn-anti* β -carboxylate linkers. In addition, the main $[\text{Co}_4]$ cubane core only has C_1 symmetry,

instead of S_4 observed for the other reported complexes based on $[\text{Co}_4]$ cubanes. The QTM at zero field observed in the isolated $[\text{Co}_4]$ complex, is suppressed in this 3D network (**49**), showing M vs H hysteresis loops with a coercivity below 0.6 K due to intermolecular interactions.

In the above $[\text{Co}_4]$ systems, their magnetic properties are clearly induced by the competition between the dynamic properties and the thermodynamic equilibrium in **48**, and the modulation of the quantum behavior of the isolated $[\text{Co}_4]$ SMM by the inter-complex magnetic interactions in **49**. These extended systems highlight once more the possibility to obtain new magnetic behaviors resulting from the interplay between SMM properties and traditional ordered magnets.

II.1.4 Higher nuclearity SMMs

II.1.4.1 $[\text{Mn}_{17}]$ SMMs

As the SMM energy barrier is largely dependent on its spin ground state (S_T) and magnetic anisotropy (D), polynuclear 3d metal complexes with the largest possible spin ground state have been of interest since the discovery of the first SMM. Even though it is difficult to predict what type of molecular structure will give a large S_T , there are now a significant number of high-spin molecules, most of them coming from the Mn chemistry, with S_T values up to 83/2 in a $[\text{Mn}_{19}]$ complex (Ako et al. 2006).

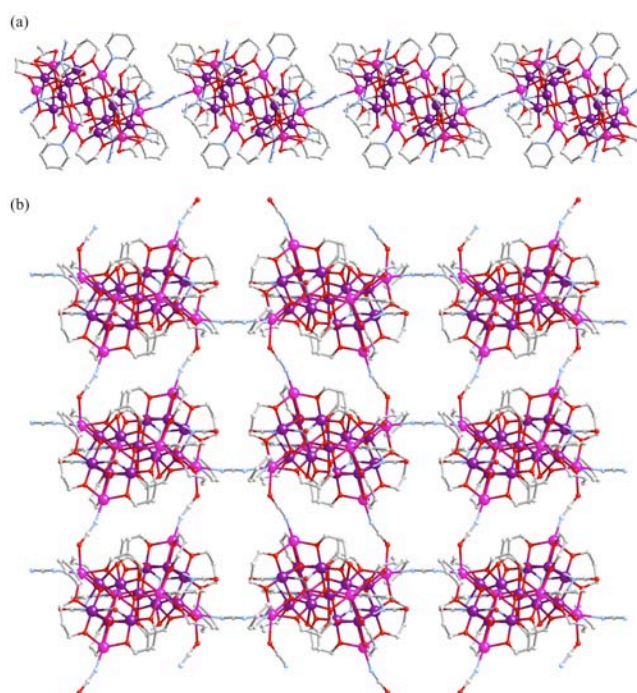


Figure II.11 View of the 1D (**51**, a) and the 2D networks (**52**, b) based on $[\text{Mn}_{17}]$ building unit. The hydrogen atoms have been omitted for clarity (Moushi et al. 2009).

Among them, coordination networks based on $[\text{Mn}_{17}]$ building units, that are themselves SMMs as exemplified by the $[\text{Mn}_{17}\text{O}_8(\text{N}_3)_4(\text{O}_2\text{CMe})_2(\text{pd})_{10}(\text{py})_{10}(\text{MeCN})_2(\text{H}_2\text{O})_2](\text{ClO}_4)_3$ complex (**50**), were reported (Moushi et al. 2009): a 1D system $[\text{Mn}_{17}\text{O}_8(\text{N}_3)_5(\text{O}_2\text{CMe})(\text{pd})_{10}(\text{py})_6]$ (**51**) and a 2D framework $[\text{Mn}_{17}\text{O}_8(\text{OCN})_7(\text{O}_2\text{CMe})_2(\text{pd})_{10}(\text{py})_4]$ (**52**) (**Figure II.11**). All these compounds were synthesized in one-pot reactions of $\text{Mn}(\text{O}_2\text{CMe})$, 1,3-propanediol (pdH_2), and NaL ($\text{L} = \text{N}_3^-$ in **50** and **51**, or OCN^- in **52**). It is worth noting that the poorly coordinating anion, ClO_4^- , was added in the

reaction of **50**, in order to stabilize a positively charged isolated object. The temperature dependence of the χT product in **50** – **52** indicates dominant ferromagnetic interactions inside the $[\text{Mn}_{17}]$ core leading to an $S_T = 37$ spin ground state for the $[\text{Mn}_{17}]$ unit. At low temperature, the χT product decreases due to magnetic anisotropy and/or weak intermolecular interactions in **50**, and due to the inter- $[\text{Mn}_{17}]$ antiferromagnetic interactions mediated by N_3^- or OCN^- in **51** and **52**, respectively. None of the networks exhibited a significant out-of-phase ac signal down to 1.8 K, but the field hysteresis of the magnetization obtained for **50** below 0.7 K allowed the estimation of Δ_{eff}/k_B and τ_0 at 13 K and 1.0×10^{-13} s, respectively. In the case of the network systems (**51** and **52**) that possess intermolecular antiferromagnetic interactions, no slow relaxation of magnetization was detected. However, it is worth mentioning that this first trial proved in a beautiful manner that it is possible to design extended networks based on large polynuclear SMMs. This proof-of-feasibility will certainly encourage researchers to find linkers, eventually paramagnetic ones, that favor larger magnetic interactions between these $[\text{Mn}_{17}]$ SMMs.

II.1.5 Concluding remarks

This section II.1 reviews the known 1D to 3D coordination compounds based on SMM building blocks. This field has expanded tremendously over the past ten years, and notable successes have been achieved and discussed here. The first 3D network of SMMs opened a promising way to obtain high-temperature magnets (Miyasaka et al. 2004b). Following this work, many systems were designed introducing simple diamagnetic or paramagnetic coordinating linkers between SMMs, displaying intriguing features like an enhancement of the SMM energy barrier, a generation of new systems such as SCMs, a modulation of the quantum behavior of the parent SMMs and a competition between the dynamic properties of SMM and the thermodynamic properties of the coordination network.

However, it is still essential to improve the characteristics and performance of these molecule-based systems to reach a new generation of magnetic materials. In order to design SCMs having slow relaxation of the magnetization at higher temperature or magnets with higher critical temperatures, one of the possible strategies is to increase the magnetic interactions between SMM building units. Thus, it is necessary to seek coordinating linkers that favor strong magnetic interactions and an effective ferromagnetic arrangement of the SMM units. In parallel, paramagnetic linkers with large anisotropy should also be considered, even though the orientation of local anisotropy axes in the final network is difficult to predict. This strategy is not thoroughly explored in most of SMMs, except for the $[\text{Mn}_2]$ ones.

In addition, the introduction of functional linkers such as photomagnetic, spin crossover, electron-transfer, paramagnetic radical, luminescent, conducting, and dielectric molecular complexes will give an unique opportunity to design multi-functional SMMs, SCMs or magnets in which two or more co-existing properties interplay. In this thesis, we are especially interested in tunable magnetic systems such as photomagnetic complexes. This area has expanded tremendously giving a considerable contribution in the library of molecule-based magnetism. Thus, we will provide, in the following paragraphs, the state-of-the-art in this field of the photoswitchable magnetic materials, especially focusing on the cyanido-based systems that have been considered in this thesis.

II.2 Photoactive cyanido-based bimetallic materials

The rational design of molecule-based systems displaying tunable optical and/or magnetic properties under external stimuli received recently a great deal of attention. Under ideal conditions, such materials may offer an appealing perspective for the realization of energy efficient molecule-based electronics (Dei 2005; Sato et al. 2007; Simão et al. 2011). In particular, Prussian blue analogues are among the most celebrated class of compounds that alter between two different physical states by temperature variation or light irradiation, with the first example reported by Hashimoto (Sato et al. 1996). Following this seminal work, several examples of 3D polymeric systems are reported to date with various combinations of two different metal spin centers connected by cyanido bridges. On the other hand, these intriguing properties in 3D cyanido-bridged materials motivated chemists to design bimetallic low dimensional complexes and molecular fragments of these systems that still conserve photo switchable magnetic properties. Herein, we provide a survey on the cyanido-bridged functional magnetic materials from 1D – 3D coordination networks to 0D molecular complexes, especially focusing on photo-induced electron transfer properties.

II.2.1 3D to 1D molecule-based systems

The most studied coordination bimetallic compounds showing photomagnetic properties are Prussian blue analogues. They have general formula of $A_xM_k[M'(CN)_6]_l \cdot nH_2O$ where A is alkali metal ions and M and M' are transition metals (**Figure II.12**). The advantages to design magnetic functionalities with these compounds can be found in their facile synthesis and the predictable magnetic couplings. Moreover, certain M-M' couples of these compounds exhibit metal-to-metal electron transfer. During the ET process, an electron is exchanged between two metal ions via a cyanide group, resulting in the change of magnetic, electronic, and/or optical properties of a whole system. Such electron transfer has been found to occur under the influence of temperature (Ohkoshi et al. 2005), pressure (Ksenofotov et al. 2005; Morimoto et al. 2003), light (Sato 2004), and even X-rays (Margadonna et al. 2004). In the following, we present the 3D systems that show tunable magnetic properties by light irradiation.

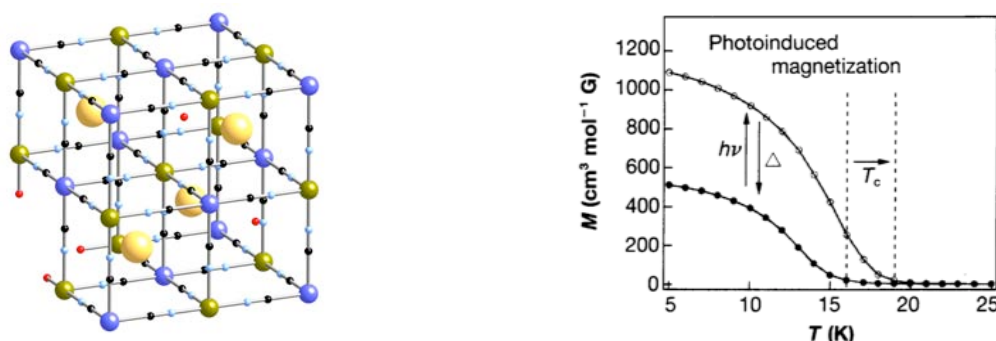


Figure II.12 General structure of Prussian blue analogues, $A_xM_k[M'(CN)_6]_l \cdot nH_2O$ (A = alkali metal ion, yellow; M and M' = transition metals, blue and green; C, black; N, sky blue; O, red; H, omitted) (left). Temperature dependence of field-cooled magnetization before and after red light irradiation for **53** (right) (Sato et al. 1999).

The first example is $K_{0.2}Co_{1.4}[Fe(CN)_6] \cdot 6.9H_2O$ (**53**), that shows light-induced reversible magnetization changes as briefly introduced in Chapter I (Sato et al. 1996). The compound exhibits an intense metal-to-metal charge transfer absorption in the visible region, ascribed to the conversion of

$\{\text{Fe}^{\text{II}}_{\text{LS}}(\mu\text{-CN})\text{Co}^{\text{III}}_{\text{LS}}\}$ ($\text{Fe}^{\text{II}}, t_{2g}^6, S = 0$; $\text{Co}^{\text{III}}, t_{2g}^6, S = 0$) into $\{\text{Fe}^{\text{III}}_{\text{LS}}(\mu\text{-CN})\text{Co}^{\text{II}}_{\text{HS}}\}$ ($\text{Fe}^{\text{III}}, t_{2g}^5, S = 1/2$; $\text{Co}^{\text{II}}, t_{2g}^5 e_g^2, S = 3/2$) pairs via electron transfer. As shown in **Figure II.12**, red light irradiation (660 nm) increases the ferrimagnetic ordering temperature (Curie temperature) from 16 to 19 K and a concomitant increase of the magnetization is observed. This effect is reversed via blue light irradiation (450 nm) or heating of the sample above 150 K.

Following this original work, Verdaguer and Hashimoto reported that the photomagnetic behavior as well as thermally induced electron transfer of Fe/Co Prussian blues can be modulated by changing the Co/Fe ratio present in the nonstoichiometric $A_{2n}\text{Co}_{(1.5-n)}[\text{Fe}(\text{CN})_6] \cdot x\text{H}_2\text{O}$ ($x = 0 - 1$; A = alkali metal ion) lattices (Bleuzen et al. 2000; Cartier et al. 2000; Champion et al. 2001; Escax et al. 2001; Sato et al. 1999; Shimamoto et al. 2002). When $n < 0.5$, the Fe sites are fractionally occupied and the Co centers consequently contain one or more water molecules to satisfy their coordination spheres. The number of water molecules tunes the ligand field strength and redox potential of the Co centers. It was indeed found that an average CoN_5O coordination environment and adjacent $[\text{Fe}(\text{CN})_6]^{n-}$ sites are paramount to result reversible photoinduced magnetization changes in the material.

The Fe/Mn Prussian blue analogues also present a temperature-dependent electron transfer process showing a large thermal hysteresis close to room temperatures (Tokoro et al. 2006; Tokoro et al. 2004). Especially one of them, $\text{Rb}_{0.88}\text{Mn}[\text{Fe}(\text{CN})_6]_{0.96} \cdot x\text{H}_2\text{O}$ (**54**), displays both thermally and photo-induced electron transfer (Tokoro et al. 2008). The compound **54** shows a transition from the high temperature phase made of $\{\text{Fe}^{\text{III}}_{\text{LS}}(\mu\text{-CN})\text{Mn}^{\text{II}}_{\text{HS}}\}$ pairs ($\text{Fe}^{\text{II}}, S = 1/2$; $\text{Mn}^{\text{II}}, S = 5/2$) to the low temperature phase made of $\{\text{Fe}^{\text{II}}_{\text{LS}}(\mu\text{-CN})\text{Mn}^{\text{III}}_{\text{HS}}\}$ pairs ($\text{Fe}^{\text{II}}, S = 0$; $\text{Mn}^{\text{III}}, S = 2$). This electron transfer process is accompanied by the Jahn-Teller distortion on Mn^{III} sites, resulting in a structural transformation from cubic to tetragonal space group. The low temperature phase shows 3D ferromagnetic order with a $T_C = 11$ K due to the interactions between Mn^{III} ions through the diamagnetic $[\text{Fe}^{\text{II}}(\text{CN})_6]$. The light irradiation (532 nm) induces the antiferromagnetic phase via metal-to-metal charge transfer, resulting in the reduced magnetization. The reverse process is also achieved by the irradiation of the light (410 nm).

Besides, Prussian blues of other combinations, such as V/Cr (Bozdog et al. 2010), Fe/Cr (Ohkoshi and Hashimoto 1999), and Co/Os (Avendano et al. 2010), are also reported to exhibit photosensitivity on their magnetic properties due to an ET mechanism.

The design of 3D heterobimetallic networks displaying similar phenomena could be also accomplished by utilizing the octacyanidometallates. Indeed, octacyanidometallates can adopt various valence states, and therefore the photo-induced states having different oxidation states can be easily stabilized. The copper octacyanidomolybdate is one example giving following complexes: $\text{Cu}_2[\text{Mo}(\text{CN})_8] \cdot x\text{H}_2\text{O}$ (**55**) (Ohkoshi et al. 2006; Rombaut et al. 2001), $\text{Cs}_2\text{Cu}_7[\text{Mo}(\text{CN})_8]_4 \cdot 6\text{H}_2\text{O}$ (**56**) (Hozumi et al. 2005) and $[\text{Cu}(\text{pn})_2][\text{Cu}(\text{pn})][\text{Mo}(\text{CN})_8] \cdot 3.5\text{H}_2\text{O}$ (**57**, pn = 1,3-diaminopropane) (Zhang et al. 2011a). In **55**, for example, a spontaneous magnetization is observed (with $T_C = 25$ K) by irradiation with light below 520 nm, and the reverse process is also possible by irradiation with light above 520 nm. The photomagnetic properties in these complexes have been attributed to a metal-to-metal charge transfer between $\{\text{Mo}^{\text{IV}}(\mu\text{-CN})\text{Cu}^{\text{II}}\}$ ($\text{Mo}^{\text{IV}}, S = 0$; $\text{Cu}^{\text{II}}, S = 1/2$) and $\{\text{Mo}^{\text{V}}(\mu\text{-CN})\text{Cu}^{\text{I}}\}$ ($\text{Mo}^{\text{V}}, S = 1/2$; $\text{Cu}^{\text{I}}, S = 0$) pairs, due to the presence of an intervalence transfer (IT) and reverse IT bands around 480 and 710 nm, respectively. Recently, however, X-ray magnetic circular dichroism (XMCD) studies on molecular complexes based on $\{\text{Mo}^{\text{IV}}(\mu\text{-CN})\text{Cu}^{\text{II}}\}$ (Arrio et al. 2009) and

nanoparticles of $\text{Cs}_2\text{Cu}_7[\text{Mo}(\text{CN})_8]_4$ (Brossard et al. 2012) have indeed shown that the conversion of $\text{Mo}^{\text{IV}}_{\text{LS}}$ ($S = 0$) into $\text{Mo}^{\text{IV}}_{\text{HS}}$ ($S = 1$) after the light irradiation is occurring in these systems. This experimental observations were also supported by the theoretical studies (Carvajal et al. 2011; Carvajal et al. 2010). Therefore, it should be stressed that an electron transfer mechanism for photomagnetic properties in $\text{Cu}^{\text{II}}\text{-Mo}^{\text{IV}}$ compounds is controversial, and a spin crossover of Mo^{IV} ions is very likely the origin of the observed properties.

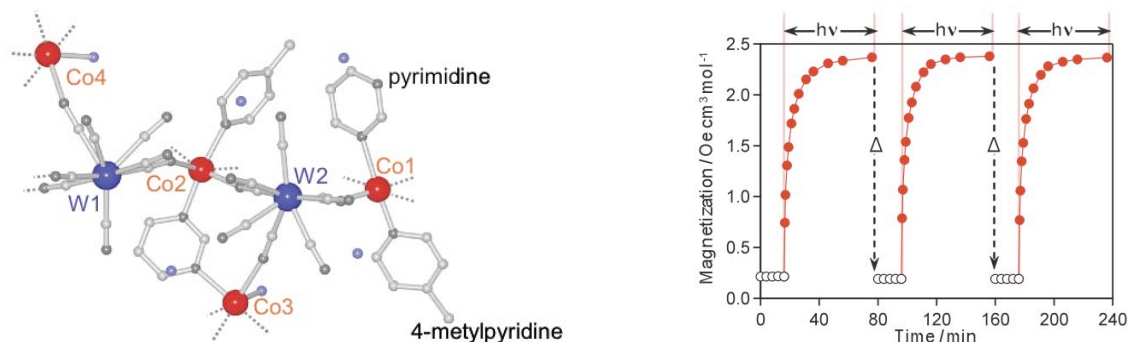


Figure II.13 View of the asymmetric unit of **60** (left). Time dependence of magnetization for **60** at 2 K under 10 Oe with 785 nm light irradiation (red circles) and after thermal treatment (white circles) at 170 K (right) (Ozaki et al. 2012).

The 2D and 3D systems based on octacyanidotungstate are also intensively studied. Their general formula can be expressed as $\text{A}_{2n}[\{\text{Co}(\text{L})_{2-x}(\text{H}_2\text{O})_x\}_2\{\text{Co}(\text{H}_2\text{O})_2\}_{1-n}\{\text{W}(\text{CN})_8\}_2] \cdot x\text{H}_2\text{O}$ where L^1 is 3-cyanopyridine (**58**) (Arimoto et al. 2003), pyrimidine (**59**) (Ohkoshi et al. 2008), or 1:1 mixture of pyrimidine and 4-methylpyridine (**60**, **Figure II.13**) (Ozaki et al. 2012). Cesium is present in **58** that is a 2D network, while no alkali metal ion is introduced in **59** and **60** that are 3D systems. In three complexes, the temperature-induced phase transition from high temperature phase made of $\{\text{W}^{\text{V}}(\mu\text{-CN})\text{Co}^{\text{II}}\}$ pairs (W^{V} , $S = 1/2$; Co^{II} , $S = 3/2$) to low temperature phase made of $\{\text{W}^{\text{IV}}(\mu\text{-CN})\text{Co}^{\text{III}}\}$ pairs (W^{IV} , $S = 0$; Co^{III} , $S = 0$) is observed due to metal-to-metal electron transfer. In addition, the light irradiation induces the ferromagnetic order in all three complexes, especially with T_{C} being 48 K for **60**. The de-excitation is reached either by another wavelength of light (532 nm, **57**) or by heating above 170 K (**59** and **60**, **Figure II.13**). It is also reported that the coordination environment of cobalt plays an important role (Ohkoshi et al. 2008), like in the case of Fe/Co Prussian blues.

Up to now, we have investigated thermal and photoinduced metal-to-metal electron transfer in cyanido-bridged heterobimetallic 3D and 2D assemblies including Prussian blue analogues. Low-temperature light irradiation gives rise to the spontaneous magnetization in most cases. Recently photomagnetic 1D systems are also reported and all of them contain an electron transfer process between Fe and Co metal centers (Hoshino et al. 2012; Liu et al. 2010a; Liu et al. 2010b). By reacting preformed cyanido-Fe precursors with Co metal salts and additional ligands, three chain complexes are obtained: $[\{\text{Fe}(\text{Tp})(\text{CN})_3\}_2\text{Co}(\text{bpe})] \cdot 5\text{H}_2\text{O}$ (Tp = trispyrazolylborate; bpe = 1,2-bis(4-pyridyl)ethane) (**61**), $[\{\text{Fe}(\text{bpy})(\text{CN})_4\}_2\text{Co}(4,4'\text{-bipyridine})] \cdot 4\text{H}_2\text{O}$ (bpy = 2,2'-bipyridine) (**62**), and $[\{\text{Fe}(\text{Tp})(\text{CN})_3\}\{\text{Co}(\text{R-pabn})\}] \cdot (\text{BF}_4) \cdot \text{MeOH} \cdot 2\text{H}_2\text{O}$ (R-pabn = $\text{R-N}(2),\text{N}(2')\text{-bis(pyridin-2-ylmethyl)-1,1'-binaphthyl-2,2'-diamine}$) (**63**). Compounds **61** and **62** are zigzag 1D network showing reversible inter-conversion between $\{\text{Fe}^{\text{II}}_{\text{LS}}(\mu\text{-CN})\text{Co}^{\text{III}}_{\text{LS}}\}$ and $\{\text{Fe}^{\text{III}}_{\text{LS}}(\mu\text{-CN})\text{Co}^{\text{II}}_{\text{HS}}\}$ pairs through thermal and light-induced electron transfer. In addition, the photo-excited state of **63** displays slow relaxation of the magnetization as demonstrated by ac susceptibility measurement. On the other hand, the introduction of chiral ligand on compound **63** resulted in a square-wave type coordination polymer

(**Figure II.14**, left) that preserves the chirality on the final complex. **64** displays thermal and light-induced electron transfer, which are coupled with thermal conductivity switching and light-induced slow relaxation of the magnetization (**Figure II.14**, right).

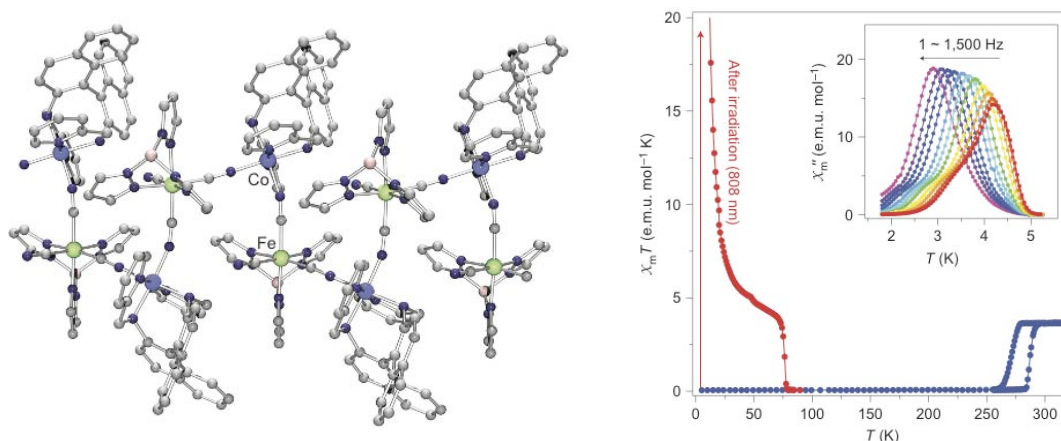


Figure II.14 View of compound **63** (left). Green, Fe; blue, Co; pink, B; grey, C; purple, N. Temperature dependence of the χT product for **63** before irradiation (blue) and after irradiation with 808 nm (red) (right). Inset: Frequency dependence of the out-of-phase susceptibility after the photo-excitation (Hoshino et al. 2012).

As introduced at the beginning of this section, the foregoing interesting photo-switchable behaviors in 1D to 3D cyanido-bridged heterometallic networks have inspired recent works into molecular analogues of these networks. Therefore an active trend in cyanidometallate research has been also directed toward synthesis of discrete molecular units. Let us summarize this topic in the following.

II.2.2 Toward molecular complexes

The high dimensionality of the bimetallic assemblies such as Prussian blue analogues is limited for studying the systematic structure-property relationships, and furthermore for advancing toward technological application due to the processing difficulties. In this respect, soluble and well-defined molecular fragments of these functional networks, while keeping the original properties, have been proposed as one of the most suitable systems to develop. In addition, it is worth noting that the design of the nanoparticles based on functional networks was also one of the strategies to increase the solubility and to create multi-functionalities at nanoscale (Catala et al. 2009). In order to generate discrete heterobimetallic polynuclear products, cyanidometallates and coordinatively unsaturated metal ions have been self-assembled using a building block synthetic strategy. Several metal couples are found to maintain the thermal and light-induced electron transfer in their polynuclear molecular analogues, such as Fe/Nd (Li et al. 2003), Cu/Mo (Herrera et al. 2004), Fe/Os (Hilfiger et al. 2010), Mn/Mo (Mathonière et al. 2005), Mn/W (Mathonière et al. 2005) and Fe/Co. Among them, the most studied couple is the latter one due to the clear mechanism, and therefore these systems will be discussed in this section.

It is only in 2004 that molecular analogues $[\text{Fe}_2\text{Co}_3]$ showed intramolecular metal-to-metal electron transfer in temperature: $\{[\text{Co}(\text{tmphen})_2]_3[\text{Fe}(\text{CN})_6]_2\}$ (**64**) (tmphen = 3,4,7,8-tetramethyl-1,10-phenanthroline) (Berlinguette et al. 2005; Berlinguette et al. 2004), although a series of dinuclear complexes and molecular squares involving CN^- ligands linking Fe and Co centers were reported

before (Bernhardt et al. 2005). The thermal metal-to-metal electron transfer occurs with the conversion behavior between two pairs of Fe/Co, resulting in one $\text{Fe}^{\text{III}}_{\text{LS}}$ not involved in this process, at low temperature phase. Later, the photo-sensitivity of compound **64** was discovered (Funck et al. 2011).

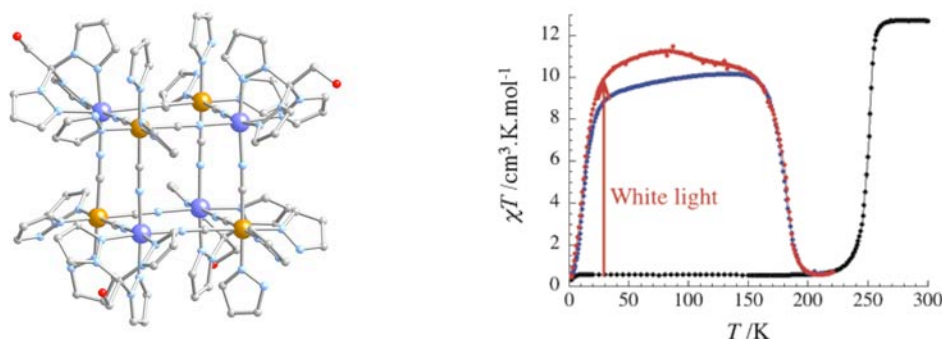


Figure II.15 View of the molecular cube **65** at 250 K. Fe(III) yellow, Co(II) blue, C grey, O red, and N light blue. Lattice solvents, anions, and hydrogen atoms are omitted for clarity (left). Temperature dependence of the χT product for **65** before (black) and after (red) irradiation, and after thermal quenching (blue) (right) (Li et al. 2008).

Not only thermal but also photoinduced electron transfer could be achieved in 2008 in the following molecular system: $[\{(\text{pzTp})\text{Fe}(\text{CN})_3\}_4[\text{Co}(\text{pz})_3\text{CCH}_2\text{OH}]_4](\text{ClO}_4)_4 \cdot 13\text{DMF} \cdot 4\text{H}_2\text{O}$ (**65**) (pzTp = tetrapyrazolylborate; $(\text{pz})_3\text{CCH}_2\text{OH}$ = 2,2,2-tris(pyrazoyl)ethanol) (Li et al. 2008). As shown in **Figure II.15** (left), compound **65** is an octanuclear complex forming a $\{\text{Fe}_4\text{Co}_4\}$ cube that can be considered as a fragment of Fe/Co Prussian blues. The intramolecular electron transfer is observed at 250 K, reversibly converting paramagnetic $\{\text{Fe}^{\text{III}}_4\text{Co}^{\text{II}}_4\}$ complexes into diamagnetic $\{\text{Fe}^{\text{II}}_4\text{Co}^{\text{III}}_4\}$ boxes without detectable thermal hysteresis. This phenomenon is also accompanied by the optical change: the red compound at room temperature turns to green at low temperature. Both thermal quenching (rapid decrease of temperature) and photoirradiation at 30 K can trap the metastable $\{\text{Fe}^{\text{III}}_4\text{Co}^{\text{II}}_4\}$ state, as shown in **Figure II.15** (right).

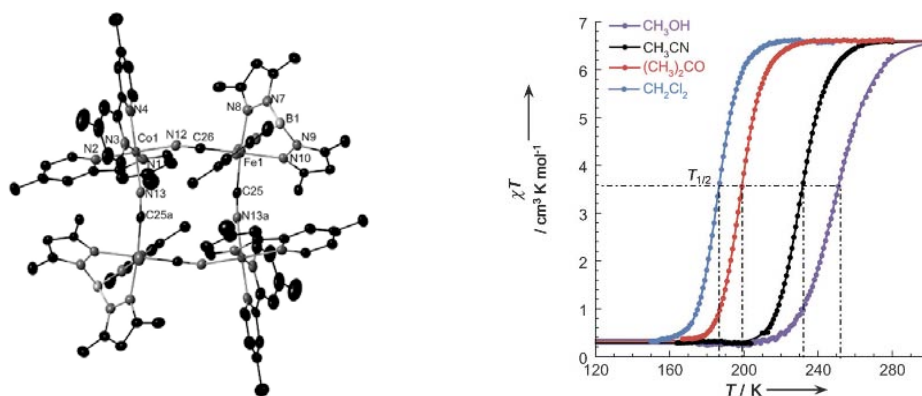


Figure II.16 ORTEP-type view of the cationic part of **67** at 120 K with thermal ellipsoids at 30% probability level. Lattice solvents, anions, and hydrogen atoms are omitted for clarity (left). Temperature dependence of the χT product for **67** in methanol, acetonitrile, acetone, and dichloromethane solutions (0.4 K min^{-1} , 1 T) (right; solid lines are fits to the Ideal solution model (see section I.3.1 in Chapter I)) (Siretanu et al. 2011).

In addition, tetranuclear $\{\text{Fe}_2\text{Co}_2\}$ squares are one of the most studied molecular objects to date, that display reversible thermally and photoinduced intramolecular electron transfer in solid state as well as in solution (Mercuriol et al. 2010; Nihei et al. 2011; Siretanu et al. 2011; Zhang et al. 2010). These compounds have the general formula as $[\{(\text{L}^1)\text{Fe}(\text{CN})_3\}_2\{\text{Co}(\text{L}^2)_2\}_2] \cdot \text{A}_2 \cdot \text{S}$, where L^1 is

derivative of trispyrazolylborate (Tp) and L^2 is bidentate ligand, mostly derivatives of 2,2'-bipyridine (bpy). A and S are counter anions and solvents, respectively. Using tris(3,5-dimethyl)pyrazolyl borate (Tp^*), bpy, and trifluoromethanesulfonate (OTf) as L^1 , L^2 , and A, the obtained compound $[(Tp^*)Fe(CN)_3]_2[Co(bpy)_2][OTf]_2$ (**66**) exhibits a first-order phase transition with a thermal hysteresis of 18 K (at 0.4 Kmin^{-1}) between 186 and 168 K, associated with an electron transfer process between paramagnetic $\{Fe^{III}_2Co^{II}_2\}$ state and diamagnetic $\{Fe^{II}_2Co^{III}_2\}$ state (Zhang et al. 2010). It was not the case for the other square complexes that shows a gradual conversion, indicating the presence of significantly weaker elastic interactions between complexes in their crystal structures (Mercuriol et al. 2010; Nihei et al. 2011; Siretanu et al. 2011). Nevertheless, solution studies of these complexes offered an opportunity to observe the unique behaviors. Through the methyl functionalization of the bpy ligands on **66**, a new square system was obtained, $[(Tp^*)Fe(CN)_3]_2[Co(bpy^{Me})_2][OTf]_2$ (**67**, **Figure II.16**) ($bpy^{Me} = 4,4'$ -methyl-2,2'-bipyridine), that proves the possibility to transfer the solid-state properties of $\{Fe_2Co_2\}$ complexes into a wide range of solvents (Siretanu et al. 2011). Furthermore, electron transfer and associated magnetic and optical properties could be modulated by the solvent nature (**Figure II.16**). On the other hand, another square system, $[(Tp^*)Fe(CN)_3]_2[Co(dtbbpy)_2][PF_6]_2 \cdot 4H_2O$ ($dtbbpy = 4,4'$ -di-tert-butyl-2,2'-bipyridine) (**68**), also maintained an electron transfer process in solution, that is induced not only thermally but also by protonation (Nihei et al. 2011). The effect of the protonation was explained by the modulation of redox potential on the metal site. All reported $\{Fe_2Co_2\}$ square complexes display metastable $\{Fe^{III}_2Co^{II}_2\}$ state by light irradiation at 10 K.

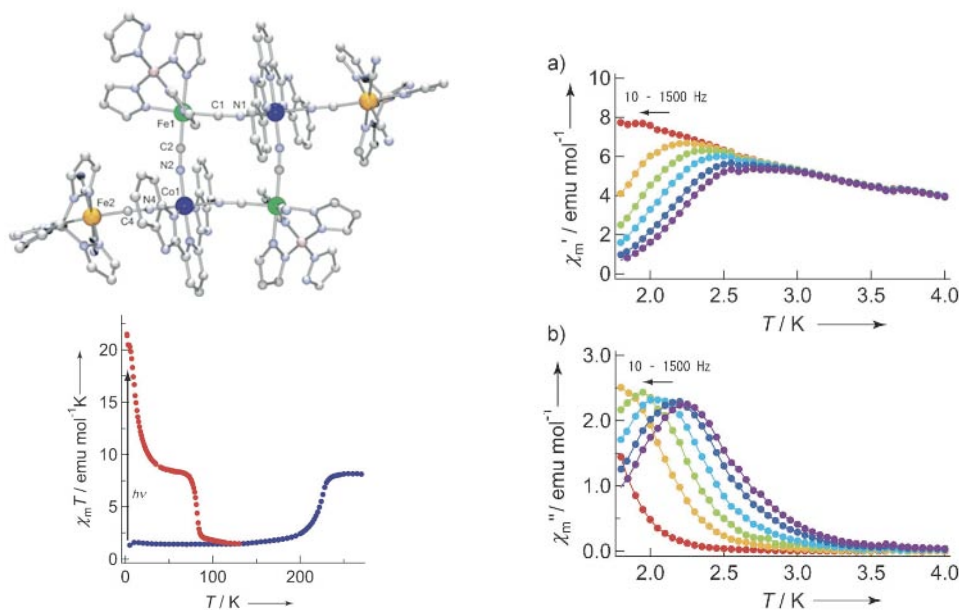


Figure II.17 View of the molecular structure of **70** at 100 K (left, top). Temperature dependence of the χT product for **70** before (blue) and after (red) irradiation (left, bottom). Plots of χ' vs T (a) and χ'' vs T (b) for **70** after light irradiation with $H_{ac} = 3\text{ Oe}$ oscillating at 10 – 1500 Hz and $H_{dc} = 500\text{ Oe}$ (right) (Nihei et al. 2012a).

Very recently, additional properties were also found to coexist with the metal-to-metal electron transfer in Fe/Co molecular complexes that can act as multi-functional materials: a trinuclear species $[FeTp(CN)_3]_2Co(Meim)_4$ (**69**) (Meim = methylimidazole) (Liu et al. 2012) and a hexanuclear complex $[Co_2Fe_4(H_2bbp)_2(CN)_6(\mu-CN)_6(pztp)_4] \cdot 2(1-PrOH) \cdot 4H_2O$ (**70**, **Figure II.17**) ($H_2bbp = 2,6$ -

bis(benzimidazol-2-yl)pyridine) (Nihei et al. 2012b). In **69**, the high temperature $\{\text{Fe}^{\text{III}}\text{Co}^{\text{II}}\text{Fe}^{\text{III}}\}$ species is converted to low temperature $\{\text{Fe}^{\text{II}}\text{Co}^{\text{III}}\text{Fe}^{\text{III}}\}$ object by thermal electron transfer. This process is accompanied by switching of the polarity: nonpolar system to polar one. Compound **69** can be also photo-excited to generate $\{\text{Fe}^{\text{III}}\text{Co}^{\text{II}}\text{Fe}^{\text{III}}\}$ species at 5 K. On the other hand, compound **70** presents both thermal and photo induced electron transfer, resulting in the interconversion between $\{\text{Fe}^{\text{III}}(\text{Co}^{\text{II}}_2\text{Fe}^{\text{III}}_2)\text{Fe}^{\text{III}}\}$ and $\{\text{Fe}^{\text{III}}(\text{Co}^{\text{III}}_2\text{Fe}^{\text{II}}_2)\text{Fe}^{\text{III}}\}$. The photoexcited species $\{\text{Fe}^{\text{III}}(\text{Co}^{\text{II}}_2\text{Fe}^{\text{III}}_2)\text{Fe}^{\text{III}}\}$ exhibits slow relaxation of the magnetization at low temperature. Even though the slow dynamics in discrete cyanido-bridged molecular complexes are already known since 2002 (Berlinguette et al. 2003; Choi et al. 2004; Ferbinteanu et al. 2005; Li et al. 2006a; Li et al. 2006c; Li et al. 2006b; Li et al. 2005; Miyasaka et al. 2005b; Pedersen et al. 2011; Schelter et al. 2007; Sokol et al. 2002; Song et al. 2005; Wang et al. 2004; Zhang et al. 2011b), this is the first example of the photo-induced SMM behavior.

II.2.3 Concluding remarks

This section II.2 offers a general view of the photoactive magnetic materials based on cyanido-bridged coordination compounds. In Prussian blue analogues, their rather flexible synthetic approach compared to solid state materials has led to many fascinating results, showing photo-induced metal-to-metal electron transfer. This interest also expanded to bimetallic 3D assemblies based on $[\text{M}(\text{CN})_8]^{n-}$ ($\text{M} = \text{Mo}$ and W) displaying the associated photoactive magnetic properties. Apart from these recent successes in preparing new metal-cyanido solids, the building block approach to design the discrete cyanido-bridged molecular complexes has also successfully produced numerous polynuclear systems. More interestingly, these molecules retain the aforementioned photoactive magnetic properties.

Keeping in mind the state-of-the-art surveyed in section II.1 and II.2, we will discuss general conclusion and perspectives, followed by the objectives of this thesis work in the following paragraph.

II.3 Conclusion and motivation

In Chapter II, we reviewed interesting high dimensional coordination compounds based on single-molecule magnets (SMMs). It is obvious that there is a veritable gold mine of opportunities for fruitful activity in this field. However, a great deal of additional work will be required to improve the characteristics and performance of these SMM-based systems to reach a new generation of magnetic materials. In order to design SCMs having slow relaxation of the magnetization at higher temperature or magnets with higher critical temperatures, one of the possible strategies is to increase the magnetic interactions between SMM building units.

At the same time, we have also briefly reviewed the current status of photomagnetic materials based on cyanido-based coordination compounds. This area can be largely divided into two streams: polymeric networks and 0D molecules, and significant successes are achieved. However, most of reported systems, even though they are molecular objects, are not really suitable as a linking unit to build a SMM networks while keeping the efficient magnetic interactions as strong enough.

In this context, we propose two different directions for this thesis work.

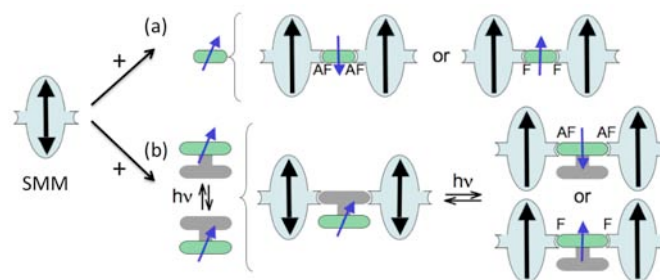


Figure II.18 Scheme illustrating the SMM arrangements with the different possible magnetic couplings through paramagnetic (a) or electron-transfer based (b) linkers. The double arrow on the SMM units indicates that the spin orientation on the SMM unit is not fixed by the magnetic interactions.

The first one is to build a network utilizing paramagnetic linkers that may favor strong magnetic interactions and an effective ferromagnetic arrangement of the SMM units (**Figure II.18 (a)**). Given the fact that only $[\text{Mn}_2]$ SMMs are thoroughly investigated in this strategy to date, we will focus on the $[\text{Mn}_4]$ SMMs. This system has been intensively studied in our group during the thesis work of Lecren (Lecren 2006), mainly concentrating on the isolated $[\text{Mn}_4]$ SMMs and the 1D networks connected by diamagnetic linkers, such as azide and acetic acid derivatives. In this thesis (Chapter III), we will continue further these works with the coordination assemblies based on $[\text{Mn}_4]$ SMMs through both diamagnetic and also paramagnetic linkers. Syntheses and comprehensive physical studies in terms of crystallographic and magnetic properties will be discussed.

As a second part of this thesis work, new molecular photomagnetic linkers will be designed that would be able to bridge SMM building units, and consequently to create a multifunctional magnetic system. We can imagine the complexes that can adopt two magnetic states (like dia- \rightleftharpoons para-magnetic) depending on the light irradiation. A diamagnetic linker will promote “isolated” (or weakly coupled) SMM behavior, while these systems will behave as an “enhanced” SMM, a SCM, or an ordered magnet, when the linker is switched by photo-excitation in its paramagnetic state (**Figure II.18 (b)**). As seen in this chapter, a photo-induced electron transfer between Fe and Co is well understood and this intriguing photoactive property is manifested also in their molecular complexes. Therefore, this thesis focuses on the Fe/Co couple to design new photomagnetic linkers. In order to keep an efficient magnetic coupling between SMMs through the linker, the Fe/Co complex should be as simple as possible with free cyanido ligands that would further coordinate the SMM units. To this end, we will develop novel cyanido-based $\{\text{FeCo}\}$ dinuclear complexes through building block approach (Chapter IV). Especially, using cyanidometallate precursors offers a distinct advantage to control the nuclearity, due to relatively facile introduction of capping ligands to metal precursors. In addition to the syntheses of $\{\text{FeCo}\}$ complexes, new SMMs will be also prepared with an ultimate goal to assemble them at the end, to realize a photo-switchable magnet (Chapter IV).

References

- Ababei R, Li Y-G, Roubeau O, Kalisz M, Bréfuel N, Coulon C, Harté E, Liu X, Mathonière C, Clérac R (2009) *New J. Chem.* 33, 1237.
- Ako AM, Hewitt IJ, Mereacre V, Clérac R, Wernsdorfer W, Anson CE, Powell AK (2006) *Angew. Chem. Int. Ed.* 45, 4926.
- Arimoto Y, Ohkoshi S, Zhong ZJ, Seino H, Mizobe Y, Hashimoto K (2003) *J. Am. Chem. Soc.* 125, 9240
- Arrio M-A, Long J, Cartier dit Moulin C, Bachschmidt A, Marvaud V, Rogalev A, Mathonière C, Wilhelm F, Saintavit P, (2009) *J. Phys. Chem. C* 114, 593.
- Avendano C, Hilfiger MG, Prosvirin A, Sanders C, Stepien D, Dunbar, KR (2010) *J. Am. Chem. Soc.* 132, 13123.
- Bai Y-L, Tao J, Wernsdorfer W, Sato O, Huang R-B, Zheng L-S (2006) *J. Am. Chem. Soc.* 128, 16428
- Beltran LMC, Long JR (2005) *Acc. Chem. Res.* 38, 325.
- Berlinguette CP, Dragulescu-Andrasi A, Sieber A, Güdel H-U, Achim C, Dunbar KR (2005) *J. Am. Chem. Soc.* 127, 6766.
- Berlinguette CP, Dragulescu-Andrasi A, Sieber A, Galán-Mascarós AR, Güdel H-U, Achim C, Dunbar KR (2004) *J. Am. Chem. Soc.* 126, 6222.
- Berlinguette CP, Vaughn D, Cañada-Vilalta C, Galán-Mascarós JR, Dunbar KR (2003) *Angew. Chem. Int. Ed.* 42, 1523.
- Bernhardt P, Bozoglian F, Macpherson B, Martinez M (2005) *Coord. Chem. Rev.* 249, 1902.
- Blagg RJ, Muryn CA, McInnes EJJ, Tuna F, Winpenny REP (2011) *Angew. Chem. Int. Ed.* 50, 6530.
- Bleuzen A, Lomenech C, Escax V, Villain F, Varret F, Cartier dit Moulin C, Verdaguer M (2000) *J. Am. Chem. Soc.* 122, 6648.
- Bozdag KD, Yoo J-W, Raju NP, McConnell AC, Miller JS, Epstein AJ (2010) *Phys. Rev. B* 82, 094449.
- Brechin EK, Huffman JC, Christou G, Yoo J, Nakano M, Hendrickson DN (1999) *Chem. Commun.* 783.
- Brossard S, Volatron F, Lisnard L, Arrio M-A, Catala L, Mathonière C, Mallah T, Cartier dit Moulin C, Rogalev A, Wilhelm F, Smekhova A, Saintavit P (2012) *J. Am. Chem. Soc.* 134, 222.
- Burzuri E, Campo J, Falvello LR, Forcén-Vázquez E, Luis F, Mayoral I, Palacio F, Sáenz de Pipaón C, Tomás M (2011) *Chem. –Eur. J.* 17, 2818.
- Cartier C, Bleuzen A, Arrio M, Saintavit P, Lomenech C, Escax V, Curie M (2000) *J. Am. Chem. Soc.* 122, 6653.
- Carvajal M-A, Caballol R, de Graaf C (2011) *Dalton Trans.* 40, 7295.
- Carvajal M-A, Reguero M, de Graaf C (2010) *Chem. Commun.* 46, 5737.
- Catala L, Volatron F, Brinzei D, Mallah T (2009) *Inorg. Chem.* 48, 3360.
- Champion G, Escax V, Cartier C, Bleuzen A, Verdaguer M (2001) *J. Am. Chem. Soc.* 123, 12544.
- Choi HJ, Sokol JJ, Long JR (2004) *Inorg. Chem.* 43, 1606.
- Clérac R, Miyasaka H, Yamashita M, Coulon C (2002) *J. Am. Chem. Soc.* 124, 12837.
- Cornia A, Mannini M, Saintavit P, Sessoli R (2011) *Chem. Soc. Rev.* 40, 3076.
- Costes J-P, Auchel M, Dahan F, Peyrou V, Shova S, Wernsdorfer W (2006) *Inorg. Chem.* 45, 1924.
- Costes J-P, Dahan F, Wernsdorfer W (2006b) *Inorg. Chem.* 45, 5.
- Costes J-P, Shova S, Wernsdorfer W (2008) *Dalton Trans.* 1843.
- Coulon C, Clérac R, Wernsdorfer W, Colin T, Miyasaka H (2009) *Phys. Rev. Lett.* 102, 2.
- Dei A (2005) *Angew. Chem. Int. Ed.* 44, 1160.
- Domingo N, Bellido E, Ruiz-Molina D (2011) *Chem. Soc. Rev.* 41, 258.
- Escax V, Bleuzen A, Cartier dit Moulin C, Villain F, Goujon A, Varret F, Verdaguer M (2001) *J. Am. Chem. Soc.* 123, 12536.
- Feng PL, Stephenson CJ, Hendrickson DN (2010) *Inorg. Chem.* 49, 6393.
- Ferbinteanu M, Miyasaka H, Wernsdorfer W, Nakata K, Sugiura K-i, Yamashita M, Coulon C, Clérac R (2005) *J. Am. Chem. Soc.* 127, 3090.
- Funck KE, Prosvirin AV, Mathonière C, Clérac R, Dunbar KR (2011) *Inorg. Chem.* 50, 2782.
- Galloway KW, Schmidtmann M, Sanchez-Benitez J, Kamenev KV, Wernsdorfer W, Murrie M (2010) *Dalton Trans.* 39, 4727.
- Galloway KW, Whyte AM, Wernsdorfer W, Sanchez-Benitez J, Kamenev KV, Parkin A, Peacock Rd, Murrie M (2008) *Inorg. Chem.* 47, 7438.
- Gatteschi D, Cornia A, Mannini M, Sessoli R (2009) *Inorg. Chem.* 48, 3408.
- Gheorghe R, Madalan AM, Costes J-P, Wernsdorfer W, Andruh M (2010) *Dalton Trans.* 39, 4734.

- Hamamatsu T, Yabe K, Towatari M, Osa S, Matsumoto N, Re N, Pochaba A, Mrozinski J, Gallani JL, Barla A, Imperia P, Paulsen C, Kappler J-P (2007) *Inorg. Chem.* 46, 4458.
- Haryono M, Kalisz M, Sibille R, Lescouëzec R, Fave C, Trippe-Allard G, Li Y, Seuleiman M, Rousselière H, Balkhy AM, Lacroix J-C, Journaux Y (2010) *Dalton Trans.* 39, 4751.
- Herrera JM, Marvaud V, Verdaguer M, Marrot J, Kalisz M, Mathonière C (2004) *Angew. Chem. Int. Ed.* 43, 5468.
- Hilfiger MG, Chen M, Brinzari TV, Nocera TM, Shatruk M, Petasis DT, Musfeldt JL, Achim C, Dunbar KR (2010) *Angew. Chem. Int. Ed.* 49, 1410.
- Hiraga H, Miyasaka H, Nakata K, Kajiwarat, Takaishi S, Oshima Y, Nojiri H, Yamashita M (2007) *Inorg. Chem.* 46, 9661.
- Hoshino N, Iijima F, Newton GN, Yoshida N, Shiga T, Nojiri H, Nakao A, Kumai R, Murakami Y, Oshio H (2012) *Nature Chem.* doi: 10.1038/nchem.1455.
- Hozumi T, Hashimoto K, Ohkoshi S (2005) *J. Am. Chem. Soc.* 127, 3864.
- Inglis R, Jones LF, Milios CJ, Datta S, Collins A, Parsons S, Wernsdorfer W, Hill S, Perlepes SP, Piligkos S, Brechin EK (2009) *Dalton Trans.* 3403.
- Inglis R, Milios CJ, Jones LF, Piligkos S, Brechin, EK (2012) *Chem. Commun.* 48, 181.
- Jones LF, Prescimone A, Evangelisti M, Brechin EK (2009) *Chem. Commun.* 2023.
- Kajiwarat, Nakano M, Takahashi K, Takaishi S, Yamashita M (2011) *Chem. –Eur. J.* 17, 196.
- Kajiwarat, Nakano M, Takaishi S, Yamashita M (2008) *Inorg. Chem.* 47, 8604.
- Kajiwarat, Takahashi K, Hiraizumi T, Takaishi S, Yamashita M (2009) *Polyhedron* 28, 1860.
- Katsenis AD, Inglis R, Prescimone A, Brechin EK, Papaefstathiou GS (2012) *CrystEngComm* 14, 1216.
- Ksenofotov V, Levchenko G, Reiman S, Gültlich P, Bleuzen A, Escax V, Verdaguer M (2003) *Phys. Rev. B* 68, 024415.
- Kushch LA, Sasnovskaya VD, Yagubskii EB, Khasanov, Salavat S, Simonov SV, Shibaeva RP, Korolev AV, Starichenko DV, Anokhin AO, Irkhin VY, Shvachko YN (2011) *Inorg. Chim. Acta* 378, 169.
- Lecren L (2006) PhD Thesis. Bordeaux University.
- Lecren L, Roubeau O, Coulon C, Li Y-G, Le Goff XF, Wernsdorfer W, Miyasaka H, Clérac R (2005a) *J. Am. Chem. Soc.* 127, 17353.
- Lecren L, Wernsdorfer W, Li Y, Roubeau O, Miyasaka H, Clérac R (2005b) *J. Am. Chem. Soc.* 127, 11311.
- Lecren L, Roubeau O, Li Y-G, Le Goff XF, Miyasaka H, Richard F, Wernsdorfer W, Coulon C, Clérac R (2008) *Dalton Trans.* 755.
- Lecren L, Wernsdorfer W, Li Y-G, Vindigni A, Miyasaka H, Clérac R (2007) *J. Am. Chem. Soc.* 129, 5045.
- Leuenberger MN, Loss D (2001) *Nature* 410, 789.
- Li D, Clérac R, Roubeau O, Harté E, Mathonière C, Le Bris R, Holmes SM (2008) *J. Am. Chem. Soc.* 130, 252.
- Li D, Clérac R, Parkin S, Wang G, Yee GT, Holmes SM (2006a) *Inorg. Chem.* 45, 5251.
- Li D, Parkin S, Clérac R, Holmes SM (2006b) *Inorg. Chem.* 45, 7569.
- Li D, Parkin S, Wang G, Yee GT, Clérac R, Wernsdorfer W, Holmes SM (2006c) *J. Am. Chem. Soc.* 128, 4214.
- Li D, Parkin S, Wang G, Yee GT, Prosvirin AV, Holmes SM (2005) *Inorg. Chem.* 44, 5593.
- Li G, Akitsu T, Sato O, Einaga Y (2003) *J. Am. Chem. Soc.* 128, 12396.
- Lin P-H, Burchell TJ, Clérac R, Murugesu M (2008) *Angew. Chem. Int. Ed.* 47, 8848.
- Liu C, Zhang D, Zhu D (2008a) *Chem Commun.* 2, 368.
- Liu C-M, Zhang D-Q, Zhu D-B (2009) *Inorg. Chem.* 48, 4980.
- Liu T, Dong D, Kanegawa S, Kang S, Sato O, Shiota Y, Yoshizawa K, Hayami S, Wu S, He C, Duan C-Y (2012) *Angew. Chem. Int. Ed.* 51, 4367.
- Liu T, Zhang Y-J, Kanegawa S, Sato O (2010a) *Angew. Chem. Int. Ed.* 49, 8645.
- Liu T, Zhang Y-J, Kanegawa S, Sato O (2010b) *J. Am. Chem. Soc.* 132, 8250.
- Liu X, Roubeau O, Clérac R (2008b) *C. R. Chimie* 11, 1182.
- Lu Z, Yuan M, Pan F, Gao S, Zhang D, Zhu D (2006) *Inorg. Chem.* 45, 3538.
- Mannini M, Pineider F, Danieli C, Totti F, Sorace L, Saintavit P, Arrio M-A, Otero E, Joly L, Cezar JC, Cornia A, Sessoli R (2010) *Nature* 468, 417.
- Mannini M, Pineider F, Saintavit P, Danieli C, Otero E, Sciancalepore C, Talarico AM, Arrio M-A, Cornia A, Gatteschi D, Sessoli R (2009) *Nature Materials* 8, 194.
- Margadonna S, Prassides K, Fitch AN (2004) *Angew. Chem. Int. Ed.* 46, 6319.
- Mathonière C, Podgajny R, Guionneau P, Labrugere C, Sieklucka B (2005) *Chem. Mater.* 17, 442.
- Mercuriol J, Li Y, Pardo E, Risset O, Seuleiman M, Rousselière H, Lescouëzec R, Julve M (2010) *Chem. Commun.* 46, 8995.
- Milios CJ, Raptopoulou CP, Terzis A, Lloret F, Vicente R, Perlepes SP, Escuer A (2004) *Angew. Chem. Int. Ed.* 43, 210.

- Milios CJ, Vinslava A, Wernsdorfer W, Moggach S, Parsons S, Perlepes SP, Christou G, Brechin EK (2007a) *J. Am. Chem. Soc.* 129, 2754.
- Milios CJ, Vinslava A, Wood PA, Parsons S, Wernsdorfer W, Perlepes SP, Christou G, Brechin EK (2007b) *J. Am. Chem. Soc.* 129, 8.
- Miyasaka H, Clérac R, Mizushima K, Sugiura K-i, Yamashita M, Wernsdorfer W, Coulon C (2003) *Inorg. Chem.* 42, 8203.
- Miyasaka H, Clérac R, Wernsdorfer W, Lecren L, Bonhomme C, Sugiura K-i, Yamashita M (2004a) *Angew. Chem. Int. Ed.* 43, 2801.
- Miyasaka H, Ieda H, Chimica D, Perugia I, Crescenzi R, Floriani C, Meoh S (1998) *Inorg. Chem.* 37, 255.
- Miyasaka H, Julve M, Yamashita M, Clérac R (2009) *Inorg. Chem.* 48, 3420.
- Miyasaka H, Matsumoto N, Ōkawa H, Re N, Gallo E, Floriani C (1996) *J. Am. Chem. Soc.* 118, 981.
- Miyasaka H, Nakata K, Lecren L, Coulon C, Nakazawa Y, Fujisaki T, Sugiura K-i, Yamashita M, Clérac R (2006) *J. Am. Chem. Soc.* 128, 3770.
- Miyasaka H, Nakata K, Sugiura K-i, Yamashita M, Clérac R (2004b) *Angew. Chem. Int. Ed.* 43, 707.
- Miyasaka H, Nezu T, Sugimoto K, Sugiura K-i, Yamashita M, Clérac R (2005) *Chem. –Eur. J.* 11, 1592.
- Miyasaka H, Saitoh A, Yamashita M, Clérac R (2008) *Dalton Trans.* 2, 2422.
- Miyasaka H, Takayama K, Saitoh A, Furukawa S, Yamashita M, Clérac R (2010) *Chem. –Eur. J.* 16, 3656.
- Morimoto M, Miyasaka H, Yamashita M, Irie M (2009) *J. Am. Chem. Soc.* 131, 9823.
- Morimoto Y, Hanawa M, Ohishi Y, Kato K, Takana M, Kuriki A, Nishibori E, Sakata M, Ohkoshi S, Tokoro H, Hashimoto K (2003) *Phys. Rev. B* 68, 144106.
- Moubaraki B, Murray KS, Hudson TA, Robson R (2008) *Eur. J. Inorg. Chem.* 4525.
- Moushi EE, Stamatatos TC, Wernsdorfer W, Christou G, Tasiopoulos AJ (2009) *Inorg. Chem.* 48, 5049.
- Murrie M (2010) *Chem. Soc. Rev.* 39, 1986.
- Ni W-W, Ni Z-H, Cui A, Liang X, Kou H-Z (2007a) *Inorg. Chem.* 46, 22.
- Ni Z-H, Zheng L, Zhang L-F, Cui A-L, Ni W-W, Zhao C-C, Kou H-Z (2007b) *Eur. J. Inorg. Chem.* 1240.
- Nihei M, Okamoto Y, Sekine Y, Hoshino N, Shiga T, Liu IP-C, Oshio H (2012) *Angew. Chem. Int. Ed.* 51, 6361.
- Nihei M, Sekine Y, Suganami N, Nakazawa K, Nakao A, Nakao H, Murakami Y, Oshio H (2011) *J. Am. Chem. Soc.* 133, 3592.
- Ohkoshi S, Hamada Y, Matsuda T, Tsunobuchi Y, Tokoro H (2008) *Chem. Mater.* 20, 3048.
- Ohkoshi S, Hashimoto K (1999) *J. Am. Chem. Soc.* 121, 10591.
- Ohkoshi S, Tokoro H, Hashimoto K (2005) *Coord. Chem. Rev.* 249, 1830.
- Ohkoshi S, Tokoro H, Hozumi T, Zhang Y, Hashimoto K, Mathonière C, Bord I, Rombaut G, Verelst M, Cartier dit Moulin C, Villain F (2006) *J. Am. Chem. Soc.* 128, 270.
- Osa S, Kido T, Matsumoto N, Re N, Pochaba A, Mrozinski J (2003) *J. Am. Chem. Soc.* 126, 420.
- Ozaki N, Tokoro H, Hamada Y, Namai A, Matsuda T, Kaneko S, Ohkoshi S (2012) *Adv. Func. Mater.* 22, 2089.
- Pasatoiu TD, Etienne M, Madalan AM, Andruh M, Sessoli R (2010) *Dalton Trans.* 39, 4802.
- Pasatoiu TD, Sutter J-P, Madalan AM, Fellah FZC, Duhayon C, Andruh M (2011) *Inorg. Chem.* 50, 5890.
- Pedersen KS, Dreiser J, Nehrkorn J, Gysler M, Schau-Magnussen M, Schnegg A, Holldack K, Bittl R, Piligkos S, Weihe H, Tregenna-Piggott P, Waldmann O, Bendix J (2011) *Chem. Commun.* 47, 6918.
- Rinehart JD, Long JR (2011) *Chem. Sci.* 2, 2078.
- Rombaut G, Verelst M, Golhen S, Ouahab L, Mathonière C, Kahn O (2001) *Inorg. Chem.* 40, 1151.
- Roubeau O, Clérac R (2008) *Eur. J. Inorg. Chem.* 4325.
- Saitoh A, Miyasaka H, Yamashita M, Clérac R (2007) *J. Mat. Chem.* 17, 2002.
- Sato O, Einaga Y, Fujishima A, Hashimoto K (1999) *Inorg. Chem.* 38, 4405.
- Sato O, Iyoda T, Fujishima A, Hashimoto K (1996) *Science* 272, 704.
- Sato O (2004) *J. Photochem. Photobiol. C* 5, 203.
- Sato O, Tao J, Zhang Y-Z (2007) *Angew. Chem. Int. Ed.* 46, 2152.
- Sawada Y, Kosaka W, Hayashi Y, Miyasaka H (2012) *Inorg. Chem.* 51, 4824.
- Saywell A, Magnano G, Satterley CJ, Perdigão LMA, Britton AJ, Taleb N, Giménez-López MdC, Champness NR, O'Shea JN, Beton PH (2010) *Nature Commun.* 1, 75.
- Schelter EJ, Karadas F, Avendano C, Prosvirin AV, Wernsdorfer W, Dunbar KR (2007) *J. Am. Chem. Soc.* 129, 8139.
- Shatruk M, Avendano C, Dunbar KR (2009) *Cyanide-Bridged Complexes of Transition Metals: A Molecular Magnetism Perspective, in Progress in Inorganic Chemistry* (ed K. D. Karlin), John Wiley & Sons, Inc., Hoboken, NJ, USA.
- Shiga T, Miyasaka H, Yamashita M, Morimoto M, Irie M (2011) *Dalton Trans.* 40, 2275.
- Shimamoto N, Ohkoshi S, Sato O, Hashimoto K (2002) *Inorg. Chem.* 41, 678.

- Simão C, Mas-Torrent M, Crivillers N, Lloveras V, Artés JM, Gorostiza P, Veciana J, Rovira C (2011) *Nature Chem.* 3, 359.
- Siretanu D, Li D, Buisson L, Bassani DM, Holmes SM, Mathonière C, Clérac R (2011) *Chem. –Eur. J.* 17, 11704.
- Sokol JJ, Hee AG, Long JR (2002) *J. Am. Chem. Soc.* 124, 7656.
- Song X, Yang P, Mei X, Li L, Liao D (2010) *Eur. J. Inorg. Chem.* 1689.
- Song Y, Zhang P, Ren X-M, Shen X-F, Li Y-Z, You X-Z (2005) *J. Am. Chem. Soc.* 127, 3708.
- Stamatatos TC, Foguet-Albiol D, Stoumpos CC, Raptopoulou CP, Terzis A, Wernsdorfer W, Perlepes SP, Christou G (2005) *J. Am. Chem. Soc.* 127, 15380.
- Tanase S, Reedijk J (2006) *Coord. Chem. Rev.* 250, 2501.
- Tao J, Zhang Y-Z, Bai Y-L, Sato O (2006) *Inorg. Chem.* 45, 4877.
- Tiron R, Wernsdorfer W, Aliaga-Alcalde N, Christou G (2003a) *Phys. Rev. B* 68, 140407.
- Tiron R, Wernsdorfer W, Foguet-Albiol D, Aliaga-Alcalde N, Christou G (2003b) *Phys. Rev. Lett.* 91, 227203.
- Tokoro H, Matsuda T, Nuida T, Moritomo Y, Ohoyama K, Dangui EDL, Boukheddaden K, Ohkoshi S (2008) *Chem. Mater.* 20, 423.
- Tokoro H, Miyashita S, Hashimoto K, Ohkoshi S (2006) *Phys. Rev. B* 73, 172415.
- Tokoro H, Ohkoshi S (2011) *Dalton Trans.* 40, 6825.
- Tokoro H, Ohkoshi S, Matsuda T, Hashimoto K (2004) *Inorg. Chem.* 43, 5231.
- Verdaguer M, Bleuzen A, Marvaud V, Vaissermann J, Seuleiman M, Desplanches C, Lomenech C, Rosenman I, Veillet P, Cartier C (1999) *Coord. Chem. Rev.* 192, 1023.
- Wang S, Zuo J-L, Zhou H-C, Choi HJ, Ke Y, Long JR, You X-Z (2004) *Angew. Chem. Int. Ed.* 43, 5940.
- Wernsdorfer W, Aliaga-Alcalde N, Hendrickson DN, Christou G (2002) *Nature* 416, 406.
- Xu H-B, Wang B-W, Pan F, Wang Z-M, Gao S (2007) *Angew. Chem. Int. Ed.* 46, 7388.
- Yang C-I, Tsai Y-J, Hung S-P, Nakano M, Tsai H-L (2010) *Chem. Commun.* 46, 5716.
- Yang E-C, Hendrickson DN, Wernsdorfer W, Nakano M, Zakharov LN, Sommer RD, Rheingold AL, Ledezma-Gairaud M, Christou G (2002) *J. Appl. Phys.* 91, 7382.
- Yoo J, Brechin EK, Yamaguchi A, Nakano M, Huffman JC, Maniero AL, Brunel LC, Awaga K, Ishimoto H, Christou G, Hendrickson DN (2000) *Inorg. Chem.* 39, 3615.
- Yoo J, Wernsdorfer W, Yang E-C, Nakano M, Rheingold AL, Hendrickson DN (2005) *Inorg. Chem.* 44, 3377.
- Yoo J, Yamaguchi A, Nakano M, Krzystek, J, Streib WE, Brunel L-C, Ishimoto H, Christou G, Hendrickson DN (2001) *Inorg. Chem.* 40, 4604.
- Zhang W-X, Shiga T, Miyasaka H, Yamashita M (2012) *J. Am. Chem. Soc.* 134, 6908.
- Zhang W, Sun H-L, Sato O (2011a) *Dalton Trans.* 40, 2735.
- Zhang Y-Z, Mallik UP, Clérac R, Rath NP, Holmes SM (2011b) *Chem. Commun.* 47, 7194.
- Zhang Y, Li D, Clérac R, Kalisz M, Mathonière C, Holmes SM (2010) *Angew. Chem. Int. Ed.* 49, 3752.

III. Coordination assemblies based on [Mn₄] SMMs

III.1 1D assemblies with diamagnetic chlorido ligands	68
III.1.1 Syntheses and general structural comments	68
III.1.2 Structural description of 1	69
III.1.3 Structural description of 2	71
III.1.4 Static magnetic properties of 1 and 2	75
III.1.5 Dynamic magnetic properties of 1 and 2	80
III.1.6 Concluding remarks for 1 and 2	84
III.2 1D and 2D assemblies with paramagnetic metal(II) picolinate	85
III.2.1 Synthetic approach	85
III.2.2 Crystallographic characterizations	86
III.2.3 Magnetic properties of 3	90
III.2.4 Magnetic properties of 4	93
III.2.5 Magnetic properties of 5	101
III.2.6 Concluding remarks for 3 – 5	103
III.3 Conclusion and perspectives	104
III.4 Supporting information	107
III.4.1 Experimental section	107
III.4.2 Supporting figures	110
III.4.3 Theoretical model: chain of alternating Ising and isotropic spins	112
References	123

We have seen in Chapter II that the idea to organize Single-molecule magnets (SMMs) in coordination networks was noticeably a successful strategy, leading to the discovery of new magnetic behaviors. These results open today a new area of research to design new types of magnetic materials based on SMMs.

During the past decade, our group has developed a wide knowledge on the isolated SMM systems as well as the coordination networks based on [Mn₄(hmp)₆]⁴⁺ SMMs (Hhmp: 2-hydroxymethylpyridine) that was firstly discovered in 2001 (Yoo et al. 2001). These tetramanganese rhombic complexes possess labile coordinating sites on external Mn^{II} ions that are helpful for a controlled step-by-step assembly. Indeed, the groups of Cl  rac and Miyasaka obtained 3D (compound **37** in Chapter II) and 2D assemblies (compound **39** – **41** in Chapter II) of [Mn₄] SMMs by reacting [Mn₄] SMMs with diamagnetic dicyanamide anions (Miyasaka et al. 2006; Miyasaka et al. 2004). Compounds **37** and **39** exhibited an 3D order in ferrimagnetic and canted antiferromagnetic phase, respectively. On the other hand, **40** behaves like a typical [Mn₄] SMM, and **41** showed the magnetic order around 2.1 K that is frozen due to the intrinsic SMM properties of the [Mn₄] units. More recently during the thesis of L. Lecren, she has shown the possibility to design 1D assemblies (compound **42** – **44** in Chapter II) with this [Mn₄] building block. These SMMs were linked by azide, acetate, and chloroacetate that are diamagnetic (Lecren et al. 2008; Lecren et al. 2005b). The [Mn₄] building units

are arranged antiferromagnetically along the chain yielding a total compensation of the spins. Nevertheless, slow relaxation was not impeded due to finite-size effects induced by the intrinsic defects of the material.

As shown in the aforementioned systems developed in our group, the coordination assemblies based on $[\text{Mn}_4]$ have led to the opportunity to observe new intriguing magnetic behaviors. However, we could remark that $[\text{Mn}_4]$ SMM building blocks have not yet been investigated to connect with paramagnetic linkers. As already proved in networks based on $[\text{Mn}_2]$ SMMs (section II.1.1.1 in Chapter II), paramagnetic linkers would favor strong magnetic interactions and consequently result in unique magnetic systems such as a SCM. Therefore, we have oriented a part of our work to organize $[\text{Mn}_4]$ SMMs with paramagnetic linkers.

To this end, we prepared 1D and 2D networks of this versatile $[\text{Mn}_4]$ unit using two different types of linkers, diamagnetic chlorido ions and paramagnetic metal complexes. The section III.1 is dedicated to 1D assemblies that are bridged by mono-chlorido and di-chlorido ligands: $[\text{Mn}_4(\text{hmp})_6(\text{H}_2\text{O})_2\text{Cl}](\text{ClO}_4)_3 \cdot 1.5\text{CH}_3\text{CN}$ (**1**) and $[\text{Mn}_4(\text{hmp})_6\text{Cl}_2](\text{ClO}_4)_2$ (**2**). In the section III.2, we present the 1D – 2D networks of $[\text{Mn}_4]$ SMMs assembled with metal(II) picolates: $[\text{Mn}_4(\text{hmp})_6(\text{H}_2\text{O})_2][\text{Ni}(\text{pic})_2(\text{H}_2\text{O})_2](\text{ClO}_4)_4 \cdot 3\text{CH}_3\text{CN}$ (**3**), $[\text{Mn}_4(\text{hmp})_6(\text{H}_2\text{O})_2][\text{Mn}(\text{pic})_2(\text{H}_2\text{O})_2](\text{ClO}_4)_4 \cdot 3\text{CH}_3\text{CN} \cdot 2\text{H}_2\text{O}$ (**4**), $[\text{Mn}_4(\text{hmp})_6\{\text{Cu}(\text{pic})_2(\text{ClO}_4)_2\}_2] \cdot 2\text{CH}_3\text{CN}$ (**5**). These compounds are firstly synthesized during the thesis of L. Lecren, and the syntheses were optimized in this thesis. This chapter also offers an extensive physical characterization and modelization of the compounds. Some magnetic properties are compared with the isolated $[\text{Mn}_4]$ SMM, $[\text{Mn}_4(\text{hmp})_6(\text{NO}_3)_2(\text{H}_2\text{O})_2](\text{NO}_3)_2 \cdot 2.5\text{H}_2\text{O}$ (**C**, see section I.1) (Lecren et al. 2005c), for better understanding.

III.1 1D assemblies with diamagnetic chlorido ligands

III.1.1 Syntheses and general structural comments

The $[\text{Mn}_4(\text{hmp})_6]^{4+}$ SMMs, that is introduced in Chapter I, have a mixed-valence $[\text{Mn}^{\text{III}}_2\text{Mn}^{\text{II}}_2]$ core with manganese ions arranged in a double-cuboidal fashion (**Figure I.1**). The oxidation states of manganese ions can be easily assigned as trivalent and divalent for respectively the inner and outer manganese sites based on charge balance consideration, bond-valence sum calculation (Brown and Altermatt 1985), and Jahn Teller (JT) distortion on Mn^{III} sites. The two internal Mn^{III} ions are connected through two μ_3 -oxido bridges from hmp ligands, and the four μ -alkoxido groups bridge each Mn^{III} ions to the two external Mn^{II} ones. The coordination sphere of the external Mn^{II} ions is completed by the solvent molecules or the anions. These solvent molecules have been found to be labile and thus easily exchanged by other coordinating species present in the reaction medium, while the core of the $[\text{Mn}_4]$ unit remains quasi-identical. Therefore, this robustness and coordination ability of $[\text{Mn}_4]$ confer high flexibility to these SMM molecules that can act as building blocks to construct new magnetic architectures.

We have adopted the one-pot synthetic approach (see experimental section for details) that was explored during the thesis of L. Lecren (Lecren 2006). Upon the addition of Hhmp (2-hydroxymethylpyridine) and tetraethylammonium hydroxide into an acetonitrile solution containing $\text{Mn}(\text{ClO}_4)_2 \cdot 6\text{H}_2\text{O}$, the $[\text{Mn}_4(\text{hmp})_6]^{4+}$ cations rapidly formed in solution. For the potentially

coordinating bridges, $\text{MnCl}_2 \cdot 4\text{H}_2\text{O}$ and NaCl were added as a source of chlorido ligands to afford a chain of $[\text{Mn}_4]$ units assembled through monochlorido and dichlorido bridges, respectively: $[\text{Mn}_4(\text{hmp})_6(\text{H}_2\text{O})_2\text{Cl}](\text{ClO}_4)_3 \cdot 1.5\text{CH}_3\text{CN}$ (**1**) and $[\text{Mn}_4(\text{hmp})_6\text{Cl}_2](\text{ClO}_4)_2$ (**2**). Single crystals of **1** and **2** suitable for the X-ray diffraction were obtained by layering diethylether on the top of the reaction solution. It is worth mentioning that the diffusion of the vapor of the diethylether to the solution of **2** leads to a mixture of **1** and **2**. Crystal data and structure refinement details of compound **1** and **2** are listed in Table III.1.

Table III.1 Crystallographic data of compound **1** and **2**. The monoclinic $C2/c$ unit-cell parameters of **2** at 298 K are also transformed to triclinic $P-1$ system for the easy comparison with the ones at 150 K.

	1 (298 K)		2 (298 K)		2 (150 K)
Empirical formula	$\text{C}_{39}\text{H}_{44.5}\text{Cl}_4\text{Mn}_4\text{N}_{7.5}\text{O}_{20}$		$\text{C}_{36}\text{H}_{36}\text{Cl}_4\text{Mn}_4\text{N}_6\text{O}_{14}$		
Formula weight, g mol^{-1}	1299.88		1138.27		
Wavelength, Å	0.71073		0.71073		
Space group	$C2/m$	$C2/m$	$C2/c$	$P-1$	$P-1$
a , Å	23.313(4)	23.341(5)	19.207(4)	11.778(0)	11.640(2)
b , Å	18.716(2)	18.703(4)	13.641(3)	11.751(0)	11.727(2)
c , Å	13.169(2)	13.134(3)	18.014(4)	18.003(4)	17.918(4)
α , °	90	90	90	73.93(6)	71.78(3)
β , °	91.16(6)	91.09(3)	109.72(3)	74.03(2)	74.97(3)
γ , °	90	90	90	70.88(3)	70.76(3)
V , Å ³	5745.0(1)	5733.0(2)	4442.7(15)	2215.2	2159.7(7)
Z		4	4		2
ρ_{calcd} , Mg m^{-3}		1.506	1.702		1.750
μ , mm^{-1}		1.121	1.423		1.463
$F(000)$		2636	2296		1148
$^a R_1$ ($I > 2\sigma(I)$)		0.0767	0.0438		0.0611
$^b wR_2$ (all)		0.2296	0.1172		0.1813
GoF		1.022	0.994		1.025

$$^a R_1 = \sum ||F_o| - |F_c|| / \sum |F_o|, \text{ and } ^b wR_2 = [\sum w(F_o^2 - F_c^2)^2 / \sum w(F_o^2)]^{1/2}.$$

III.1.2 Structural description of **1**

Compound **1** crystallizes in monoclinic $C2/m$, having centrosymmetrical $[\text{Mn}_4(\text{hmp})_6]^{4+}$ units (**Figure III.1**, bottom left) that are linked together *via* monochlorido ion leading to a one dimensional organization along the crystallographic b axis (**Figure III.1**, top). Perchlorate anions compensate the charge and fill the vacant space inside the crystal packing with acetonitrile molecules. Both Mn^{III} and Mn^{II} ions are hexa-coordinated, and the coordination of the latter is completed by a chlorido ion and a water molecule. The JT axes are slightly bent leading N2-Mn1-O3 angle at 160.8° and the central Mn1-O3-Mn1' angle is 100.1° . These two angles are in the range of previously reported $S_T = 9$ SMMs containing $[\text{Mn}_4(\text{hmp})_6]^{4+}$ units (Table III.2).¹ The $[\text{Mn}_4]$ units along the chain have two different orientations resulting in an angle between neighboring JT axes (Mn1-O3) as *ca.* 11.4° (**Figure III.2**). Meanwhile, all chains are identical in the structure. The individual chains are in close contact with their neighbors by $\pi \cdots \pi$ interactions with the shortest distance being 3.42 Å between C4 and C5, forming the layers parallel to ab plane (**Figure III.1**, bottom right). In addition, oxygen atoms from one of perchlorate anions act as weak hydrogen bond acceptors with C-H groups of the disordered

¹ The main structural variations of $S_T = 1$ $[\text{Mn}_4]$ cores are found on the larger $\text{Mn}^{\text{III}}\text{-O-Mn}^{\text{III}}$ angles and the longer $\text{Mn}^{\text{III}} \cdots \text{Mn}^{\text{III}}$ separations: for example, the tetranuclear compound $[\text{Mn}_4(\text{hmp})_6(\text{Hhmp})_2](\text{ClO}_4)_4 \cdot 2\text{CH}_3\text{CN}$, that displays an $S_T = 1$ spin ground state, shows 102.9° and 3.353 Å for $\text{Mn}^{\text{III}}\text{-O-Mn}^{\text{III}}$ angles and $\text{Mn}^{\text{III}} \cdots \text{Mn}^{\text{III}}$ distances, respectively. Consequently, the bending angle of JT axes is also smaller, resulting in 151.2° (Lecren et al. 2005).

hmp ligands from four neighboring chains ($d_{C\cdots O} = 3.20$ (C9 – O41), 3.21 (C8 – O42), 3.26 (C16 – O43), 3.46 (C16 – O41) Å) (**Figure III.1**, bottom right). Therefore, these short interactions allow the chains to form a network also through *bc* plane. The distances between Mn(II) ions from the adjacent chains are 8.7 Å and 11.3 Å along the crystallographic *a*- and *c*-axes, respectively. Thus, all aforementioned features indicate the chains are not perfectly isolated in the crystal packing. It is worth noting that a comparison of the unit-cell parameters at 120 and 298 K (Table III.1) suggests the absence of a structural transition in this temperature range.

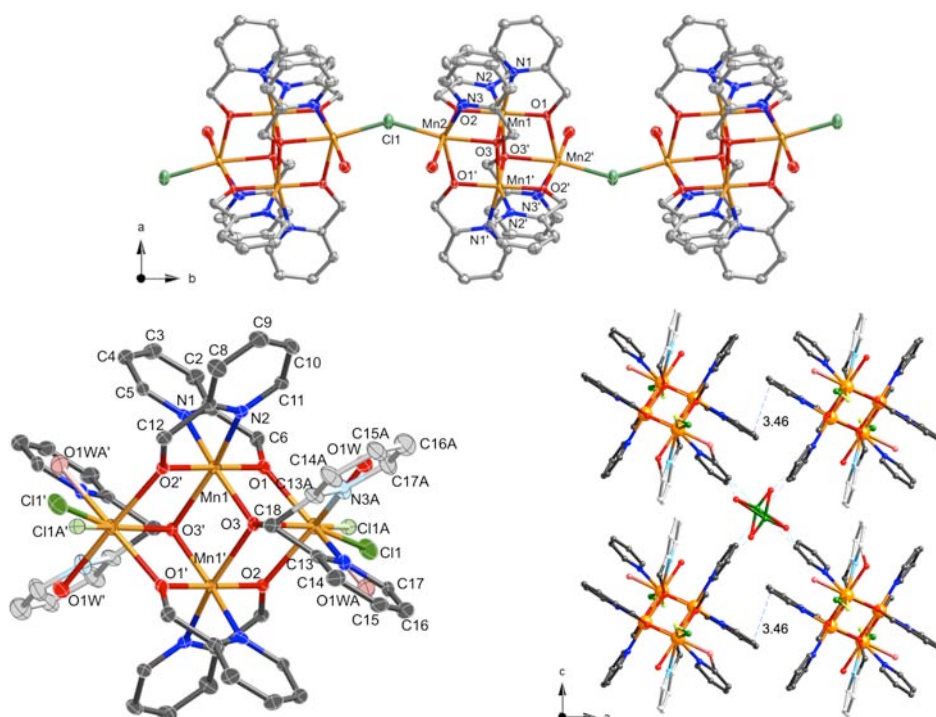


Figure III.1 Top: ORTEP-type view of the structure of **1**, emphasizing the 1D arrangement of $[Mn_4]$ units. The orange, grey, blue, and red thermal ellipsoids correspond to Mn, Cl, C, N, and O atoms, respectively, with 40 % probability level. Bottom: ORTEP-type view of the $[Mn_4]$ core structure in **1**, highlighting the disordered hmp, water molecule, and chlorido ion in lighter colors (left). Ball and stick view for the crystal packing of **1** in the *ac* plane, illustrating $\pi\cdots\pi$ interactions and short contacts between chains (dashed line, distances are indicated in Å). One of perchlorate anions that creates short contacts with neighboring chains is depicted, while the rest, solvent molecules, and hydrogen atoms are omitted for clarity.

Table III.2 Selected interatomic distances (Å) and angles ($^\circ$) for **1** at 120 K.

Mn1-N1	2.068(6)	Mn2-O3	2.251(5)
Mn1-N2	2.171(6)	Mn2-O2'	2.185(5)
Mn1-O1	1.866(5)	Mn2-O1	2.153(5)
Mn1-O2	1.870(5)	Mn2-N3	2.173(7)
Mn1-O3	2.009(5)	Mn2-Cl1	2.409(3)
Mn1-O3'	2.203(5)	Mn2-O1W	2.267(8)
N2-Mn1-O3	160.8(2)	Mn1-O3-Mn1'	100.17(19)
Mn1-O1-Mn2	106.6(2)	Mn1'-O2-Mn2	108.8(2)
Mn1...Mn1'	3.232(2)	Mn2-Cl1-Mn2''	144.5(4)

Symmetry transformations used to generate equivalent atoms (A): A', $-x+1/2, -y+1/2, -z+1$; A'', $x, -y+1, z$.

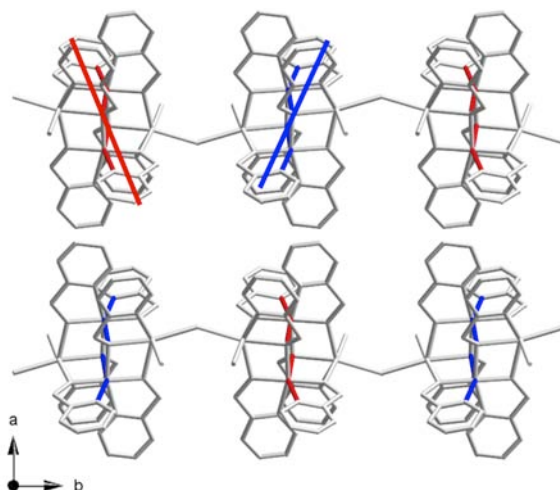


Figure III.2 View of crystal packing perpendicular to c axis for compound **1**, highlighting two different orientations of JT axes along the chain in red and blue. H atoms, solvent molecules, and counter anions are omitted for clarity.

III.1.3 Structural description of **2**

Crystal data and structure refinement details of compound **2** are listed in Table III.1. At 298 K, Compound **2** crystallizes in $C2/c$ space group, containing a one-dimensional assembly of $[\text{Mn}_4(\text{hmp})_6\text{Cl}_2]^{2+}$ units along the crystallographic c axis (**Figure III.3a**). The centrosymmetrical $[\text{Mn}_4]$ core (**Figure III.3c**) has trivalent manganese ions in the middle (Mn2 and Mn2'), exhibiting a distorted octahedral geometry as expected for the JT elongation, and divalent ones at the external sites (Mn1 and Mn1'). These JT axes of alternating $[\text{Mn}_4]$ units along the chain have different orientations resulting in a separation of Mn(2)-O(1) axes by an angle of *ca.* 34.3° . In the crystal structure, all chains are identical and the perchlorate counter anions compensate the charge and fill the void spaces. The weak interchain short contacts (≤ 3.50 Å) are present through $\pi\cdots\pi$ interactions between hmp rings (**Figure III.3e**).

With decreasing temperature, the structure of compound **2** adopted the lower symmetry ($P-1$) (**Figure III.3b**). Loosing the symmetry elements induced the doubling of the asymmetric unit in the unit-cell (**Figure III.3d**). The neighboring $[\text{Mn}_4]$ units along the chain and two chlorido ions on the same bridge are not anymore identical, leading to slight differences on bond lengths and angles (Table III.3). The central Mn2-O1-Mn2' and Mn4-O4-Mn4' angles are 98.5° and 98.4° , respectively, with the Mn2 \cdots Mn2' and Mn4 \cdots Mn4' distances being 3.22 and 3.21 Å. These values are in the range of previously reported $S_T = 9$ SMMs containing $[\text{Mn}_4(\text{hmp})_6]^{4+}$ units, indicating the geometry in the $[\text{Mn}_4]$ core of **2** would favor the ferromagnetic arrangement of Mn ions.¹ The angle between alternating JT axes along the chain is *ca.* 34.8° and all chains in the crystal structure are identical (**Figure III.4**). The interchain short contacts (≤ 3.50 Å) are shorter than those at 298 K, through both $\pi\cdots\pi$ and $\sigma\cdots\pi$ interactions (*ca.* 3.37 – 3.50 Å, **Figure III.3f**). The nearest Mn(II) \cdots Mn(II) distances between the adjacent chains are 9.9 and 8.8 Å along the a and b axes, respectively. It should be also noted that an isostructural compound with **2** was reported in 2005 by Hendrickson *et al* (Yoo *et al.* 2005), and was obtained by treating NaClO_4 to the ethanol solution containing MnCl_2 , *n*-tetrabutylammonium permanganate, and Hhmp. But the structural characterization was only done at 112 K.

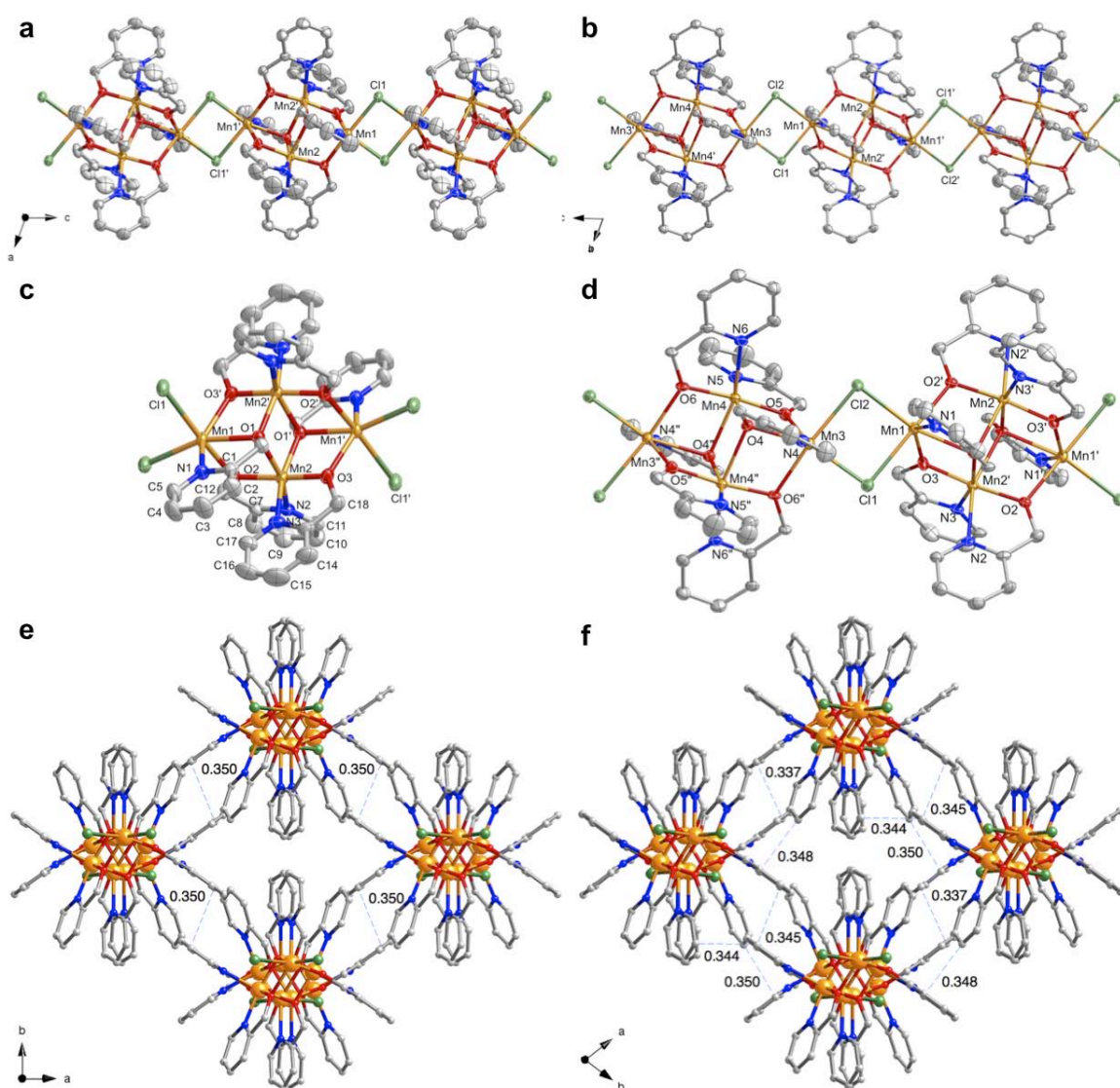


Figure III.3 ORTEP-type view illustrating chain structures (a and b) and the [Mn₄] core structure (c and d) of **2** with the thermal ellipsoids at 40 %. Ball and stick view for the crystal packing of **2**, illustrating $\pi\cdots\pi$ interactions and short contacts between chains (e and f, distances are indicated in nm). The figures marked as a, c, e and b, d, f respectively correspond to 298 K and 150 K, and Mn, C, N, O, and Cl atoms are represented in orange, gray, blue, red, and green, respectively. Counter anions and hydrogen atoms are omitted for clarity.

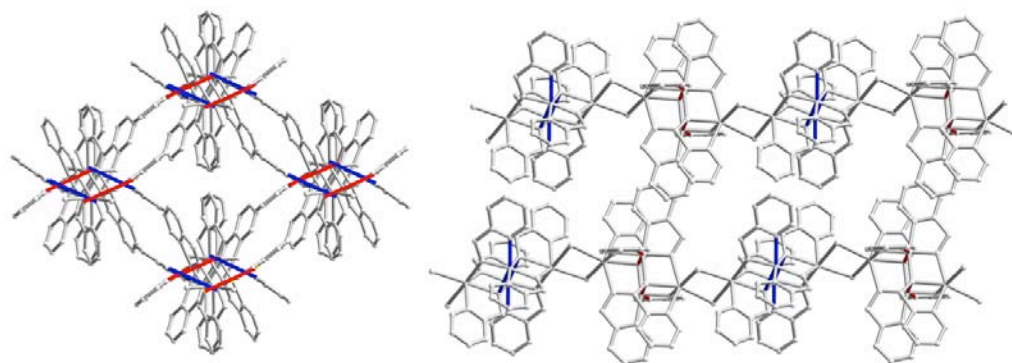


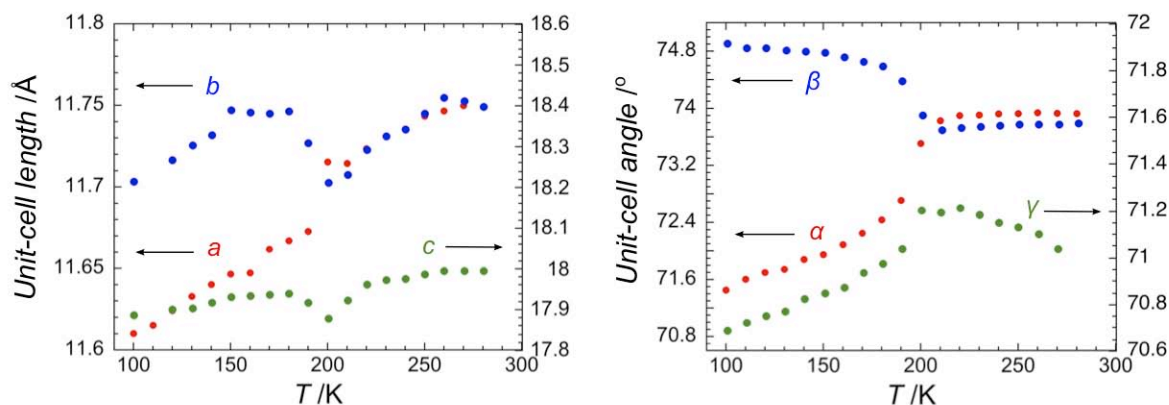
Figure III.4 View of crystal packing perpendicular to *c* axis (left) and *a* axis (right) for the compound **2** at 150 K, highlighting two different orientations of JT axes along the chain in red and blue.

Table III.3 Selected interatomic distances (Å) and angles (°) for **2** at 298 and 150 K.

	298 K	150 K		150 K
Mn2-N2	2.208(4)	2.231(6)	Mn4-N6	2.192(6)
Mn2-O1	2.258(3)	2.266(4)	Mn4-O4''	2.237(5)
N2-Mn2-O1	158.1(1)	157.4(2)	N6-Mn4-O4''	158.8(2)
Mn2-O1'	1.989(3)	1.976(4)	Mn4-O4	1.994(5)
Mn2-N3	2.046(4)	2.042(6)	Mn4-N5	2.045(6)
Mn2-O2	1.878(2)	1.876(4)	Mn4-O5	1.866(5)
Mn2-O3	1.865(3)	1.872(5)	Mn4-O6	1.874(4)
Mn1-O1	2.252(2)	2.250(4)	Mn3-O4	2.244(4)
Mn1-O2	2.180(3)	2.164(4)	Mn3-O5	2.163(5)
Mn2-O1-Mn2'	98.2(1)	98.5(2)	Mn4-O4-Mn4''	98.4(2)
Mn1-O1-Mn2'	100.1(1)	99.8(2)	Mn3-O4-Mn4	99.8(2)
Mn1'-O3-Mn2	107.3(1)	106.8(2)	Mn3-O5-Mn4	107.1(2)
Mn2-Mn2'	3.214(1)	3.219(2)	Mn4-Mn4''	3.206(2)
Mn1-Mn2	3.320(1)	3.317(2)	Mn3-Mn4''	3.307(2)
Mn1-Mn2'	3.254(1)	3.237(2)	Mn3-Mn4	3.246(2)
Mn1-Cl1	2.592(2)	2.580(2)		
Mn1-Cl1'	2.452(1)		Mn3-Cl2	2.590(2)
Mn1-Cl1-Mn1''	93.26(4)	92.91(7) ^a	Mn1-Cl2-Mn3	92.76(7)

^aMn1-Cl1-Mn3 for 150 K. Symmetry transformations used to generate equivalent atoms (A): A', -x,-y+2,-z; A'', -x,y,-z+1/2 (298 K); A', -x+2,-y+2,-z+1; A'', -x+2,-y+2,-z+2 (150 K).

To further study the structural changes with the temperature, the unit-cell parameters every 10 K were analyzed between 298 and 100 K, at a ramping rate of 60 K/h. The monoclinic unit-cell parameters were converted into triclinic ones to facilitate the comparison.² As shown in the evolution of the unit-cell lengths and angles, an anomaly was observed around 200 K suggesting a structural transition (**Figure III.5**). It is worth mentioning that the cycles of increasing and decreasing temperatures did not show any significant differences, exhibiting the anomalies superposed at the same temperature.

**Figure III.5** Temperature-dependences of the unit-cell parameters in cooling rate of 60 K/h. The unit-cell lengths *a*, *b*, *c* and the unit-cell angles α , β , γ are in red, blue, and green, respectively.

² To convert from monoclinic to triclinic, the following matrix was applied:

$$\begin{bmatrix} 1 & 1 & 0 \\ 1 & -1 & 0 \\ 0 & 0 & -1 \end{bmatrix}^{-1}$$

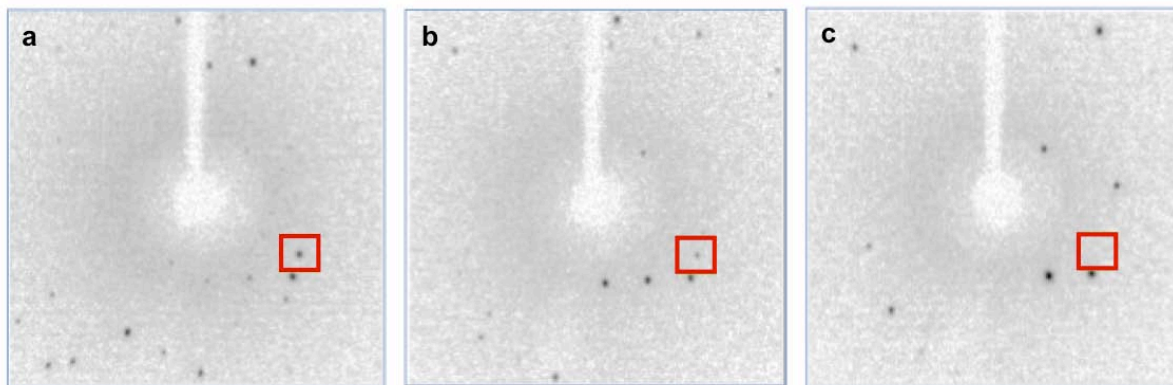


Figure III.6 Diffraction images at 100 K (a), 200 K (b), and 290 K (c), highlighting the (3 3 3) Bragg peak of the *P*-1 structure in red square that corresponds to (6 0 -3) one in the *C2/c* space group.

To understand the nature of the transition, the intensity of the characteristic bragg diffractions corresponding to the systematic extinctions for the monoclinic phase were followed depending on the temperature. In *C2/c* space group, the only *h0l* diffractions in which *h* and *l* are even are supposed to be observed. Thus, we have chosen (6 0 -3), (4 0 -7), and (2 0 -3) diffractions that are (3 3 3), (2 2 7), and (1 1 3), respectively, in *P*-1. Careful analyses of the diffraction images show clearly the apparition of the characteristic bragg peak (**Figure III.6**) upon decreasing the temperature. As shown in **Figure III.7** (left), the temperature dependence of the normalized intensities for the three selected diffraction peaks are well superposed in one curve that compare perfectly with the temperature variation of the square of the Ising order parameter (m^2) in the mean-field approximation (that is, the solution of the self-consistent equation $m = \tanh(mT_C/T)$) (Chaikin and Lubensky 2000; Coulon and Moreau 2000). This confirms the second-order single-crystal-to-single-crystal transition with $T_C = 219$ K. This structural transition was also supported by heat capacity measurements that display a peak at *ca.* 219 K (**Figure III.7**, right).

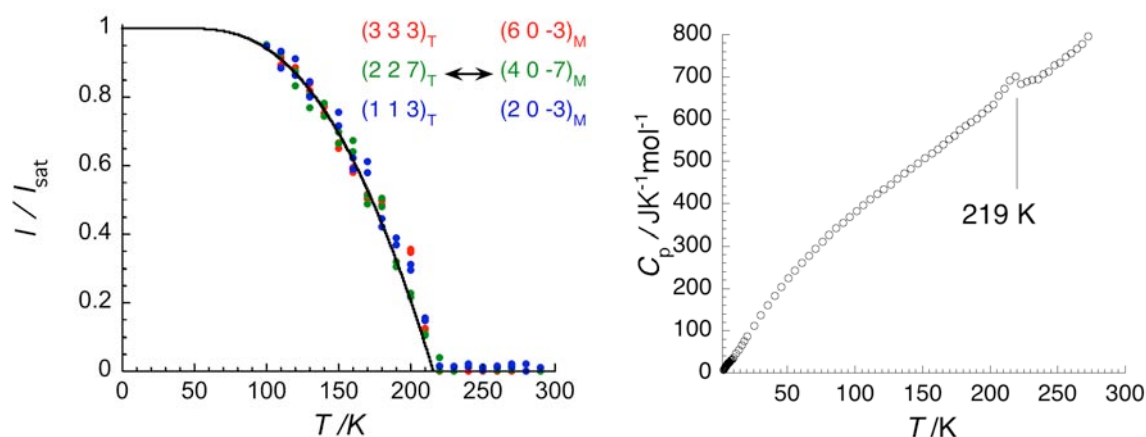


Figure III.7 Temperature dependences of the intensity for the characteristic diffraction peaks for **2**. (3 3 3), (2 2 7), and (1 1 3) diffraction peaks in the *P*-1 space group, that correspond to (6 0 -3), (4 0 -7), and (2 0 -3) in *C2/c*, are shown in red, green, and blue, respectively, and the black solid line represents m^2 described in the main text (left). Temperature dependence of the heat capacity C_p between 1.9 K and 270 K for a polycrystalline sample of **2** at a zero magnetic field during the cooling process (right).

III.1.4 Static magnetic properties of **1** and **2**

dc magnetic susceptibilities of **1** and **2** were measured on the polycrystalline samples between 1.8 K and 300 K at 1000 Oe, and compared with the isolated $[\text{Mn}_4]$ SMM, $[\text{Mn}_4(\text{hmp})_6(\text{NO}_3)_2(\text{H}_2\text{O})_2](\text{NO}_3)_2 \cdot 2.5\text{H}_2\text{O}$ (**C**) (Lecren et al. 2005c), in **Figure III.8**. The χT product at 300 K for **1** and **2** is respectively 14.5 and 15.8 $\text{cm}^3\text{Kmol}^{-1}$, that are in agreement with the expected value for uncoupled two Mn^{II} ($S = 5/2$) and two Mn^{III} ($S = 2$) ions, *i.e.* 14.75 $\text{cm}^3\text{Kmol}^{-1}$ for $g = 2$. This is also coherent with the isolated compound **C**. For **1**, the χT product stays fairly at a constant value between 300 K and 100 K and then drops down to 1.6 $\text{cm}^3\text{Kmol}^{-1}$ at 1.9 K with a small increase showing a maximum of the peak being 2.8 $\text{cm}^3\text{Kmol}^{-1}$ at 4.5 K. As indicated by the decrease of the χT product in **1**, antiferromagnetic interactions are dominant. For **2**, the χT product increases gradually upon lowering the temperature to a maximum of 24.8 $\text{cm}^3\text{Kmol}^{-1}$ at 22 K. Further cooling down to 6.8 K induces the decrease of the χT product to 16.5 $\text{cm}^3\text{Kmol}^{-1}$, and successively an increase and an abrupt decrease was observed at lower temperatures with a peak at *ca.* 4 K being 22.1 $\text{cm}^3\text{Kmol}^{-1}$.

A comparative analysis of the $[\text{Mn}_4]$ core structural parameters of **1** and **2** indicates that intra- $[\text{Mn}_4]$ magnetic interactions in **1** and **2** are not in favor of antiferromagnetic interactions, as mentioned in the structural description. Therefore, the systems can be considered as $[\text{Mn}_4]$ complexes linked by weak inter-tetramer interaction (J) along the chain (inset of **Figure III.8**), in which the Hamiltonian for the tetranuclear $[\text{Mn}_4]$ unit is given by (Yoo et al. 2001):

$$H = -2J_{bb}(s_a s_b) - 2J_{wb}(s_a + s_b)(S_a + S_b) \quad \text{Eq III.1}$$

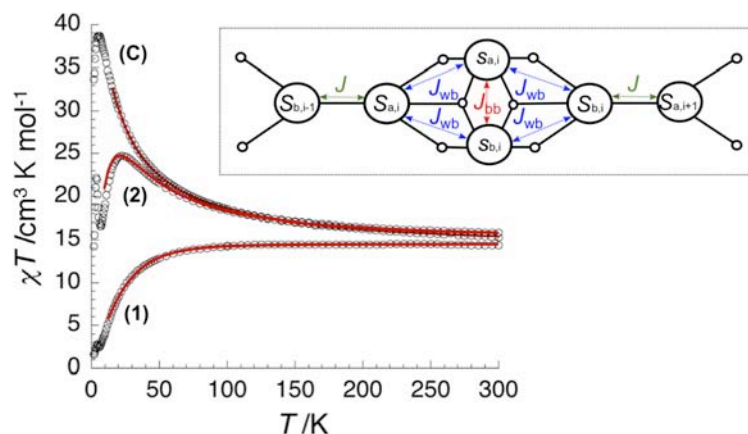


Figure III.8 Temperature dependence of χT product (where χ is the molar magnetic susceptibility that is equal to M/H) collected in an applied dc field of 1000 Oe for compounds **1**, **2**, and **C**; the red line is the best fit discussed in the text. Inset: Topology of the magnetic interactions among magnetic centers in the $[\text{Mn}_4]$ core and intrachain interactions between $[\text{Mn}_4]$ units. S_a and S_b represent the Mn^{II} spins while s_a and s_b stand for Mn^{III} spins. The letters a and b differentiate the two Mn ions with the same valence.

Table III.4 The best sets of parameters estimated through the susceptibility fits for **1** and **2** compared with **C**.

Compounds	g	J_{wb}/k_B	J_{bb}/k_B	J/k_B ($z = 2$)
1	1.96	1.6(1)	8.2(4)	-0.655(5)
2	1.97	1.5(1)	8.8(1)	-0.075(5)
C	1.93(1)	1.2(1)	13.3(2)	-

The experimental χT data have been fitted above 15 K to this model treating the weak exchange interactions through the mono- or di-chlorido bridges (J) in the mean-field approximation.³ A satisfactory agreement between theory and experience was obtained with fixing $g = 1.96$ and 1.97 for **1** and **2** and with the following set of parameters: $J_{wb}/k_B = +1.6(1)$ K, $J_{bb}/k_B = +8.2(4)$ K, $zJ/k_B = -1.31(1)$ K for **1**, and $J_{wb}/k_B = +1.5(1)$ K, $J_{bb}/k_B = +8.8(1)$ K, $zJ/k_B = -0.15(1)$ K for **2**. These values are summarized in Table III.4, in comparison with compound **C**. The obtained J_{bb}/k_B and J_{wb}/k_B values for **1** and **2** are positive and comparable to those found in **C**, implying that the intramolecular ferromagnetic interactions are preserved even after the formation of 1D networks. Meanwhile, the inter-[Mn₄] interactions along the chain, through the chlorido bridges, were estimated to be antiferromagnetic. For **2**, the obtained zJ/k_B is *ca.* 10 times smaller than the J_{wb}/k_B , implying the reliability of the model based on the mean-field approximation. However, it should be noted that the value of zJ/k_B for **1** might be over-estimated, since the obtained parameters are in the limit of using the mean-field approximation in which a small zJ/k_B was assumed compared to J_{wb}/k_B . With $z = 2$, the $J/k_B = -0.65$ and -0.075 K for **1** and **2**, respectively, correspond to the coupling between $S_T = 9$ [Mn₄] units *via* monochlorido and dichlorido bridges. Indeed the direct coupling between the 5/2 spin amounts to $J^*/k_B = -8.4$ and -1.0 K for **1** and **2**, respectively.⁴ It is worth to note that the magnetic interactions between Mn^{II} ions through the dichlorido bridge is indeed very versatile, showing both antiferromagnetic and ferromagnetic in literature (Romero et al. 2005). However, a generalized magnetostructural relation was not found. Nevertheless, the estimated value J^* is in the range of the reported values for antiferromagnetically coupled chain possessing [Mn^{II}-(μ -Cl)₂-Mn^{II}] moieties (Martin et al. 2004; Wu et al. 2003; Zhang et al. 1997). On the other hand, the magnetic studies of Mn^{II} compounds bridged by monochlorido ion have not been reported to our best knowledge.

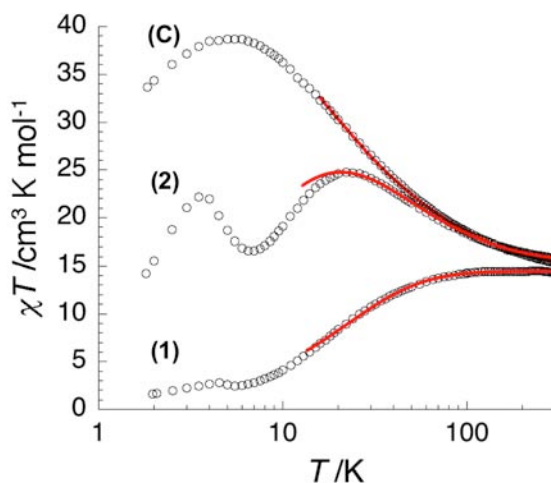


Figure III.9 Temperature dependence of χT product collected in an applied dc field of 1000 Oe for compounds **1**, **2**, and **C** in semi-logarithmic scale; the red line is the best fit discussed in the text.

³ To take into account the intercomplex interaction, the following definition of the susceptibility has been used:

$$\chi = \chi_0 \left[1 - \frac{2zJ}{Ng^2\mu_B^2} \chi_0 \right]^{-1}$$

where χ_0 is the susceptibility of the noninteracting units, z the number of the nearest neighbors, and J is the magnetic interaction between units (Meyers et al. 1969; O'Connor 1982).

⁴ The interactions between Mn^{II} ions (J^*) can be deduced from J , by the following relation: $J^* S_{Mn}^2 = JS_T^2$, where $S_{Mn} = 5/2$ and $S_T = 9$.

The low-temperature increase of the χT products for **1** and **2** (Figure III.9) are due to the canting of two different $[\text{Mn}_4]$ units along the chain as shown in the structural analyses. When the canting is present, one can consider two projections of spins in their plane: ferromagnetic and antiferromagnetic directions. The former giving the uncompensated component of the magnetic moment of canted spins causes an increase in χT product, whereas the latter projection leading compensated component results in a decrease of χT product monotonically to zero. As the canting angle is bigger in **2** compared to the one in **1**, the increase of χT product is more pronounced in **2**. Therefore, compounds **1** and **2** can be viewed as canted 1D arrangements of antiferromagnetically coupled $S_T = 9$ $[\text{Mn}_4]$ SMM units.

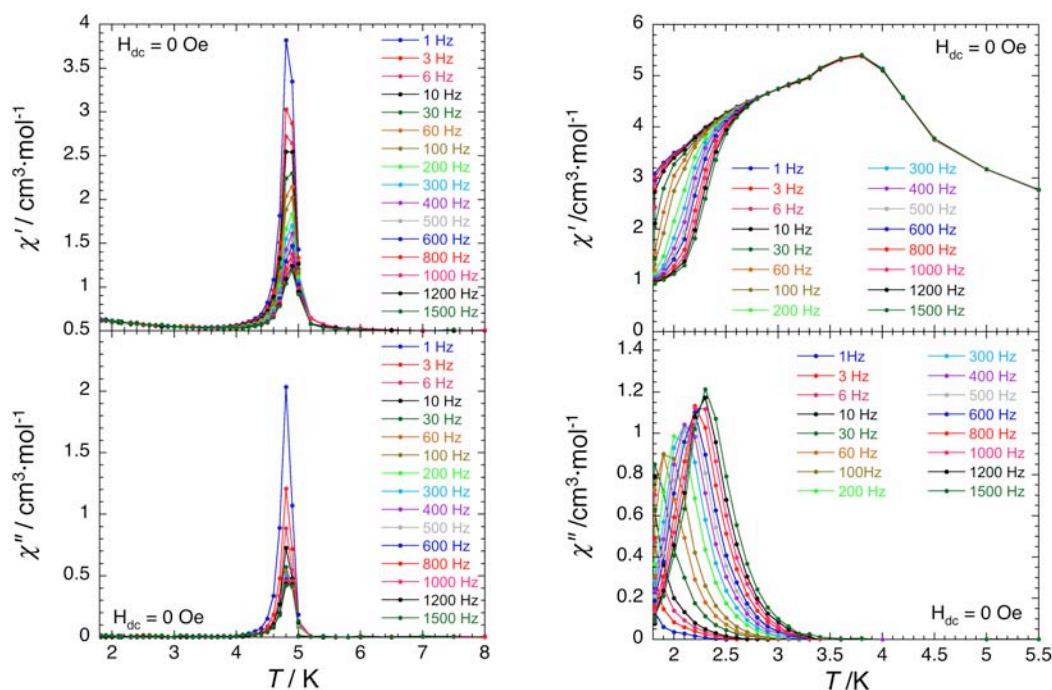


Figure III.10 Temperature dependence of the real (χ' , top) and imaginary (χ'' , down) parts of the ac susceptibility for a polycrystalline sample of **1** (left) and **2** (right) in zero dc-field at different ac frequencies. Solid lines are guides for eye.

Given the fact that both compounds **1** and **2** display a peak of the χT product in low temperature before a continuous decrease, further analyses were performed by measuring temperature-dependent ac susceptibility in zero dc field and with an ac field of 3 Oe (Figure III.10). Compound **1** exhibits a marked ac response below 5 K on both in-phase (χ') and out-of-phase (χ'') components of the ac susceptibility. The intensity of the ac response is decreasing with increasing frequency, but the position of the maximum remains quasi-constant versus the frequency dependence. It strongly suggests the presence of a 3D magnetic order in canted antiferromagnetic phase. On the other hand, compound **2** shows a frequency independent maximum of χ' response at 4 K, while no χ'' was observed at this temperature. This implies that an antiferromagnetic ground state is stabilized for **2**. Then, strongly frequency-dependent ac signals were detected below 3 K on both χ' and χ'' , indicating slow relaxation of the magnetization, even in 3D antiferromagnetic phase (this will be further discussed in the following part). Furthermore, heat capacity (C_p) measurements on **1** and **2** respectively exhibit an anomaly at *ca.* 4.6 and 4.2 K (Figure III.11). The combined temperature-

dependent ac susceptibility and heat capacity measurements on both compounds show unambiguously the presence of a long-range order magnetic transition at 4.6 K and 4.2 K, corresponding to the canted antiferromagnetic phase and the antiferromagnetic phase for **1** and **2**, respectively.

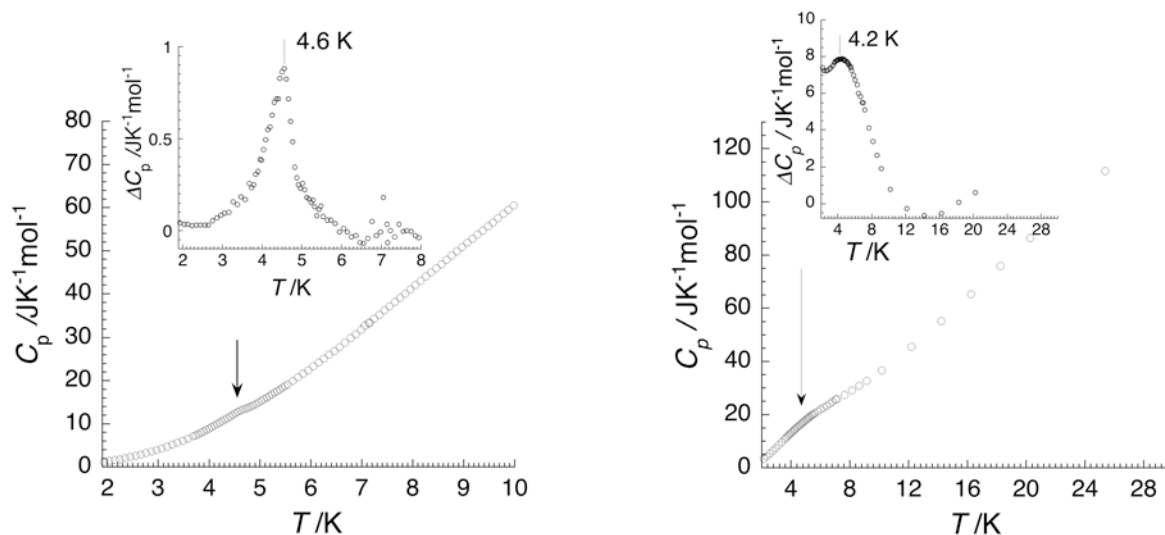


Figure III.11 Temperature dependence of the heat capacity C_p for a polycrystalline sample of **1** (left) and **2** (right) at a zero magnetic field during the cooling process. Inset: Temperature dependence of the excess heat capacity around the anomaly.

To further investigate the properties under the external magnetic field, M vs H measurements have also been performed below 25 and 10 K for compounds **1** and **2**, respectively. Compound **1** reveals the presence of a hysteresis effect with a coercive field of 50 Oe at 1.8 K (at about 80 Oe/min), which is also confirmed by a single-crystal measurement (**Figure III.12**, left). At higher field, the magnetization increases almost linearly up to 7×10^4 Oe and reaches $6.2 \mu_B$ at 2 K (**Figure III.12**, right), that is much lower than the expected one ($17.6 \mu_B$ taking $g = 1.96$) for all aligned $S_T = 9$ $[\text{Mn}_4]$ moments. Furthermore, it exhibits a typical “S” shape curve with an inflection point at $ca. 5.7 \times 10^4$ Oe that is not depending on the temperature, up to 10 K (**Figure III.12**, right). Concerning that the 3D magnetic transition is at 4.6 K, this field is a characteristic for the chain itself at which the applied magnetic field overcomes antiferromagnetic interaction between $[\text{Mn}_4]$ units along the chain. Knowing the characteristic field (H^*) and the canting angle, 2α , being 11.4° from the structural analysis, the corresponding J/k_B interaction can be estimated at - 0.22 K in the frame of anisotropic Heisenberg model:⁵

$$H^* = \frac{4|J|S_T \cos(2\alpha)}{g\mu_B \cos(\alpha)} \quad \text{Eq III.2}$$

This value is significantly smaller than the evaluation deduced from the fitting of the susceptibility found at - 0.655(5) K. This feature indeed supports an overestimation of J through the mean-field approximation as discussed previously. In addition, it is worth noting that we could not observe any signature of the para- canted antiferromagnetic phase transition in M vs H curves, since it is probably hidden by the presence of the hysteresis effect.

⁵ This is obtained simply by equalizing the exchange and Zeeman energies, $g\mu_B S_T H^* = 2zJS_T^2$ (with $z = 2$). Due to the different orientations of $[\text{Mn}_4]$ units along the chain with an angle of 2α , the effective field seen by each spin is $H^* \cos \alpha$ instead of H^* . In a same way, the effective interaction between two spins is $J \cos 2\alpha$ instead of J .

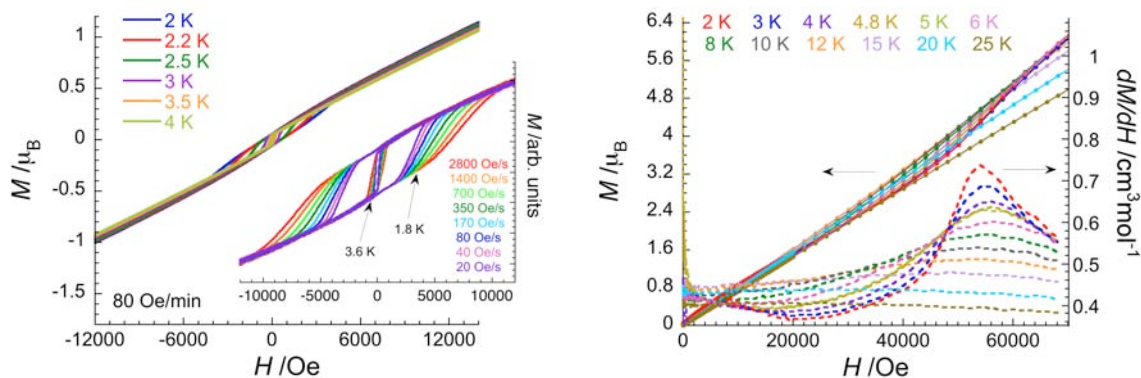


Figure III.12 Field dependence of the magnetization for a polycrystalline sample of **1** between 2 and 4 K with sweep-rates of 80 Oe/min (left). Inset: Hysteresis loops for a single crystal sample of **1** at 1.8 and 3.6 K with sweep-rates between 20 and 2800 Oe/s. The field is applied to the crystallographic monoclinic *b* axis (left). Field dependence of the magnetization and its derivatives for a polycrystalline sample of **1** between 2 K and 25 K, up to 70000 Oe (right).

In compound **2**, the magnetization, under 70000 Oe at 1.8 K, is not saturated reaching $16.8 \mu_B$, that is close to the expected value for all $S_T = 9$ [Mn_4] units in a parallel direction ($17.7 \mu_B$ taking $g = 1.97$) (**Figure III.13**, top left). Two inflection points were observed in M vs H curves: one at low field and the second at higher field being *ca.* 16600 Oe (**Figure III.13**, top). The second inflection point stays almost at the same field with increasing temperatures up to 6 K, suggesting that the observed behavior is not a magnetic transition but a characteristic of one-dimensional system (**Figure III.13**, bottom right). At this characteristic field, H^* , the applied magnetic field overcomes antiferromagnetic zJ interactions along the chain. By equalizing the exchange and Zeeman energies in the frame of the anisotropic Heisenberg model as shown in Eq III.2, the corresponding J/k_B can be estimated at -0.073 K. The obtained intrachain magnetic interaction J agrees well with the value estimated by mean-field approximation.

The inflection point at low field has been followed as a function of the temperature using combined M vs H and χ vs T data and taking the maximum of the dM/dH vs H and χ vs T plots (inset of **Figure III.13** (top left) and **Figure III.13** (bottom left)). Using this approach, the (T, H) magnetic phase diagram has been built for **2** (**Figure III.13**, bottom right). These results demonstrate the presence of a 3D antiferromagnetic order in **2** with $T_N = 4$ K. The topology of this diagram is characteristic of a metamagnetic behavior with only an antiferromagnetic – paramagnetic transition line that is induced by the magnetic anisotropy brought by the [Mn_4] SMM units. In a simple 3D mean-field model that supposes the intrachain magnetic interactions (J) is of the same order of magnitude as the interchain magnetic interactions (J'), the critical field (H_C) is in the following relation with the Néel temperature (T_N) considering [Mn_4] units as Ising spins (de Jongh and Miedema 1974):

$$g\mu_B H_C \cos(\alpha) = T_N \quad \text{Eq III.3}$$

Using the experimental critical field extrapolated at 0 K ($H_C(0) \approx 620$ Oe) and the canting angle ($2\alpha = 34.8^\circ$ from the structural analysis), the expected value of T_N is *ca.* 0.7 K that is much lower than the experimental value. This estimation indeed supports that the compound **1** can be viewed as a canted antiferromagnetic chain with small interchain antiferromagnetic interactions. Therefore, the interchain interactions (J') should be estimated in the frame of quasi-1D Ising model ($J \gg J'$). The corresponding Hamiltonian is given by:

$$H = -2JS_T^2 \sum_{n,p} \sigma_{n+1,p} \sigma_{n,p} - 2J'S_T^2 \sum_{n,p,p'} \sigma_{n,p} \sigma_{n,p,p'} \quad \text{Eq III.4}$$

and the T_N can be expressed as below (Coulon et al. 2009; Scalapino et al. 1975):

$$k_B T_N = 2zJ' \exp(4JS_T^2 \cos(2\alpha) / k_B T_N) \quad \text{Eq III.5}$$

Taking the intrachain interaction J/k_B (-0.073 K) into above relation allowed an estimation of the interchain interaction $zJ'/k_B \approx -0.016$ K.

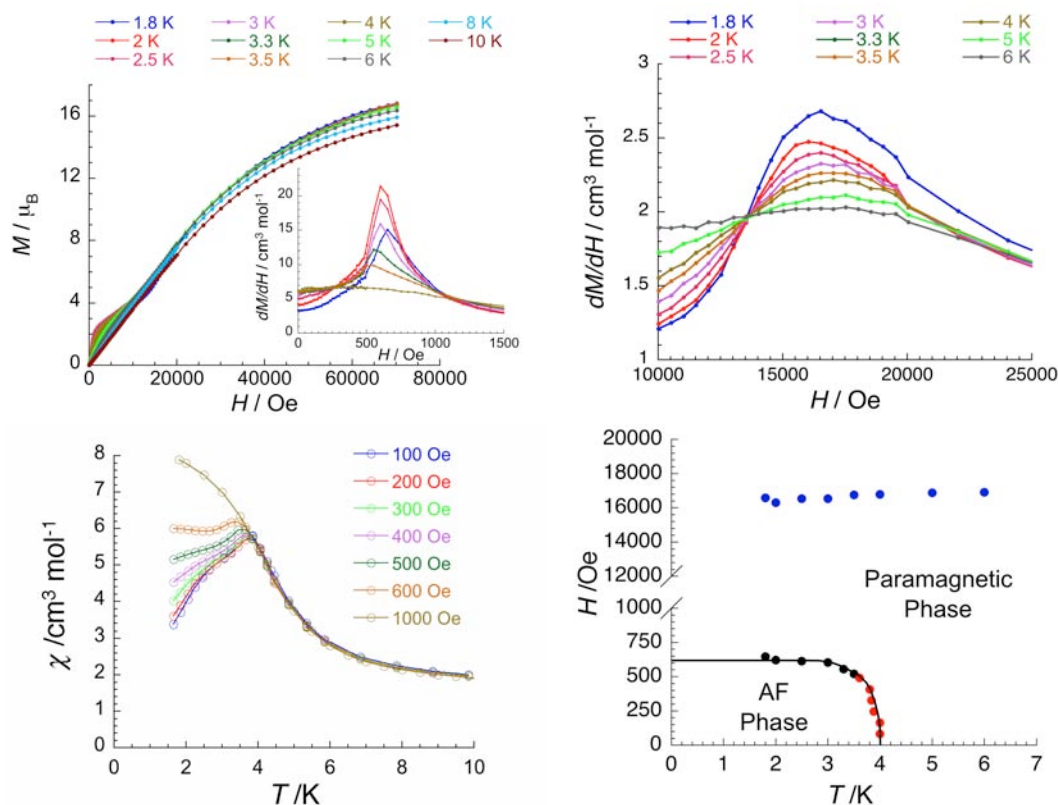


Figure III.13 Top: Field-dependences of the magnetization of **2** between 10 K and 1.8 K. Inset: low-field zoom of dM/dH vs H between 4 K and 1.8 K. (left). High-field zoom of dM/dH vs H between 6 K and 1.8 K (right). Bottom: χ vs T plot between 10 and 1.8 K measured on a polycrystalline sample of **2** at different applied dc magnetic field (left). H vs T magnetic phase diagram for **2**. The black, blue, and red dots are respectively the experimental points deduced from the dM/dH vs H at low and high field, and χ vs T data. The solid black line is a guide for the eye.

III.1.5 Dynamic magnetic properties of **1** and **2**

Since the slow relaxation was not detected for compound **1** by ac susceptibility measurements at zero dc field, a question on the origin of the slow dynamics shown by hysteresis of the magnetization was raised. As shown in **Figure III.12** (inset) and **Figure III.14** (left), the hysteresis loops, measured by μ -SQUID apparatus (Wernsdorfer 2001), are strongly temperature and field sweep rate dependent. As expected for a thermally activated process, the coercive field (H_C) increases with decreasing temperature T and increasing field sweep rate v (dH/dt). Furthermore, it showed an almost logarithmic dependence of H_C on the field sweep rate (inset of **Figure III.14**, right). Thus, we analyzed the set of $H_C(T, v)$ data with a model of thermally activated magnetization reversal that was proposed at the

beginning for a magnetic single-domain particle (Brown 1963; Néel 1949) and has been also applied to characterize the relaxation dynamics of SMM and SCM (Wernsdorfer 2008; Wernsdorfer et al. 2005b; Wernsdorfer et al. 2005a). At a given temperature, the high energy barrier (E) between two states of opposite magnetization can be lowered by applying external dc magnetic field. When the applied field is close enough to field necessary for the nucleation of a domain wall, thermal fluctuations are sufficient to allow the system to overcome the energy barrier, and the magnetization is reversed. Therefore, this process can be studied by measuring the probability that the magnetization has not reversed after a certain time that is given by:

$$P(t) = \exp(-t / \tau) \quad \text{Eq III.6}$$

and τ can be expressed by an Arrhenius law of the form:

$$\tau(T, H) = \tau_0 \exp(E(H) / k_B T) \quad \text{Eq III.7}$$

where E is the energy barrier, and τ_0 is a pre-exponential factor that is supposed to be a constant. It should be noted that the probability defined above assumes that the energy barrier E , and therefore τ , are functions of the applied field. In our experiment, the system goes from its metastable state to the reversal of the magnetization upon the applied field. Thus, E and τ are functions decreasing in time. The probability density can be written by:

$$dP / dt = -P / \tau \quad \text{Eq III.8}$$

and the maximum of the probability, that is likely the coercive field, can be derived from:

$$d^2 P / dt^2 = P / \tau^2 (1 + d\tau / dt) = 0 \quad \text{Eq III.9}$$

This gives $d\tau/dt = -1$, and the application to Eq III.7 leads to:

$$E(H) = k_B T \ln(k_B T / (\tau_0 v dE / dH)) \quad \text{Eq III.10}$$

The Eq III.10 is a self-consistent equation, thus an iterative method⁶ was applied to approach the optimized solution that resulted in a $E(H)$ vs H master curve from the $H_C(T, v)$ set of data (**Figure III.14**, right). The obtained energy barrier (E/k_B) at zero field is 98(5) K. To verify the origin of the observed slow dynamics, the theoretical gap of the relaxation time in a chain of canted anisotropic spins was compared with the experimental value. The energy barrier of the canted antiferromagnetic chain with a canting angle between two different anisotropy axes being 2α is as below (Bernot et al. 2008):

$$E(H) = \Delta_\tau = \Delta_A + \Delta_\xi = \langle |D| + 4n |J| \cos 2\alpha \rangle S_T^2 \quad \text{Eq III.11}$$

with $n = 1$ for the finite-size and $n = 2$ for the infinite-size regime.⁷ Taking into account the intrachain interaction $J/k_B = -0.22$ K obtained from the characteristic field, Δ_τ can be estimated introducing the previously reported value of D/k_B on $[\text{Mn}_4]$ units estimated by resonant quantum tunneling of the magnetization ($0.32 \text{ K} < |D|/k_B < 0.37 \text{ K}$) (Lecren et al. 2008; Lecren et al. 2005a; Lecren et al. 2005c).

⁶ We guess a field-dependent energy $E_0(H) = E_i(H)$, and we calculate the correction in a iterative way by: $E_{i+1}(H) = f(E_i(H))$.

⁷ In the presence of spin canting, however, it was shown that the larger canting the system has, the further from $D/J = 4/3$ the Ising limit is. Indeed, the strictly sharp domain wall is not observed as long as there is a canting. Therefore, the above equation should be taken with a special caution for the systems with a spin canting. This work is a part of the thesis project of V. Pianet (thesis in CRPP, 2011 – 2014). For compounds **1** and **2**, recent calculations have shown that the estimation of Δ_ξ as $4|J|S^2 \cos(2\alpha)$ is very close to the deduced values. Thus, we use this equation to estimate the energy barrier.

It gives the expected range of Δ_τ between 95 and 100 K for $n = 1$, and between 166 and 170 K for $n = 2$. Thus, it proves unambiguously that the observed slow dynamics in **1** is induced by the finite size chains of canted spins. It demonstrates that this 1D dynamics, induced by the presence of SMM units and their interactions along the chain, can be observed by applying a dc field even in the three-dimensional ordered magnetic phase. For the first time, this technique was applied to estimate the energy barrier of a system showing 3D canted antiferromagnetic phase. In addition, the obtained result supports well the estimated value of the intrachain antiferromagnetic interaction. It is also worth mentioning that this is first time to observe chain dynamics in 3D canted antiferromagnetic phase, although it was already seen in 3D antiferromagnetic phase (Coulon et al. 2009; Miyasaka et al. 2010). The foregoing method, however, is not adapted to estimate the exact value of the pre-exponential factor, τ_0 , as the solution of Eq III.10 is obtained by iterative way and varying τ_0 that is in logarithm part does not lead a significant change in final E .

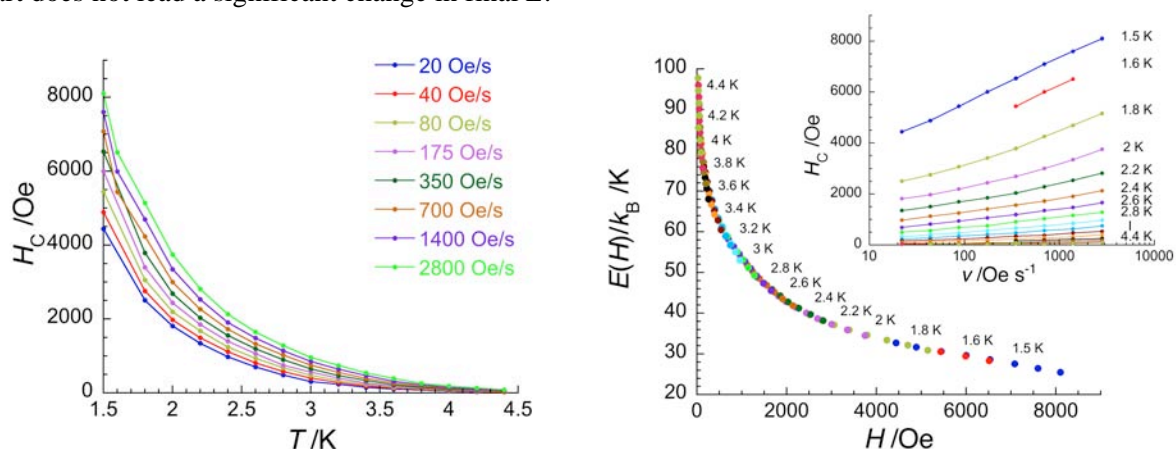


Figure III.14 Temperature dependence of the coercive field for **1** at different field sweep rate (left). Field dependence of the energy barrier of **1**, obtained from Eq III.10 using the set of $H_C(\nu, T)$ data in the inset (right). Inset: The coercive field for **1** as a function of field sweep-rate at temperatures between 1.5 K and 4.4 K.

Considering that the ground state of compound **2** is a 3D ordered antiferromagnetic phase, the compound exhibits surprisingly a slow relaxation of the magnetization as shown in **Figure III.10** (right): it shows clearly (i) a frequency independent peak only in χ' around 4 K, expected at the paramagnetic/antiferromagnetic transition and (ii) below 3 K a strongly frequency dependent relaxation mode in both χ' and χ'' . In order to follow the relaxation time in a clean manner ac susceptibility as a function of the frequency at different temperatures was also measured (**Figure III.15**, left). The associated relaxation time was deduced from the maxima of χ'' vs ν plots at fixed Temperature (with $\tau = 1/(2\pi\nu)$, ν being the ac frequency). The relaxation time is plotted as τ vs $1/T$ on a semi-logarithmic scale in **Figure III.18**. The relaxation time follows thermally activated laws (i.e., Arrhenius behavior, $\tau(T) = \tau_0 \exp(\Delta_\tau/k_B T)$) between 1.8 and 2.6 K with $\Delta_\tau/k_B = 36$ K and $\tau_0 = 3 \times 10^{-11}$ s. As already reported, the application of a dc-field can slow down the observed dynamics in 3D antiferromagnetic ordered phase of SCMs (Coulon et al. 2009). Therefore, ac susceptibility as a function of the frequency at each 100 Oe up to 1500 Oe was also measured to verify the influence of the external magnetic field (**Figure III.16**). Treating the characteristic frequencies, at which the maximum of out-of-phase signal was observed, versus different dc fields gives one minimum placed at *ca.* 500 Oe (**Figure III.17**). It means the dynamics is slowest at this characteristic field (H'). It is interesting to note that H' is very close to H_C (620 Oe), as expected (Coulon et al. 2009). Thus, we have also performed the ac susceptibility measurements at this optimum field, 500 Oe (**Figure III.15**,

right). The compound still revealed a strong frequency dependence of both components of the ac susceptibility. The relaxation times at 500 Oe were also deduced from the χ'' vs ν data below 2.6 K. Linear regression fits of the experimental $\ln(\tau)$ vs $1/T$ data allow an estimation of Δ_r/k_B at 38 K with $\tau_0 = 2 \times 10^{-11}$ s, giving a quantitative estimation of the attempt time of relaxation from the chain bath (Figure III.18).

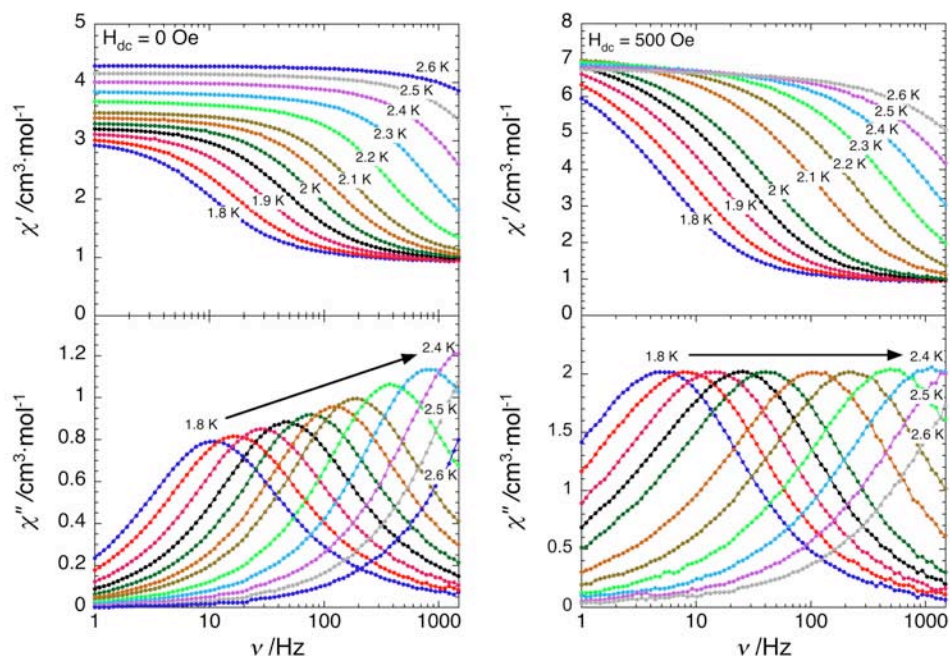


Figure III.15 Frequency dependences of the real (χ' , up) and imaginary (χ'' , down) parts of the ac susceptibility for **2** in zero dc-field (left) and 500 Oe (right) at different temperatures and with a 3 Oe ac field. Solid lines are guides.

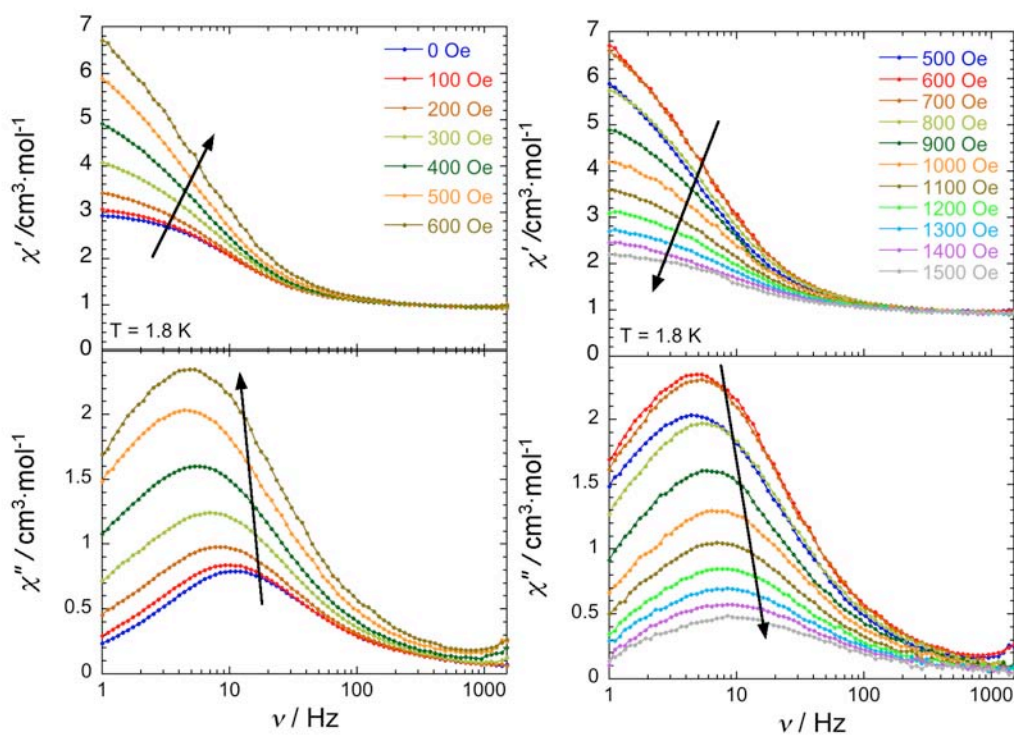


Figure III.16 Frequency dependence of the real (χ' , top) and imaginary (χ'' , bottom) parts of the ac susceptibility for a polycrystalline sample of **2** at 1.8 K in different dc fields. Solid lines are guides for eye.

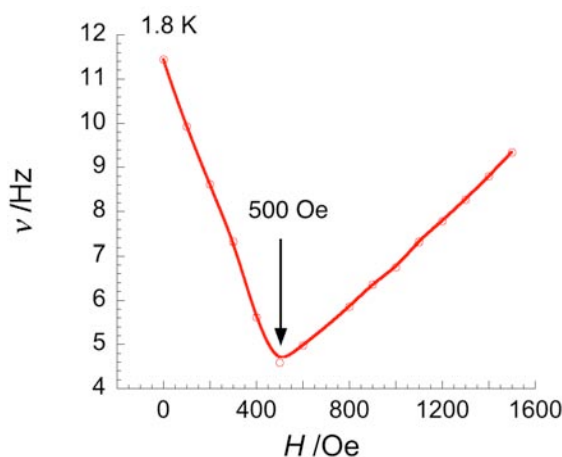


Figure III.17 Field dependence of the characteristic frequency as a function of the applied dc field for **2** at 1.8 K.

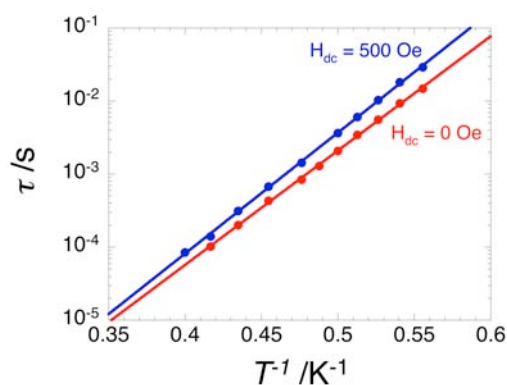


Figure III.18 Magnetization relaxation time (τ) vs T^{-1} plot for **2** in zero dc-field (red) and 500 Oe (blue). Solid lines are the best fits of the experimental data to the Arrhenius laws discussed in the text.

To verify whether the observed slow dynamics of **2** is related with the 1D arrangement like in compound **1**, the theoretical energy barrier of a chain of canted anisotropic spins, described in Eq III.11, was compared with the experimental values. Taking the intrachain interaction deduced from the characteristic field ($J/k_B = -0.073$ K), canting angle ($2\alpha = 34.8^\circ$), and the energy gap of the longer relaxation time ($E/k_B = 38$ K) into Eq III.11, the Δ_A was estimated at 19 K for $n = 1$ and 0 K for $n = 2$. The value of 19 K is in excellent agreement with the Δ_A experimentally found for $[\text{Mn}_4(\text{hmp})_6]^{4+}$ SMM units and related chains (Lecren et al. 2008; Lecren et al. 2005b). Thus, the observed slow dynamics is clearly induced by the 1D organization of interacting SMMs, and thus the finite size chains of canted $S_T = 9$ spins in the ordered antiferromagnetic phase.

III.1.6 Concluding remarks for **1** and **2**

The $[\text{Mn}_4(\text{hmp})_6]^{4+}$ SMMs were assembled with mono- and di-chlorido bridges to lead one dimensional systems, $[\text{Mn}_4(\text{hmp})_6(\text{H}_2\text{O})_2\text{Cl}](\text{ClO}_4)_3 \cdot 1.5\text{CH}_3\text{CN}$ (**1**) and $[\text{Mn}_4(\text{hmp})_6\text{Cl}_2](\text{ClO}_4)_2$ (**2**). The structural analyses reveal that both compounds **1** and **2** consist of the $[\text{Mn}_4]$ units along the chain with two different orientations, resulting in an angle between neighboring Jahn-Teller axes as *ca.* 11.4° and 34.8° , respectively. For compound **2**, the detailed crystallographic analyses and the heat capacity

study showed a single-crystal-to-single-crystal second order phase transition at 219 K. In both compounds **1** and **2**, hydrogen bonds, short contacts, and weak $\pi\cdots\pi$ interactions cause the formation of 3D supramolecular architectures, that strongly influence the magnetic ground state of these systems: a canted antiferromagnetic ground state for **1** below $T_C = 4.6$ K and an antiferromagnetic ground state for **2** below $T_N = 4$ K. The experimental (T , H) magnetic phase diagram of **2** established its metamagnetic behavior with a $H_C \approx 620$ Oe, while H_C was not experimentally observed for compound **1** due to the presence of the M vs H hysteresis. The nature of the inter-[Mn₄] magnetic interactions through the chlorido bridges along the chain have been determined by (i) mean-field approximation of magnetic susceptibility and (ii) characteristic field from the M vs H measurements. The deduced intrachain interactions from both estimations for **2** were coherent, giving $J/k_B = -0.073$ K. Meanwhile, the mean-field approximation for **1** was at the physical limit of the model, resulting in an over-estimation compared to the value ($J/k_B = -0.22$ K) obtained from the characteristic field. On the basis of various dc and ac magnetic measurements, **1** and **2** can be viewed as chains of antiferromagnetically coupled $S_T = 9$ [Mn₄] anisotropic spins in canted arrangements. Indeed, slow dynamics in **1** and **2** were detected respectively by M vs H hysteresis loops and by ac susceptibility, confirming their magnet behavior. This property is induced by the uncompensated magnetic moment due to the presence of the non-parallel anisotropy axes along the antiferromagnetic 1D arrangements of [Mn₄] SMM units. The foregoing results highlight that the approach to organize SMMs in 1D geometry is indeed an efficient way to design molecule-based magnets, even though these chains are not completely isolated in both structural and magnetic point of view.

III.2 1D and 2D assemblies with paramagnetic metal(II) picolines

The organization of [Mn₄] SMMs in networks has been intensively explored using diamagnetic linking units, as explained at the beginning of this chapter. The very first example of coordination assemblies based on SMMs is 3D compound, [Mn₄(hmp)₄(OH)₂Mn(dcn)₆] \cdot 2MeCN \cdot 2THF (dcn⁻ = dicyanamide), in which [Mn₄] SMM unit is indeed connected by [Mn^{II}(dcn)₆]⁴⁺ paramagnetic linkers (Miyasaka et al. 2004). However, this bridging unit is formed *in-situ* during the reaction in the presence of dcn⁻ ligands. In this regard, we wanted to apply a step-by-step building block approach to confirm the synthetic rationalization of incorporating paramagnetic metal complexes. Our first choice was metal(II) picolinate (metal = nickel, manganese, and copper), since the coordinating ability of carboxylate functionalities to [Mn₄] unit was well confirmed through the derivatives of the acetic acid (Lecren et al. 2008).

III.2.1 Synthetic approach

Three metal(II) picolines were synthesized in weak alkaline aqueous media in the presence of metal(II) salts (Ni(ClO₄)₂ \cdot 6H₂O, Mn(CH₃CO₂)₂ \cdot 4H₂O, and CuCl₂ \cdot 2H₂O) and picolinic acid (Hpic), to afford [Ni(pic)₂(H₂O)₂] \cdot 2H₂O, [Mn(pic)₂(H₂O)₂] \cdot 0.3H₂O, and [Cu(pic)₂] \cdot 2H₂O, respectively. Then, self-assembly reactions of Mn(ClO₄)₂ \cdot 6H₂O and Hhmp was performed in acetonitrile with added base to form [Mn₄(hmp)₆]⁴⁺ cations. The pre-formed metal(II) picolinate complexes were added successively to this solution. The layering of diethylether and toluene with the reaction solution

respectively afforded single crystals of 1D compounds $[\text{Mn}_4(\text{hmp})_6(\text{H}_2\text{O})_2][\text{Ni}(\text{pic})_2(\text{H}_2\text{O})_2](\text{ClO}_4)_4 \cdot 3\text{CH}_3\text{CN}$ (**3**) and $[\text{Mn}_4(\text{hmp})_6(\text{H}_2\text{O})_2][\text{Mn}(\text{pic})_2(\text{H}_2\text{O})_2](\text{ClO}_4)_4 \cdot 3\text{CH}_3\text{CN} \cdot 2\text{H}_2\text{O}$ (**4**). Meanwhile, 2D compound $[\text{Mn}_4(\text{hmp})_6\{\text{Cu}(\text{pic})_2(\text{ClO}_4)_2\}_2] \cdot 2\text{CH}_3\text{CN}$ (**5**) was crystallized by the slow evaporation of the reaction solution.

III.2.2 Crystallographic characterizations

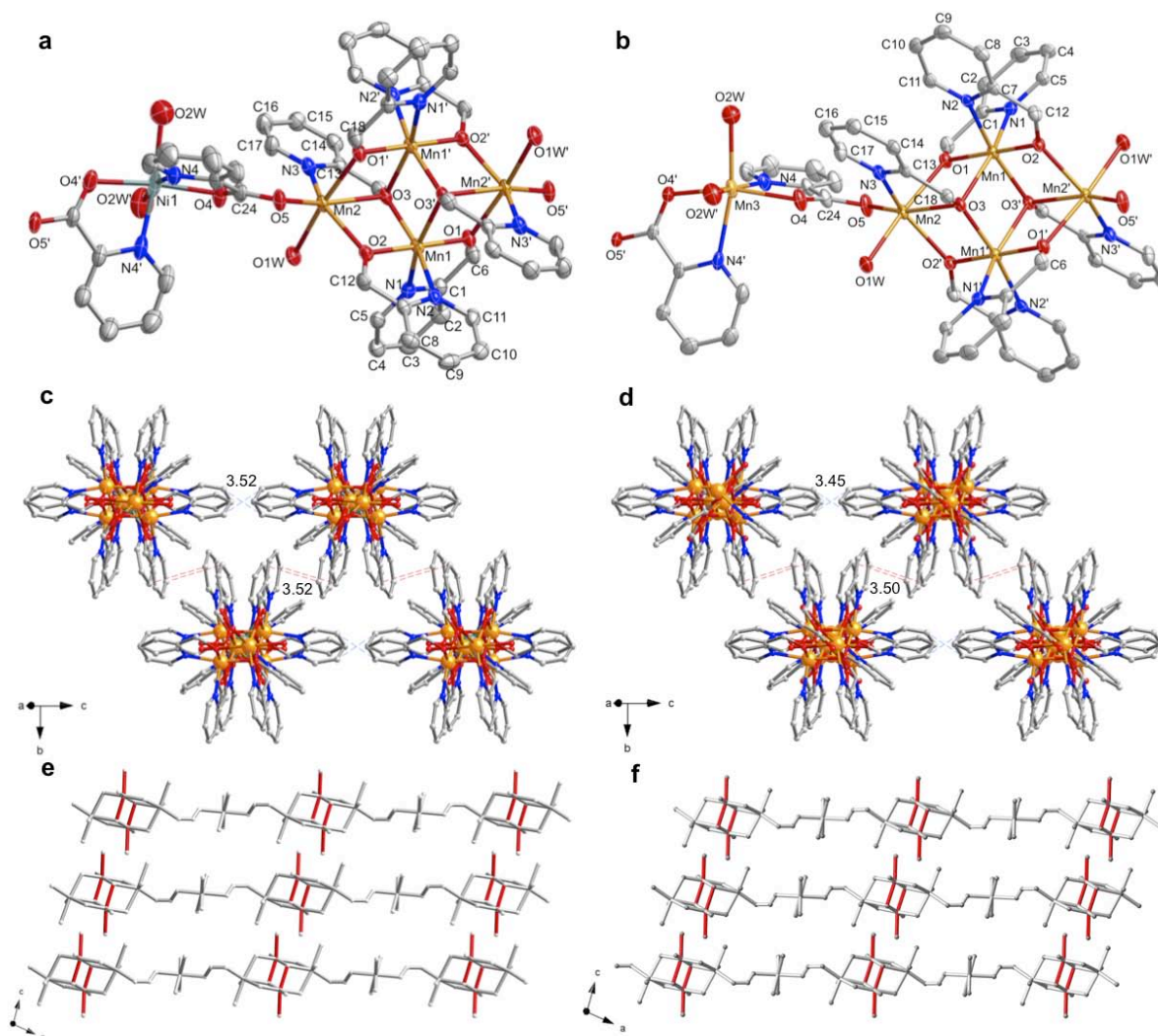


Figure III.19 Top: ORTEP-type view of **3** (a) and **4** (b) with the thermal ellipsoids at 30 %. Middle: Crystal packing of **3** (c) and **4** (d), illustrating $\pi \cdots \pi$ interactions (red dashed line) and short contacts (blue dashed line) between chains (distances in Å); Mn, Ni, C, N, O, and Cl: orange, green, gray, blue, red, and green, respectively. Bottom: Crystal packing for **3** (e) and **4** (f), highlighting JT axes in red. Counter anions, solvent molecules and hydrogen atoms are omitted for clarity.

Structural Description of 3 and 4. Compounds **3** and **4** are quasi-isostructural, crystallizing in the $C2/c$ monoclinic space group. Both compounds contain one centrosymmetrical tetranuclear $[\text{Mn}_4(\text{hmp})_6]^{4+}$ cation coordinated to mononuclear $[\text{Ni}(\text{pic})_2(\text{H}_2\text{O})_2]$ or $[\text{Mn}(\text{pic})_2(\text{H}_2\text{O})_2]$ complexes through the *syn-anti* carboxylato bridge to form a chain (**Figure III.19**). All manganese ions in the tetranuclear unit are hexa-coordinated. Six coordination sites around the internal Mn ion (Mn1) and four sites on the external Mn ion (Mn2) are occupied by oxygen and nitrogen donor atoms from six deprotonated hmp ligands. The coordination sphere on Mn2 is completed by O1W atom from a water

molecule and carboxylate O5 atom of the pic^- ligand coming from the $[\text{Ni}(\text{pic})_2(\text{H}_2\text{O})_2]$ and $[\text{Mn}(\text{pic})_2(\text{H}_2\text{O})]$ building blocks for **3** and **4**, respectively (**Figure III.19a** and **Figure III.19b**). The valence of the Mn ions in the tetranuclear core is confirmed by bond-valence sum calculation (Brown et al. 1985). The external Mn ions are divalent, while the internal Mn ions present a JT distortion indicative of trivalent ions. Indeed, the bond distances in axial position around Mn1 ($\text{N1-Mn1} = 2.144(6)$ and $\text{Mn1-O3}' = 2.150(4)$ Å for **3**; $\text{N1-Mn1} = 2.175(6)$ and $\text{Mn1-O3}' = 2.210(4)$ Å for **4**) are significantly longer than the ones in the equatorial planes (average value = $1.976(4)$ and $1.955(3)$ Å for **3** and **4**). The elongated JT axes ($\text{N1-Mn1-O3}'$) are slightly bent ($161.2(2)$ and $160.5(2)^\circ$ for **3** and **4**) and parallel each other in the tetranuclear core (Table III.6). The alternating $[\text{Mn}_4]$ units along the chain are almost parallel with a separation of JT axes ($\text{Mn1-O3}'$) by a small angle of 4.5 and 3.3° for **3** and **4**.⁸ All chains in the crystal structure are identical possessing their JT axes perpendicular to the crystallographic monoclinic b axis (**Figure III.19** (bottom) and **Figure SIII.1**). The pic^- ligands are coordinated to Ni1 and Mn3 sites of **3** and **4** in *cis* fashion, and two water molecules complete the coordination sphere. The torsion angles through the carboxylate bridge (Mn2-O5-C24-O4) for **3** and **4** respectively are $14.8(7)^\circ$ and $10.3(1)^\circ$, indicating the $\text{Mn2}\cdots\text{Mn3}$ in **4** along the chain is more in plane than the $\text{Mn2}\cdots\text{Ni1}$ in **3**. The detailed structural analyses revealed the short interchain contacts between the adjacent aromatic rings of hmp groups, showing the one of the shortest distances ($\text{C}\cdots\text{C} = 3.52(2)$ and $3.49(4)$ Å for **3** and **4**) in $\pi\cdots\pi$ stacking mode that generate four nearest neighbors around the chain (**Figure III.19c** and **Figure III.19d**). In addition, the short contacts between aromatic rings of the ligand are also observed with the shortest $\text{C}\cdots\text{C}$ distances being $3.51(8)$ and $3.44(7)$ Å for **3** and **4**, respectively. As a consequence, the shortest intermetallic $\text{Mn}\cdots\text{Mn}$ distances are $9.34(1)$ and $9.21(3)$ Å along the b axis, and $9.79(5)$ and $9.68(4)$ Å along the c axis, for **3** and **4**. It is worth noting that the interchain distances are slightly longer for **3** than those for **4**.

Table III.5 Crystallographic data of compounds **3** – **5**, collected at 150 K.

	3	4	5
Empirical formula	$\text{C}_{54}\text{H}_{61}\text{N}_{11}\text{O}_{30}\text{Cl}_4\text{NiMn}_4$	$\text{C}_{54}\text{H}_{59}\text{N}_{11}\text{O}_{32}\text{Cl}_4\text{Mn}_5$	$\text{C}_{64}\text{H}_{58}\text{N}_{12}\text{O}_{30}\text{Cl}_4\text{Cu}_2\text{Mn}_4$
Formula weight, g mol^{-1}	1764.41	1790.62	1963.86
Wavelength, Å	0.71073	0.71073	0.71073
Space group	$C2/c$	$C2/c$	$P-1$
a , Å	32.050(6)	32.139(6)	11.968(2)
b , Å	17.280(4)	16.994(3)	12.369(3)
c , Å	14.050(3)	14.059(3)	14.349(3)
α , °	90	90	97.20(3)
β , °	100.15(3)	99.06(3)	112.67(3)
γ , °	90	90	101.36(3)
V , Å ³	7659(3)	7583(3)	1873.5(7)
Z	4	4	1
ρ_{calcd} , g cm^{-3}	1.530	1.607	1.741
μ , mm^{-1}	1.108	1.043	1.448
$F(000)$	3592	3736	992
$^a R_1$ ($I > 2\sigma(I)$)	0.0872	0.0821	0.0479
$^b wR_2$ (all)	0.2561	0.2038	0.1388
GoF	1.042	1.045	0.941

^a $R_1 = \Sigma||F_o| - |F_c||/\Sigma|F_o|$, and ^b $wR_2 = [\Sigma w(F_o^2 - F_c^2)^2/\Sigma w(F_o^2)^2]^{1/2}$.

⁸ This canting angle is extremely small, and therefore, we will neglect for the characterization of the magnetic properties in the following sections.

Table III.6 Selected interatomic distances (Å) and angles (°) for **3** and **4** at 150 K.

3		4	
Mn1-N1	2.143(5)	Mn1-N1	2.175(5)
Mn1-O3'	2.151(4)	Mn1-O3	2.210(4)
Mn1-N2	2.110(5)	Mn1-N2	2.070(5)
Mn1-O1	1.867(4)	Mn1-O1	1.872(4)
Mn1-O2	1.878(4)	Mn1-O2	1.879(4)
Mn1-O3	2.053(4)	Mn1-O3'	1.999(4)
Mn2-N3	2.239(5)	Mn2-N3	2.230(5)
Mn2-O1'	2.201(4)	Mn2-O1	2.210(4)
Mn2-O2	2.177(4)	Mn2-O2'	2.173(4)
Mn2-O3	2.270(4)	Mn2-O3	2.282(4)
Mn2-O5	2.088(5)	Mn2-O5	2.083(5)
Mn2-O1W	2.208(5)	Mn2-O1W	2.202(4)
Ni1-N4	2.051(8)	Mn3-N4	2.257(7)
Ni1-O4	2.074(5)	Mn3-O4	2.153(5)
Ni1-O2W	2.250(9)	Mn3-O2W	2.27(2)
O4-C24	1.253(10)	O4-C24	1.257(9)
O5-C24	1.256(8)	O5-C24	1.262(8)
N1-Mn1-O3'	161.21(17)	N1-Mn1-O3	160.5(2)
Mn1-O3-Mn1'	98.88(2)	Mn1-O3-Mn1'	98.5(2)
Mn1-Mn1'	3.194(1)	Mn1-Mn1'	3.191(2)
Mn1-O1-Mn2'	108.6(2)	Mn1-O1-Mn2	109.4(2)
Mn1-O3-Mn2	97.9(2)	Mn1-O3-Mn2	95.9(1)
Mn1-O2-Mn2	106.9(2)	Mn1-O2-Mn2'	106.7(2)
Mn2-O5-C24-O4	14.6(1)	Mn2-O5-C24-O4	10.3(1)
Ni1-O4-C24-O5	175.6(6)	Mn3-O4-C24-O5	178.1(6)
Mn2-Ni1	5.339(1)	Mn2-Mn3	5.435(2)

Symmetry transformations used to generate equivalent atoms (A): A', -x+1/2, -y+1/2, -z+1 for **3** and -x+1/2, -y+1/2, -z for **4**.

Structural Description of 5. Compound **5** crystallized in the *P*-1 triclinic space group. The final 2D structure based on the $[\text{Mn}_4(\text{hmp})_6]^{4+}$ core and $[\text{Cu}(\text{pic})_2(\text{ClO}_4)_2]^{2-}$ bridging units is illustrated in **Figure III.20**. The centro-symmetrical $[\text{Mn}_4(\text{hmp})_6]^{4+}$ core composed of four hexa-coordinated Mn ions arranged in double-cuboidal fashion like in compounds **1** – **4**. The coordination sphere of the Mn2 sites is completed by carboxylate O2 and O3 atoms of two pic⁻ ligands coming from the $[\text{Cu}(\text{pic})_2]$ building blocks. This is the main difference with 1D compounds **3** and **4** in which Mn2 is coordinated by only one carboxylate O atom. The oxidation states of the two Mn ion sites, Mn1 and Mn2 ions in the $[\text{Mn}_4]$ moiety, can be easily assigned as trivalent and divalent respectively based on charge balance consideration, bond valence sum calculation (Brown et al. 1985), and the presence of JT elongation axis (N3-Mn1-O7') on Mn1. As expected, bond distances around the Mn1 are significantly longer in the axial position (N3-Mn1 = 2.220(4) Å and O7'-Mn1 = 2.261(3) Å) than in the equatorial plane (average value of 1.956 Å), revealing a JT distortion (Table III.7). The JT axes on Mn1 and Mn1' are parallel to each other and individually slightly bent N3-Mn1-O7' = 156.57(12)°. Both Cu1 and Cu2 sites, adopt the “4+2” axially distorted geometry, characteristic of the d⁹ JT distortion. Their equatorial and axial positions are occupied by N- or O-donors from chelating pic⁻ ligands and oxygen atoms from ClO₄⁻ anions, respectively. Careful structural analysis reveals that all $[\text{Mn}_4]$ cores in the layer are arranged in the same orientation. Additionally, adjacent layers are stacked together *via* the $\pi\cdots\pi$

packing interactions between the adjacent aromatic rings of hmp^- groups, and the average distance of adjacent aromatic planes is about 3.46 Å (**Figure III.20**).

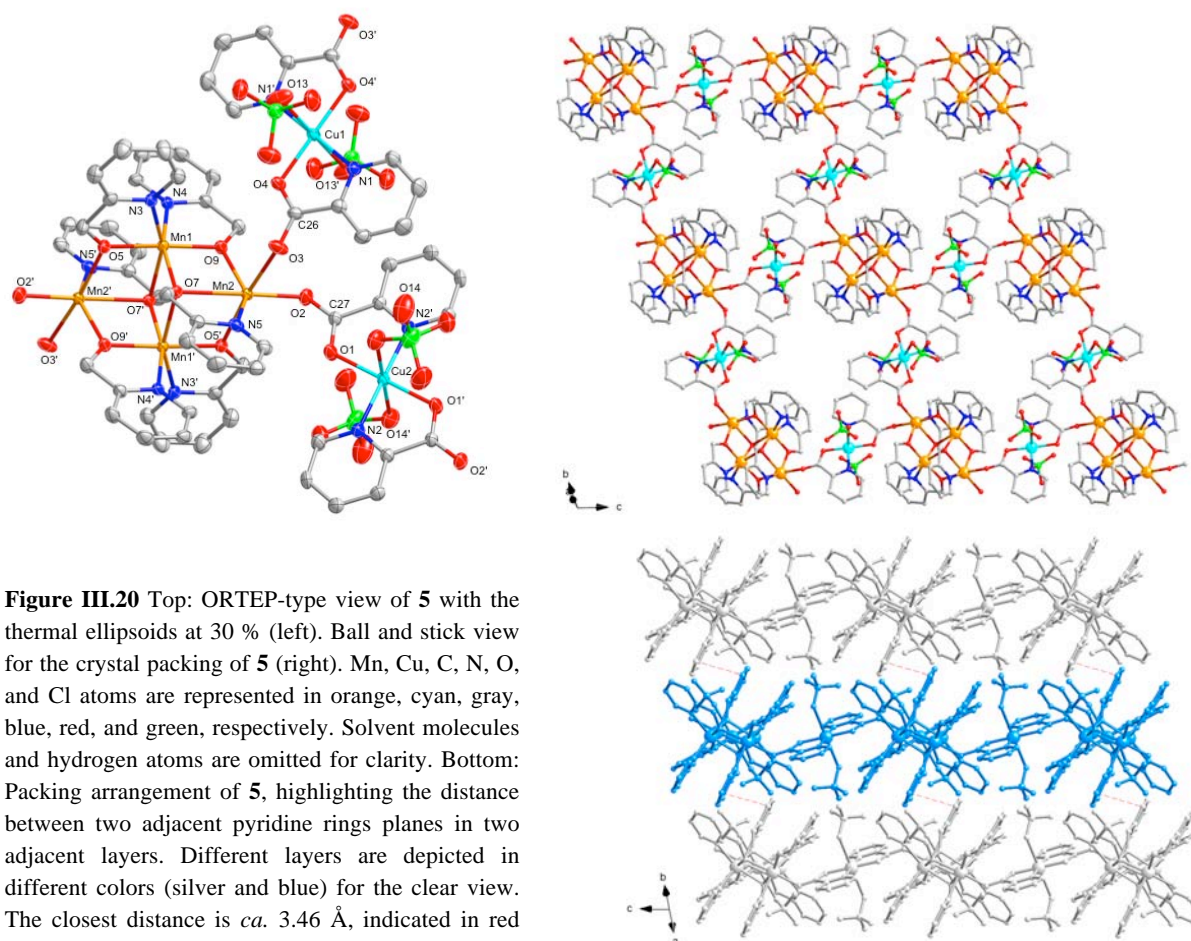


Table III.7 Selected interatomic distances (Å) and angles (°) for **5** at 150 K.

Mn1-O7'	2.261(3)	Mn2-O2	2.120(3)
Mn1-N3	2.220(4)	Mn2-O9	2.121(3)
Mn1-N4	2.073(4)	Mn2-O5'	2.167(3)
Mn1-O5	1.883(3)	Mn2-O3	2.179(3)
Mn1-O9	1.880(3)	Mn2-N5	2.200(4)
Mn1-O7	1.987(3)	Mn2-O7	2.288(3)
Cu1-O4	1.942(3)	Cu2-O1	1.960(3)
Cu1-N1	1.971(4)	Cu2-N2	1.985(4)
Cu1-O13	2.526(4)	Cu2-O14	2.630(4)
N3-Mn1-O7'	156.5(1)	Mn1-O7-Mn1'	98.8(1)
Mn1-O5-Mn2'	111.2(1)	Mn1-O9-Mn2	107.9(1)
Mn1-Mn1'	3.191(1)		

Symmetry transformations (A') used to generate equivalent atoms (A): $-x+1, -y+1, -z$.

III.2.3 Magnetic properties of **3**

The temperature dependence of the χT product was measured for compound **3** between 300 and 1.8 K (**Figure III.21**, left). The room temperature χT product is $18.1 \text{ cm}^3 \text{K mol}^{-1}$ that is somewhat bigger than the expected Curie constant for uncoupled two Mn^{II} ions ($S = 5/2$), two Mn^{III} ions ($S = 2$), and one Ni^{II} ion ($S = 1$) ($C = 15.75 \text{ cm}^3 \text{K mol}^{-1}$ with $g = 2$). The continuous increase is observed by decreasing temperature, showing the maximum $46.7 \text{ cm}^3 \text{K mol}^{-1}$ at 4.4 K. At lower temperatures, the χT product decreases to $38.7 \text{ cm}^3 \text{K mol}^{-1}$ at 1.8 K. The high-temperature thermal dependent increase is clearly due to the presence of the intra-complex ferromagnetic interactions between Mn ions inside $[\text{Mn}_4(\text{hmp})_6]^{4+}$ core, explaining the significantly higher χT product at room temperature than expected (vide supra). Therefore, the data above 15 K was simulated using the Heisenberg-Van Vleck model (Eq III.1), with the contribution of $[\text{Ni}(\text{pic})_2(\text{H}_2\text{O})_2]$ linker treated as the simple addition of the Curie constant for Ni^{II} . A reasonable fit was achieved with final optimized parameters being $g_{\text{av}} = 2.04(1)$, $J_{\text{bb}}/k_{\text{B}} = 6.39(10)$ K, and $J_{\text{wb}}/k_{\text{B}} = 1.45(4)$ K, indicating the ferromagnetic coupling between Mn ions inside $[\text{Mn}_4]$ core to give an $S_{\text{T}} = 9$ ground state. The low-temperature drop of the χT product is most probably due to the magnetic anisotropy of the high-spin $[\text{Mn}_4]$ cation and possible inter- and intra-chain interactions. Given the fact that the fitting result almost perfectly compare with the experimental data down to 10 K with a little deviation between 10 and 4 K (**Figure III.21**), the intrachain interactions between $[\text{Mn}_4]$ and $[\text{Ni}(\text{pic})_2(\text{H}_2\text{O})_2]$ through *syn-anti* carboxylate bridges seem to be very weak. Indeed, it agrees with the fact that no significant 1D correlation is observed in $\ln(\chi T)$ vs T^{-1} plot (**Figure III.22**, left). The field dependence of the magnetization was measured on polycrystalline sample of **3**, between 10 and 1.8 K up to 70000 Oe (**Figure III.22**, right). The magnetization value at 1.8 K under 70000 Oe is $19.3 \mu_{\text{B}}$ that is still increasing to approach the expected magnetic moment of $20 \mu_{\text{B}}$ for all aligned spins in a same direction. In addition, M vs H data show no S-shape curve down to 1.8 K that would be characteristic for antiferromagnetic interactions. Nevertheless, a broad anomaly at 0.4 – 0.7 K was observed in heat capacity measurement down to 0.2 K (**Figure III.23**), suggesting a frozen long-range order due to the slow relaxation of the anisotropic $[\text{Mn}_4]$ units, as observed previously in a related 2D network (Miyasaka et al. 2006).

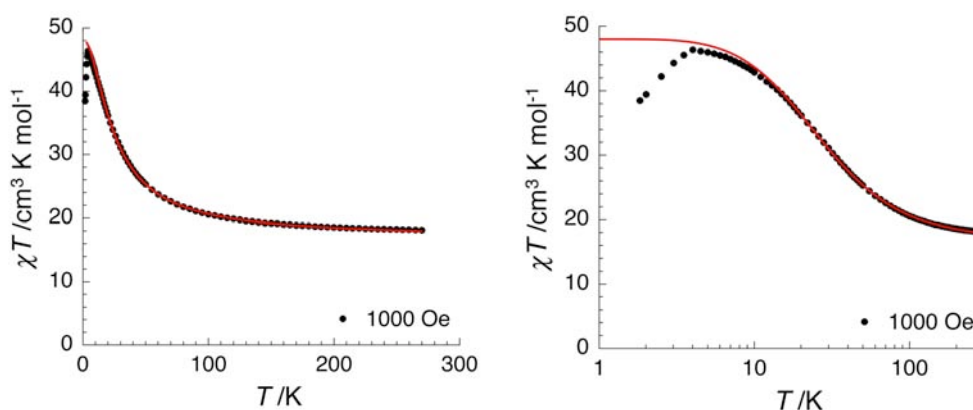


Figure III.21 Temperature dependence of the χT product of **3** at 1000 Oe (black circles), compared with the fitting result based on the Heisenberg model described in the text (red line), in linear (left) and in semi-logarithmic scale (right).

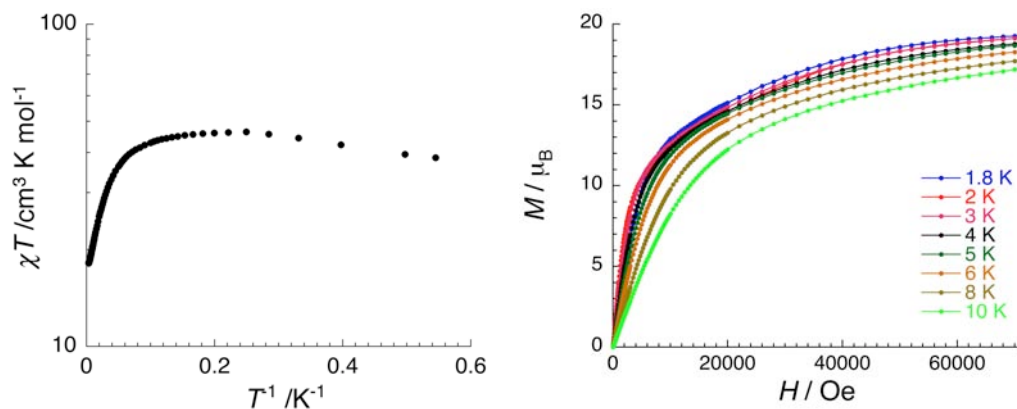


Figure III.22 $\ln(\chi T)$ vs T^{-1} plot of **3** (left) and field dependence of the magnetizations between 10 and 1.8 K (right).

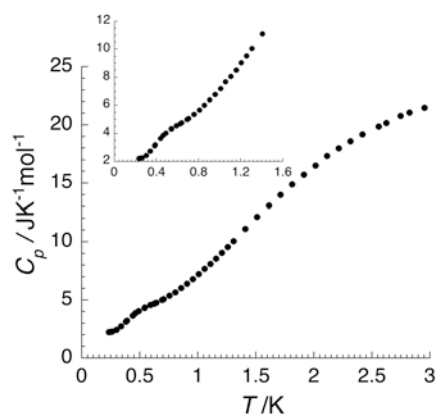


Figure III.23 Temperature dependence of the heat capacity for **3** at zero dc field, with the zoom in the inset.

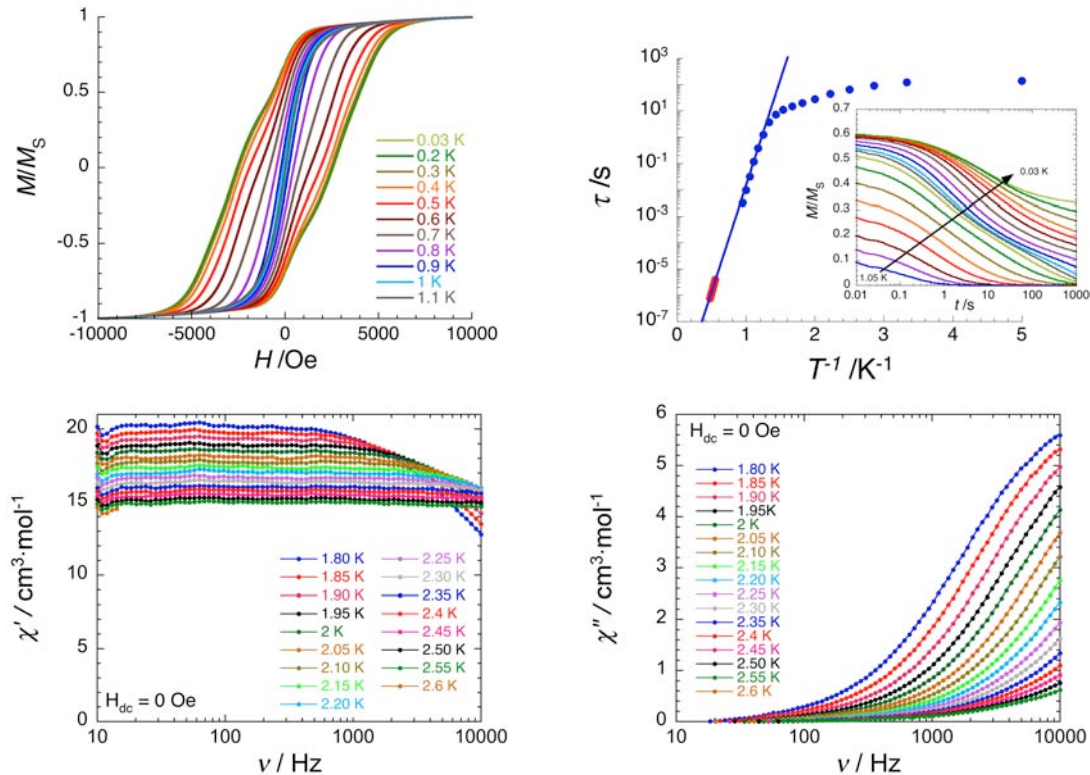


Figure III.24 Top: M/M_S vs H curves of **3** on a single crystal with a sweep-field rate of 700 Oe/s (left). τ vs T^{-1} plot with red and blue dots from ac and M/M_S vs t measurements, respectively; The blue line represents the best fit to Arrhenius law above 0.75 K; Inset: M/M_S vs t plots (right). Bottom: χ' vs ν (left) and χ'' vs ν (right) at different temperatures ($H_{dc} = 0$ Oe).

In order to probe possible slow relaxation of the magnetization, M vs H measurement below 1.8 K with μ -SQUID apparatus were performed (Wernsdorfer 2001). The hysteresis of the magnetization was observed under the dc field applied along the easy direction. The coercive field varies strongly with temperature (**Figure III.24**, top left), showing slow relaxation of the magnetization. The relaxation time, τ , was extracted by scaling method (Labarta et al. 1993) from the time dependence of the magnetization data, as shown in **Figure III.24** (top right). Above 0.7 K, the relaxation time is thermally activated with an energy gap of $\Delta_r/k_B = 18.6$ K and $\tau_0 = 9 \times 10^{11}$ s. This is also in agreement with the ac measurement that displays temperature and frequency dependences of the in-phase and out-of-phase components of the susceptibility (**Figure III.24** (bottom) and **Figure SIII.2**). The out-of-phase susceptibility signal increases without giving a maximum at 1.8 K up to 10000 Hz. Nevertheless, we could scale into one curve to extract at least the energy gap that corresponds to the one obtained from the M/M_S vs t data ($\Delta_r/k_B = 18.6$ K). Since τ_0 could not be deduced by this method, red points in **Figure III.24** (top right) were normalized in τ to fit to the blue line of the **Figure III.24** (top right). The obtained gap value compares well with the effective energy barriers for isolated $[\text{Mn}_4]$ SMM units (typically between 11 – 27 K) (Roubeau et al. 2008). Considering that the intrachain magnetic interactions should be very small as discussed above, the energy gap is almost decided only by the anisotropic gap of the SMM units without the significant contribution of the 1D correlation. Below 0.7 K, the relaxation time does not follow anymore an Arrhenius law and saturates slowly when ground state quantum tunneling of the magnetization (QTM) becomes the fastest pathway of relaxation in SMMs. The foregoing dynamic behavior could be also confirmed by analyzing the set of $H_C(T, \nu)$ data (**Figure III.25**, left) based on a model of thermally activated magnetization reversal (Wernsdorfer 2008), as described in the section III.1.4. As shown in **Figure III.25** (right), the deduced energy barrier ($E/k_B = \Delta_r/k_B$) at zero field is 18.2 K that is in accord with the one deduced from the relaxation of the magnetization and the ac measurement. Additionally, the low temperature deviation below 0.7 K from the master curve indeed indicates the presence of quantum tunneling. It is worth noting that ac measurement was also performed under the external dc field up to 3000 Oe, but the maximum of the out-of-phase component at 1.8 K was not shifted to lower frequencies below 10000 Hz for further studies (**Figure SIII.3**).

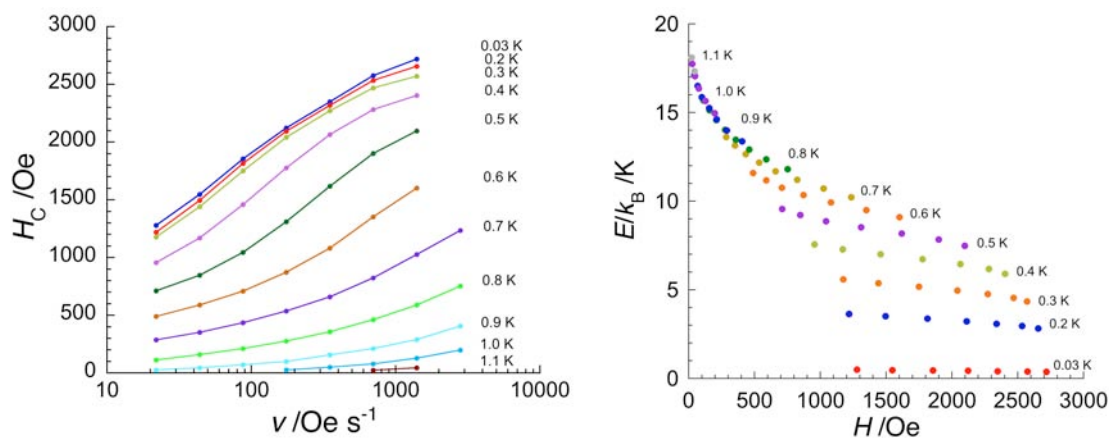


Figure III.25 The coercive field for **3** as a function of field sweep-rate at temperatures between 0.2 K and 1.1 K (left). Field dependence of the energy barrier of **3**, obtained from Eq. 5 using the set of $H_C(\nu, T)$ data (right).

III.2.4 Magnetic properties of **4**

The temperature dependence of the χT product was measured for compound **4** between 300 and 1.8 K (**Figure III.26a**). The room temperature χT product is $20.7 \text{ cm}^3\text{Kmol}^{-1}$ that is in agreement with the expected Curie constant for uncoupled three Mn^{II} ions ($S = 5/2$) and two Mn^{III} ions ($S = 2$) ($C = 19.1$ with $g = 2$). The gradual and abrupt increases of the χT product are successively observed to reach $37.0 \text{ cm}^3\text{Kmol}^{-1}$ at 9 K and then a maximum of $55.2 \text{ cm}^3\text{Kmol}^{-1}$ at 2.4 K. At lower temperatures, the χT product decreases to $49.7 \text{ cm}^3\text{Kmol}^{-1}$ at 1.8 K. The high-temperature thermal dependent increase is clearly due to the presence of the ferromagnetic interactions between Mn ions inside $[\text{Mn}_4]$ core. Then the low-temperature behavior including the drop of the χT product should be linked to the magnetic anisotropy of the high-spin $[\text{Mn}_4]$ cation, magnetic interactions along the chain between $[\text{Mn}_4]$ unit and Mn^{II} ions, and possible interchain interactions. Therefore, the data above 20 K were simulated using the Heisenberg-Van Vleck model already employed for many systems based on $[\text{Mn}_4]$ (Eq III.1). In addition, the Mn^{II} ions from the $[\text{Mn}(\text{pic})_2(\text{H}_2\text{O})_2]$ linker were treated as a simple Curie contribution. A reasonable fit was achieved with final optimized parameters being $g_{\text{av}} = 2.01(2)$, $J_{\text{bb}}/k_{\text{B}} = 9.61(9)$ K, and $J_{\text{wb}}/k_{\text{B}} = 0.92(5)$ K that correspond well those reported in literature. Indeed, the fitting results clearly show the ferromagnetic coupling between Mn ions to give an $S_{\text{T}} = 9$ ground state. As shown in **Figure III.26b**, the experimental data below 20 K are lower than the calculated result for the uncoupled Mn^{II} ion and $[\text{Mn}_4]$ SMM unit (red line), suggesting the presence of the antiferromagnetic interaction between $[\text{Mn}_4]$ units and Mn^{II} ions through *syn-anti* carboxylate bridges. In addition, the 1D correlation seems to play a significant role below 3.4 K as indicated by the exceeded value of the experimental χT product from the fitting result (**Figure III.26b**). Based on the 1D Ising-like or anisotropic Heisenberg model, the correlation length, ξ , of a chain and therefore the χT product increase exponentially with lowering temperature (section I.2.1 in Chapter I): $\chi T = C_{\text{eff}} \exp(\Delta_{\xi}/k_{\text{B}}T)$ (C_{eff} : effective Curie constant). Indeed, as shown in the inset of **Figure III.26a**, the $\ln(\chi'T)$ vs $1/T$ plot is linear in a small temperature regime between 4.5 and 2.8 K, implying the magnetic 1D behavior. With applying the above relation, the slope of the $\ln(\chi'T)$ vs $1/T$ plot gives an evaluation of Δ_{ξ} at *ca.* 2.9 K.

In order to verify the low temperature χT drop and to probe the nature of the magnetic ground state of **4**, we performed the field dependences of the magnetization between 1.8 and 10 K (**Figure III.26c**). The magnetization value (*ca.* $22.7 \mu_{\text{B}}$) at 1.8 K with $H = 70000$ Oe is not yet saturated and increases close to the expected magnetic moment of $23 \mu_{\text{B}}$ for all aligned spins (three Mn^{II} ($S = 5/2$) and two Mn^{III} ($S = 2$) ions) in a same direction.

The M vs H plots display two “S shape” variations, one at low field below 2.5 K and the other one at high field below 4 K. The magnetic (T , H) phase diagram shown in **Figure III.26f** was built based on the maximum of the dM/dH vs H data at low field (**Figure III.26d**). The topology of this phase diagram indicates the presence of a 3D antiferromagnetic order state that is stabilized below $T_{\text{C}} = 2.2$ K in zero-dc field. It was also confirmed by heat capacity measurement showing a typical λ -type peak at *ca.* 2.2 K (**Figure III.27**). Upon applying the external dc field, a metamagnetic behavior is observed giving an estimation of the critical field (H_{C}^0) at *ca.* 280 Oe by extrapolating at 0 K. From this field, considering the dominating interchain interactions only between $[\text{Mn}_4]$ SMM units based on the crystal packing, the average interchain interaction, zJ'/k_{B} , can be deduced at -1.5 mK using the following well-known relation: $2z|J'|S_{\text{T}}^2 = g\mu_{\text{B}}H_{\text{C}}^0(S_{\text{T}}-s)$ with s being a spin of Mn^{II} ion.

Meanwhile, the high field inflection point was showing the maximum of dM/dH at *ca.* 29000 Oe that is independent to temperature and observable up to 3 K (**Figure III.26e** and **Figure SIII.4**). In addition, we have verified that H^* is also independent on the orientation of the sample, meaning that the polycrystalline sample and single-crystal will not show a difference at the position of the maximum.⁹ The Zeeman energy corresponds to this characteristic field, H^* , compensates the antiferromagnetic exchange energy between $[Mn_4]$ and Mn^{II} ions along the chain, resulting in the aforementioned S-shape behavior on M vs H curves. Therefore, the intrachain interaction, J/k_B , of -0.108 K can be estimated by equalizing above two energies: $4|J|Ss = g\mu_B S H^*$.

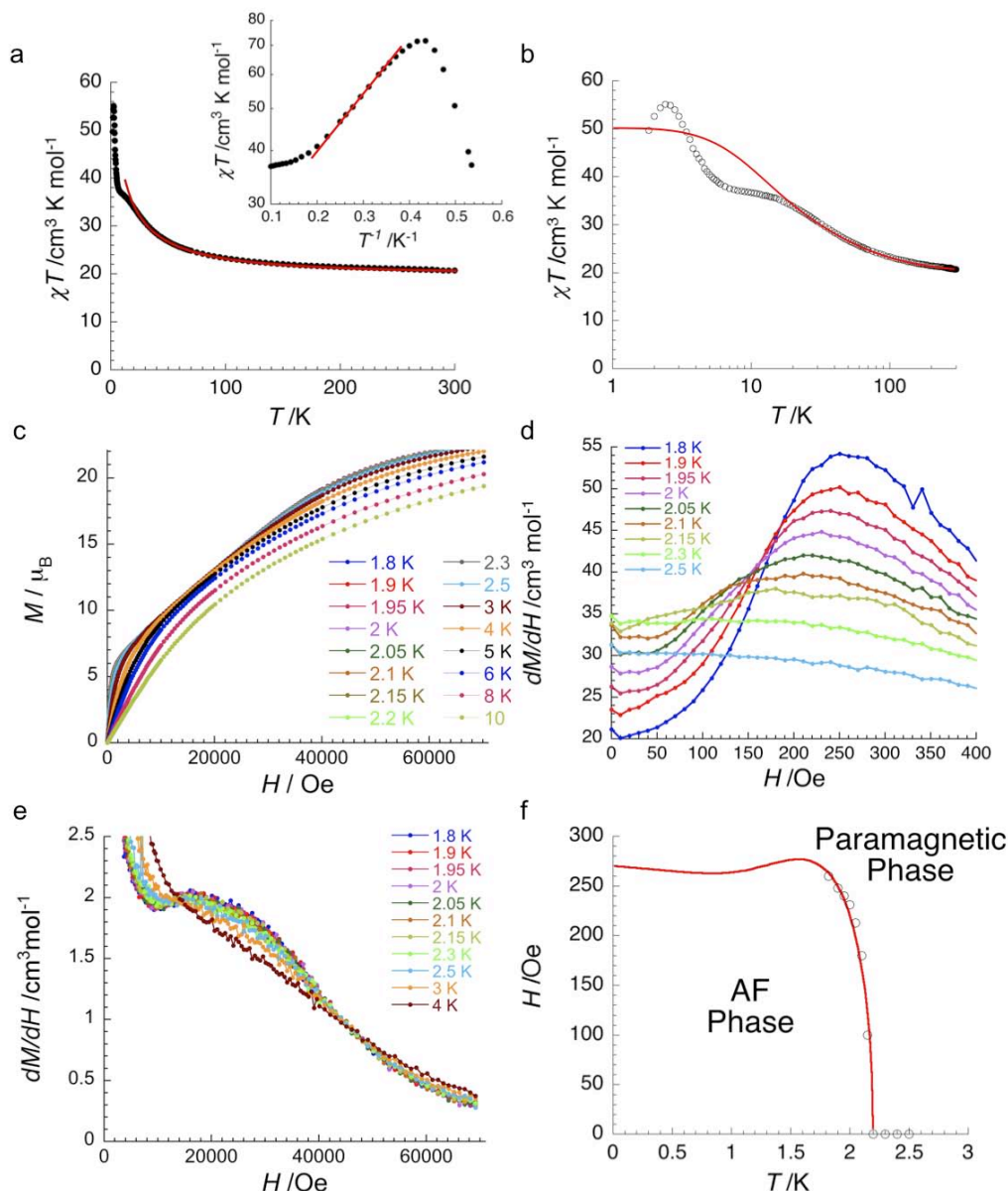


Figure III.26 Temperature dependence of the χT product of **4** at 1000 Oe (black circles), compared with the fit described in the text (red line); Inset: $\ln(\chi T)$ vs T^{-1} plot (a). Semi-log plot of χT vs T (b). M vs H curves between 10 and 1.8 K (c). dM/dH vs H plots at low field (d) and at high field (e). Phase diagram built from the dM/dH vs H plot (empty circles) and the fit described in the text (red line) (f).

⁹ See supporting information III.4.2, « simple description of chain at 0 K ».

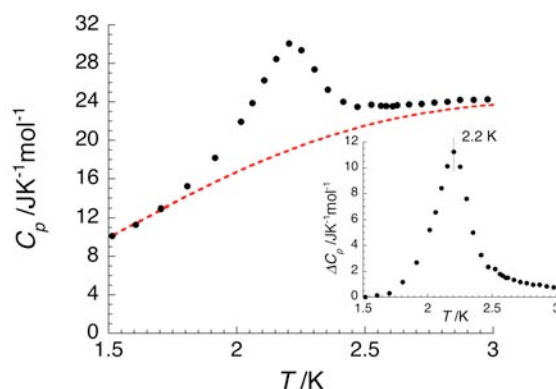
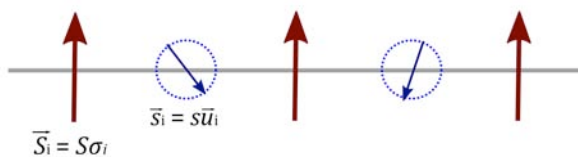


Figure III.27 Temperature dependence of the heat capacity C_p between 1.5 K and 3 K for **4** (f). The red dashed line is the empirical baseline used to determine the critical part of C_p that is shown in the inset.

Based on the Ising-like or anisotropic Heisenberg model, the theoretical correlation energy, Δ_ξ , are given by the following relationship: $\Delta_\xi = 4JSs$. Considering the intrachain interaction obtained from the characteristic field ($J/k_B = -0.108$ K), the calculated Δ_ξ/k_B is 9.7 K that is ~ 3.3 times bigger than the one deduced from the low-temperature slope of the $\ln(\chi'T)$ vs $1/T$ plot ($(\Delta_\xi/k_B = 2.9$ K). It indicates that the compound **4** does not fit into the pure Ising model. The explanation might be found in the presence of Mn(II) ions that is isotropic spin in the chain. Therefore, let us consider our system as a 1D object formed by alternating Ising (S) and isotropic (s) spins described by the following Hamiltonian:



$$H = -2JSs \sum_{-\infty}^{+\infty} (\sigma_i + \sigma_{i+1}) \vec{u}_{zi} - g\mu_B s H \sum_{-\infty}^{+\infty} \sigma_i - g\mu_B s H \sum_{-\infty}^{+\infty} \vec{u}_{zi} \quad \text{Eq III.12}$$

where vector \vec{u}_i is a unit vector and $\sigma_i = \pm 1$. J is the sum of the interactions with the nearest neighbors and the field is applied parallel to the z axis. The method of transfer matrix allows us to solve the above Hamiltonian finally to obtain an expression of susceptibility at the low field approximation as below ($K = 2JSs/k_B T$, $C_{1/2}$ = Curie constant for $S = 1/2$):¹⁰

$$\frac{\chi T}{C_{1/2}} = \frac{A(K)}{1 + C(K)} (gs)^2 - 2B(K) g^2 s S + C(K) (gS)^2 \quad \text{Eq III.13}$$

where

$$A(K) = \left[\frac{4K^2 \sinh 2K - 4K \cosh 2K + 2 \sinh 2K}{8K^3} + \left(\frac{2K \cosh 2K - \sinh 2K}{4K} \right)^2 + \frac{1}{3} \right]$$

$$B(K) = \frac{2K \cosh 2K - \sinh 2K}{4K^2}$$

¹⁰ See supporting information III.4.2, « Low field approximation ».

$$C(K) = \frac{\sinh 2K}{2K}$$

As shown in Eq III.13, the χT product in this model is not simply exponential depending on the temperature variation. It makes a difference with the 1D Ising-like or anisotropic Heisenberg model. Supposing the intrachain interaction (J/k_B) as -0.108 K, large deviation from exponential dependence is indeed observed in the thermal behavior of the χT product at high temperature regime and this deviation is negligible only below 2 K (**Figure III.28**, left). Considering the presence of the 3D antiferromagnetic order at 2.2 K for compound **4** that induces marked decrease of the χT product at zero field, it implies that the Δ_ξ estimated from the slope of the $\ln(\chi T)$ vs $1/T$ plot between 4.5 and 2.8 K is undoubtedly under-estimated.

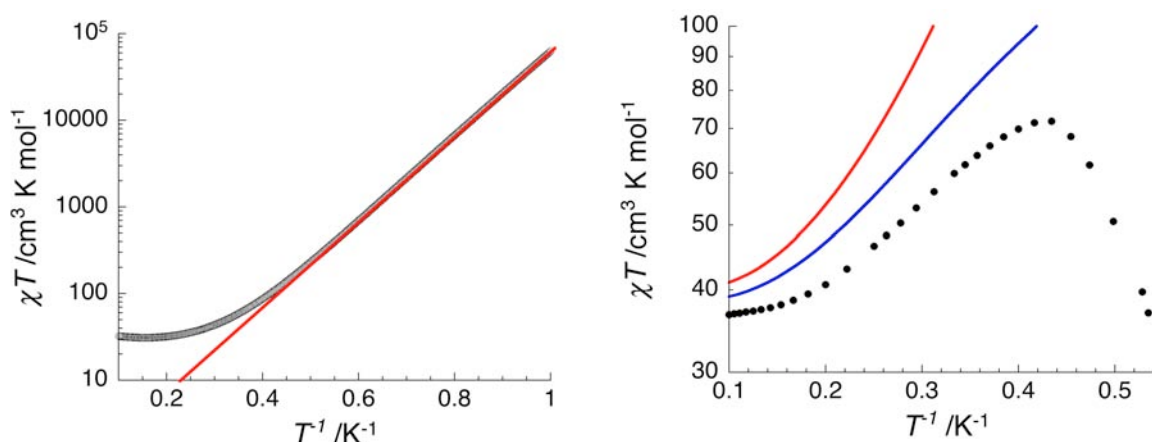


Figure III.28 Black empty circles show calculated χT product from Ising-iso model (Eq III.13 with $J/k_B = -0.108$ K, $S = 9$, and $s = 5/2$) (left). The red solid line indicates an exponential dependence (left). Experimental χT product (black full circles) compared with 1D Ising-iso model (Eq III.13, red line) and Quasi 1D model (Eq SIII.41, blue line) with $J/k_B = -0.108$ K and $zJ'/k_B = -1.45$ mK.

However, fitting of the low temperature χT product with Eq III.13 was not achieved, due to the possible overlap of two regimes that prohibits the observation of 1D behavior: high temperature regime for the excited states of $[\text{Mn}_4]$ units and low temperature one for quasi-1D behavior. As shown in **Figure III.28** (right), the simulated χT product (red line) with $J/k_B = -0.108$ K, $S = 9$, and $s = 5/2$ (red line) is compared with the experimental one (black circles), showing a large deviation. Nevertheless, we could extend the obtained Ising-iso 1D model to the quasi-1D model. A simple two-sublattice model is considered with treating the interchain couplings in the mean-field approximation with applying the method already developed by Coulon et al (Coulon et al. 2009).¹¹ Considering the magnetic exchange interactions only between different sub-lattices, the theoretical phase diagram is given by:

¹¹ See supporting information III.4.2, « Quasi-1D model at low temperature ».

$$\frac{H_C}{H_C^0} = \frac{13(1 + \alpha^{2/3})\sqrt{1 - \alpha^{2/3}}}{18 - 5\left(\tanh^{-1} 2K - \frac{1}{2K}\right)} \quad \text{Eq III.14}$$

where

$$\alpha = \frac{k_B T}{2z|J|S^2 C(K)}$$

Eq III.14 has been optimized in order to simulate the experimental data (**Figure III.26e**). The best agreement could be made with the following parameters: $J/k_B = -0.108$ K, $H_C^0 = 270$ Oe, and $T_C = 2.2$ K. The intrachain exchange energy (J) is in good accord with the one deduced from the characteristic field (H^*). Moreover, a reasonable estimation of the interchain coupling, $zJ'/k_B \approx -1.45$ mK ≈ 0.013 J/k_B , is obtained, which is in good agreement with the simple estimation (-1.5 mK) made from the H_C^0 .

The Eq III.13 could be also modified in the frame of mean-field approximation with taking into account the interchain interactions:¹²

$$\frac{\chi T}{C_{1/2}} = G(K)g_s^2 s - g_s g_s s S [H(K) - E(K)] + F(K)g_s^2 S \quad \text{Eq III.15}$$

where

$$E(K) = \frac{-B(K)}{1 - C(K) \frac{2zJ'S^2}{k_B T}}$$

$$F(K) = \frac{C(K)}{1 - C(K) \frac{2zJ'S^2}{k_B T}}$$

$$G(K) = \frac{A(K)}{1 + C(K)} + \frac{[B(K)]^2 2zJ'S^2}{k_B T \left[1 - C(K) \frac{2zJ'S^2}{k_B T} \right]}$$

$$H(K) = B(K) \left[1 + \frac{F(K) 2zJ'S^2}{k_B T} \right]$$

By introducing both J and J' obtained from H^* and H_C^0 , the simulated $\chi_{\text{Q1D}} T$ (χ_{Q1D} : magnetic susceptibility in quasi-1D regime) still does not compare perfectly with the experimental χT data, as shown by blue line in **Figure III.28** (right). In general, this approximation gives good agreement in the paramagnetic regime that is not very close to the transition. As already mentioned, we are limited to look at only below *ca.* 3 K to keep the ground state of $[\text{Mn}_4]$ units only thermally populated, which is indeed at vicinity of the transition observed at 2.2 K. Although our model illustrates well the critical behavior such as the phase diagram, we can conclude that our approach is limited and an appropriate model describing the χT product of compound **4** in an analytical way is not possible in this case.

¹² See supporting information III.4.2, « Magnetic susceptibility in quasi-1D model ».

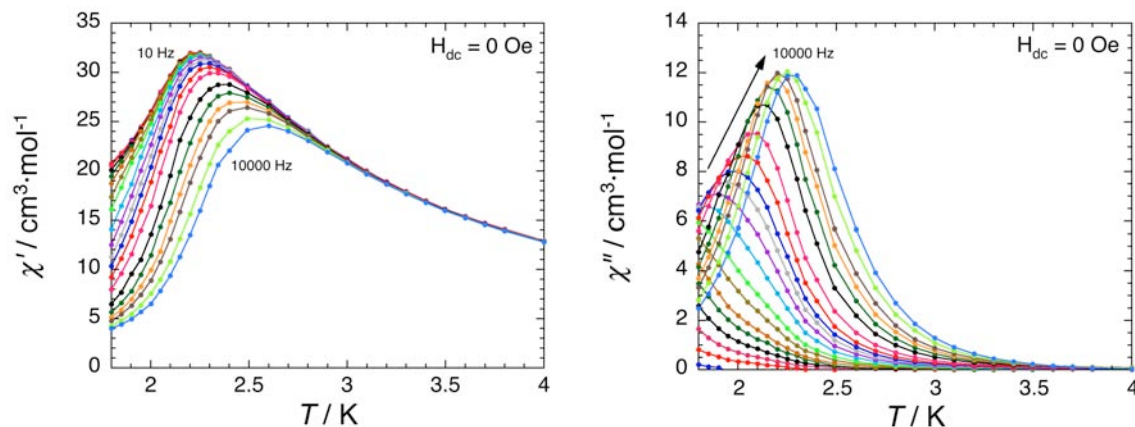


Figure III.29 Temperature dependence of the in-phase (left) and the out-of-phase (right) susceptibility of **4** at different frequencies and at zero dc field.

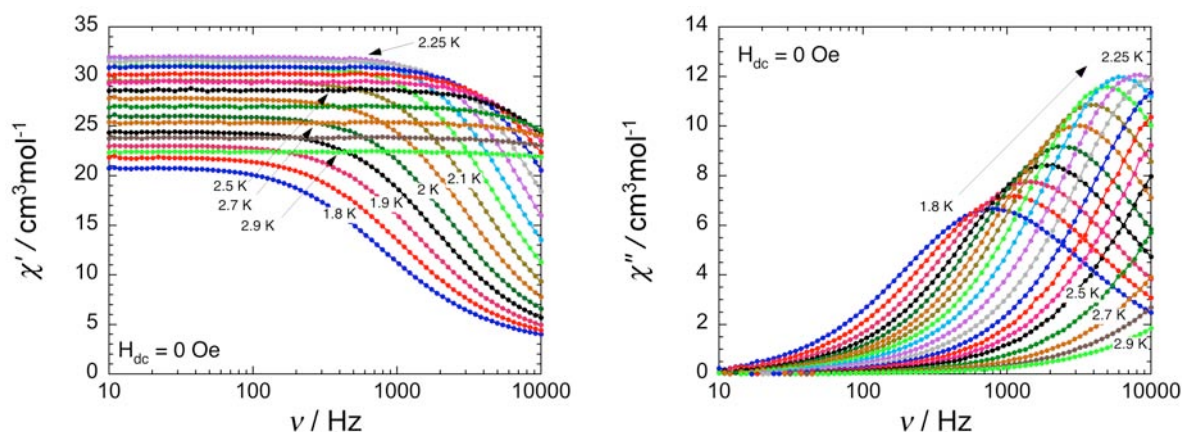


Figure III.30 Frequency dependence of the in-phase (left) and the out-of-phase (right) susceptibility of **4** at different temperatures and at zero dc field.

The slow dynamics of the magnetization in **4** was studied by ac susceptibility measurements on polycrystalline samples (**Figure III.29** and **Figure III.30**). At zero dc field, frequency-dependent in-phase (χ') and out-of-phase (χ'') ac signals are detected below 3.5 K for frequencies ranging from 10 to 10000 Hz. A maximum of the intensity on the χ'' vs T data was observed around 2.2 K expected at the paramagnetic/AF phase transition and the intensities are decreasing with lowering the frequencies clearly indicating the presence of the 3D AF order phase (**Figure III.29**). The associated relaxation time between 1.8 and 2.5 K was deduced from the χ'' vs ν data (**Figure III.30**, right) and found to follow an Arrhenius law with $\Delta_{\tau}/k_B = 21.4$ K ($\tau_0 = 1.8 \times 10^{-9}$ s) (**Figure III.34**, red circles at the bottom right).

Since the external magnetic field was demonstrated to influence strongly the relaxation time in a material showing 3D AF order phase (Coulon et al. 2009), ac measurements were performed also at different dc fields up to 1200 Oe (**Figure III.31**). As expected, the slowest dynamics was observed at 250 Oe for 1.8 K (from 890 Hz at 0 Oe to 110 Hz at 250 Oe, **Figure III.32**) that is nearby the AF/paramagnetic transition line at 1.8 K. Therefore, ac susceptibility measurements at 250 Oe were also performed (**Figure III.33**). The relaxation time at 250 Oe was estimated from the χ'' vs ν data

(Figure III.33, right) that shows a thermally activated regime with $\Delta/k_B = 32.1$ K and $\tau_0 = 1.6 \times 10^{-12}$ s (Figure III.34, blue circles at the bottom right).

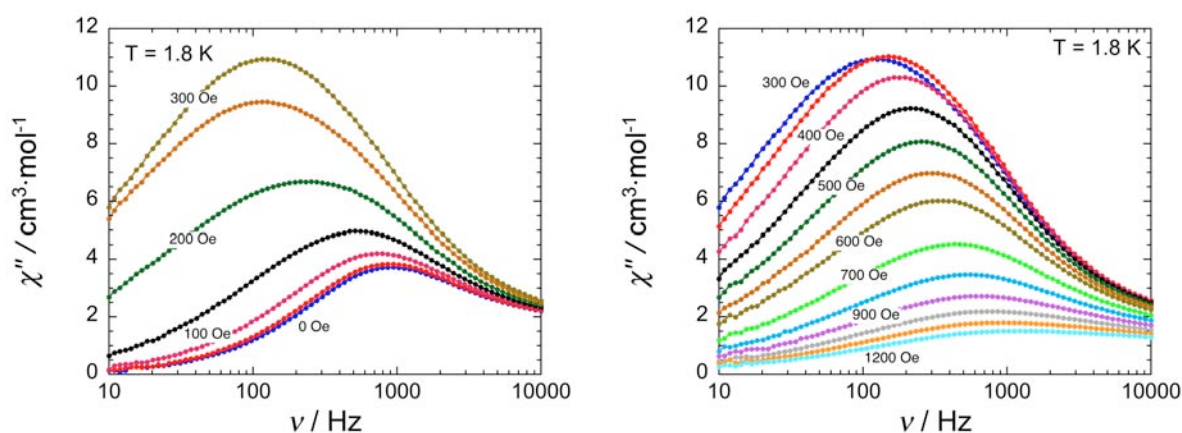


Figure III.31 Frequency dependence of the in-phase (left) and the out-of-phase (right) susceptibility of **4** at different fields and at 1.8 K.

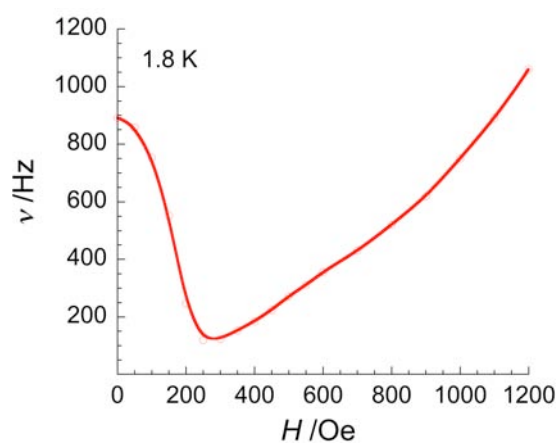


Figure III.32 Field dependence of the characteristic frequency as a function of the applied dc field for **4** at 1.8 K, giving a minimum at 250 Oe.

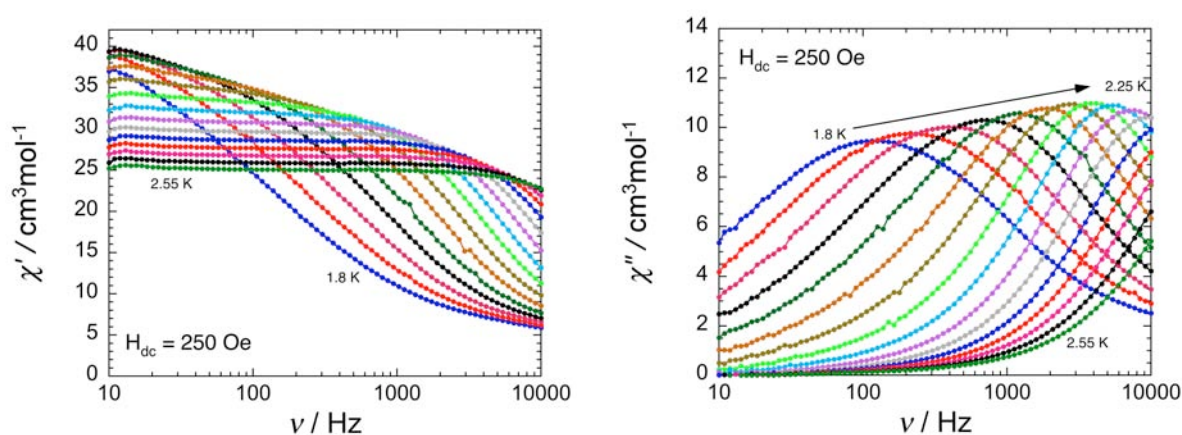


Figure III.33 Frequency dependence of the in-phase (left) and the out-of-phase (right) susceptibility of **4** at different temperatures and at 250 Oe.

By using ^3He -refrigeration system (see supporting information), we could complete ac susceptibility measurements between 1.7 and 0.9 K (**Figure III.34**, top). The relaxation time in this temperature range was deduced from the χ'' vs ν data (**Figure III.34**, top). At zero dc field, a crossover to a different regime was observed below 1.2 K, with $\Delta_{\tau 2}/k_B = 11.0$ K ($\tau_0 = 7.0 \times 10^{-6}$ s) (**Figure III.34**, red circles at the bottom right). For the experiment at 250 Oe, the relaxation time below 1.4 K could only with difficulty be extracted even through the scaling method. Nevertheless, the relaxation time between 1.7 and 1.45 K follows the Arrhenius law with the energy gap deduced from the one above 1.8 K ($\Delta_{\tau}/k_B = 32.1$ K with $\tau_0 = 1.6 \times 10^{-12}$ s).

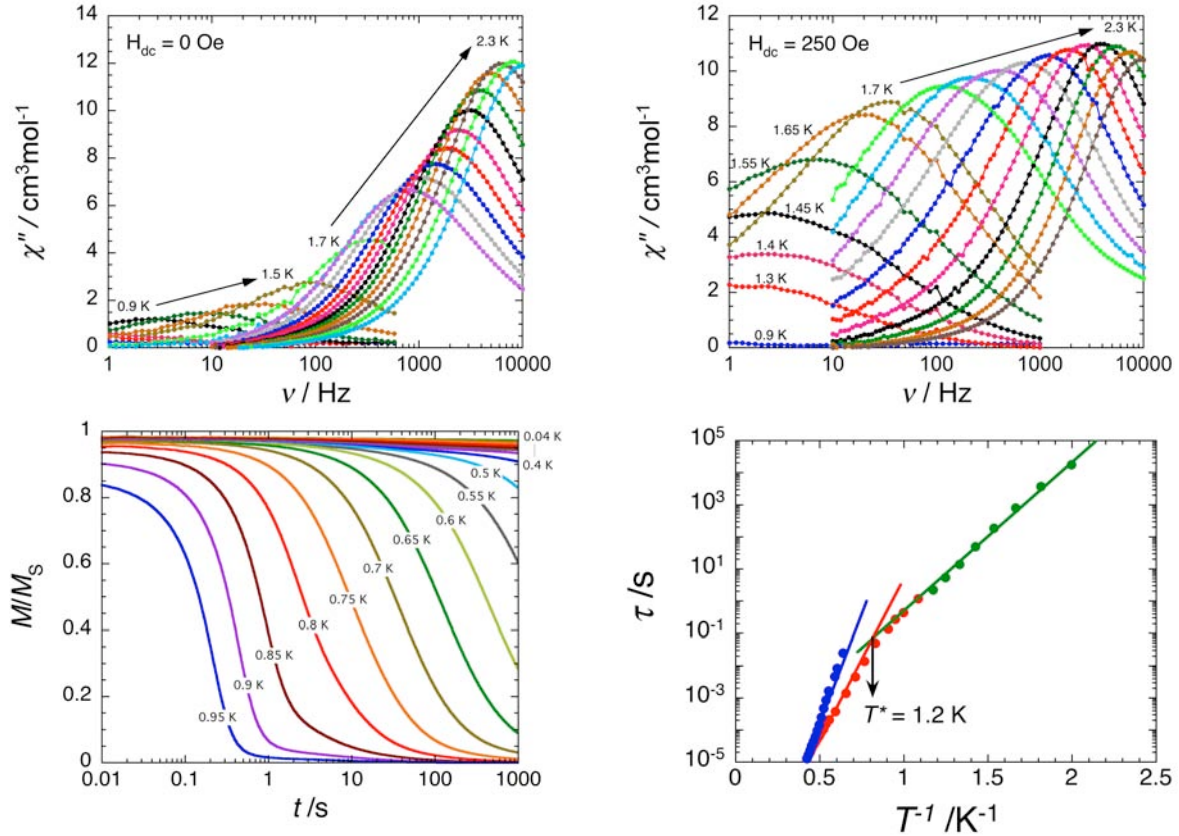


Figure III.34 Top: Frequency dependences of the imaginary (χ'') parts of the ac susceptibility for **4** in zero dc-field (left) and at 250 Oe (right). Bottom: M/M_S vs t (left) and τ vs T^{-1} plots (right) for **4**. Red, blue, and green dots are obtained from ac data at zero field, ac data at 250 Oe, and M/M_S vs t measurements, respectively. The straight lines represent the best fits to Arrhenius law.

In order to follow the slow dynamics at lower temperatures at zero dc field, we have also performed the relaxation experiments (time decay of the magnetization) on an oriented single crystal with μ -SQUID apparatus (Wernsdorfer 2001). The relaxation time, τ , was extracted by scaling method (Labarta et al. 1993) from M/M_S vs t data (**Figure III.34**, bottom left), which compares well with the energy gap of the low temperature regime ($\Delta_{\tau 2} = 11.0$ K with $\tau_0 = 7.0 \times 10^{-6}$ s) (**Figure III.34**, green circles at the bottom right).

It is worth mentioning that the obtained $\Delta_{\tau 1}/k_B$ is almost identical to the anisotropic energy experimentally found for the isolated $[\text{Mn}_4]$ SMMs (Roubeau and Clérac 2008). Moreover, the difference between the energy barriers at 0 Oe ($\Delta_{\tau 1}/k_B$) and 250 Oe (Δ_{τ}/k_B) is *ca.* 10.7 K that is in agreement with the experimental characteristic energy ($\Delta_{\xi}/k_B = 4JS/k_B = 9.7$ K taking $J/k_B = -0.108$ K,

$S = 9$, and $s = 5/2$). It means that the low-temperature limit of 1D correlations can be detected in slow dynamics by applying the external field close to the AF/paramagnetic transition, which could not be observed in $\ln(\chi'T)$ vs T^{-1} plot due to the presence of 3D magnetic ordering. On the other hand, we are not able to explain yet the origin of the low-temperature crossover at 1.2 K on the relaxation time at zero dc field. However, it is interesting to note that the low-temperature relaxation time at zero dc field ($\Delta_{\tau 2}/k_B = 11.0$ K) shows an energy barrier close to (i) the difference of Δ_{τ}/k_B and $\Delta_{\tau 1}/k_B$ (10.7 K) and (ii) Δ_{ξ}/k_B (9.7 K).

III.2.5 Magnetic properties of **5**

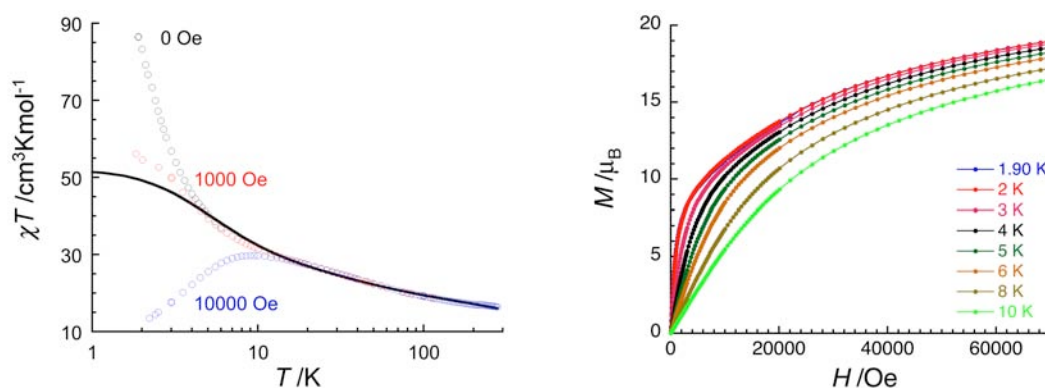


Figure III.35 Temperature dependence of the χT product of **5** at given fields, compared with the fit based on the Heisenberg model described in the text (black line) (left). Field dependence of the magnetization between 10 and 1.9 K (right).

The dc magnetic susceptibility measurements on a polycrystalline sample of **5** kept in $\text{CH}_3\text{CN}/\text{Et}_2\text{O}$ solution are reported in **Figure III.35** (left). At room temperature, the χT product of **5** is $16.4 \text{ cm}^3\text{molK}^{-1}$ which is in good agreement with expected Curie constant, $C = 15.5 \text{ cm}^3\text{molK}^{-1}$ (with $g = 2$), for two Mn^{II} ($S = 5/2$), two Mn^{III} ($S = 2$), and two Cu^{II} ($S = 1/2$) ions. Upon lowering the temperature, χT is increasing up to $86.5 \text{ cm}^3\text{molK}^{-1}$ in zero-dc field, while when applying even 1000 Oe saturation effects of the applied dc field are observed. This thermal behavior is typical of $[\text{Mn}_4(\text{hmp})_6]^{4+}$ units exhibiting ferromagnetic intra-complex interactions: J_{bb} between Mn^{III} ions and, J_{wb} between Mn^{II} and Mn^{III} ions (**Figure III.8**). The parameters g -factor, J_{wb} and J_{bb} were determined using the Heisenberg-Van Vleck model (Eq III.1) and treating the Cu^{II} metal ions as Curie contributions. Data below 13 K were omitted in the fitting procedure to stay in the low field limit of the model. A reasonable fit was achieved, with final optimized parameters being $g_{\text{av}} = 2.13(2)$, $J_{\text{wb}}/k_B = +0.40(5)$ K, and $J_{\text{bb}}/k_B = +7.7(3)$ K. Clearly Mn ions in **5** are ferromagnetically coupled to give an $S_T = 9$ ground state for the $[\text{Mn}_4]$ moieties. The maximum of the χT product at zero dc-field ($86.5 \text{ cm}^3\text{molK}^{-1}$) is much bigger than the calculated one ($45.75 \text{ cm}^3\text{molK}^{-1}$) for uncoupled $[\text{Mn}_4]$ SMM unit ($S_T = 9$) and two Cu^{II} ($S = 1/2$), implying the presence of ferromagnetic interactions between SMM and Cu ions through the *syn-anti* carboxylate bridges. This is coherently supported by the magnetization value ($18.9 \mu_B$) at 1.9 K under 7 T, which is not saturated and increases close to the expected magnetic moment of $20 \mu_B$ for all aligned spins in a same direction. In addition, M vs H data show no inflection point or S-shape curve that would be characteristic for antiferromagnetic interactions (**Figure III.35**, right). It is worth mentioning that the heat capacity measurement shows a broad hump at *ca.* 1.5 K (**Figure III.36**), indicating the competition between dynamic properties and the thermodynamic

behavior for long range order, as observed for compound **3** and a related 2D network (Miyasaka et al. 2006).

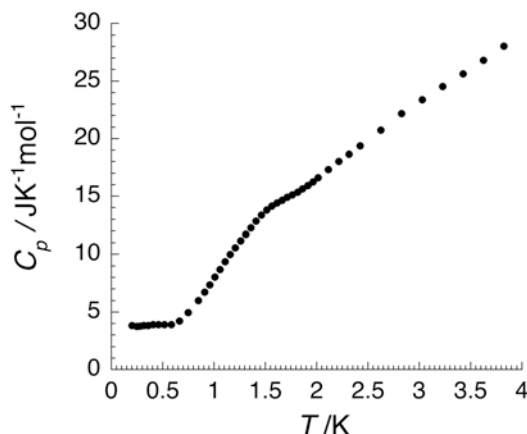


Figure III.36 Temperature dependence of the heat capacity for **5** at zero dc field.

In order to probe possible slow relaxation of magnetization, measurements below 1.9 K with μ -SQUID apparatus (Wernsdorfer 2001) were performed on an oriented single crystal (**Figure III.37**). The hysteresis phenomenon was observed under a dc field applied along the easy direction. The coercive field varies strongly with both temperature and sweep-field rate (**Figure III.37**), showing slow relaxation of the magnetization in agreement with the ac measurements (**Figure III.38**). The relaxation time, τ , was extracted by scaling method (Labarta et al. 1993) from M/M_S vs t data, and shown in **Figure III.39**. Above 0.5 K, the relaxation time is thermally activated with an energy gap of $\Delta/k_B = 14$ K and $\tau_0 = 5.6 \times 10^{-8}$ s. The gap value compares well with the effective energy barriers obtained for isolated $[\text{Mn}_4]$ SMM units (typically between 11 and 27 K) (Roubeau and Clérac 2008). Below 0.5 K, the relaxation time does not follow anymore an Arrhenius law and saturates slowly as expected when ground state quantum tunneling of the magnetization (QTM) becomes the fastest pathway of relaxation in SMMs. A pure QTM regime is observed below 0.1 K with a characteristic time $\tau_{\text{QTM}} = 1.5 \times 10^6$ s which is larger than any of the τ_{QTM} observed of $[\text{Mn}_4]$ SMMs. The same trend can be noticed for τ_0 , the characteristic time of relaxation from the thermal bath, that is also among the higher values for previously studied $[\text{Mn}_4]$ SMMs or related materials (Lecren et al. 2008; Lecren et al. 2005a; Lecren et al. 2005c; Miyasaka et al. 2006; Miyasaka et al. 2004; Roubeau and Clérac 2008; Yoo et al. 2005; Yoo et al. 2001).

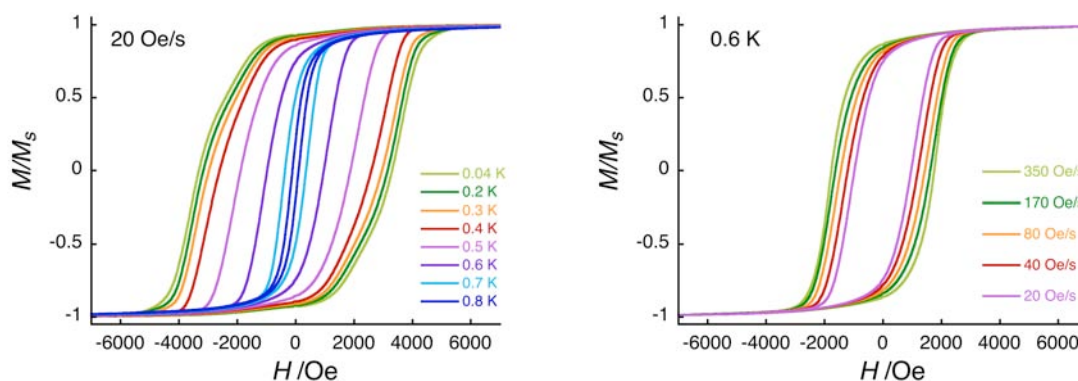


Figure III.37 M/M_S vs H curves of **5** on a single crystal at different temperatures with a sweep-field rate of 20 Oe/s (left) and at 0.6 K with the sweeping rate of the dc field in the range of 20 – 350 Oe/s (right).

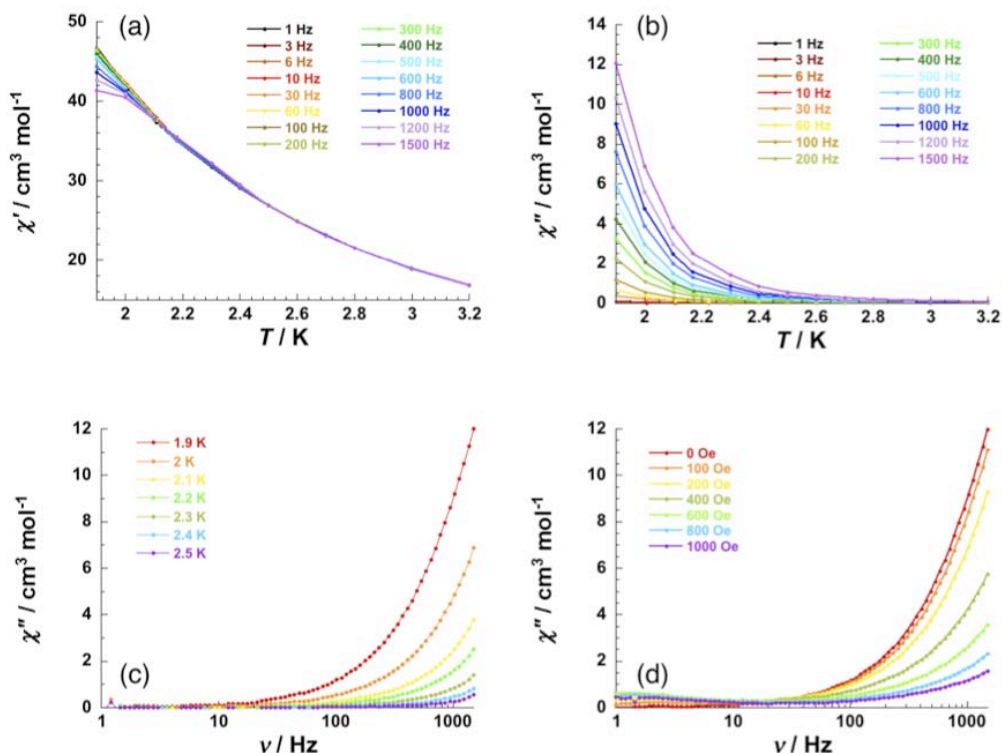


Figure III.38 Temperature dependence of (a) the in-phase, χ' , and (b) out-of-phase, χ'' , components of the ac magnetic susceptibility for **5**, collected in a 3 Oe ac field oscillating at frequencies between 1 and 1500 Hz in zero-dc field. Frequency dependence of the out-of-phase, χ'' , components of the ac magnetic susceptibility for **5**, collected in a 3 Oe ac field (c) between 1.9 and 2.5 K in zero-dc field and (d) between 0 and 1000 Oe dc field at 1.9 K.

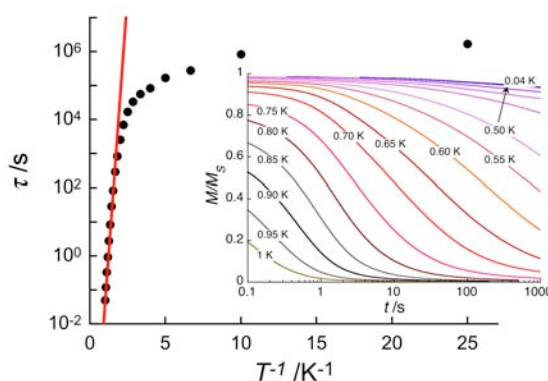


Figure III.39 τ vs T^{-1} plot for **5** from M/M_S vs t measurements with the red line representing the best fit to Arrhenius law above 0.65 K.

III.2.6 Concluding remarks for 3 – 5

We obtained unique 1D and 2D networks of $[\text{Mn}_4(\text{hmp})_6]^{4+}$ anisotropic units linked by paramagnetic metal(II) picolates: $[\text{Mn}_4(\text{hmp})_6(\text{H}_2\text{O})_2][\text{Ni}(\text{pic})_2(\text{H}_2\text{O})_2](\text{ClO}_4)_4 \cdot 3\text{CH}_3\text{CN}$ (**3**), $[\text{Mn}_4(\text{hmp})_6(\text{H}_2\text{O})_2][\text{Mn}(\text{pic})_2(\text{H}_2\text{O})_2](\text{ClO}_4)_4 \cdot 3\text{CH}_3\text{CN} \cdot 2\text{H}_2\text{O}$ (**4**), and $[\text{Mn}_4(\text{hmp})_6\{\text{Cu}(\text{pic})_2(\text{ClO}_4)_2\}_2] \cdot 2\text{CH}_3\text{CN}$ (**5**). The preformed paramagnetic precursors, $[\text{Ni}(\text{pic})_2(\text{H}_2\text{O})_2]$, $[\text{Mn}(\text{pic})_2(\text{H}_2\text{O})_2]$, and $[\text{Cu}(\text{pic})_2] \cdot 2\text{H}_2\text{O}$, were added to the basic acetonitrile solution containing $\text{Mn}(\text{ClO}_4)_2 \cdot 6\text{H}_2\text{O}$ and Hhmp to afford compounds **3**

– **5**. The structural characterization shows well-preserved double-cuboidal $[\text{Mn}_4]$ cores connected with metal(II) picolates *via syn-anti* carboxylate bridges. Only one carboxylate group is coordinated to the external Mn ion of the $[\text{Mn}_4]$ cores in compounds **3** and **4**, while oxygen atoms from two different carboxylate groups of pic^- occupy the coordination sphere of the external Mn ion in compound **5**. As a consequence, **3** and **4** are chains in the structural point of view, and **5** displays a 2D framework.

The magnetic susceptibility of **3** – **5** was compared with the Heisenberg-Van Vleck model for $[\text{Mn}_4]$ unit (Eq III.1) treating the additional Mn^{II} , Ni^{II} , or Cu^{II} metal ions as Curie contributions. The fitting results confirm the presence of the ferromagnetic interactions inside the tetranuclear core for **3** – **5**, to give an $S_T = 9$ ground state for $[\text{Mn}_4]$ units along the networks. Then, the inter- $[\text{Mn}_4]$ interactions through the *syn-anti* carboxylate bridges for **4** and **5** were found to be antiferromagnetic and ferromagnetic, respectively, while we could not estimate those for **3** that should be at least very small. Compounds **3** and **5** exhibit the competition between the dynamics of the anisotropic $[\text{Mn}_4]$ units and thermodynamic behavior for long-range order, as shown by the broad anomalies in heat-capacity measurements at *ca.* 0.6 and 1.5 K, respectively. On the other hand, compound **4** shows 3D AF order at 2.2 K, as confirmed by M vs H , ac susceptibility, and heat capacity measurements. Under the external field, **4** shows typical metamagnetic behavior induced by the anisotropic $[\text{Mn}_4]$ units. The (T, H) phase diagram of **4** was almost perfectly simulated by quasi-1D model based on the chain model for alternating Ising and isotropic spins that was developed in this thesis. From this model, we could estimate the following parameters: $J/k_B = -0.108$ K, $H_C^0 = 270$ Oe, $T_C = 2.2$ K, and $zJ'/k_B \approx -1.45$ mK. It is worth mentioning that the magnetic behavior of the chain consisting alternating Ising and isotropic spins is completely different from the chain consisting of only Ising-type spins.

All three compounds **3** – **5** display slow relaxation of the magnetization undoubtedly induced by the presence of SMM $[\text{Mn}_4]$ units. The estimated energy barriers at zero-field for **3** ($\Delta/k_B = 18.6$ K) and **5** ($\Delta/k_B = 14$ K) correspond to the effective energy barriers obtained for isolated $[\text{Mn}_4]$ SMM units that is typically between 11 and 27 K (Roubeau and Clérac 2008). However, **4** shows two different thermally activated regimes above and below 1.2 K with $\Delta_{\text{t1}}/k_B = 21.4$ K and $\Delta_{\text{t2}}/k_B = 11$ K. By applying a dc field on **4**, a slowest dynamics was observed at 250 Oe, nearby the AF/paramagnetic transition line. The relaxation time at 250 Oe follows thermally activated regime with the energy gap ($\Delta/k_B = 32.1$ K) corresponds to the one for chain dynamics: the contribution of both anisotropy barrier of $[\text{Mn}_4]$ unit ($\Delta/k_B = 21.4$ K) and the 1D correlation energy ($\Delta_{\text{c}}/k_B = 9.7$ K).

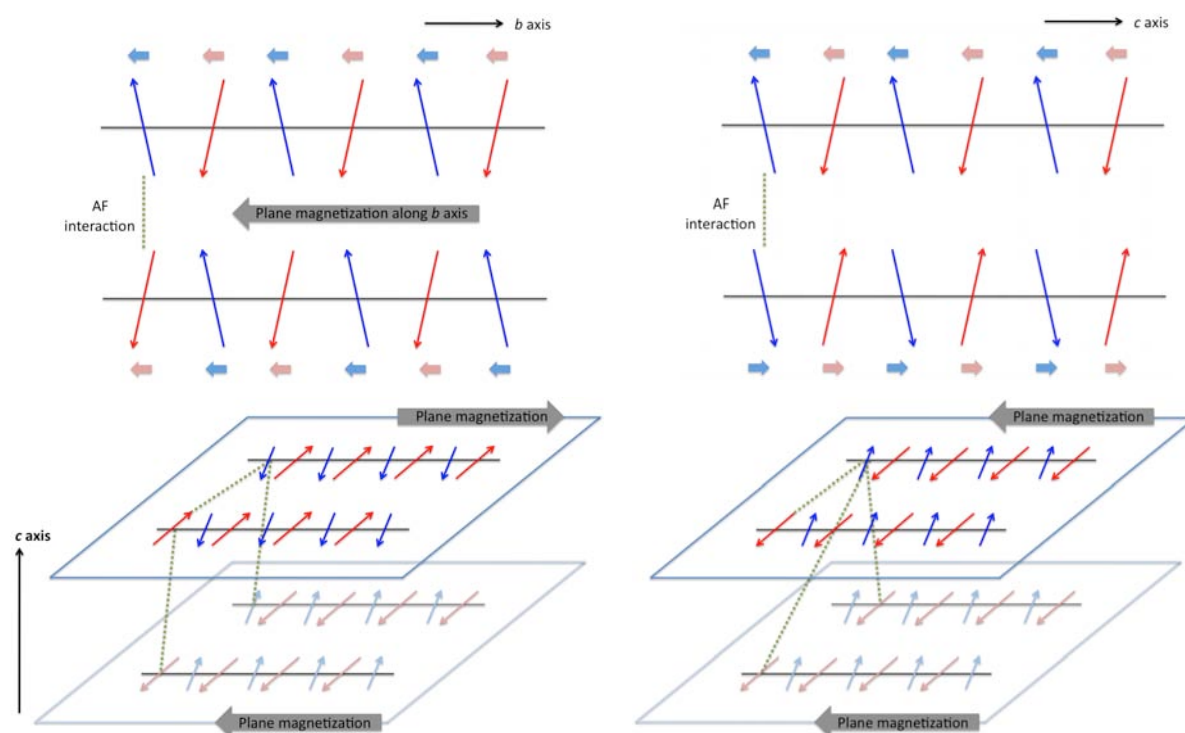
III.3 Conclusion and perspectives

In Chapter III, the coordination networks of $[\text{Mn}_4]$ SMMs (**1** – **5**) bridged by diamagnetic and paramagnetic linkers were described in terms of syntheses, crystallographic characterizations, and magnetic properties. The detailed remarks can be consulted in “concluding remarks” that is at the end of each section. Here we will focus more on the perspectives for the questions left unanswered during this work.

Compounds **1** and **2** are 1D systems with mono- and di-chlorido bridges, showing antiferromagnetically coupled $[\text{Mn}_4]$ SMM units along the chain. All diamagnetic linkers used for the 1D coordination networks of $[\text{Mn}_4]$ SMMs mediate the antiferromagnetic interactions (Lecren et al. 2008; Lecren et al. 2005b). Nevertheless, slow relaxation of the magnetization was observed due to

the finite size effect in the previously reported systems. For the present compounds **1** and **2**, we discovered that the canting of the anisotropic $[\text{Mn}_4]$ spins along the chain played an important role in the slow dynamics. Even though **1** and **2** respectively display a 3D canted antiferromagnetic and antiferromagnetic orders, the 1D correlations of the non-compensated moments due to the spin canting in both systems indeed induce slow relaxations with an enhanced energy barrier, compared to those observed for the isolated $[\text{Mn}_4]$ SMMs.

Now a question has to be asked: why these two similar systems stabilize different magnetic ground states (canted antiferromagnetic and antiferromagnetic phase)? We suppose the following hypothesis as an answer. As shown in **Figure III.4** (right), chains of **2** in bc plane are stacked in a fashion where same orientation of $[\text{Mn}_4]$ units from the neighboring chain are face to face (blue-to-blue and red-to-red). Considering that the significant antiferromagnetic interactions are present only between face-to-face $[\text{Mn}_4]$ units, the total magnetization in plane will be compensated (**Scheme III.1**, top right), and therefore it stabilizes antiferromagnetic phase. For compound **1**, face-to-face $[\text{Mn}_4]$ units between adjacent chains in ab plane are in different orientations (red-to-blue), as shown in **Figure III.2**. Considering again that the significant antiferromagnetic interactions are present only between face-to-face $[\text{Mn}_4]$ units, the non-compensated plane magnetization will be along b axis (**Scheme III.1**, top left). Then, we need to consider the magnetic interactions between these ab planes along c axis. The face-to-face $[\text{Mn}_4]$ units in neighboring ab plane have same orientations in their packing. Here we can think about two different situations: (i) If major antiferromagnetic interactions are between face-to-face $[\text{Mn}_4]$ units, then magnetization between plane will be compensated and antiferromagnetic phase will be stabilized (**Scheme III.1**, bottom left); (ii) Nevertheless, if major antiferromagnetic interactions are between different orientations of $[\text{Mn}_4]$ units there will be still non-compensated magnetization in a whole system (**Scheme III.1**, bottom right), and therefore a canted antiferromagnetic phase is stabilized.



Scheme III.1

Furthermore, the coordination frameworks of [Mn₄] SMMs linked with Mn^{II}, Ni^{II}, and Cu^{II} metal centers offered an opportunity to observe unique magnetic behaviors. We have seen the frozen long-range order for compounds **3** and **5** due to the slow dynamics of the anisotropic [Mn₄] units. For both compounds **3** and **5**, magnet behavior was observed with the estimated energy gaps in the range of the effective energy barrier for isolated [Mn₄] SMMs. However, it is worth noting that the τ_{QTM} and τ_0 for **5** stays larger than any of those observed for [Mn₄] SMMs. Therefore, the influence of the ferromagnetic interactions within 2D network between [Cu(pic)₂] and [Mn₄] building blocks on the dynamic properties need to be still investigated. This might be studied by performing high-frequency/high-field EPR.

In addition, the presence of isotropic Mn^{II} ions in **4** between anisotropic [Mn₄] units along the chain displayed the unprecedented magnetic behavior different from Ising chain behavior. This fact motivated us to develop a new chain model that indeed compares with the experimental data. Compound **4** shows 3D magnetic order, and the slow dynamics corresponding to the chain was observed at 250 Oe that is nearby the transition line. One can naively say that the applied dc field cancels the interchain magnetic interactions, and therefore, one can observe the intrinsic behavior of the 1D coordination polymer composing this material. At zero dc field, we have observed two thermally activated regimes: one with an energy barrier of the isolated [Mn₄] SMMs above 1.2 K and the other with an energy barrier close to the 1D correlation energy. At the moment, we do not fully understand the dynamics of the latter. In this regard, the effect of the applied dc field on quasi-1D systems should be studied in detail. This work is currently developed by V. Pianet (PhD thesis, 2011 – 2014) in our group.

As introduced in the general introduction and conclusion of Chapter II, the initial objective to introduce paramagnetic linkers was to favor strong magnetic interactions. However, we have found that the *syn-anti* carboxylate bridges in metal(II) picolinate complexes mediate not strong enough interactions. Therefore, new linkers should be sought such as metal cyanides and radical ions. Indeed, the possibility to coordinate the N atoms of the cyanide groups to [Mn₄] SMMs was recently reported (Kushch et al. 2011) offering a proof-of-feasibility.

III.4 Supporting information

III.4.1 Experimental section

Syntheses. All chemicals were reagent grade and used as received, and the reactions were performed in aerobic condition. $[\text{Ni}(\text{pic})_2(\text{H}_2\text{O})_2]$, $[\text{Mn}(\text{pic})_2(\text{H}_2\text{O})_2]$, and $[\text{Cu}(\text{pic})_2]\cdot 2\text{H}_2\text{O}$ were prepared as described in the thesis of L. Lecren (Lecren 2006). *Caution!* Although we have experienced no problems while working with them, perchlorate salts are potentially explosive and should be handled with extreme care and only in small quantities. The reaction for all complexes **1** – **5** have the common initial step that is the one to form $[\text{Mn}_4(\text{hmp})_6(\text{CH}_3\text{CN})_2(\text{H}_2\text{O})_4]^{4+}$ (Lecren et al. 2005a): $\text{Mn}(\text{ClO}_4)_2\cdot 6\text{H}_2\text{O}$ (0.500 g, 1.38 mmol) and hmpH (0.378 g, 3.45 mmol) were dissolved by stirring in 20 mL of CH_3CN . To this solution, 510 μL (0.72 mmol) of a 20wt % water solution of $(\text{Et}_4\text{N})\text{OH}$ was added dropwise. This solution was stirred for 5 mins, and then the following steps were performed.

$[\text{Mn}_4(\text{hmp})_6(\text{H}_2\text{O})_2\text{Cl}](\text{ClO}_4)_3\cdot 1.5\text{CH}_3\text{CN}$ (1). As the initial step, 40 mL of CH_3CN was used instead of 20 mL. $\text{MnCl}_2\cdot 4\text{H}_2\text{O}$ (0.034 g, 0.18 mmol) was added to the solution, and it was stirred for 1 h at room temperature. After filtration, diethylether was layered on the top of the resulting solution. The whole crystallization set-up was closed hermetically and then kept undisturbed for diffusion. Purple-brown crystals with a shape of elongated hexagon were isolated in 7 days. (Yield based on Mn: 58 %). Anal. Calc. for $\text{C}_{36}\text{H}_{40}\text{Cl}_4\text{Mn}_4\text{N}_6\text{O}_{20}$: C, 34.92; H, 3.26; Cl, 11.45; Mn, 17.75; N, 6.79 %; Found: C, 34.47; H, 3.34; N, 6.27 %. Selected IR data (KBr, cm^{-1}): 3300 (br), 2950 (w), 2850 (m), 1607 (s), 1550 (w), 1455 (w), 1450 (m), 1415 (m), 1365 (w), 1280 (m), 1150 (s), 765 (s), 685 (w), 570 (w).

$[\text{Mn}_4(\text{hmp})_6\text{Cl}_2](\text{ClO}_4)_2$ (2). NaCl (0.034 g, 0.58 mmol) was added to the solution, and it was stirred for 1 h at room temperature. After filtration, diethylether was carefully layered on the top of the resulting solution. The whole crystallization set-up was closed hermetically and then kept undisturbed for diffusion. Purple-brown crystals with a shape of needle were isolated in 7 days. (Yield based on Mn: 48 %). Anal. Calc. for $\text{C}_{36}\text{H}_{36}\text{Cl}_4\text{Mn}_4\text{N}_6\text{O}_{14}$: C, 37.98; H, 3.19; Cl, 12.46; Mn, 19.31; N, 7.38 %; Found: C, 37.68; H, 3.19; N, 7.38 %. Selected IR data (KBr, cm^{-1}): 3300 (br), 2950 (w), 2850 (m), 1607 (s), 1550 (w), 1485 (w), 1440 (m), 1415 (m), 1365 (w), 1280 (m), 1150 (s), 765 (s), 685 (w), 570 (m).

$[\text{Mn}_4(\text{hmp})_6(\text{H}_2\text{O})_2][\text{Ni}(\text{pic})_2(\text{H}_2\text{O})_2](\text{ClO}_4)_4\cdot 3\text{CH}_3\text{CN}$ (3). $[\text{Ni}(\text{pic})_2(\text{H}_2\text{O})_2]\cdot 2\text{H}_2\text{O}$ (0.243 g, 0.649 mmol) was added to solution. The purple-brown solution was stirred for 1 h at 50 °C. After filtration, toluene was layered on the top of the resulting solution. The whole crystallization set-up was closed hermetically and then kept undisturbed for diffusion. Purple-brown rhombus crystals were isolated in 7 days. (Yield based on Mn: 61 %). Anal. Calc. for $\text{C}_{48}\text{H}_{52}\text{N}_8\text{O}_{30}\text{Cl}_4\text{NiMn}_4$: C, 35.13; H, 3.19; N, 6.83 %; Found: C, 36.11; H, 3.17; N, 6.90. Selected IR data (KBr, cm^{-1}): 3438 (br), 1615 (s), 1620 (s), 1598 (s), 1482 (m), 1443 (m), 1400 (m), 1384 (m), 1295 (w), 1269 (w), 1093 (br), 1047 (br), 860 (w), 763 (m), 622 (m), 565 (w), 413 (w).

$[\text{Mn}_4(\text{hmp})_6(\text{H}_2\text{O})_2][\text{Mn}(\text{pic})_2(\text{H}_2\text{O})_2](\text{ClO}_4)_4\cdot 3\text{CH}_3\text{CN}\cdot 2\text{H}_2\text{O}$ (4). $[\text{Mn}(\text{pic})_2(\text{H}_2\text{O})_2]\cdot 0.3\text{H}_2\text{O}$ (0.117 g, 0.345 mmol) was added to the solution, and it was stirred for 1 h at 50 °C. After filtration, the resulting solution was carefully layered with diethylether in a test tube. The crystallization tube was

closed hermetically and then kept undisturbed at room temperature. Purple-brown rhombus crystals were isolated in 7 days. (Yield based on Mn: 40 %). Anal. Calc. for $C_{48}H_{50}N_8O_{32}Cl_4Mn_5$: C, 34.58; H, 3.02; N, 6.72 %; Found: C, 34.13; H, 3.08; N, 6.71 %. Selected IR data (KBr, cm^{-1}): 3425 (br), 1616 (s), 1595 (s), 1565 (s), 1485 (m), 1411 (m), 1365 (m), 1288 (w), 1040 (br), 925 (w), 825 (m), 620 (m), 565 (w), 411 (w).

[Mn₄(hmp)₆{Cu(pic)₂(ClO₄)₂}]₂·2CH₃CN (5). [Cu(pic)₂]₂·2H₂O (0.237 g, 0.69 mmol) was added to solution. The purple-brown solution was stirred for 1 h at 50 °C. After filtration, the resulting solution was slowly evaporated. Purple-brown rhombus crystals were isolated in 7 days. (Yield based on Mn: 53 %). Anal. Calc. for $C_{60}H_{52}N_{10}O_{30}Cl_4Cu_2Mn_4$: C, 38.30; H, 2.79; Cl, 7.54; Cu, 6.75; Mn, 11.68; N, 7.44 %; Found: C, 37.56; H, 2.69; N, 7.64; Cu, 6.22; Mn, 11.13 %. Selected IR data (KBr, cm^{-1}): 3438 (br), 1635 (s), 1620 (s), 1598 (s), 1482 (m), 1443 (m), 1400 (m), 1384 (m), 1295 (w), 1269 (w), 1093 (br), 1047 (br), 860 (w), 763 (m), 622 (m), 565 (w), 413 (w).

Physical Methods. Elemental analysis for C, H and N were performed following the classical Pregl-Dumas technique on a ThermoFischer Flash EA1112. FT-IR spectra were recorded in the range 400-4000 cm^{-1} on a Nicolet 750 Magna-IR spectrometer using a KBr pellet. Heat capacity was measured on polycrystalline samples by a thermal relaxation technique with a Quantum Design Physical Property Measurement System (PPMS-9). Sample environment controls include fields up to ± 9 tesla and temperature range of 1.9 – 400 K. Using $^3He/^4He$ dilution refrigerator option, heat capacity measurement can be performed also down to 50 mK. In each measurement, the blank heat capacity including a small amount of Apiezon N grease used for adhesion was measured prior to the sample mounting. The heat capacities of the compound are determined by subtracting the blank data from the measured total heat capacity. Magnetic data were collected using a Quantum Design MPMS-XL SQUID magnetometer in the 1.8 - 300 K temperature range and between -7 and +7 T. Magnetic measurements were obtained reproducibly on microcrystalline powders in polyethylene bag ($3 \times 0.5 \times 0.02$ cm) for **1** – **4** and on microcrystalline powders restrained in frozen CH₃CN/Et₂O mother liquor for **5**. The alternating current (ac) magnetic susceptibility data were collected under an ac field of 3 Oe. All data were corrected for diamagnetic contributions from the sample holder, as well as for the intrinsic core diamagnetism of the compound. ac measurements below 1.8 K were done by integrating i Helium3 (IQUANTUM, 3He -refrigeration system) into MPMS. Magnetization measurements on oriented single crystals were carried out with an array of micro-SQUIDs (Wernsdorfer 2001). This magnetometer works in the temperature range of 0.04 to ca. 5 K and in fields of up to 1.4 T with sweeping rates as high as 0.28 Ts⁻¹, and exhibits field stability of better than μT . The time resolution is approximately 1 ms. The field can be applied in any direction of the micro-SQUID plane with precision much better than 0.1° by separately driving three orthogonal coils. In order to ensure good thermalization, a single crystal was fixed with apiezon grease.

General aspects on crystallography. X-ray crystallographic data were collected on a Nonius Kappa CCD diffractometer with graphite-monochromated Mo K α radiation ($\lambda = 0.71073$ Å) at 150 K. The single crystal of **1** – **5** was affixed to the end of a glass fiber using paratone N and quickly transferred to the goniostat where it was cooled for data collection. DENZO-SMN (Otwinowski et al. 1997) was used for data integration and SCALEPACK (Otwinowski et al. 1997) corrected data for Lorentz-polarisation effects. All structures were solved by the direct method and refined by a full-matrix least-squares method on F^2 using the SHELXTL crystallographic software package (Sheldrick 1997).

Crystallography for 1. In the asymmetric unit, there is a half Mn_4 cation, two normal ClO_4^- anion and two disordered ClO_4^- anions, and one and a half disordered CH_3CN solvent molecules. It is noteworthy that the hmp⁻ ligand and the water molecules coordinated to the Mn(2) center are both disordered into two positions and the occupancies are refined to ca. 70% and 30%, respectively. The Cl bridge on the complex is also disordered with two positions and both refined with the occupancies of 50%. The Cl(4)O₄⁻, Cl(5)O₄⁻ ions and one CH_3CN molecule (N(31), C(31), and C(32)) exist two main disordered positions, while the other CH_3CN (N(21), C(21) and C(22)) molecule exists four disordered positions on the basis of the symmetry of the structure. All of the non-hydrogen atoms were refined anisotropically except for the O(41), O(42), O(43), O(51), O(52), O(53) oxygen atoms. During the refinement, some non-H atoms with ADP problems are restrained with the command "ISOR". These atoms are as follows: C12, C13, C15, C16, C15A, C16A, O11, O12, O13, O21, O22, O23, Cl1, Cl1A, Cl5. Furthermore, the pyridine ring of the disordered hmp ligands were restrained with the commands "AFIX 69", "AFIX 0", and "DELU". The bond distances and angles of ClO_4^- anions were also restrained with the command "DFIX". All above restraint refinement led to a relatively high restraint value of 165.

Crystallography for 2. For the careful analysis of unit-cell parameters depending on the temperature, two full scans of decrease and increase have been done in the temperature range of 280 K to 100 K with the ramp rate of 60 K/h. 55 images were collected at each 10 K with the following identical conditions for all temperatures: ψ was scanned from 0° to 55° with 1° of the step, while θ , ω , κ were fixed to 0°, -171.933°, -24.878°, respectively. Then, X-ray crystallographic data were collected at 298 and 150 K. All of the non-hydrogen atoms were refined anisotropically, whereas the hydrogen atoms on the parent carbon atoms were included in fixed calculated positions.

Crystallography for 3. During the refinement, the restraint command 'isor' was used to restrain 22 non-H atoms with ADP problems. Such restrained refinement led to a high restraint value of 164.

Crystallography for 4. During the refinement, the command 'omit -3 50' is used to omit the weak reflections above 50 degrees. The solvent CH_3CN molecules are all disordered in two positions with half occupancies in each case. There are still some solvent accessible voids in the crystal structure, but no solvent molecules can be found from the weak residual peaks. Thus, the SQUEEZE program was used to estimate the rest of the solvent molecules in the crystal structure. The result shows that two more water molecules possibly in the void. These two water molecules were included in the final molecular formula directly. The highest residual peaks and the deepest hole both reside in the Cl(2) center but featureless, which may be due to the series termination errors. All of the non-hydrogen atoms were refined anisotropically except the disordered CH_3CN molecules (C(32)-C(31)-N(31), C(42)-C(41)-N(41), C(32A)-C(31A)-N(31A) and C(42A)-C(41A)-N(41A)). The hydrogen atoms on the parent carbon atoms were included in fixed calculated positions. The short distance between O2W...O22 suggests the obvious H-bonding interaction between coordinated water molecule and the ClO_4^- anion, however, the H atoms on O2W cannot be found from the weak residual peak.

Crystallography for 5. All of the non-hydrogen atoms were refined anisotropically, whereas the hydrogen atoms on the parent carbon atoms were included in fixed calculated positions.

III.4.2 Supporting figures

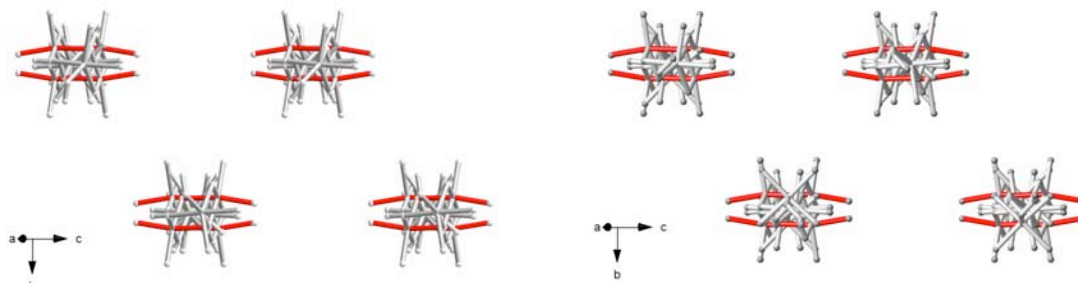


Figure SIII.1 View of crystal packing perpendicular to the chain direction for the compound **3** (left) and **4** (right), highlighting JT axes along the chain in red.

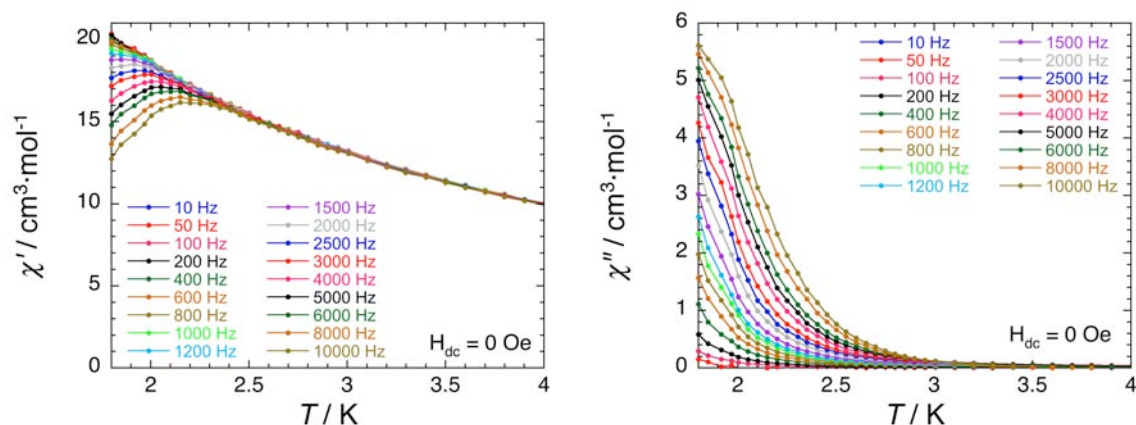


Figure SIII.2 Temperature dependence of the in-phase (left) and the out-of-phase (right) susceptibility of **3** at different frequencies and at zero dc field.

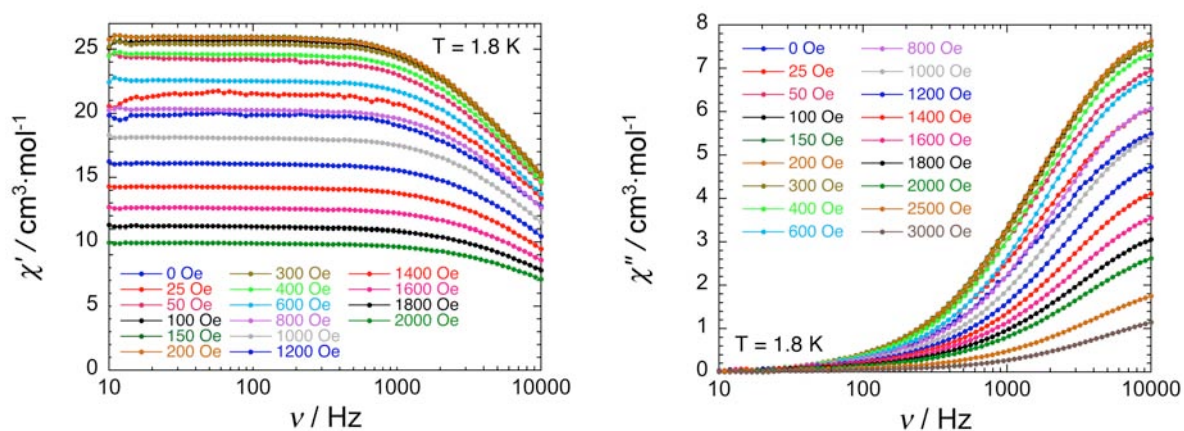


Figure SIII.3 Frequency dependence of the in-phase (left) and the out-of-phase (right) susceptibility of **3** at different dc fields and at 1.8 K.

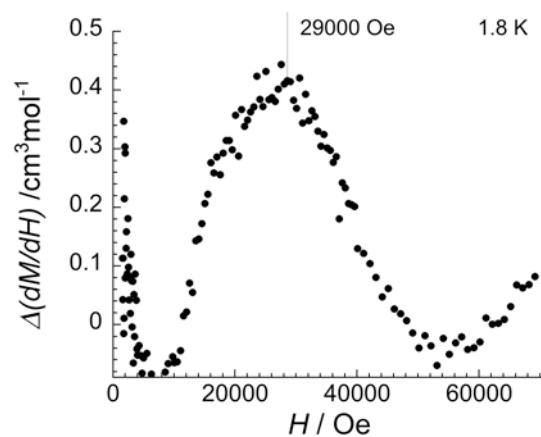
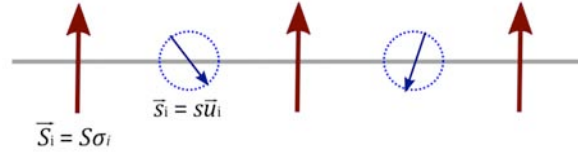


Figure SIII.4 Field dependence of the derivative of the magnetization at 1.8 K for **4**, in which the base line was subtracted to estimate the position of the maximum, H^* .

III.4.3 Theoretical model: chain of alternating Ising and isotropic spins



Scheme SIII.1

Let us consider the 1D system formed by the alternating Ising and isotropic spins as described in **Scheme SIII.1**. An infinite magnetic anisotropy for the spin S is considered, whereas spin s is treated as a classical Heisenberg one. In the absence of the external applied field, the exchange interaction term can be described by the following Hamiltonian:

$$H = -2J \sum_{-\infty}^{+\infty} (\vec{S}_i \vec{s}_i + \vec{s}_i \vec{S}_{i+1}) = -2JSs \sum_{-\infty}^{+\infty} (\sigma_i + \sigma_{i+1}) \vec{u}_{zi} \quad \text{Eq SIII.1}$$

where vector \vec{u}_i is a unit vector and $\sigma_i = \pm 1$, and J is the sum of the interactions with the nearest neighbors.

When the field is applied parallel to the z axis, the Zeeman term can be written:

$$H = -g\mu_B SH \sum_{-\infty}^{+\infty} \sigma_i - g\mu_B sH \sum_{-\infty}^{+\infty} \vec{u}_{zi} \quad \text{Eq SIII.2}$$

Thus, total Hamiltonian becomes as below:

$$H = -2JSs \sum_{-\infty}^{+\infty} (\sigma_i + \sigma_{i+1}) \vec{u}_{zi} - g\mu_B SH \sum_{-\infty}^{+\infty} \sigma_i - g\mu_B sH \sum_{-\infty}^{+\infty} \vec{u}_{zi} \quad \text{Eq SIII.3}$$

The partition function is simply given by:

$$\begin{aligned} Z &= \sum_{\{\sigma_i\}} \int \frac{d\Omega_0}{4\pi} \int \frac{d\Omega_1}{4\pi} \dots \int \frac{d\Omega_N}{4\pi} \exp(-\beta H) \\ &= \sum_{\{\sigma_i\}} \int \prod_{i=1}^N \frac{d\Omega_i}{4\pi} \exp(-\beta H) \end{aligned} \quad \text{Eq SIII.4}$$

where $d\Omega_i$ is the element of solid angle for the vector \vec{u}_i and $\beta = 1/k_B T$. Let us introduce $K = -2JSs\beta$ (> 0), $h_S = g_S\mu_B SH\beta$, and $h_s = g_s\mu_B sH\beta$. Then, the summation for the isotropic spins yields:

$$A = \iint \frac{d\Omega_i}{4\pi} \exp\left[(-K(\sigma_i + \sigma_{i+1}) + h_s)\vec{u}_{zi}\right] \quad \text{Eq SIII.5}$$

The integration over the degrees of freedom of the isotropic spins can be made using a technique described by Fisher (Fisher 1964):

$$A = \frac{1}{2} \int_0^\pi \exp\left[(-K(\sigma_i + \sigma_{i+1}) + h_s)\cos\theta_i\right] \sin\theta_i d\theta_i = \frac{\sinh[h_s - K(\sigma_i + \sigma_{i+1})]}{[h_s - K(\sigma_i + \sigma_{i+1})]} \quad \text{Eq SIII.6}$$

by applying the following formula:

$$d\Omega = \sin\theta d\theta d\phi, \quad \frac{1}{2} \int_0^\pi \exp(a\cos\theta) \sin\theta d\theta = \frac{\sinh a}{a}$$

Thus, the partition function of the system can be written:

$$Z = \sum_{\sigma_1=\pm 1} \sum_{\sigma_2=\pm 1} \cdots \sum_{\sigma_N=\pm 1} \prod_{i=1}^{i=N} \frac{\sinh[h_s - K(\sigma_i + \sigma_{i+1})]}{[h_s - K(\sigma_i + \sigma_{i+1})]} \exp\left(\frac{h_s}{2}(\sigma_i + \sigma_{i+1})\right) \quad \text{Eq SIII.7}$$

where the magnetic field term has been trivially rearranged. If we define a term inside the multiplication operator as below:

$$T(\sigma_i, \sigma_{i+1}) = \frac{\sinh[h_s - K(\sigma_i + \sigma_{i+1})]}{[h_s - K(\sigma_i + \sigma_{i+1})]} \exp\left(\frac{h_s}{2}(\sigma_i + \sigma_{i+1})\right) \quad \text{Eq SIII.8}$$

the transfer matrix can be identified as following:¹³

$$\begin{pmatrix} T_{++} & T_{+-} \\ T_{-+} & T_{--} \end{pmatrix} = \begin{pmatrix} \frac{\sinh(h_s - 2K)}{h_s - 2K} \exp(h_s) & \frac{\sinh(h_s)}{h_s} \\ \frac{\sinh(h_s)}{h_s} & \frac{\sinh(h_s + 2K)}{h_s + 2K} \exp(-h_s) \end{pmatrix} \quad \text{Eq SIII.9}$$

Thus, from Eq SIII.7:

$$Z = \text{Tr}(T^N)$$

and hence:

$$Z = \lambda_+^N + \lambda_-^N,$$

where λ_+ and λ_- are the eigenvalues of T with $\lambda_+ > \lambda_-$. For large N , the first term dominates and we find that:

$$Z \approx \lambda_+^N \quad \text{Eq SIII.10}$$

and from Eq SIII.9, we have:

$$\begin{aligned} \det \begin{pmatrix} T_{++} - \lambda & T_{+-} \\ T_{-+} & T_{--} - \lambda \end{pmatrix} &= 0 \\ \Rightarrow \lambda^2 - (T_{++} + T_{--})\lambda + T_{++}T_{--} - T_{+-}^2 &= 0 \\ \Rightarrow \lambda_+ &= \frac{T_{++} + T_{--}}{2} + \frac{1}{2} \sqrt{(T_{++} - T_{--})^2 + 4T_{+-}^2} \end{aligned} \quad \text{Eq SIII.11}$$

Hence, the normalized magnetization can be written:

$$\left\langle \sum_{i=1}^N u_{zi} \right\rangle = N \langle u_{zi} \rangle = \frac{1}{Z} \frac{\partial Z}{\partial h_s} = \frac{\partial \ln Z}{\partial h_s} = \frac{N \partial \ln \lambda_+}{\partial h_s} \quad \text{Eq SIII.12}$$

$$\left\langle \sum_{i=1}^N \sigma_i \right\rangle = N \langle \sigma_i \rangle = \frac{1}{Z} \frac{\partial Z}{\partial h_s} = \frac{\partial \ln Z}{\partial h_s} = \frac{N \partial \ln \lambda_+}{\partial h_s} \quad \text{Eq SIII.13}$$

¹³ See section I.5 to compare with 1D Ising model.

Low field approximation (M vs H is linear)

Supposing that we are at the limit of weak field, T_{++} and T_{--} can be developed as below in the second-order approximation in order to obtain susceptibility:

$$T_{++} = \frac{\sinh 2K}{2K} - \frac{2K \cosh 2K - \sinh 2K}{4K^2} h_s + \frac{1}{2} \frac{4K^2 \sinh 2K - 4K \cosh 2K + 2 \sinh 2K}{8K^3} h_s^2 + \frac{\sinh 2K}{2K} h_s - \frac{2K \cosh 2K - \sinh 2K}{4K^2} h_s h_s + \frac{\sinh 2K}{2K} \frac{h_s^2}{2} \quad \text{Eq SIII.14}$$

$$T_{--} = \frac{\sinh 2K}{2K} + \frac{2K \cosh 2K - \sinh 2K}{4K^2} h_s + \frac{1}{2} \frac{4K^2 \sinh 2K - 4K \cosh 2K + 2 \sinh 2K}{8K^3} h_s^2 - \frac{\sinh 2K}{2K} h_s - \frac{2K \cosh 2K - \sinh 2K}{4K^2} h_s h_s + \frac{\sinh 2K}{2K} \frac{h_s^2}{2} \quad \text{Eq SIII.15}$$

and T_{+-} can be developed in a same way to give:

$$T_{+-} = T_{-+} = 1 + \frac{h_s^2}{6} \quad \text{Eq SIII.16}$$

Hence, Eq SIII.11 leads to:

$$\lambda_+ = 1 + \frac{\sinh 2K}{2K} + h_s^2 \left[\frac{4K^2 \sinh 2K - 4K \cosh 2K + 2 \sinh 2K}{16K^3} + \frac{1}{2} \left(\frac{2K \cosh 2K - \sinh 2K}{4K} \right)^2 + \frac{1}{6} \right] + h_s^2 \left[\frac{\sinh 2K}{4K} + \frac{\sinh^2 2K}{8K^2} \right] - h_s h_s \left[\frac{2K \cosh 2K - \sinh 2K}{4K^2} + \frac{\sinh 2K (2K \cosh 2K - \sinh 2K)}{8K^3} \right] \quad \text{Eq SIII.17}$$

From Eq SIII.12 and Eq SIII.13, the normalized magnetization, $\langle u_z \rangle$ and $\langle \sigma \rangle$, can be given as:

$$\langle u_z \rangle = \frac{\partial \ln \lambda_+}{\partial h_s} = \frac{1}{\lambda_+} \frac{\partial \lambda_+}{\partial h_s} = \left(1 + \frac{\sinh 2K}{2K} \right)^{-1} A(K) h_s - B(K) h_s \quad \text{Eq SIII.18}$$

and:

$$\langle \sigma \rangle = \frac{\partial \ln \lambda_+}{\partial h_s} = \frac{1}{\lambda_+} \frac{\partial \lambda_+}{\partial h_s} = -B(K) h_s + C(K) h_s \quad \text{Eq SIII.19}$$

where:

$$A(K) = \left[\frac{4K^2 \sinh 2K - 4K \cosh 2K + 2 \sinh 2K}{8K^3} + \left(\frac{2K \cosh 2K - \sinh 2K}{4K} \right)^2 + \frac{1}{3} \right]$$

$$B(K) = \frac{2K \cosh 2K - \sinh 2K}{4K^2}$$

$$C(K) = \frac{\sinh 2K}{2K} \quad \text{Eq SIII.20}$$

and:

$$(\lambda_+)^{-1} \approx \left(1 + \frac{\sinh 2K}{2K}\right)^{-1}$$

at the zero order in zero field. Thus, total magnetization can be written as:

$$\begin{aligned} \mu &= g_s \mu_B S \langle u_z \rangle + g_s \mu_B S \langle \sigma \rangle \\ &= g_s \mu_B S \left[\frac{A(K)}{1 + C(K)} h_s - B(K) h_s \right] + g_s \mu_B S [-B(K) h_s + C(K) h_s] \\ &= \beta H \left[\frac{A(K)}{1 + C(K)} g_s^2 \mu_B^2 S^2 - 2B(K) g_s g_s S \mu_B^2 + C(K) g_s^2 \mu_B^2 S^2 \right] \end{aligned} \quad \text{Eq SIII.21}$$

and hence:

$$\frac{\chi T}{C_{1/2}} = \frac{A(K)}{1 + C(K)} (g_s S)^2 - 2B(K) g_s g_s S + C(K) (g_s S)^2 \quad \text{Eq SIII.22}$$

where $C_{1/2} = N \mu_B^2 / k_B$ that is Curie constant for $S = 1/2$. This expression was used to simulate the data of compound **4** (Figure III.28).

Quasi-1D model at low temperature

In order to describe the topology and the main characteristics of the phase diagram when the magnetic field is applied along the easy axis, results from the 1D model without the low-field approximation are necessary. Eq SIII.11 gives:

$$\frac{\partial \lambda_+}{\partial h_s} = \frac{(T_{++} + T_{--})}{\sqrt{(T_{++} + T_{--})^2 + 4T_{+-}^2}} \lambda_+ \quad \text{Eq SIII.23}$$

as we have following relations:

$$\frac{\partial T_{++}}{\partial h_s} = T_{++}, \quad \frac{\partial T_{--}}{\partial h_s} = -T_{--}, \quad \frac{\partial T_{+-}}{\partial h_s} = 0$$

Therefore, the normalized magnetization for Ising spin is as below without any approximation:

$$\langle \sigma \rangle = \frac{1}{\lambda_+} \frac{\partial \lambda_+}{\partial h_s} = \frac{(T_{++} + T_{--})}{\sqrt{(T_{++} + T_{--})^2 + 4T_{+-}^2}} \quad \text{Eq SIII.24}$$

In the low temperature limit, Eq SIII.24 gives saturation of the magnetization at low field. Hence, Eq SIII.24 can be simplified as below through the Taylor expansion of field in second order:

$$\langle \sigma \rangle = \frac{C(K) h_s - B(K) h_s}{\sqrt{1 + [C(K) h_s - B(K) h_s]^2}} \quad \text{Eq SIII.25}$$

Let us now consider interchain couplings only between Ising spins. Introducing a unique coupling constant (J') for all interchain interactions, the Hamiltonian becomes:

$$H = -2JS \sum_{i,j} (\sigma_i + \sigma_{i+1}) \vec{u}_{zi,zj} - g\mu_B SH \sum_{i,j} \vec{\sigma}_{i,j} - g\mu_B sH \sum_{i,j} \vec{u}_{zi,zj} - 2J'S^2 \sum_{i,j,j'} \sigma_{i,j} \sigma_{i,j'} \quad \text{Eq SIII.26}$$

where the sum over j' in the last term is extended over all the neighboring pairs of the chain j .

At the mean field approximation, the last term becomes:

$$\begin{aligned} H_{\perp, MF} &= -2J'S^2 \sum_{i,j,j'} \left[\langle \sigma_{i,j} \rangle + \delta\sigma_{i,j} \right] \left[\langle \sigma_{i,j'} \rangle + \delta\sigma_{i,j'} \right] \\ &= -2J'S^2 \sum_{i,j,j'} \left[\langle \sigma_{i,j} \rangle \langle \sigma_{i,j'} \rangle + \delta\sigma_{i,j} \langle \sigma_{i,j'} \rangle + \delta\sigma_{i,j'} \langle \sigma_{i,j} \rangle \right] \\ &= -2J'S^2 \sum_{i,j,j'} \left[\sigma_{i,j} \langle \sigma_{i,j'} \rangle + \sigma_{i,j'} \langle \sigma_{i,j} \rangle + \text{const} \right] \\ &= -2J'S^2 \sum_{i,j,j'} \left[\sigma_{i,j} \langle \sigma_{i,j'} \rangle + \sigma_{i,j'} \langle \sigma_{i,j} \rangle \right] \\ &= -4J'S^2 \sum_{i,j,j'} \langle \sigma \rangle \sigma_{i,j} \sum_{j'} 1 \\ &= -2zJ'S^2 \sum_{i,j} \langle \sigma \rangle \sigma_{i,j} \end{aligned} \quad \text{Eq SIII.27}$$

The above expressions should be generalized in the antiferromagnetic phase considering two sub-lattices, A and B. In this model, we suppose interchain interactions only between two different sub-lattices. Hence, the generalized Hamiltonian can be written:

$$H_{\perp, MF} = -2zJ'S^2 \left[\sum_{i,j \in A} \left[\sigma_{i,j} \langle m_B \rangle \right] + \sum_{i,j \in B} \left[\sigma_{i,j} \langle m_A \rangle \right] \right]$$

that gives total Hamiltonian for the sub-lattice A as below:

$$H = -2J \sum_{i,j \in A} (\sigma_i + \sigma_{i+1}) \vec{u}_{zi,zj} - \sum_{i,j \in A} \sigma_{i,j} (g_S \mu_B SH + 2zJ'S^2 \langle m_B \rangle) - \sum_{i,j} \vec{u}_{zi,zj} (g\mu_B sH) \quad \text{Eq SIII.28}$$

Therefore, the effective value of h_S for the sub-lattice A is:

$$h_{S,eff}^A = h_S + \frac{2zJ'S^2}{k_B T} \langle m_B \rangle \quad \text{Eq SIII.29}$$

and for the sub-lattice B, it gives:

$$h_{S,eff}^B = h_S + \frac{2zJ'S^2}{k_B T} \langle m_A \rangle \quad \text{Eq SIII.30}$$

By applying Eq SIII.29 and Eq SIII.30 to Eq SIII.25, we obtain the normalized magnetizations ($h = \mu_B H \beta$):

$$m_A = \frac{\left[C(K)g_s S - B(K)g_s s \right] h - \frac{C(K)2z|J'|S^2}{k_B T} m_B}{\sqrt{1 + \left[\left(C(K)g_s S - B(K)g_s s \right) h - \frac{C(K)2z|J'|S^2}{k_B T} m_B \right]^2}} \quad \text{Eq SIII.31}$$

that can be expressed as below:

$$m_A = \frac{b - m_B}{\sqrt{(b - m_B)^2 + \alpha^2}} \quad \text{Eq SIII.32}$$

and the expression for m_B can be done in a same way:

$$m_B = \frac{b - m_A}{\sqrt{(b - m_A)^2 + \alpha^2}} \quad \text{Eq SIII.33}$$

where

$$b = \frac{(C(K)g_s S - B(K)g_s s)h}{C(K) \frac{2z|J'|S^2}{k_B T}}$$

and

$$\alpha = \frac{k_B T}{2z|J'|S^2 C(K)}$$

Magnetic susceptibility in quasi-1D model

In quasi-1D regime, magnetic susceptibility (χ_{Q1D}) before the magnetic transition can be defined in a relation with 1D susceptibility (χ_{1D}) as below:

$$M = \chi_{Q1D} H = \chi_{1D} (H + H_{\text{int}}) \quad \text{Eq SIII.34}$$

where H_{int} is the internal field induced by the presence of the interchain couplings. From the Eq SIII.27, we can define internal field as below:

$$\begin{aligned} H_{\perp} &= -2zJ'S^2 \sum_{i,j} \langle \sigma \rangle \sigma_{i,j} \\ &= \frac{2zJ'S^2 \langle \sigma \rangle}{g\mu_B S} \left(-g\mu_B S \sum_{i,j} \sigma_{i,j} \right) \\ &= H_{\text{int}} \left(-g\mu_B S \sum_{i,j} \sigma_{i,j} \right) \end{aligned}$$

where two different sub-lattices are considered identical as we are looking at the paramagnetic state. Hence, H_{int} can be written:

$$h_{\text{int}} = \frac{g\mu_B H_{\text{int}} S}{k_B T} = \frac{2zJ'S^2 \langle \sigma \rangle}{k_B T} \quad \text{Eq SIII.35}$$

By introducing Eq SIII.35 to Eq SIII.18 and Eq SIII.19, we have:

$$\langle u_z \rangle = \left(1 + \frac{\sinh 2K}{2K} \right)^{-1} A(K)h_s - B(K)h_s - \frac{B(K)2zJ'S^2}{k_B T} \langle \sigma \rangle \quad \text{Eq SIII.36}$$

and

$$\langle \sigma \rangle = -B(K)h_s + C(K)h_s + \frac{C(K)2zJ'S^2}{k_B T} \langle \sigma \rangle \quad \text{Eq SIII.37}$$

Then, Eq SIII.36 and Eq SIII.37 lead:

$$\langle \sigma \rangle = E(K)h_s + F(K)h_s \quad \text{Eq SIII.38}$$

and

$$\langle u_z \rangle = G(K)h_s - H(K)h_s \quad \text{Eq SIII.39}$$

where:

$$E(K) = \frac{-B(K)}{1 - C(K) \frac{2zJ'S^2}{k_B T}}$$

$$F(K) = \frac{C(K)}{1 - C(K) \frac{2zJ'S^2}{k_B T}}$$

$$G(K) = \frac{A(K)}{1 + C(K)} + \frac{[B(K)]^2 2zJ'S^2}{k_B T \left[1 - C(K) \frac{2zJ'S^2}{k_B T} \right]}$$

$$H(K) = B(K) \left[1 + \frac{F(K) 2zJ'S^2}{k_B T} \right]$$

Then, Eq SIII.21 gives the total magnetization:

$$\mu = g_s \mu_B s [G(K)h_s - H(K)h_s] + g_s \mu_B S [E(K)h_s + F(K)h_s] \quad \text{Eq SIII.40}$$

and hence,

$$\frac{\chi T}{C_{1/2}} = G(K)g_s^2 s - g_s g_s s [H(K) - E(K)] + F(K)g_s^2 S \quad \text{Eq SIII.41}$$

This expression was used to simulate the data of compound **4** (Figure III.28).

Phase diagram of antiferromagnetic-paramagnetic transition

Let us now search for the antiferromagnetic-paramagnetic transition line. As only interchain couplings between Ising spins are considered, it becomes equivalent with the phase diagram of the simple Ising model done by Coulon *et al* (Coulon et al. 2009).

In the antiferromagnetic state, each normalized sub-lattice magnetization is different ($m_A \neq m_B$), while they are identical in the paramagnetic state ($m_A = m_B$). Therefore, at the vicinity of the transition line we can define:

$$m_A = m_0 + \delta m \quad \text{Eq SIII.42}$$

and

$$m_B = m_0 - \delta m \quad \text{Eq SIII.43}$$

where $\delta m = 0$ at the transition line. By defining $f(m)$ as below:

$$f(m) = \frac{b-m}{\sqrt{(b-m)^2 + \alpha^2}} \quad \text{Eq SIII.44}$$

we have following relations from Eq SIII.32 and Eq SIII.33:

$$m_A = f(m_B) \text{ and } m_B = f(m_A).$$

In order to solve analytically, Taylor expansion for δm in the first order was applied, that leads to:

$$f(m_0 - \delta m) = m_0 + \delta m = f(m_0) - f'(m_0)\delta m$$

and

$$f(m_0 + \delta m) = m_0 - \delta m = f(m_0) + f'(m_0)\delta m$$

and hence,

$$m_0 = f(m_0) \quad \text{Eq SIII.45}$$

and

$$f'(m_0) = -1 \quad \text{Eq SIII.46}$$

at the phase transition. By applying Eq SIII.45 and Eq SIII.46 to the derivative of Eq SIII.44, the location of AF-paramagnetic transition line is given by:

$$b_c = (1 + \alpha^{2/3})\sqrt{1 - \alpha^{2/3}} \quad \text{Eq SIII.47}$$

On this transition line, two limits can be expressed as:

$$b_c^0 = 1 \quad (T \rightarrow 0)$$

$$\alpha_c^0 = 1 \quad (H \rightarrow 0)$$

that lead to following conditions at H_c^0 and T_c^0 on the AF-paramagnetic phase transition line:

$$(g_s S - g_s s)\mu_B H_c^0 = 2z|J|S^2 \quad \text{Eq SIII.48}$$

and

$$k_B T_C^0 = 2z |J| S^2 \frac{\sinh(4JSs\beta_c)}{4JSs\beta_c} \quad \text{Eq SIII.49}$$

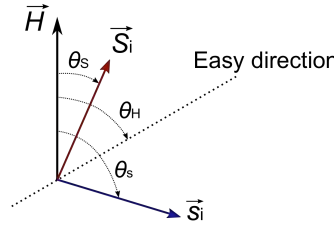
At the vicinity of $T = 0$ K, $B(K)/C(K)$ in Eq SIII.48 is supposed to be 1, therefore, $K \rightarrow \infty$. Considering the temperature dependence of $B(K)/C(K)$, Eq SIII.47 becomes:

$$\frac{H_c}{H_c^0} = \frac{13(1 + \alpha^{2/3})\sqrt{1 - \alpha^{2/3}}}{18 - 5\left(\tanh^{-1} 2K - \frac{1}{2K}\right)} \quad \text{Eq SIII.50}$$

where $g_s = g_S = 2$. This equation has been used to simulate the phase diagram of compound **4** shown in **Figure III.26e**.

Simple description of chain at 0 K

Let us now consider the chain of alternating anisotropic (S) and isotropic (s) spins with a same topology as described in **Scheme SIII.1**. In this model, a finite anisotropy of spin S is considered that is different from the previous description. The chain is under the external magnetic field (H) that forms angles of θ_S , θ_s , and θ_H with spin S , s , and the easy axis of the magnetization, respectively (**Scheme SIII.2**).



Scheme SIII.2

Those angles have following conditions:

$$0 < \theta_H < \frac{\pi}{2},$$

$$0 < \theta_s < \theta_H,$$

$$0 < \theta_S < \pi.$$

In this case, the corresponding Hamiltonian can be written:

$$H = -2J \sum_{-\infty}^{+\infty} (\vec{S}_i \cdot \vec{S}_i + \vec{S}_i \cdot \vec{S}_{i+1}) + D \sum_{-\infty}^{+\infty} \vec{S}_{iz}^2 - g\mu_B \sum_{-\infty}^{+\infty} \vec{S}_i \cdot \vec{H} - g\mu_B \sum_{-\infty}^{+\infty} \vec{s}_i \cdot \vec{H} \quad \text{Eq SIII.51}$$

The normalized total energy of the system per magnetic unit-cell, then, is given by:

$$\frac{E}{N} = -4JSs \cos(\theta_S - \theta_s) + DS^2 \sin^2(\theta_H - \theta_s) - (\mu_S \cos \theta_S + \mu_s \cos \theta_s) H \quad \text{Eq SIII.52}$$

where $\mu_S = g_S \mu_B S$ and $\mu_s = g_s \mu_B s$. In order to search the θ_s values that result a minimum of the energy at fixed D and θ_H , numerical calculations have been done to obtain **Figure SIII.5**.

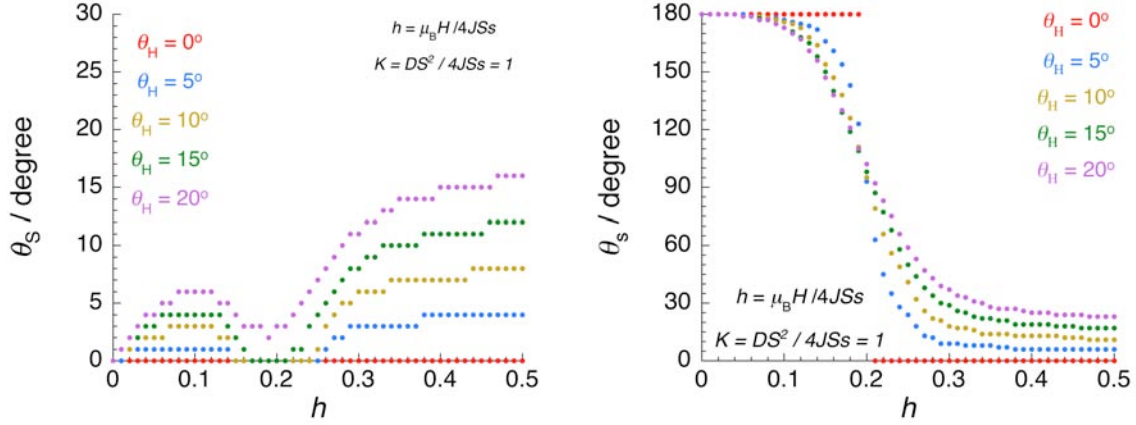


Figure SIII.5 The h -dependence of θ_S (left) and θ_s (right) at different directions of the external field.

Figure SIII.5 indicates that the isotropic spin reverse its direction when $h = 0.2$ independently with the direction of the external field. This means that when isotropic spins are alternatively positioned with anisotropic spins along the chain, the position of the inflection point in M vs H curves of polycrystalline samples will be same with the one for single crystal.

With the obtained set of (θ_S, θ_s) that minimize the energy, we can obtain the average magnetization of the polycrystalline sample by integrating magnetization over all θ_H :

$$\begin{aligned}
 \langle M \rangle &= \mu_S \langle \cos \theta_S \rangle + \mu_s \langle \cos \theta_s \rangle \\
 &= \mu_S \int_0^{\pi/2} \cos \theta_S \sin \theta_H d\theta_H + \mu_s \int_0^{\pi} \cos \theta_s \sin \theta_H d\theta_H
 \end{aligned} \tag{Eq SIII.53}$$

The integration in Eq SIII.53 could be done in numerical way by applying trapezoidal rule. The deduced h -dependence of the magnetization curves is shown in **Figure SIII.6** where $S = 9$ and $s = 5/2$.

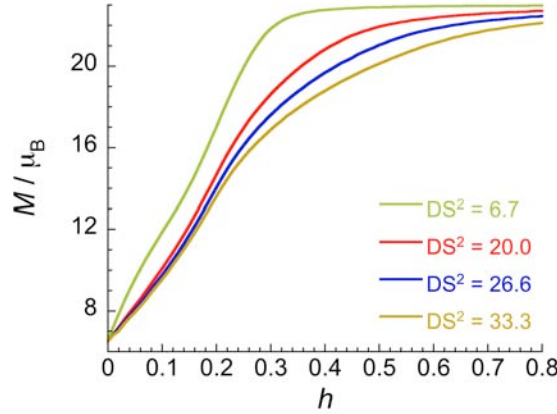
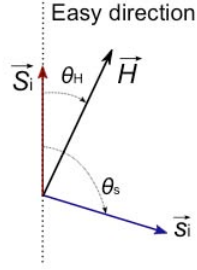


Figure SIII.6 The h -dependence of the average magnetization with different anisotropies of spin S .

To approach this model in an analytical way, we can assume the anisotropy of spin S is infinite. In this Ising limit, spin S stays on the axis of the anisotropy without being affected by the external field.



Scheme SIII.3

In this case, the corresponding normalized total energy can be written:

$$\frac{E}{N} = -4JSs \cos \theta_s - (\mu_s \cos \theta_H + \mu_s \cos(\theta_s - \theta_H)) H \quad \text{Eq SIII.54}$$

Through the derivation of Eq SIII.54, the equilibrium of θ_s at minimum energy depending on the external field can be expressed as below:

$$h = \frac{\sin \theta_s}{\sin(\theta_s - \theta_H)} \quad \text{Eq SIII.55}$$

For different θ_H , the variation of θ_s is plotted in **Figure SIII.7**, showing the continuous variation of θ_s as long as the θ_H is not zero. It is worth mentioning that the inflection point of the variation curves, at which the isotropic spin is inverted by the external field, appears at the same field (h) that indeed corresponds to the previously described model with a finite anisotropy on spin S (**Figure SIII.5**). It means that the main physics is originated from the presence of isotropic spin and the anisotropic one does not have a significant effect on the physical behavior of the system.

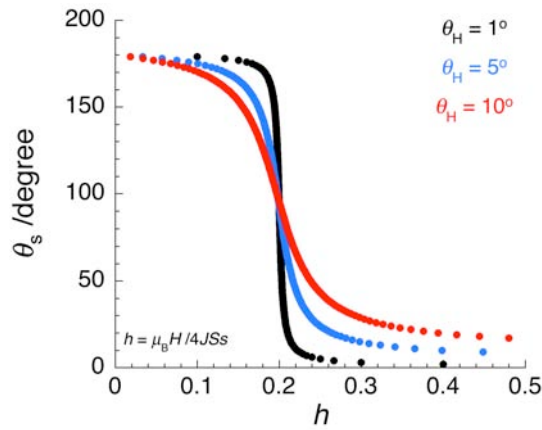


Figure SIII.7 The h -dependence of θ_s with different directions of the external field.

References

- Bernot K, Luzon J, Sessoli R, Vindigni A, Thion J, Richeter S, Leclercq D, Larionova J, Van der Lee A (2008) *J. Am. Chem. Soc.* 130, 1619.
- Brown ID, Altermatt D (1985) *Acta Crystallogr. B* 41, 244.
- Brown WF (1963) *Phys. Rev.* 130, 1677.
- Chaikin PM, Lubensky TC (2000) *Principles of Condensed Matter Physics*. Cambridge University Press.
- Coulon C, Clérac R, Wernsdorfer W, Colin T, Miyasaka H (2009) *Phys. Rev. Lett.* 102, 2.
- Coulon C, Moreau S (2000) *Physique statistique et thermodynamique*. Dunod
- Fisher ME (1964) *Am. J. Phys.* 32, 343.
- de Jongh LJ, Miedema AR (1974) *Adv. Phys.* 23, 1.
- Kushch LA, Sasnovskaya VD, Yagubskii EB, Khasanov, Salavat S, Simonov SV, Shibaeva RP, Korolev AV, Starichenko DV, Anokhin AO, Irkhin VY, Shvachko YN (2011) *Inorg. Chim. Acta* 378, 169.
- Labarta A, Iglesias O, Balcells L, Badia F (1993) *Phys. Rev. B* 48, 10240.
- Lecren L (2006) PhD Thesis. Bordeaux University
- Lecren L, Li Y-G, Wernsdorfer W, Roubeau O, Miyasaka H, Clérac R (2005a) *Inorg. Chem. Commun.* 8, 626.
- Lecren L, Roubeau O, Coulon C, Li Y-G, Le Goff XF, Wernsdorfer W, Miyasaka H, Clérac R (2005b) *J. Am. Chem. Soc.* 127, 17353.
- Lecren L, Roubeau O, Li Y-G, Le Goff XF, Miyasaka H, Richard F, Wernsdorfer W, Coulon C, Clérac R (2008) *Dalton Trans.* 755.
- Lecren L, Wernsdorfer W, Li Y, Roubeau O, Miyasaka H, Clérac R (2005c) *J. Am. Chem. Soc.* 127, 11311.
- Martin JD, Hess RF, Boyle PD (2004) *Inorg. Chem.* 43, 3242.
- Mayers BE, Berger L, Friedberg S (1969) *J. Appl. Phys.* 40, 1149.
- Miyasaka H, Nakata K, Lecren L, Coulon C, Nakazawa Y, Fujisaki T, Sugiura K-i, Yamashita M, Clérac R (2006) *J. Am. Chem. Soc.* 128, 3770.
- Miyasaka H, Nakata K, Sugiura K-i, Yamashita M, Clérac R (2004) *Angew. Chem. Int. Ed.* 43, 707.
- Miyasaka H, Takayama K, Saitoh A, Furukawa S, Yamashita M, Clérac R (2010) *Chem. –Eur. J.* 16, 3656.
- Néel L (1949) *Ann. Geophys.* 5, 99.
- O'Connor CJ (1982) *Prog. Inorg. Chem.* 29, 203.
- Otwinowski Z, Minor W (1997) *Macromolecular Crystallography Part A*, 276, 307.
- Romero I, Rodríguez M, Llobet A, Corbella M, Fernández G, Collomb M-N (2005) *Inorg. Chim. Acta* 358, 4459.
- Roubeau O, Clérac R (2008) *Eur. J. Inorg. Chem.* 4325.
- Scalapino DJ, Imry Y, Pincus P (1975) *Phys. Rev. B* 11, 2042.
- Sheldrick GM (1997) *SHELXL97, Program for Crystal Structure Refinement*. University of Göttingen.
- Wernsdorfer W (2001) *Adv. Chem. Phys.* 118, 99.
- Wernsdorfer W (2008) *C. R. Chimie* 11, 1086.
- Wernsdorfer W, Clérac R, Coulon C, Lecren L, Miyasaka H (2005a) *Phys. Rev. Lett.* 95, 237203.
- Wernsdorfer W, Murugesu M, Tasiopoulos A, Christou G (2005b) *Phys. Rev. B* 72, 212406.
- Wu J-Z, Tanase S, Bouwman E, Reedijk J, Mills AM, Spek AL (2003) *Inorg. Chim. Acta* 351, 278.
- Yoo J, Wernsdorfer W, Yang E-C, Nakano M, Rheingold AL, Hendrickson DN (2005) *Inorg. Chem.* 44, 3377.
- Yoo J, Yamaguchi A, Nakano M, Krzystek, J., Streib WE, Brunel L-C, Ishimoto H, Christou G, Hendrickson DN (2001) *Inorg. Chem.* 40, 4604.
- Zhang W, Jeitler JR, Turnbull MM, Landee CP, Wei M, Willett RD (1997) *Inorg. Chim. Acta* 256, 183.

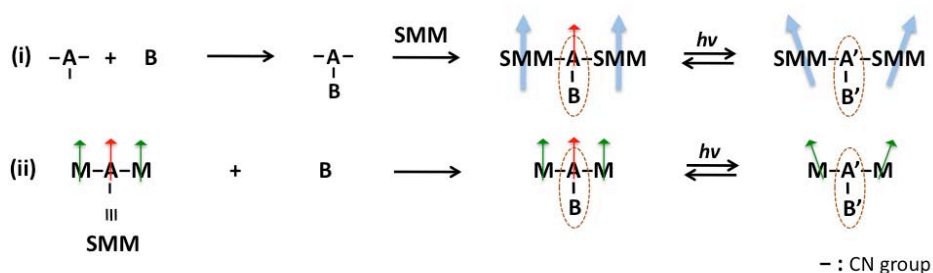
IV. Heterometallic molecular systems based on [Fe(bbp)(CN)₃]²⁻ building block

IV.1 Dinuclear [FeCo] system	128
IV.1.1 Synthetic approach, compounds 6 , 7 and 8	128
IV.1.2 Structures and magnetic properties of precursor complexes, 6 and 7	129
IV.1.3 Solid-state properties.....	132
IV.1.4 Solution properties	137
IV.1.5 Model of the protonation mechanism	142
IV.1.6 Concluding remark.....	146
IV.2 Trinuclear [Mn₂Fe] system	147
IV.2.1 Synthetic approach.....	147
IV.2.2 Structural description	148
IV.2.3 Magnetic properties.....	150
IV.2.4 Concluding remark.....	154
IV.3 Conclusion and perspectives	154
IV.4 Preliminary results	156
IV.4.1 Dinuclear [(bbp)Fe(CN) ₃ Co(PY5R ₂)] systems (R = Me, H, OH)	156
IV.4.2 Dinuclear [(Tp)Fe(CN) ₃ Co(PY5Me ₂)] ⁺ system	159
IV.4.3 Heterometallic [MnFe] systems	172
IV.5 Supporting information.....	174
IV.5.1 Experimental section.....	174
IV.5.2 Supporting figures.....	178
References	181

The second part of this thesis is dedicated to the design of novel electron transfer complexes and new SMMs with an ultimate goal to assemble them to realize a photo-switchable magnet. The main idea behind is to connect SMM building units with functional linkers that can adopt two magnetic states (see **Figure II.18(b)** in Chapter II). As a functional linker, the molecular electron transfer complexes have been considered in our group. Given the fact that the fundamental requirement for the metal-to-metal electron transfer is to have two metal ions, A and B, two different approach can be imagined (Scheme IV.1): (i) Molecular precursors of A and B metal ions are assembled to make a dinuclear AB complex, and then this dinuclear A-B complex is assembled with SMMs; (ii) A trinuclear M-A-M complex (M being other metal ions), that behaves as a SMM, is designed in advance, and then a molecular precursor of B is coordinated to A metal in this trinuclear complex.

Based on the literature reviewed in Chapter II, the fascinating electron transfer properties of Prussian blue materials have been observed in several discrete molecular complexes based on Fe/Co couples (see section II.2.2 in Chapter II), including [Fe₄Co₄] cube (**65** in Chapter II), [Fe₂Co₂] squares

(66 – 68 in Chapter II), linear [Fe₂Co] (69 in Chapter II), are reported to date (Li et al. 2008; Liu et al. 2012; Nihei et al. 2012; Nihei et al. 2011; Siretanu et al. 2011; Zhang et al. 2010). On the other hand, keeping in mind that Fe ion should be in the middle of the trinuclear complex for the second strategy, a [Mn-Fe-Mn] trinuclear complex was found to show a SMM behavior (33 in section II.1.2.2 of Chapter II) and furthermore, SCM behavior through assembling them. In this regard, we have envisaged two strategies: (i) Preparation of a dinuclear complex of one Fe and one Co (A and B being Fe and Co), in order to provoke an electron transfer property, with trans-coordinating abilities opened on Fe center; (ii) Design of a [Mn-Fe-Mn] trinuclear complex exhibiting a SMM behavior, while having one available coordinating ability on Fe center.



Scheme IV.1

One method for synthesizing heterometallic molecular complexes relies on the use of building block approach where metal ions are linked by cyanido bridging ligands (Beltran et al. 2005; Shatruck et al. 2009). This method exploits the predictable coordination chemistry of the cyanido linkage as one cyanide ion is expected to coordinate two metal centers on each end in an approximate linear geometry. Furthermore, the introduction of well-designed capping ligands for the cyanidometal precursor plays a crucial role as it can control the nuclearity, topology, and the dimensionality of resulting products. A typical bimetallic complex preparation involves two metal building units, where one unit features one or more terminal cyanide ligands and the other unit bears one or more coordination sites occupied by labile solvent molecules.

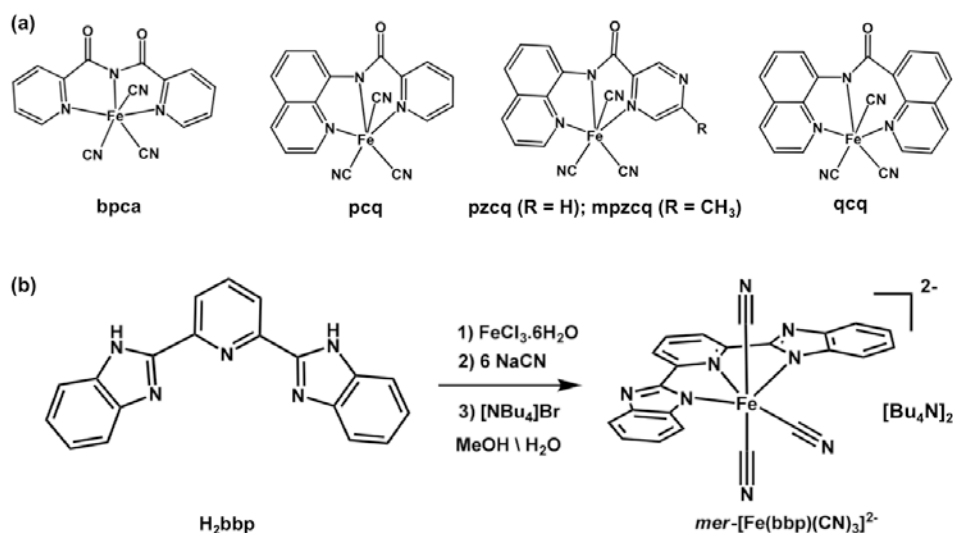
Given the fact that both of our strategies (Scheme IV.1), for a dinuclear [FeCo] complex and a trinuclear [Mn₂Fe] complex, require Fe^{III} sites, we carefully made a choice for Fe^{III} building blocks possessing three cyanido ligands. Indeed, the use of tricyanidoferrate(III) with tridentate facially coordinate blocking ligands have led to numerous cyanido low-dimensional heterometallic systems including electron-transfer complexes and SMMs (see section II.2.2 in Chapter II). Along with *fac*-Fe^{III} compounds, some meridionally capped precursors (*mer*-[(L)Fe^{III}(CN)₃]ⁿ⁻) have been also described in the literature: with L being, for example, bis(2-pyridylcarbonyl)amidate anion (bpca⁻), 8-(pyridine-2-carboxamido)quinoline anion (pcq⁻), 8-(pyrazine-2-carboxamido)-quinoline anion (pzcq⁻), 8-(5-methylpyrazine-2-carboxamido)quinoline anion (mpzcq⁻), 8-(2-quinoline-2-carboxamido)quinoline anion (qcq⁻), and dianion 2,6-*bis*-(benzimidazo-2-yl)pyridine (bbp²⁻) (Kim et al. 2009; Kim et al. 2007a; Kim et al. 2007b; Lescouëzec et al. 2004; Ni et al. 2005; Panja et al.; Senapati et al. 2012) (Scheme IV.2).

In our quest to obtain new [FeCo] and [Mn₂Fe] bimetallic complexes while leaving free cyanide groups that would further coordinate to Mn and Co ions, respectively, tricyanido *mer*-Fe^{III}

complexes attracted our interest. This T-shape geometry of cyanides could stabilize linear arrangement of “Mn-Fe-Mn” that could further assemble to a chain, while the one cyanido left could coordinate mononuclear Co complexes, or *vice versa* (Scheme IV.1). Thus, we have chosen the use of Fe^{III} building block having three cyanide groups in a meridional configuration. Under the assumption that the charge will play a key role in self-assembly process, we first limited our initial investigations to complexes containing bbp^{2-} in this thesis. This ligand has a planar geometry that enforces meridional configuration. The addition of excess cyanide in solution containing Fe^{3+} and bbp^{2-} would likely affords a $(\text{NBu}_4)_2[\text{Fe}^{\text{III}}(\text{bbp})(\text{CN})_3]$ complex (**6**, Scheme IV.2).

With a goal to design a $[\text{FeCo}]$ dinuclear unit, a pentadentate capping ligand would be suitable for Co building block, in order to give only one accessible position for the cyanide of **6**. On the other hand, tetradentate planar ligand such as salen-type ligand would be appropriate for a Mn building block, to make a trinuclear complex. In addition, this type of Mn building blocks is also attractive for preparing SMMs due to the available *trans* coordinating sites along their Jahn-Teller (JT) axis corresponding to their local magnetic anisotropy easy axis. Therefore, as complementary metal building blocks to assemble with complex **6**, we selected the following precursors, $[\text{Co}(\text{PY5Me}_2)(\text{H}_2\text{O})](\text{BF}_4)_2$ (**7**) (PY5Me₂: 2,6-bis(1,1-bis(2-pyridyl)ethyl)pyridine) and $[\text{Mn}_2(\text{saltmen})_2(\text{ReO}_4)_2]$ (saltmen: N,N'-Bis(salicylidene)-1,1,2,2-tetramethylethylenediamine) (Miyasaka et al. 2004).

Herein, we present two heterometallic molecular systems: $[(\text{bbp})\text{Fe}(\text{CN})_3\text{Co}(\text{PY5Me}_2)] \cdot 2.5\text{CH}_3\text{OH}$ (**8**) and $\{[\text{Mn}(\text{saltmen})(\text{MeOH})]_2[\text{Fe}(\text{bbp})(\text{CN})_3]\} \cdot 4\text{CH}_3\text{OH}$ (**10**) that illustrate the success of our synthetic strategy. The other heterometallic complexes obtained in the frame of this work are also summarized in part IV.4.

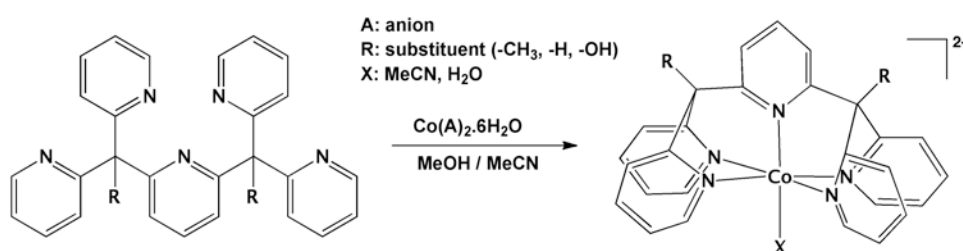


Scheme IV.2

IV.1 Dinuclear [FeCo] system

IV.1.1 Synthetic approach, compounds **6**, **7** and **8**

To direct the formation of a dinuclear complex, the molecular building block approach was exploited, as mentioned in introduction. Treatment of bbp with $\text{FeCl}_3 \cdot 6\text{H}_2\text{O}$ in the presence of an excess of NaCN readily affords $\text{mer-}[\text{Fe}(\text{bbp})(\text{CN})_3]^{2-}$ in high yield ($\approx 90\%$) (Panja et al. 2012). The presence of excess aqueous cyanide is sufficiently basic to deprotonate the bbp ligand *in situ* (Scheme IV.2). Then, the cation exchange of the crude reaction mixture was performed through the addition of tetrabutylammonium bromide ($[\text{NBu}_4]\text{Br}$) in aqueous solution, to afford the corresponding complex **6**. As a Co^{II} building block, a pentadentate ligand PY5Me₂ was chosen as a capping ligand (Bechlars et al. 2010) that was synthesized by S. Calancea (PhD thesis, 2010 – 2013). By the simple metal-ligand bond formation between $\text{Co}(\text{BF}_4)_2 \cdot 6\text{H}_2\text{O}$ and PY5Me₂ in the mixture of methanol and acetonitrile, $[\text{Co}(\text{PY5Me}_2)(\text{H}_2\text{O})](\text{BF}_4)_2$ (**7**) was synthesized (Scheme IV.3). The pentadentate ligand blocks the coordination to Co ion, while leaving only one opened site occupied by a water molecule for the free cyanido bridging ligand of complex **6**. Complexes **6** and **7** are soluble in most common polar organic solvents making them promising building units for the construction of multinuclear complexes. In addition, the ligands from both Fe^{III} and Co^{II} complexes help to assemble each building block in a way to avoid the higher dimensionality of the final compound, and at the same time to shield magnetically the complex with neighboring ones. Furthermore, two free cyanide groups of the Fe^{III} complex in a trans configuration, which are not involved in the formation of dinuclear complexes, will be suitable later on to bind another metal complexes or SMM building units. By adding a methanolic solution of complex **6** to an acetonitrile solution of complex **7** in equimolar quantities, a discrete Fe-Co dinuclear complex, $[(\text{bbp})\text{Fe}(\text{CN})_3\text{Co}(\text{PY5Me}_2)] \cdot 2.5\text{CH}_3\text{OH}$ (**8**), was prepared. It is worth mentioning that structurally similar [FeCo] dinuclear complexes are obtained by performing the above reaction in different mixture of solvents and also by changing the methyl substituents on PY5 ligands. Preliminary results on these complexes are summarized in annexes IV.4.



Scheme IV.3

The stretching band of the cyanide groups for **6** is seen in the infrared spectrum at 2109 cm^{-1} (Figure IV.1). In compound **8**, this band is shifted in higher energy with the splitting in three, 2118 , 2137 , and 2161 cm^{-1} (Figure IV.1), indicating the formation of cyanido-bridged compounds with terminal cyanides left. The absorption for the bridging cyanido ligand is likely attributed to the highest energy one with a small intensity (2161 cm^{-1}) that exactly falls into the range for bridging CN^- in $\text{Fe}^{\text{III}}_{\text{LS}}\text{-CN-Co}^{\text{II}}_{\text{HS}}$ systems ($2153 - 2169\text{ cm}^{-1}$) (Berlinguette et al. 2005). The two cyanides left are split

in two different energies due to the presence of different short contact interactions in crystal packing, as discussed in the following (paragraph IV.1.3).

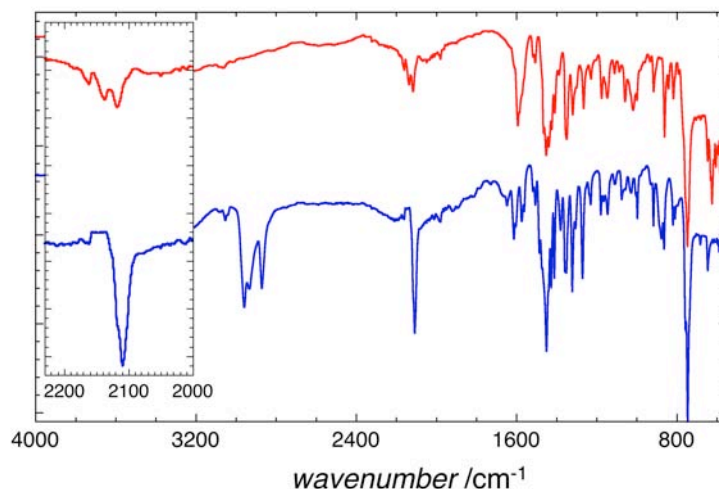


Figure IV.1 FT-IR spectra of compounds **6** (blue) and **8** (red) at 298 K, highlighting cyanide stretching in inset.

IV.1.2 Structures and magnetic properties of precursor complexes, **6** and **7**

Structural descriptions. Single crystals of complex **6** and **7** are characterized in order to verify the formation of the expected mononuclear structures (**Table IV.1**). The sheet-like blue crystals of **6** have been obtained by slow evaporation of methanol/water solution. The compound crystallizes in $P2_1$ and consists of $[\text{Fe}(\text{bbp})(\text{CN})_3]^{2-}$ anions, tetrabutylammonium cations, and interstitial solvent molecules. The asymmetric unit contains two $[\text{Fe}(\text{bbp})(\text{CN})_3]^{2-}$ units. The tridentate N_3 planar ligand (bbp) coordinates the Fe^{III} center in a meridional fashion and the three cyanide ligands occupy the remaining meridional sites (**Figure IV.2**). The distances between the iron(III) and the nitrogen of the bbp ligand vary in the range of 1.935(6) to 1.960(5) Å (**Table IV.2**), considerably shorter than the reported distances for high spin Fe^{III} complexes with the similar ligand, $\text{Fe}(\text{Me-bbp})\text{Cl}_3$ (2.111(3) – 2.168(3) Å) (Me-bbp: 2,6-bis(N-methylbenzimidazo-2-yl)pyridine) (Wang et al. 2003). These bond distances together with the Fe-C distances (1.897(8) – 1.978(7) Å) are in good agreement with those reported for the other cyanido-containing mononuclear Fe^{III} low-spin complexes. The Fe^{III} ion has distorted octahedral coordination geometry mainly due to the geometrical requirement of the bbp ligand. The uncoordinated nitrogen on the imidazole rings of the ligand and the nitrogen from the cyanides are interacting with the crystallization water molecules through the hydrogen bonds to form an extensive network. The void spaces in **6** are occupied by NBu_4^+ cations that are extremely disordered.

The yellow colored crystals of **7** were obtained by the ether vapor diffusion to the reaction solution. X-ray crystallographic analyses of **7** revealed an octahedral coordination environment for Co^{II} center, featuring five coordination sites blocked by a PY5Me_2 ligand and the other bound by a H_2O molecule: $[\text{Co}(\text{PY5Me}_2)(\text{H}_2\text{O})](\text{BF}_4)_2$ (**7**) (**Figure IV.3**, left). The five $\text{Co}^{\text{II}}\text{-N}_{\text{py}}$ distances for **7** are similar giving the mean $\text{Co}^{\text{II}}\text{-N}_{\text{py}}$ bond distances being 2.125(3) Å (**Table IV.2**). This value is similar to those observed in the previously reported high spin Co^{II} complex coordinated to the same ligand, $[\text{Co}(\text{PY5Me}_2)(\text{MeCN})](\text{PF}_6)_2$ ($\text{Co}^{\text{II}}\text{-N}_{\text{py}}$: 2.130(12) Å) (Zadrozny et al. 2010). It is worth to mention that the orange colored crystal could be also obtained as a minor byproduct from the same

crystallization set-up. X-ray crystallographic analyses of this crystal showed a distorted octahedral coordination environment for Co^{II} center, featuring five coordination sites blocked by a PY5Me₂ ligand and the other bound by a MeCN molecule: $[\text{Co}(\text{PY5Me}_2)(\text{MeCN})](\text{BF}_4)_2$ (**7a**) (**Figure IV.3**, right). The coordination sphere of **7a** is significantly distorted, leading one axis on the equatorial plane (average $\text{Co}^{\text{II}}\text{-N}$: 1.914(2) Å) is contracted compared to the others (average $\text{Co}^{\text{II}}\text{-N}$: 2.175(2) Å) (**Table IV.2**). In addition, the mean $\text{Co}^{\text{II}}\text{-N}_{\text{py}}$ bond distances for **7a** (2.061(2) Å) is slightly shorter than those for **7** (2.125(3) Å). These bonding features imply that the Co^{II} center in **7a** might be in low spin state, as observed in the literatures (Goodwin 2004; Hayami et al. 2011; Krivokapic et al. 2007). Although we could control the reaction condition to obtain only **7**, the isolation of pure **7a** was not possible to date. Therefore, we have done the following characterizations with **7**.

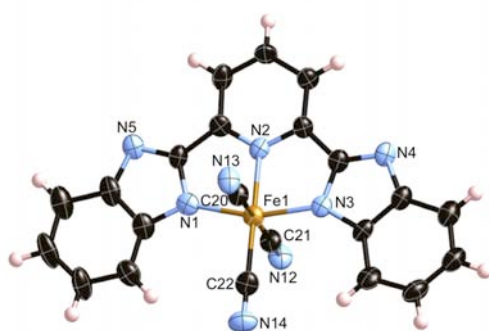


Figure IV.2 ORTEP-type view of the mononuclear complex **6** at 100 K with thermal ellipsoids at 30 % level. Yellow, Fe; blue, N; black, C; pink, H. Lattice solvents and counter cations are omitted for clarity.

Table IV.1 Crystallographic data of compounds **6**, **7**, and **7a**.

	6 (100 K)	7 (120 K)	7a (150 K)
Empirical formula	$\text{C}_{54}\text{H}_{95}\text{FeN}_{10}\text{O}_6$	$\text{C}_{29}\text{H}_{27}\text{B}_2\text{CoF}_8\text{N}_5\text{O}$	$\text{C}_{31}\text{H}_{28}\text{B}_2\text{CoF}_8\text{N}_6$
Formula weight, g mol^{-1}	1036.25	694.11	717.14
Crystal system	Monoclinic	Monoclinic	Triclinic
Space group	$P2_1$	$C2/c$	$P-1$
Wavelength, Å	0.71073	0.71073	0.71069
a , Å	21.267(2)	21.346(5)	11.367(3)
b , Å	11.4830(13)	12.362(5)	12.108(5)
c , Å	26.049(3)	12.855(4)	12.972(4)
α , °	90	90	59.314(2)
β , °	111.875(2)	120.033(13)	68.887(2)
γ , °	90	90	85.687(2)
V , Å ³	5903.4(11)	2936.5(17)	1419.25(8)
Z	2	4	2
ρ_{calcd} , Mg m^{-3}	1.166	1.570	1.678
μ , mm^{-1}	0.309	0.670	0.694
$^a R_1$ ($I > 2\sigma(I)$)	0.0846	0.0314	0.0459
$^b wR_2$ (all)	0.2525	0.0842	0.1284
GoF^a	1.028	1.058	1.034

^a $R_1 = \Sigma||F_o| - |F_c||/\Sigma|F_o|$, and ^b $wR_2 = [\Sigma w(F_o^2 - F_c^2)^2/\Sigma w(F_o^2)^2]^{1/2}$.

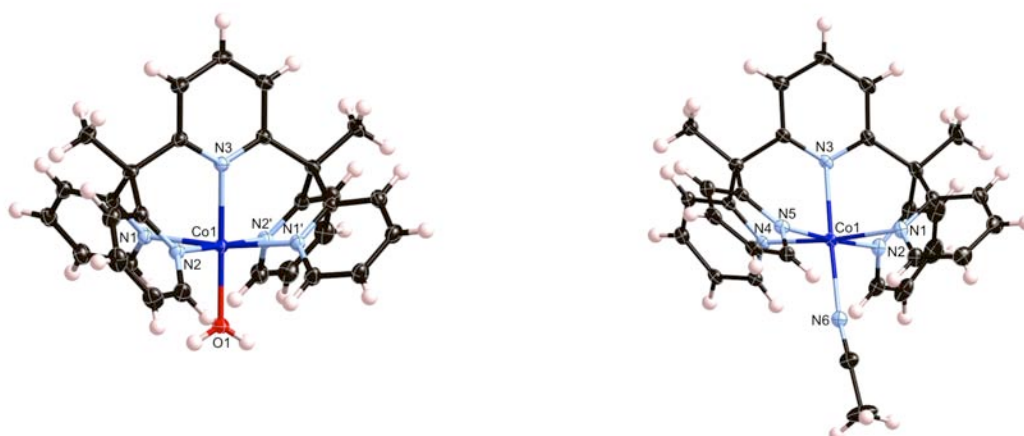


Figure IV.3 ORTEP-type view of the mononuclear complex **7** (120 K) and **7a** (150 K) with thermal ellipsoids at 50 % level. Yellow, Fe; blue, N; black, C; pink, H. Counter anions are omitted for clarity.

Table IV.2 Selected bond lengths [Å] and angles [°] for **6**, **7**, and **7a**.

6 (100 K)				7 (120 K)		7a (150 K)	
Fe1-N1	1.941(6)	Fe2-N6	1.949(5)	Co1-N1	2.141(1)	Co1-N1	2.157(2)
Fe1-N2	1.955(6)	Fe2-N7	1.960(5)	Co1-N2	2.133(2)	Co1-N2	1.906(2)
Fe1-N3	1.935(6)	Fe2-N8	1.950(6)	Co1-N3	2.093(2)	Co1-N3	2.173(3)
Fe1-C20	1.958(7)	Fe2-C42	1.959(7)	Co1-O6	2.057(2)	Co1-N4	2.149(2)
Fe1-C21	1.975(7)	Fe2-C43	1.971(7)			Co1-N5	1.922(2)
Fe1-C22	1.958(9)	Fe2-C44	1.897(8)			Co1-N6	2.220(3)
Fe1-N14-C22	179.4(8)	Fe2-C43-N16	179.1(8)	N7-Co1-O6	180.00(6)	N3-Co1-N6	177.7(9)

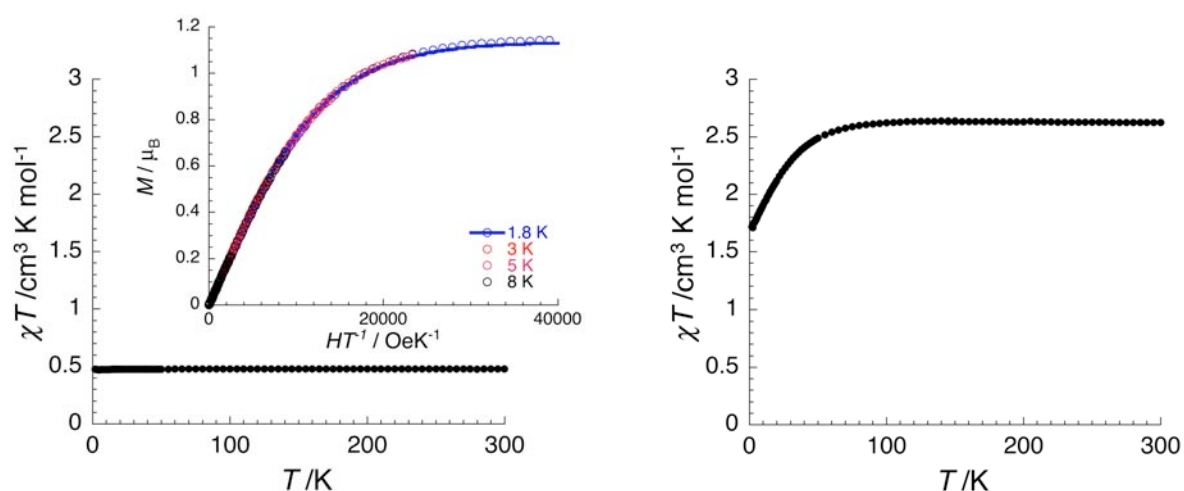


Figure IV.4 Temperature-dependence of the χT product of **6** (left) and **7** (right) collected in an applied field of 1000 Oe. Inset: M vs HT^{-1} of **6** at different temperatures. Solid line is fitting result with Brillouin function.

Magnetic properties. The temperature dependence of the χT product ($\chi = M/H$) for **6** shows nearly constant value of *ca.* $0.47 \text{ cm}^3 \text{Kmol}^{-1}$ in the range between 280 and 1.8 K (**Figure IV.4**, left).

This value is higher than the expected value ($0.375 \text{ cm}^3\text{Kmol}^{-1}$) for a Fe^{III} complex that contains one isotropic $S = 1/2$ ion, suggesting that orbital contributions to the magnetic moment are present with the g value of about 2.26. Consistent with this assumption fitting of the M vs H curve measured with an $S = 1/2$ Brillouin function (**Figure IV.4** (inset, left) and **Figure SIV.1**) indicates that g is equal to 2.27, a value that is consistent with those reported for other low spin cyanidoferrate(III) complexes (Kim et al. 2009; Kim et al. 2007a; Kim et al. 2007b; Lescouëzec et al. 2004; Ni et al. 2005; Panja et al.; Senapati et al. 2012).

The room temperature χT product for **7** reveals *ca.* $2.62 \text{ cm}^3\text{Kmol}^{-1}$ that remains constant down to 100 K (**Figure IV.4**, right). This value is also higher than the expected value ($1.875 \text{ cm}^3\text{Kmol}^{-1}$) for an isolated complex possessing an isotropic high spin Co^{II} ion ($S = 3/2$). The g value of **7** could be estimated at 2.36 from the room temperature χT product. The low temperature decrease in the χT product for **7** is associated with spin-orbit coupling of the high spin Co^{II} ion (Kahn 1993).

IV.1.3 Solid-state properties

The square-like blue crystals of **8** have been obtained directly from the tube reaction in which two solutions of metal precursors are layered to slowly diffuse. The compound **8** crystallizes as a neutral species in a monoclinic $P2_1/c$ space group (**Figure IV.5**). One of the cyanide groups in the equatorial plane of the Fe^{III} building unit, **6**, is coordinated to the axial position of the Co-precursor **7** to form a dinuclear complex with a $\{\text{Fe}(\mu\text{-CN})\text{Co}\}$ linkage. At 370 K, the Fe centers adopt distorted octahedral geometries showing Fe-N and Fe-C distances being $1.932(3) - 1.946(3)$ and $1.892(3) - 1.972(4)$ Å, respectively, as seen in structure of **6**. On the other hand, the average Co-N_{py} bond length is $2.128(2)$ Å without significant distortion, as observed in the precursor complex **7** that contains high spin Co^{II} (**Table IV.4**). Therefore, this comparison indicates the complex **8** at 370 K contains low spin Fe^{III} and high spin Co^{II} metal ions, that is also supported by the valence bond sum analysis and charge compensation. Two axial cyanido ligands on the Fe^{III} ions are left uncoordinated. In the crystal packing, the dinuclear complexes are stabilized through $\pi\cdots\pi$ interactions and short contacts between adjacent aromatic rings along the crystallographic a direction and in the ab plane (**Figure IV.6**). One of the terminal cyanides has also short contacts with the adjacent aromatic rings of PY5Me₂ ligands (**Figure IV.6**, left). The interstitial methanol molecules fill the void space in the crystal packing.

Knowing the presence of $\text{Fe}^{\text{III}}_{\text{LS}}$ and $\text{Co}^{\text{II}}_{\text{HS}}$ at 370 K from the single crystal diffraction study, we measured the magnetic susceptibility of **8** as a function of temperature to verify the occurrence of an eventual thermally induced electron transfer. The temperature-dependent χT product displays the S-shaped curve around 220 K that could be a signature of electron transfer process. The high temperature χT product is close to the expected value ($3.1 \text{ cm}^3\text{Kmol}^{-1}$) for $\text{Fe}^{\text{III}}_{\text{LS}}$ ($S = 1/2$, $g = 2.27$ obtained from the **6**) and $\text{Co}^{\text{II}}_{\text{HS}}$ ($S = 3/2$, $g = 2.36$ obtained from **7**) (**Figure IV.7**). Nevertheless, a Fe-Co electron transfer should involve a transformation of a paramagnetic $\{\text{Fe}^{\text{III}}_{\text{LS}}\text{-CN-Co}^{\text{II}}_{\text{HS}}\}$ unit into a diamagnetic $\{\text{Fe}^{\text{II}}_{\text{LS}}\text{-CN-Co}^{\text{III}}_{\text{LS}}\}$ pair (see **Figure I.11** in Chapter I), while experimentally a significant χT value ($0.93 \text{ cm}^3\text{Kmol}^{-1}$) is measured below 100 K. In order to clarify the origin of a partial electron transfer process or the possibility of another phenomenon involving a change of the electronic spin state, the crystallographic data collected at different temperatures, 370 and 90 K, were investigated in details.

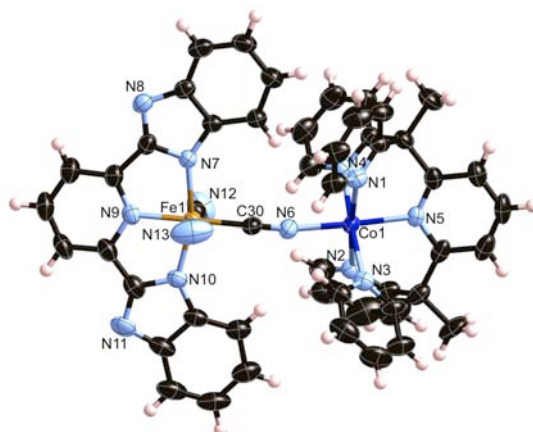


Figure IV.5 ORTEP-type view of the dinuclear complex $[(\text{bbp})\text{Fe}(\text{CN})_3\text{Co}(\text{PY5Me}_2)] \cdot 2.5\text{CH}_3\text{OH}$ (**8**) at 370 K with thermal ellipsoids at 50 % level. Yellow, Fe; blue, Co; skyblue, N; black, C; pink, H. Lattice solvents are omitted for clarity.

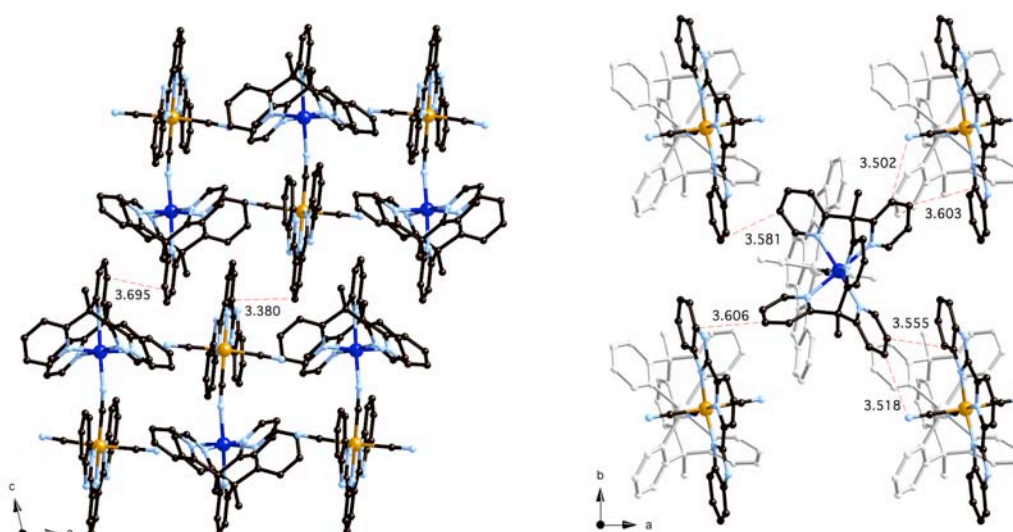


Figure IV.6 Packing diagram of **8** in the ac plane (left) and in the ab plane (right), illustrating intercomplex $\pi \cdots \pi$ interactions between adjacent PY5Me₂ ligands and adjacent bbbp/cyano ligands for data collected at 370 K. Ligands associated in the further layer along the crystallographic c direction are shown in silver (right). Lattice solvent molecules and hydrogen atoms are omitted for clarity.

At a first look, the temperature does not have a notable effect on the structure (at 90 and 370 K, **8** crystallizes in the same $P2_1/c$ monoclinic space group), unit-cell parameters (**Table IV.3**) and average bond distances (**Table IV.4**). Nevertheless, significant differences are seen on individual Co–N bond lengths and in the coordination geometry of the cobalt ion. A remarkable elongation on the Co–N1 and Co–N2 bonds was observed with values of 2.242(3) Å and 2.228(3) Å, respectively (from 2.191(2) Å and 2.182(3) Å at 370 K), while all other Co–N bond lengths decreased of about 0.1 Å. Consequently, the {Fe– μ -CN–Co} unit became more linear as judged by the evolution of the Co–N6–C30 angle from 168.2(3)° at 370 K to 172.0(3)°. The strong distortion on the coordination geometry is normally expected for a Co^{II} in its low spin state due to the Jahn-Teller (JT) effect induced by only one electron in the e_g orbital (Goodwin 2004; Krivokapic et al. 2007). It is also important to note that the experimental powder diffraction of [FeCo] at 298 K corresponds well to the simulated one from the single-crystal data at 270 K (**Figure SIV.2**). This result excludes the possibility of a mixture of different species responsible for the observed magnetic properties (**Figure IV.7**). Moreover, no proof of statistical structural disorder has been observed on the thermal ellipsoids of the atoms of the

complex at 90 K (**Figure IV.8**), demonstrating a full transformation of the Co coordination sphere during the spin-crossover process in the material upon lowering the temperature. The aforementioned features and the unvaried Fe-C bond lengths with temperature imply that there might be a temperature-dependent spin crossover on the Co^{II} ion from high spin state to low spin state, rather than the electron-transfer on the Fe-Co pair.

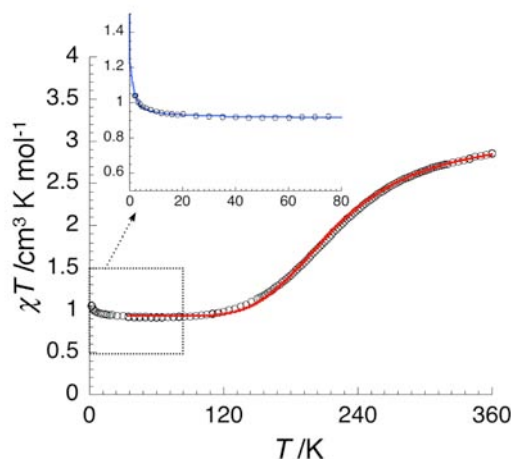


Figure IV.7 Temperature-dependence of the χT product of **8** (black empty circles) collected in an applied field of 1000 Oe and the red solid line represents the best fit based on the ideal solution model (see section I.3.1 in Chapter I). Inset, zoom of low temperature area highlighted by dotted line. Data in this area are fitted by applying the van Vleck equation in the weak field approximation based on dinuclear Heisenberg Hamiltonian ($H = -2J\mathbf{S}_{\text{Co}} \cdot \mathbf{S}_{\text{Fe}}$), as shown in blue line (see main text).

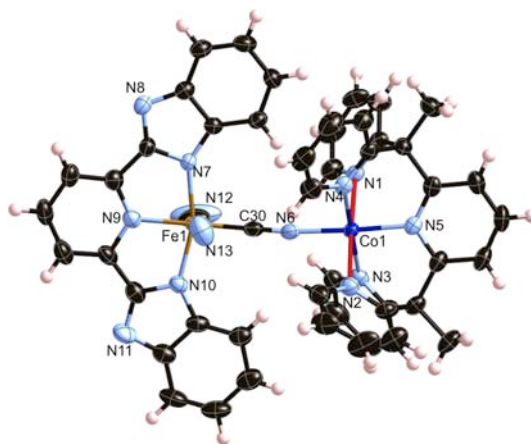


Figure IV.8 ORTEP-type view of the dinuclear complex **8** at 90 K with thermal ellipsoids at 50 % level. JT elongation is highlighted in red. Yellow, Fe; blue, Co; skyblue, N; black, C; pink, H. Lattice solvents are omitted for clarity.

In order to further support the Co^{II} spin crossover scenario in **8**, ^{57}Fe Mössbauer studies were performed at 298 and 4.2 K. As shown in **Figure IV.9**, a quadrupole doublet was observed at 4.2 K, and its Mössbauer parameters were found as $\delta = 0.002$ and $\Delta_{\text{EQ}} = 2.99 \text{ mm.s}^{-1}$ (δ is isomer shift and Δ_{EQ} is quadrupole splitting), that is characteristic for Fe^{III} in low spin state (Fultz 2011). As the temperature was raised, a low spin Fe^{III} doublet with $\delta = -0.052$ and $\Delta_{\text{EQ}} = 2.96 \text{ mm.s}^{-1}$ was still observed. The small difference on the isomer shift depending on the temperature is due to the relativistic second order Doppler shift (Greenwood et al. 1971). This confirms that there is no intramolecular electron-transfer process occurring between Co^{II} and Fe^{III} in the solid state depending on the temperature, as the electronic state of the iron ion was unchanged between 293 K and 4.2 K.

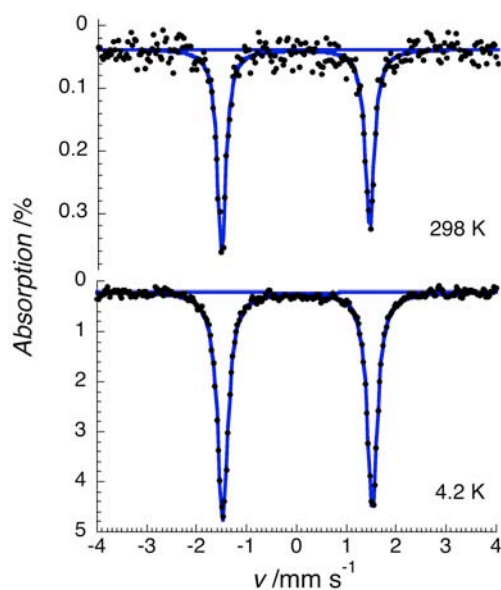
Table IV.3 Crystallographic data of compound **8**, collected at 370 and 90 K.

	370 K	90 K
Empirical formula	C ₁₀₇ H ₉₂ Co ₂ Fe ₂ N ₂₆ O ₅	C ₁₀₇ H ₉₂ Co ₂ Fe ₂ N ₂₆ O ₅
Formula weight, g mol ⁻¹	2051.63	2051.63
Crystal system	Monoclinic	Monoclinic
Space group	<i>P</i> 2 ₁ / <i>c</i>	<i>P</i> 2 ₁ / <i>c</i>
Wavelength, Å	0.71069	0.71069
<i>a</i> , Å	13.655(2)	13.560(1)
<i>b</i> , Å	14.348(2)	14.209(1)
<i>c</i> , Å	25.328(3)	24.965(2)
β , °	102.313(5)	103.148(3)
<i>V</i> , Å ³	4747.9(10)	4697.7(6)
<i>Z</i>	2	2
ρ_{calcd} , Mg m ⁻³	1.405	1.450
μ , mm ⁻¹	0.700	0.722
^a <i>R</i> ₁ (<i>I</i> > 2 σ (<i>I</i>))	0.0511	0.0500
^b <i>wR</i> ₂ (all)	0.1356	0.1364
GoF ^a	1.103	1.125

$$^a R_1 = \sum ||F_o| - |F_c|| / \sum |F_o|, \text{ and } ^b wR_2 = [\sum w(F_o^2 - F_c^2)^2 / \sum w(F_o^2)^2]^{1/2}.$$

Table IV.4 Selected bond lengths [Å] and angles [°] for **8**.

	370 K	90 K		370 K	90 K
av(Co-N)	2.108(3)	2.058(3)	av(Fe-N)	1.938(3)	1.934(3)
Co1-N1	2.191(2)	2.242(3)	av(Fe-C)	1.943(4)	1.948(4)
Co1-N2	2.182(3)	2.228(3)	Fe1-N7	1.946(3)	1.945(3)
Co1-N3	2.100(3)	1.999(3)	Fe1-N9	1.936(3)	1.928(3)
Co1-N4	2.106(3)	2.001(3)	Fe1-N10	1.932(3)	1.929(3)
Co1-N5	2.062(2)	1.958(3)	Fe1-C30	1.892(3)	1.890(4)
Co1-N6	2.009(3)	1.923(3)	Fe1-C31	1.972(4)	1.978(4)
Co1-N6-C49	168.2(3)	172.0(3)	Fe1-C32	1.966(4)	1.977(4)
			N6-C49-Fe1	178.0(3)	177.1(3)

**Figure IV.9** ⁵⁷Fe Mössbauer spectra of **8** collected at 298 K (top) and at 4.2 K (bottom). The dark points correspond to the experimental data, and the blue lines represent the spectral simulation for Fe^{III}_{LS}.

The spin crossover of the cobalt ion in **8** is also supported by the magnetic properties shown in **Figure IV.7** that are in agreement with a $\{\text{Fe}^{\text{III}}_{\text{LS}}\text{-CN-Co}^{\text{II}}_{\text{LS}}\}$ ground state observed below 100 K and a $\{\text{Fe}^{\text{III}}_{\text{LS}}\text{-CN-Co}^{\text{II}}_{\text{HS}}\}$ excited state thermally populated above 100 K. At 360 K, the χT product is not reaching a well-defined plateau as unfortunately measurements at higher temperatures led to an irreversible alteration of the compound induced by the loss of the interstitial solvent molecules observed by thermogravimetric analysis (**Figure SIV.3**). Nevertheless, as routinely done for spin-crossover systems, the χT vs. T data were well fitted between 25 and 360 K to an ideal solution model (see section I.3.1 in Chapter I)¹ with the following best set of parameters: $\chi T_{\text{LT}} = 3.19(4) \text{ cm}^3\text{Kmol}^{-1}$, $\chi T_{\text{HT}} = 0.94(1) \text{ cm}^3\text{Kmol}^{-1}$, $T_{1/2} = 228(2) \text{ K}$ and $\Delta H = 9.2(2) \text{ kJmol}^{-1}$. The χT_{LT} and χT_{HT} values for the low spin and high spin states corresponding well to the expected ones for $\{\text{Fe}^{\text{III}}_{\text{LS}}\text{-CN-Co}^{\text{II}}_{\text{LS}}\}$ and $\{\text{Fe}^{\text{III}}_{\text{LS}}\text{-CN-Co}^{\text{II}}_{\text{HS}}\}$ pairs respectively ($\text{Fe}^{\text{III}}_{\text{LS}}$: $S = 1/2$, $g \approx 2.26$; $\text{Co}^{\text{II}}_{\text{LS}}$: $S = 1/2$, $g \approx 2.19$ and $\text{Co}^{\text{II}}_{\text{HS}}$: $S = 3/2$, $g \approx 2.36$). Furthermore, it is worth noting that the obtained thermodynamic parameters, ΔH and $\Delta S = \Delta H/T_{1/2} = 40(1) \text{ JK}^{-1}\text{mol}^{-1}$, of the spin-crossover process are well in the range for a Co^{II} spin crossover (Goodwin 2004). Decreasing the temperature below 20 K, the small increase of the χT product evidences for the first time a ferromagnetic interaction, J , between $\text{Fe}^{\text{III}}_{\text{LS}}$ ($S_{\text{Fe}} = 1/2$) and $\text{Co}^{\text{II}}_{\text{LS}}$ ($S_{\text{Co}} = 1/2$) magnetic centers through the cyanido bridge (**Figure IV.7**). On the basis of dinuclear Heisenberg spin Hamiltonian, $\mathbf{H} = -2JS_{\text{Co}} \cdot \mathbf{S}_{\text{Fe}}$, the experimental susceptibility can be expressed by applying the van Vleck equation² in the weak field approximation:

$$\chi T = \frac{2Ng^2\mu_B^2}{k_B} \frac{1}{3 + \exp(-2J/k_B T)} \quad \text{Eq IV.1}$$

The exchange coupling was estimated at + 0.68(9) K from the fitting of the experimental data below 80 K (with $g_{\text{av}} = 2.21(5)$). As a consequence of this intramolecular ferromagnetic interaction, the dinuclear **8** complex possesses an $S_{\text{T}} = 1$ spin ground state.

This complete set of physical characterizations allows us to conclude that, to the best of our knowledge, **8** is the only known complex exhibiting a cobalt(II) spin crossover in a heterobimetallic system.

¹ The following equation was used with X being the χT product; X_{LT} and X_{HT} being the limit values of the χT product at low and high temperatures, respectively.

$$X = X_{\text{LT}} + \frac{X_{\text{HT}} - X_{\text{LT}}}{1 + \exp\left(\frac{\Delta H}{R} \left(\frac{1}{T} - \frac{1}{T_{1/2}}\right)\right)}$$

² The Van Vleck equation reads :

$$\chi = \frac{N \sum_{i=1}^n (g\mu_B m_{Si})^2 \exp(-E_i^{(0)} / k_B T)}{k_B T \sum_{i=1}^n \exp(-E_i^{(0)} / k_B T)}$$

where $E_i^{(0)}$ is the energy of the i state in zero field, and N is the number of moles of trinuclear complexes.

IV.1.4 Solution properties

The absence of intra-molecular electron transfer property in solid-state prompted us to study this complex in solution. Very recently our group as well as the group of H. Oshio have studied the electron-transfer in $[\text{Fe}_2\text{Co}_2]$ squares in solution due to the possibility to fine-tune the its characteristics such as $T_{1/2}$, as described in Chapter II (section II.2.2) (Nihei et al. 2011; Siretanu et al. 2011). Since **8** is a neutral complex, it is hardly soluble in most of organic solvents and shows best solubility in dimethyl sulfoxide (DMSO). Thus, **8** was dissolved in DMSO to examine the potential electron-transfer properties that can be favored by different solvents and/or protonation. The possibility of thermal spin crossover or electron-transfer processes in solution was tested by the magnetic susceptibility measurement of **8** solution, but only the paramagnetic $\{\text{Fe}^{\text{III}}_{\text{LS}}\text{-CN-Co}^{\text{II}}_{\text{HS}}\}$ species was detected in all the experimental temperature, showing the χT product being $3.15 \text{ cm}^3\text{Kmol}^{-1}$ (Figure IV.10).

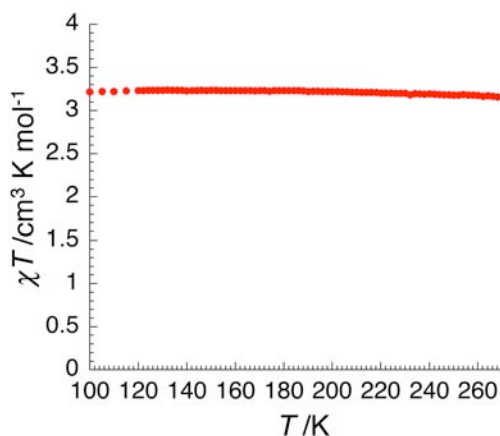


Figure IV.10 Temperature dependence of χT product for **8** in DMSO solution ($3.05 \times 10^{-5} \text{ M}$). Data are collected at an applied field of 10000 Oe.

To examine the effect of protonation, UV/vis absorption spectra were measured upon addition of the trifluoroacetic acid (TFA) to a solution of **8**. As can be seen in the spectra and the photos upon acid addition (Figure IV.11, left), a dramatic spectrum modification is accompanied by the color change of the solution from dark green to purple. The intense absorption at 14820 cm^{-1} before adding acid may be attributed to $\text{Co}^{\text{II}} \rightarrow \text{Fe}^{\text{III}}$ metal-to-metal charge transfer (MMCT), whereas the shoulder at 16000 cm^{-1} is the characteristic band of Fe^{III} complex (compound **6**) as show in Figure IV.12. As the amount of TFA increased, the intensity of $\text{Co}^{\text{II}} \rightarrow \text{Fe}^{\text{III}}$ MMCT band decreased, and a new absorption band appeared at 18670 cm^{-1} . This band at 18670 cm^{-1} may be the signature of $\text{Fe}^{\text{II}} \rightarrow \text{Co}^{\text{III}}$ MMCT as it has been reported previously in Fe-Co compounds (Bernhardt et al. 2004; Sato et al. 1999). Furthermore, the small absorption band at 21900 cm^{-1} also observed in the Fe^{III} precursor (**6**) (Figure IV.12, left top) is shifted to 23200 cm^{-1} after protonation as expected with the change of the Fe oxidation state. The aforementioned results reveal the presence of an intramolecular electron transfer process induced by protonation of **8** in DMSO solution. The paramagnetic $\{\text{Fe}^{\text{III}}_{\text{LS}}\text{-CN-Co}^{\text{II}}_{\text{HS}}\}$ complex is progressively converted in a controlled manner upon proton addition into a diamagnetic $\{\text{Fe}^{\text{II}}_{\text{LS}}\text{-CN-Co}^{\text{III}}_{\text{LS}}\}$ species. It is worth mentioning here that the presence of an isosbestic point at 17390 cm^{-1} might indicate that only two species are involved in the interconversion of $\{\text{Fe}^{\text{III}}_{\text{LS}}\text{-CN-}$

$\text{Co}^{\text{II}}_{\text{HS}}\}$ into $\{\text{Fe}^{\text{II}}_{\text{LS}}\text{-CN-Co}^{\text{III}}_{\text{LS}}\}$ pairs. Nevertheless, the two curves representing the variation of the absorptions at 14800 cm^{-1} and 18700 cm^{-1} upon acid addition (**Figure IV.11**, right) display an asymmetric evolution, with the crossing point not located at 0.5, therefore demonstrating the presence of more than two species in solution (see section IV.1.4 for additional discussion).

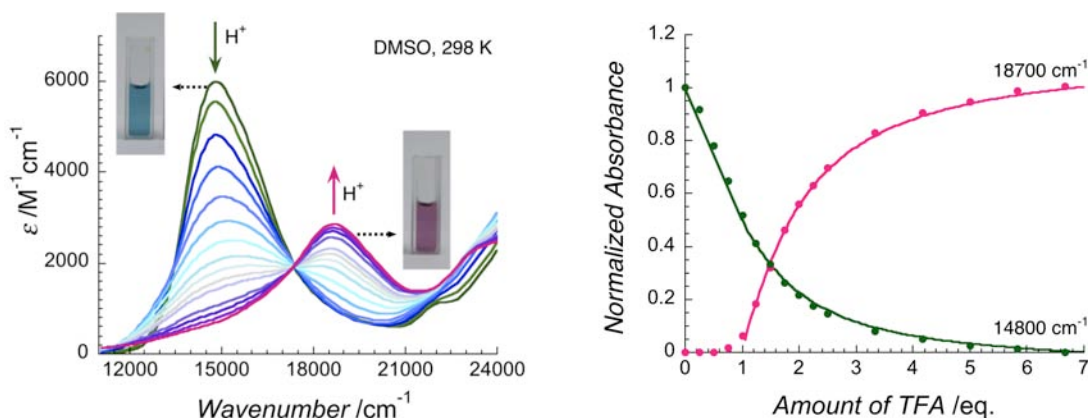


Figure IV.11 UV-vis spectroscopic characterization of **8** in DMSO ($2.68 \times 10^{-4}\text{ M}$) at 298 K, showing a spectral evolution upon the addition of TFA (left). From green to purple, the acid addition is increasing with the interval of (i) 0.25 eq. up to 2.5 eq, and (ii) 0.84 eq. up to 6.7 eq. The normalized absorbance of each characteristic band (right); dark green for 14800 cm^{-1} ($\text{Co}^{\text{II}} \rightarrow \text{Fe}^{\text{III}}$ MMCT) and purple for 18700 cm^{-1} ($\text{Fe}^{\text{II}} \rightarrow \text{Co}^{\text{III}}$ MMCT). The solid lines after the first equivalence point (TFA > 1 eq.) are the results of the modeling based on the acid-base titration (see main text, Eq IV.17 & Eq IV.18).

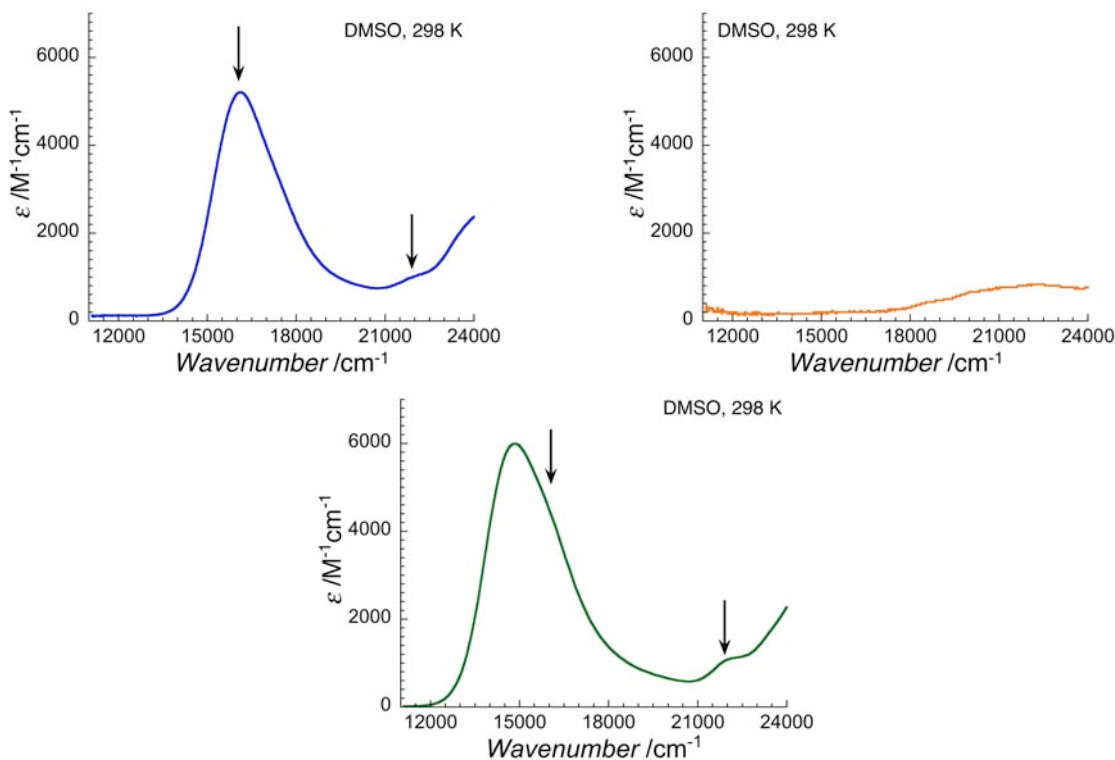


Figure IV.12 UV-vis spectra of **6** (right, top), **7** (left, top), and **8** (bottom) in DMSO ($2.68 \times 10^{-4}\text{ M}$) at 298 K.

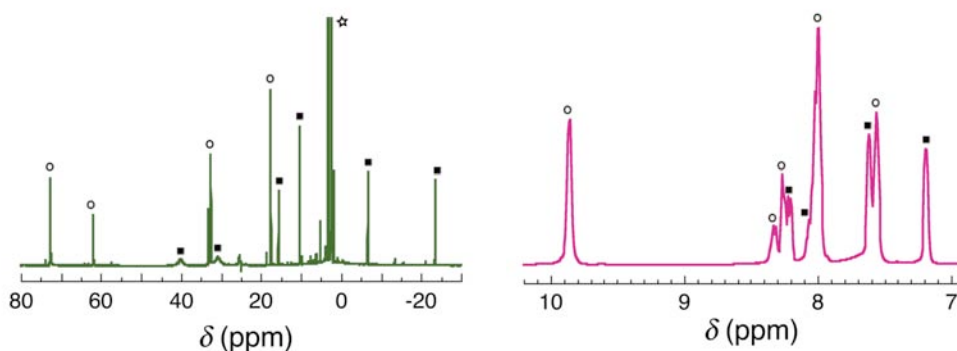


Figure IV.13 ^1H NMR spectra of **8** in *d*-DMSO solutions at 298 K; paramagnetic $\{\text{Fe}^{\text{III}}_{\text{LS}}\text{-CN-Co}^{\text{II}}_{\text{HS}}\}$ species is present in solution before the treatment of *d*-TFA (left); diamagnetic $\{\text{Fe}^{\text{II}}_{\text{LS}}\text{-CN-Co}^{\text{III}}_{\text{LS}}\}$ species is detected after 10 eq. addition of *d*-TFA (right). Empty circles are for the resonances from PY5Me₂ ligand coordinated to cobalt, and full squares are those from bbp ligand coordinating the iron center. The intense peak marked with an empty star is from the solvents, H₂O and DMSO.

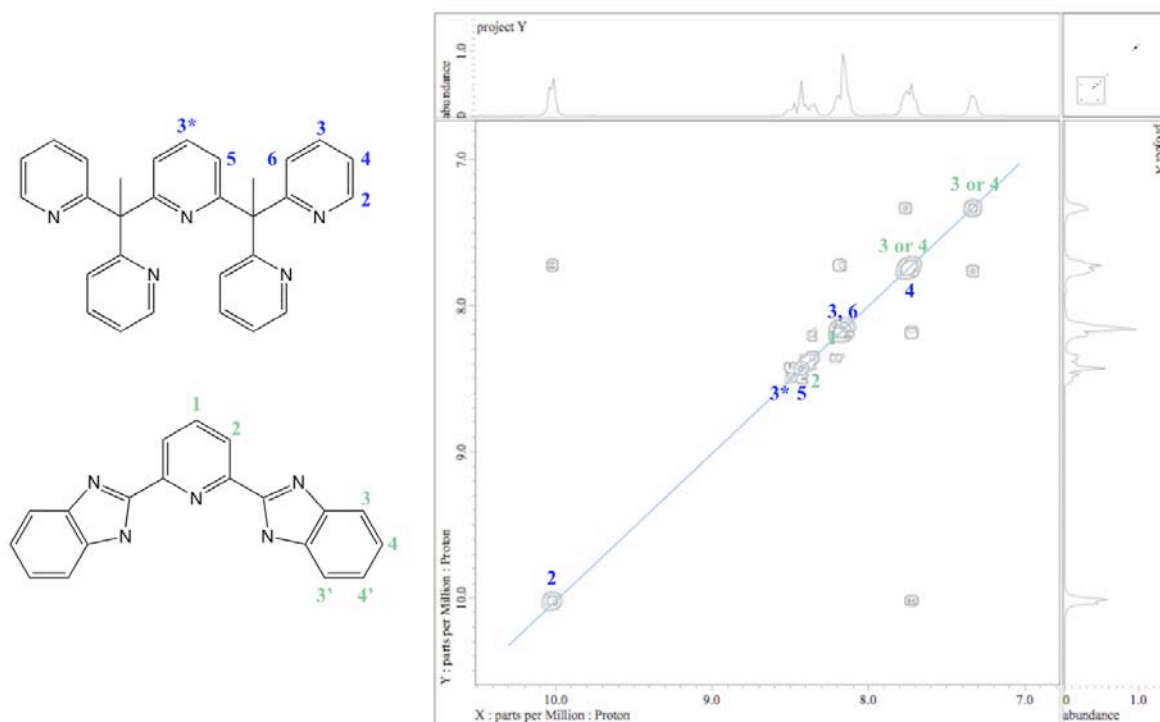


Figure IV.14 ^1H - ^1H COSY spectrum of **8** in *d*-DMSO solutions at 298 K after 10 eq. addition of *d*-TFA. The resonance peaks are attributed to each ^1H of the ligands.

To further probe the intramolecular electron transfer and spin-state changes in solution upon the addition of TFA, two deuterated-DMSO (*d*-DMSO) solutions of **8**, before and after adding excess of deuterated-TFA (*d*-TFA; 10 eq.), were measured by ^1H NMR spectroscopy. The untreated solution showed remarkable paramagnetic shifts of all resonances, in agreement with the presence of the paramagnetic $\{\text{Fe}^{\text{III}}_{\text{LS}}\text{-CN-Co}^{\text{II}}_{\text{HS}}\}$ species. The resonance peaks could be attributed quite well to each ligand as shown in **Figure IV.13**, based on ^1H - ^1H COSY measurements of **7** and **8** (**Figure SIV.5** and **Figure SIV.6**). Due to weak and broad signals in ^1H NMR of **6** (**Figure SIV.4**, left), ^1H - ^1H COSY measurement was not informative for **6**. In contrast, the purple-colored solution after treatment with 10 eq. of *d*-TFA did not show any paramagnetic shifts, and all resonances could be assigned perfectly

for the two PY5Me₂ and BBP ligands for the complex with an 1:1 ratio (**Figure IV.14** and **Figure SIV.7**). The NMR data unambiguously demonstrate the presence of diamagnetic {Fe^{II}_{LS}-CN-Co^{III}_{HS}} species in solution resulting from an electron transfer process triggered by acid addition.

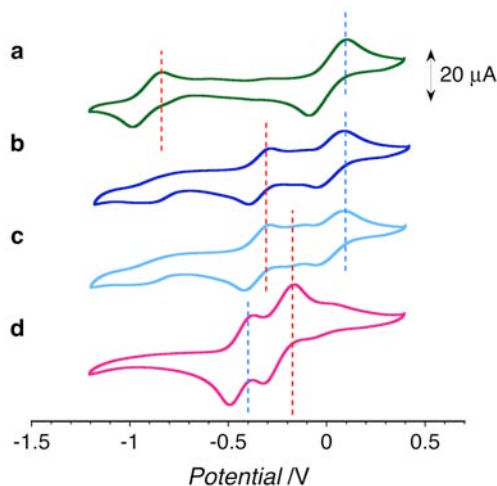


Figure IV.15 Cyclic voltammogram of **8** collected in a 0.1 M solution of NBu₄(PF₆) in DMSO with a scan rate of 0.1 V s⁻¹. Potentials were referenced to the [Cp₂Fe]^{1+/0} couple; as-prepared (a), after 0.8 eq. of TFA (b), after 1 eq. of TFA (c), and after 4 eq. of TFA (d). For an easy comparison, blue and red dashed lines indicate the maximum of the characteristic oxidation waves of Co and Fe centers, respectively.

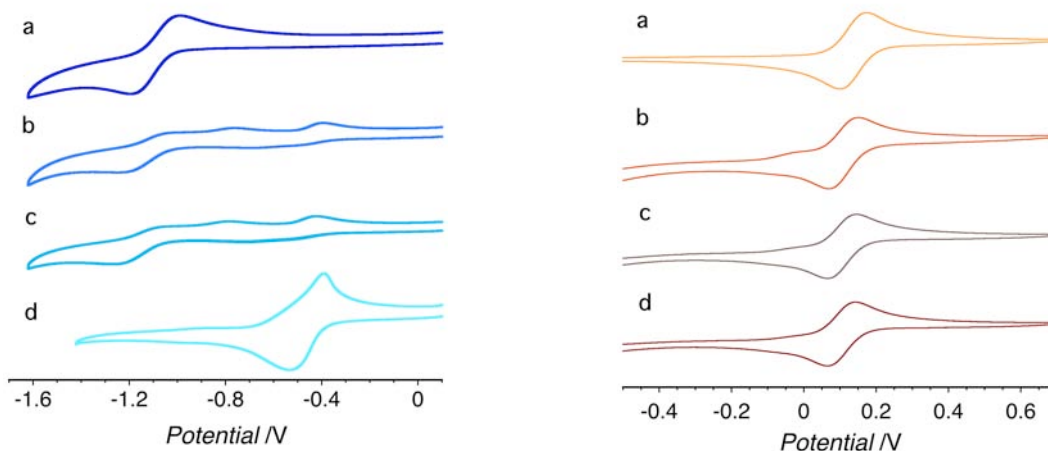


Figure IV.16 Cyclic voltammograms of **6** (left) and **7** (right) collected in a 0.1 M solution of NBu₄(PF₆) in DMSO (left) and in CH₃CN (right) with a scan rate of 0.1 V s⁻¹; as prepared (a), after 2 eq. of TFA (b), and after 4 eq. of TFA (c). Potentials were referenced to the [Cp₂Fe]^{1+/0} couple.

Additional experimental evidence on the protonation-induced electron transfer in **8** solutions is given by cyclic voltammetry experiments performed upon acid addition (**Figure IV.15**). Before the acid addition in a DMSO solution of **8**, the two reversible redox waves were detected for the {Fe^{III}Co^{II}/Fe^{II}Co^{II}} and the {Fe^{III}Co^{III}/Fe^{III}Co^{II}} couples at -0.91 V and 0.01 V (vs Fc/Fc⁺), respectively (**Figure IV.15a**). After adding 0.8 eq. of acid addition (**Figure IV.15b**), the former wave almost vanished, while the latter remained almost unaffected, and concomitantly, a new reversible redox wave appeared at -0.39 V. This result demonstrates that the proton addition significantly affects the redox properties of the Fe site and not those of the Co part. This behaviour was confirmed by the

redox properties of **6** and **7** upon acid addition (**Figure IV.16**). Independently of TFA addition, the Co precursor, **7**, showed at +0.13 V a reversible one-electron redox wave corresponding to the $\text{Co}^{\text{III}}/\text{Co}^{\text{II}}$ couple. The redox properties of **7** are thus not modified by protonation as observed for the Co part of **8**. In contrast, the redox potential of the Fe precursor, **6**, is drastically changed upon proton addition: from -1.05 V without acid, up to -0.46 V for 3 eq. of TFA. Fortunately, the diprotonated complex, $[\text{Fe}(\text{H}_2\text{bbp})(\text{CN})_3]\cdot 2\text{H}_2\text{O}$ (**9**) was crystallized and revealed that two protons are positioned on the nitrogen of the benzimidazole on bbp ligand (**Figure IV.17** and **Table IV.5**). The Fe centers adopt distorted octahedral geometries showing Fe-N and Fe-C distances being 1.934(3) – 1.961(3) and 1.933(4) – 1.972(3) Å, respectively, as seen in structure of **6**, implying a Fe^{III} site. Consequently, these nitrogen atoms in **6**, and thus in **8**, act as weak bases, and their protonation results in the positive shift of the $\text{Fe}^{\text{III/II}}$ redox potential. Keeping in mind that the electron transfer is governed by the redox potential difference (ΔE) between metal ion sites (Ratera et al. 2007), it is worth noting that ΔE between Co and Fe metal centres is remarkably reduced after the protonation, as illustrated by **8** as well as by **6** and **7**. Only around 1 eq. of acid addition to **8**, two new reversible redox waves appeared progressively at -0.45 V and -0.26 V (**Figure IV.15c** and **Figure IV.15d**). Given the fact that the diamagnetic $\{\text{Fe}^{\text{II}}\text{Co}^{\text{III}}\}$ species is present in solution after the acid treatment, the two redox couples at -0.45 V and -0.26 V can be straightforwardly attributed to $\{\text{Fe}^{\text{II}}\text{Co}^{\text{III}}/\text{Fe}^{\text{II}}\text{Co}^{\text{II}}\}$ and $\{\text{Fe}^{\text{III}}\text{Co}^{\text{III}}/\text{Fe}^{\text{II}}\text{Co}^{\text{III}}\}$ couples, respectively. Thus, the redox waves corresponding to the cobalt and iron sites are inversed after protonation as expected for a complex experiencing an electron transfer process. This study demonstrates that the protonation of bbp ligand decreased ΔE between Fe and Co centres, and consequently, induced an electron transfer process in final systems as evidenced by the inversion of redox waves.

Table IV.5 Crystallographic data of compound **9**.

Empirical formula	$\text{C}_{22}\text{H}_{15}\text{FeN}_8\text{O}$
Formula weight, g mol^{-1}	463.27
Crystal system	Monoclinic
Space group	$P2_1/c$
Wavelength, Å	0.71073
Temperature, K	100
a , Å	10.9398(12)
b , Å	22.107(3)
c , Å	16.8809(19)
β , °	92.003(6)
V , Å ³	4080.1(8)
Z	8
ρ_{calcd} , Mg m^{-3}	1.508
μ , mm^{-1}	0.773
$^a R_1$ ($I > 2\sigma(I)$)	0.0513
$^b wR_2$ (all)	0.1563
GoF	1.020

^a $R_1 = \sum ||F_o| - |F_c|| / \sum |F_o|$, and ^b $wR_2 = [\sum w(F_o^2 - F_c^2)^2 / \sum w(F_o^2)^2]^{1/2}$



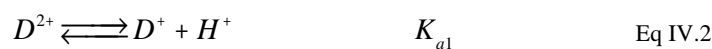
Figure IV.17 View of the molecular structure of the **9** at 100 K with thermal ellipsoids at 30 % level. Yellow, Fe; skyblue, N; black, C; pink, H. Lattice solvents are omitted for clarity.

IV.1.5 Model of the protonation mechanism

Based on the experimental proof that the protonation occurs on two nitrogen atoms of the bbp ligand for Fe building block (**6**) as seen in compound **9**, we assume that the protonation on the dinuclear complex **8** upon the addition of the acid also occurs on these two sites. Thus, the possible species in the solution can be unprotonated [FeCo] (= D), mono-protonated [HFeCo]⁺ (= D^+), and di-protonated [H₂FeCo]²⁺ (= D^{2+}), and we know the latter one corresponds to the diamagnetic {Fe^{II}_{LS}-CN-Co^{III}_{LS}} species. The reaction scheme is described as acid-base titration with the acidity of added acid (AH) given as K_a . The di-protonated species D^{2+} is considered as diprotic acid with K_{a1} and K_{a2} .

As seen in **Figure IV.11**, we can remark that the UV-vis spectra around 18700 cm⁻¹ (related to the Fe^{II} → Co^{III} MMCT) were hardly modified before the first equivalence point (< 1eq.). Also cyclic voltammetry data shows appearance of the two new reversible redox waves at -0.45 V and -0.26 V only around 1 eq. of acid addition to **8**. It suggests the quasi-absence of di-protonated D^{2+} species and thus at a first approximation that all added protons produce mono-protonated D^+ species. Then, the absorption around 14800 cm⁻¹ that is related to the Co^{II} → Fe^{III} MMCT is the contribution of both mono-protonated D^+ and non-protonated D species. The linear variation of the green curve in **Figure IV.11** (right) confirms also the absence of D^{2+} before 1 eq. of acid and furthermore, its slope of -0.5 indicates that the absorbance of the mono-protonated D^+ species is twice weaker than the unprotonated D species (the observed slope would be 0 if the two species had the same absorbance intensity). From this, we can suppose that $K_{a1} \gg K_{a2}$ ($K_{a1} < 1$ and $K_{a2} \ll 1$). This is also true for the experiment with strong acid (see below and **Figure IV.18**)

Protonation with a strong acid. In order to simplify the calculations, we first consider the protonation of D with a strong acid, in which the added acids are completely dissociated to generate protons. Therefore, we can define $[H^+]_0 = C_A$ (initial acid concentration) and $[D]_0 = C_0$ (initial concentration of D). Then the equilibriums of D^{2+} and D^+ are described as:



Since $K_{a1} \gg K_{a2}$, the predominant reaction is the reverse reaction of Eq IV.3: $D + H^+ \longrightarrow D^+$. After this reaction, new initial states are as: $[H^+]_0 = 0$, $[D]_0 = C_0 - C_A$, $[D^+]_0 = C_A$. Then until the first equivalence point ($C_A \leq C_0$), the predominant reaction is given by Eq IV.4 ($x = [D^{2+}]$):



$$K = \frac{K_{a2}}{K_{a1}} = \frac{x(C_0 - C_A + x)}{(C_A - 2x)^2}$$

Considering $K_{a2}/K_{a1} \ll 1$, we obtain following normalized concentration of each species ($r = C_A/C_0$):

$$\frac{[D^{2+}]}{C_0} = -0.5 + 0.5r + 0.5\sqrt{(1-r)^2 + 8rK - 4r^2K} \quad \text{Eq IV.5}$$

$$\frac{[D^+]}{C_0} = 1 - \sqrt{(1-r)^2 + 8rK - 4r^2K} \quad \text{Eq IV.6}$$

$$\frac{[D]}{C_0} = 0.5 - 0.5r + 0.5\sqrt{(1-r)^2 + 8rK - 4r^2K} \quad \text{Eq IV.7}$$

And at the first equivalence point ($C_A = C_0$):

$$x = C_0\sqrt{K} \quad \text{Eq IV.8}$$

After the first equivalence point ($C_A > C_0$), the predominant reaction is then the reverse reaction of Eq IV.2: $D^+ + H^+ \longrightarrow D^{2+}$ and thus new initial state is:

(i) when $C_0 < C_A < 2C_0$, $[H^+]_0 = 0$, $[D^+]_0 = 2C_0 - C_A$, $[D]_0 = 0$, $[D^{2+}]_0 = C_A - C_0$;

(ii) when $C_A > 2C_0$, $[H^+]_0 = C_A - 2C_0$, $[D^+]_0 = 0$, $[D]_0 = 0$, $[D^{2+}]_0 = C_0$;

(iii) when $C_A = 2C_0$, $[H^+]_0 = 0$, $[D^+]_0 = 0$, $[D]_0 = 0$, $[D^{2+}]_0 = C_0$.

At the second equivalence point ($C_A = 2C_0$), the only possible reaction is Eq IV.2 (dissociation of the D^{2+} in D^+ and H^+) and thus:

$$q = \frac{\alpha^2}{1-\alpha} \quad \text{Eq IV.9}$$

with $[D^{2+}] = C_0(1-\alpha)$. If we make an approximation that reaction of Eq IV.2 is the only possible one also for the regimes $C_0 < C_A < 2C_0$ and $C_A > 2C_0$, then, the equilibrium constants can be written as below:

$$K_{a1} = \frac{[H^+](2C_0 - C_A + [H^+])}{C_A - C_0 - [H^+]} \quad \text{for } C_0 < C_A < 2C_0 \quad \text{Eq IV.10}$$

$$K_{a1} = \frac{[D^+](C_A - 2C_0 + [D^+])}{C_0 - [D^+]} \quad \text{for } C_A > 2C_0 \quad \text{Eq IV.11}$$

Both equations give the identical solutions for $[D^{2+}]/C_0$ and $[D^+]/C_0$ as below ($q = K_{a1}/C_0$, $r = C_A/C_0$):

$$\frac{[D^{2+}]}{C_0} = 0.5r + 0.5q - \sqrt{(1-0.5r)^2 + 0.5rq + 0.25q^2} \quad \text{Eq IV.12}$$

$$\frac{[D^+]}{C_0} = 1 - 0.5r - 0.5q + \sqrt{(1 - 0.5r)^2 + 0.5rq + 0.25q^2} \quad \text{Eq IV.13}$$

Protonation with a weak acid. When the pK_a of the added acid (AH) is close to the pK_{a1} of D^{2+} , the following equilibriums of D^{2+} and D^+ should be considered:



with $[AH]_0 = C_A$ (initial acid concentration) and $[D]_0 = C_0$ (initial concentration of D). After the predominant reaction that is the reverse reaction of Eq IV.15 ($D + AH \longrightarrow D^+ + A^-$), the new initial state is: $[AH]_0 = 0$, $[D]_0 = C_0 - C_A$, $[D^+]_0 = [A^-]_0 = C_A$. Therefore before the first equivalence point ($C_A \leq C_0$), the reaction Eq IV.4 (K_{a2}/K_{a1}) and the reverse reaction of Eq IV.15 (K_{a2}/K_a) are in competition and thus it is not possible to establish simple analytical expressions of $[D]$ and $[D^+]$.

After the first equivalence point ($C_A > C_0$), the predominant reaction that is the reverse of Eq IV.14 ($D^+ + AH \longrightarrow D^{2+} + A^-$), and the new initial state is:

- (i) when $C_0 < C_A < 2C_0$, $[AH]_0 = 0$, $[D^+]_0 = 2C_0 - C_A$, $[D]_0 = 0$, $[D^{2+}]_0 = C_A - C_0$, $[A^-]_0 = C_A$;
- (ii) when $C_A > 2C_0$, $[AH]_0 = C_A - 2C_0$, $[D^+]_0 = 0$, $[D]_0 = 0$, $[D^{2+}]_0 = C_0$, $[A^-]_0 = 2C_0$;
- (iii) when $C_A = 2C_0$, $[H^+]_0 = 0$, $[D^+]_0 = 0$, $[D]_0 = 0$, $[D^{2+}]_0 = C_0$, $[A^-]_0 = 2C_0$.

At the second equivalence point ($C_A = 2C_0$), the existing two reactants (D^{2+} and A^-) can make Eq IV.2 and Eq IV.14 as the possible reactions and thus with $[H^+] = \beta C_0$:

$$\frac{K_{a1}}{C_0} = \frac{\beta^2(1 + 2C_0 / K_a)}{1 - \beta(1 + 2C_0 / K_a)} \quad \text{Eq IV.16}$$

For both $C_0 < C_A < 2C_0$ and $C_A > 2C_0$ regimes, the solutions for $[D^{2+}]/C_0$ and $[D^+]/C_0$ are identical (with $q = K_{a1}/C_0$, $r = C_A/C_0$, $p = K_a/C_0$):

$$\frac{[D^{2+}]}{C_0} = \frac{pr}{p + \beta} - 1 - \beta \quad \text{Eq IV.17}$$

$$\frac{[D^+]}{C_0} = -\frac{pr}{p + \beta} + 2 + \beta \quad \text{Eq IV.18}$$

$$\left(\text{with } r = \beta \left(1 + \frac{\beta}{p} \right) + \left(\frac{q + 2\beta}{q + \beta} \right) \left(1 + \frac{\beta}{p} \right) \right)$$

In order to make an analysis with the foregoing developed model, we have conducted the additional UV/vis absorption measurement upon addition of a strong acid, trifluoromethanesulfonic acid (TfOH). TfOH was treated to **8** in DMSO at a regular interval, in order to see the protonation dependence of the absorbance (**Figure IV.18**). As seen for the experimental data with TFA before the first equivalence (**Figure IV.11**), a straight line with a slope of -0.5 also compares perfectly with the normalized absorbance at 14800 cm^{-1} before 1 eq. of TfOH addition ($C_A < C_0$) (**Figure IV.18**, right). This result confirms that the experimental green points in **Figure IV.18** (absorption band at 14800 cm^{-1}) are only influenced by D and D^+ species. On the basis of the -0.5 slope, it is straightforward to conclude that the absorbance of D^+ is twice weaker than the one of D . Meanwhile, the absorption band

at 18700 cm^{-1} can be attributed to D^{2+} . Experimentally, a little increase of the normalized absorbance around 18700 cm^{-1} below 1 eq. was observed (**Figure IV.11** and **Figure IV.18**), which can be explained by a reaction, where two D^+ dissociate into a D and a D^{2+} complex (Eq IV.4). Then, the deduced normalized concentrations of D^+ and D^{2+} depending on $[H^+]$ (Eq IV.12 and Eq IV.13) were compared with the experimental data above 1 eq. of TfOH addition ($C_A > C_0$) (**Figure IV.18**, right). A remarkable agreement is found between the experimental curves (green and purple) and the theoretical $[D^+]/C_0$ and $[D^{2+}]/C_0$ expressions. The best simulation of the experimental results is obtained with $K_{a1} = 6.7 \times 10^{-5}\text{ M}^{-1}$ and $K_{a2} = 3.8 \times 10^{-7}\text{ M}^{-1}$, respectively ($\text{p}K_{a1} = 4.17$ and $\text{p}K_{a2} = 6.42$). In the case of the weak acid (TFA, **Figure IV.11**), three unknown variables (K_{a1} , K_{a2} , and K_a of the treated acid) exist in the equations of $[D^{2+}]$ and $[D^+]$. Therefore, the K_{a1} and K_{a2} values deduced from modeling the experimental data with TfOH were introduced as fixed parameters in the equations (Eq IV.17 and Eq IV.18), and then used to reproduce the experimental normalized absorbance upon TFA addition (**Figure IV.11**, right). The best simulation resulted in the $\text{p}K_a$ of TFA as 3.54 that corresponds well to the reported value in DMSO (Bordwell 1988).

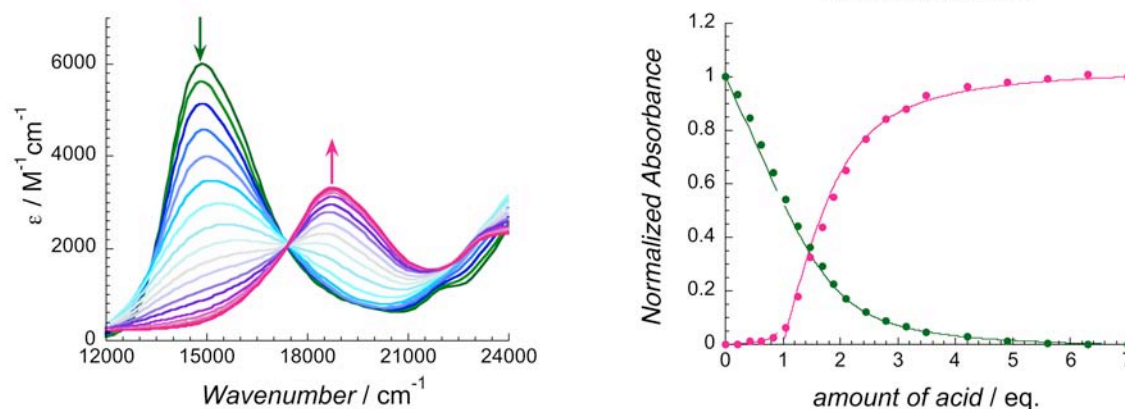


Figure IV.18 UV-vis spectroscopic characterization of **8** in DMSO ($2.68 \times 10^{-4}\text{ M}$) at 298 K, showing a spectral evolution upon the addition of TfOH (left). From green to purple, the equivalence of acid is increasing with the intervals of 0.21 up to 2.1 eq., of 0.35 up to 3.5 eq., and of 0.7 up to 7 eq. The normalized absorption intensities of each MMCT band; Dark green for 14800 cm^{-1} and purple for 18700 cm^{-1} (right). The solid line is the result of the modeling based on the acid-base titration described in the main text.

Based on the excellent theory/experience agreement as discussed above, the following results can be considered: (i) the mono-protonated species ($[\text{HFeCo}]^+$) is produced prior to the di-protonated one ($[\text{H}_2\text{FeCo}]^{2+}$), since $[\text{HFeCo}]^+$ (estimated $\text{p}K_{a2} = 6.42$) is a weaker acid than $[\text{H}_2\text{FeCo}]^{2+}$ ($\text{p}K_{a1} = 4.17$). Therefore, the introduced protons contribute first to the production of $[\text{HFeCo}]^+$ until the initial $[\text{FeCo}]$ (**8**) is consumed. This result explains well the cyclic voltammetry data (appearance of the two new reversible redox waves at -0.45 V and -0.26 V only around 1 eq. of acid addition to **8**) and also why the normalized intensity of the 18700 cm^{-1} absorption band (proportional to the $[\text{H}_2\text{FeCo}]^{2+}$ concentration) stays at almost zero up to adding 1 eq. of acid (**Figure IV.11** (right) and **Figure IV.18** (right)). (ii) The absorption band at 14820 cm^{-1} can be attributed to both $[\text{FeCo}]$ and $[\text{HFeCo}]^+$ species. It is clear that the mono-protonated $[\text{HFeCo}]$ is also in a $\{\text{Fe}^{\text{III}}_{\text{LS}}\text{-CN-Co}^{\text{II}}_{\text{HS}}\}$ state, and consequently shows the characteristic $\text{Co}^{\text{II}} \rightarrow \text{Fe}^{\text{III}}$ MMCT band at the same energy as $[\text{FeCo}]$. These observations and model provide an explanation on the unique UV-vis spectral changes upon protonation. Three different species are involved in the protonation process, explaining the asymmetric shape of the normalized absorption upon proton addition. However, the two $[\text{FeCo}]$ and $[\text{HFeCo}]^+$ species have rather similar spectra, allowing the existence of an isosbestic point. Furthermore, the diamagnetic

species created by intramolecular electron transfer upon protonation is the di-protonated $[\text{H}_2\text{Fe}^{\text{II}}_{\text{LS}}\text{Co}^{\text{III}}_{\text{LS}}]^{2+}$ complex.

IV.1.6 Concluding remark

We have investigated the new cyanido-bridged dinuclear $[(\text{bbp})\text{Fe}(\text{CN})_3\text{Co}(\text{PY5Me}_2)] \cdot 2.5\text{CH}_3\text{OH}$ (**8**) complex both in solid state and in solution, by structural, spectroscopic, electrochemical, and magnetic methods. In order to limit the dimensionality of the final complex and to follow our synthetic strategy, *mer*- $[\text{Fe}(\text{bbp})\text{CN}_3]^{2-}$ (**6**) and $[\text{Co}(\text{PY5Me}_2)(\text{H}_2\text{O})]^{2+}$ (**7**) units have been synthesized as precursors. In the solid state of compound **8**, an unprecedented spin crossover on the cobalt ion was observed showing a transformation from $\{\text{Fe}^{\text{III}}_{\text{LS}}\text{Co}^{\text{II}}_{\text{HS}}\}$ to $\{\text{Fe}^{\text{III}}_{\text{LS}}\text{Co}^{\text{II}}_{\text{LS}}\}$ species. The possible electron transfer process could be ruled out through detailed crystallographic studies as well as ^{57}Fe Mössbauer spectra at different temperatures. To our knowledge, this compound **8** is the first example of a bimetallic complex exhibiting a spin crossover on a cobalt ion. Remarkably, our studies in solution reveal the optical and magnetic changes of compound **8**, accompanied by the intramolecular metal-to-metal electron transfer that was triggered and modulated by the protonation on the complex. Therefore, the compound **8** acts as two different molecular switches depending on its physical states and external stimuli: spin crossover in solid-state induced by “temperature”, and intramolecular electron transfer in solution induced by “proton”.

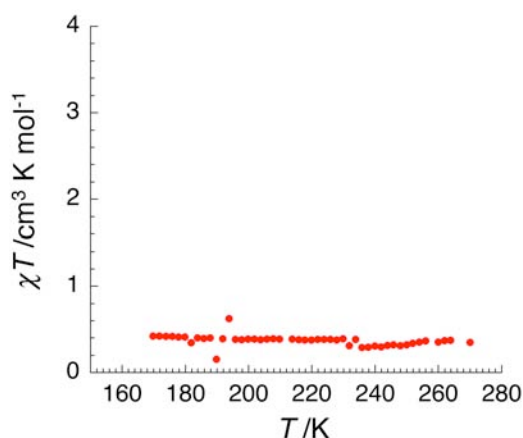


Figure IV.19 Temperature dependence of χT product for **8** in DMSO solution (3.05×10^{-5} M) after treating 1 eq. of TFA. Data are collected at an applied field of 10000 Oe.

We have also measured the magnetic susceptibility for the DMSO solution of the compound **8**, upon adding acid. We observed that compound **8** is in $\text{Fe}^{\text{III}}_{\text{LS}}\text{Co}^{\text{II}}_{\text{HS}}$ state between 270 and 170 K without acid treatment, as shown in **Figure IV.10**. However, solution treated with 1 eq. of TFA exhibits already dominant diamagnetic state below 270 K (**Figure IV.19**). It is also important noting that the color of solution treated with 1 eq. of TFA at room temperature is still blue-green, while it turns to violet below 270 K. The violet color is observed at room temperature only after adding 4 eq. of TFA. It suggests that there might be a thermally induced electron transfer in solution after adding ~ 1 eq. of acid. Therefore, we tried to measure the magnetic susceptibility for the solution treated with 1 eq. of TFA above 270 K, but it was not possible due to the high polarity of DMSO in liquid state (mp

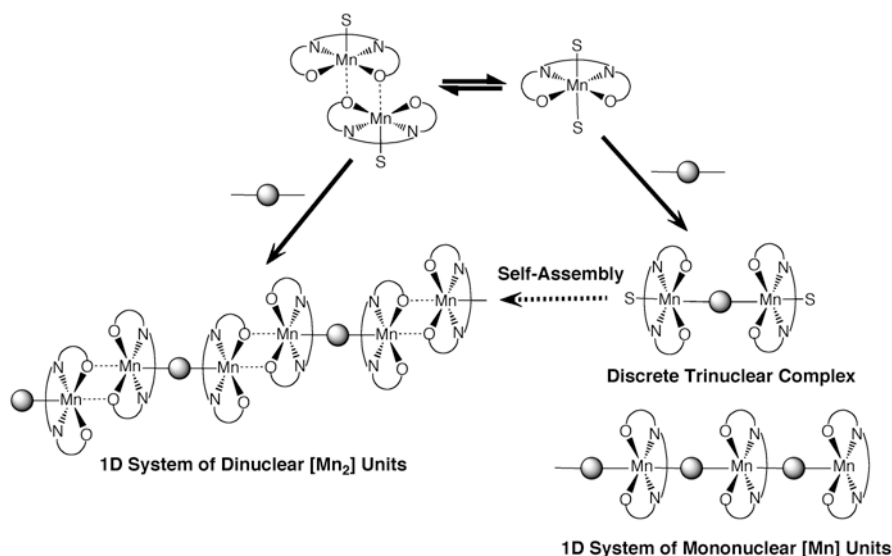
of DMSO: 292 K). For further studies, it should be studied more in detail with an acid treatment between 0 and 1 eq. In addition, it will be conceivable to use a gel to increase viscosity of the solution.

Additional future perspectives for this project will be discussed in “conclusion and perspectives” of this chapter.

IV.2 Trinuclear [Mn₂Fe] system

IV.2.1 Synthetic approach

As molecular building units, we have exploited (NBu₄)₂[Fe^{III}(bbp)(CN)₃] (**6**) and [Mn^{III}₂(saltmen)₂-(ReO₄)₂] complexes (compound **1** in Chapter II). The latter was synthesized as described in the literature (Miyasaka et al. 2004). The self-assembly reaction was performed in methanol with an equimolar amount of both Fe and Mn precursors (Fe:Mn = 1:2), leading to a Fe:Mn = 1:2 ratio, in order to obtain either [Mn-Fe-Mn] trinuclear unit or [Mn-Fe-Mn]_∞ chain (Scheme IV.4). Even though the Mn-precursor is a dinuclear complex in solid state, it is worth mentioning that generally Mn^{III}/SB (SB: Schiff-base) complexes are present in solution as an equilibrium mixture of a mononuclear form [Mn(SB)(S)₂]⁺ and an out-of-plane dinuclear complex [Mn₂(SB)₂(S)₂]²⁺ (S = solvent or anion) (Miyasaka et al. 2005). Thus they can crystallize in the solid state as one of two forms depending on the steric characteristics of the SB ligand (Scheme IV.4) (Miyasaka et al. 2007). Due to this versatility, it is well known that the dinuclear precursor can be dissociated in mononuclear species and eventually form a network incorporating the mononuclear unit (Miyasaka et al. 2012; Miyasaka et al. 2005). This was also the case in our synthesis, affording a bimetallic complex, {[Mn(saltmen)(MeOH)]₂-[Fe(bbp)(CN)₃]}·4CH₃OH (**10**), in which mononuclear [Mn(saltmen)]⁺ units are coordinated to each axial position of **6** (see following paragraph). We have also used other Mn complexes, coordinated with different SB as ligands, as a precursor to perform the reactions with an identical protocol. However, the obtained compounds are not in the frame of our strategy based on the nuclearity and structural geometry. Therefore, their syntheses and structures are summarized in part IV.4.



Scheme IV.4

As discussed in the previous section IV.1.1, the stretching band for the cyanide in compound **6** is seen at 2109 cm⁻¹ in the infrared spectrum (**Figure IV.1**). In compound **10**, this band split into two with one shifted in higher energy (2128 cm⁻¹) while the other remains almost at similar energy (2105 cm⁻¹) (**Figure IV.20**), indicating the formation of cyanido-bridged compounds with terminal cyanide left. The one cyanides left may be the origin to the lower absorption present in the infrared spectrum.

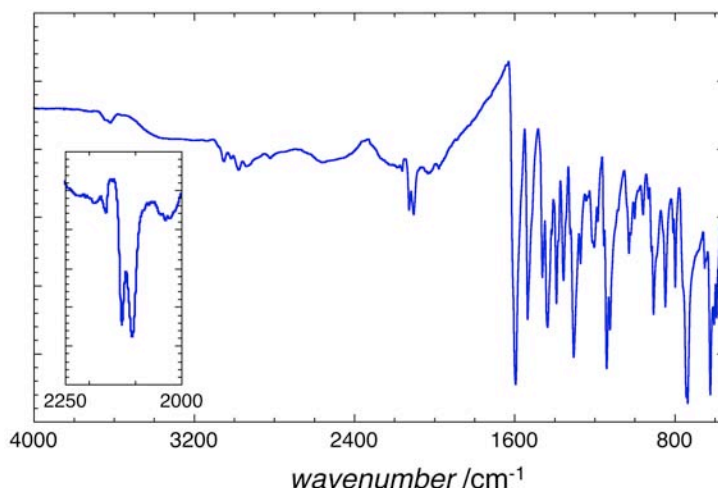


Figure IV.20 FT-IR spectra of compound **10** at 298 K, highlighting cyanide stretching in inset.

IV.2.2 Structural description

Crystal data and structure refinement details of compound **10** are listed in **Table IV.6**. Complex **10** crystallizes as a trinuclear complex in the monoclinic *C2/c* space group (**Figure IV.21**). The neutral {Mn^{III}₂Fe^{III}} complex is composed of two [Mn(saltmen)]⁺ cations linked via cyanido ligands to a central *mer*-[Fe(bbp)(CN)₃]²⁻ forming a *trans*-{Fe(μ-CN)₂Mn₂} unit. The terminal cyanido ligand remains uncoordinated and is perpendicular to the long axis of **10**.

In the structure of **10**, the iron center adopts a meridional arrangement of cyanido ligands as a consequence of the planar tridentate bbp ligand (**Figure IV.21**). As shown in **Table IV.7**, the Fe-C (1.905(7) – 1.972(4) Å) and the Fe-N (1.927(5) – 1.937(3) Å) bond distances are comparable to those seen in the precursor **6** and other cyanoferrate(III) complexes in which the Fe site adopts a distorted *mer*-[FeN₃C₃] conformation (Kim et al. 2009; Kim et al. 2007a; Kim et al. 2007b; Lescouëzec et al. 2004; Ni et al. 2005; Panja et al.; Senapati et al. 2012). The remaining [Mn(saltmen)(μ-NC)(MeOH)] fragments are related by two-fold symmetry. The Mn-N and the Mn-O distances in the equatorial plane of the saltmen ligand range between 1.873(3) and 1.996(3) Å, while the distances of the Mn-O from the axial MeOH and the Mn-N for the bridging cyanido are significantly longer, being 2.307(3) and 2.271(3) Å, respectively (**Table IV.7**). This JT elongation and other bond lengths are also in agreement with the reported value for [Mn₂(saltmen)₂(ReO₄)₂] (Miyasaka et al. 2004). This characterization of selected bond distances on Mn and Fe metal ions unambiguously indicate their oxidation state as trivalent for both. The terminal Fe-CN angle is linear while those of the bridging cyanido (Fe1-C22-N7) are close to linearity, being 172.9(3)°. Meanwhile, the Mn1-N7-C22 angle is significantly bent leading to 154.2(3)°. The intramolecular Mn...Fe and Mn...Mn distances are

5.219(5) and 10.012(7) Å, respectively, while the shortest intermolecular Mn...Fe and Mn...Mn distances are 7.691(7) and 7.610(7) Å. Additionally intermolecular short contacts are found to propagate along the crystallographic *c* direction (**Figure IV.22**, left). One of the nitrogens of the bbp imidazole have short contacts with one of the benzene rings of the saltmen ligand and axial MeOH molecule, showing N3'...O3 and N3'...C16 distances of 2.668(4) and 3.195(5) Å (**Figure IV.22**, right). Short O1'...C17 distances are also found to be 3.231(4) Å between saltmen ligands of the adjacent trinuclear complexes.

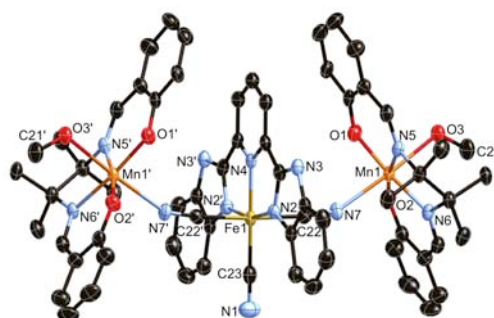


Figure IV.21 ORTEP-type view of the molecular structure for **10** with thermal ellipsoids at 30 % level. Mn, Fe, C, N, O atoms are in orange, yellow, black, blue, red. The solvent molecules and hydrogen atoms are omitted for clarity.

Table IV.6 Crystallographic data of compound **10**, collected at 150 K.

Empirical formula	$C_{67}H_{77}FeMn_2N_{12}O_{10}$
Formula weight, g mol ⁻¹	1384.11
Crystal system	Monoclinic
Space group	<i>C2/c</i>
Wavelength, Å	0.71069
<i>a</i> , Å	15.163(1)
<i>b</i> , Å	26.222(3)
<i>c</i> , Å	16.567(1)
β , °	92.479(4)
<i>V</i> , Å ³	6581.2(9)
<i>Z</i>	4
ρ_{calcd} , Mg m ⁻³	1.397
μ , mm ⁻¹	0.664
^a <i>R</i> ₁ (<i>I</i> > 2σ(<i>I</i>))	0.0600
^b <i>wR</i> ₂ (all)	0.1580
GoF ^a	1.014

^a*R*₁ = $\sum ||F_o| - |F_c|| / \sum |F_o|$, and ^b*wR*₂ = $[\sum w(F_o^2 - F_c^2)^2 / \sum w(F_o^2)^2]^{1/2}$.

Table IV.7 Selected bond lengths [Å] and angles [°] for **10**.

Mn1-O1	1.873(3)	Fe1-N2	1.937(3)
Mn1-O2	1.895(3)	Fe1-N4	1.927(5)
Mn1-N5	1.990(3)	Fe1-C22	1.972(4)
Mn1-N6	1.996(3)	Fe1-C23	1.905(7)
Mn1-O3	2.271(3)	Fe1-C22-N7	172.9(3)
Mn1-N7	2.307(3)	Mn1-N7-C22	154.2(3)

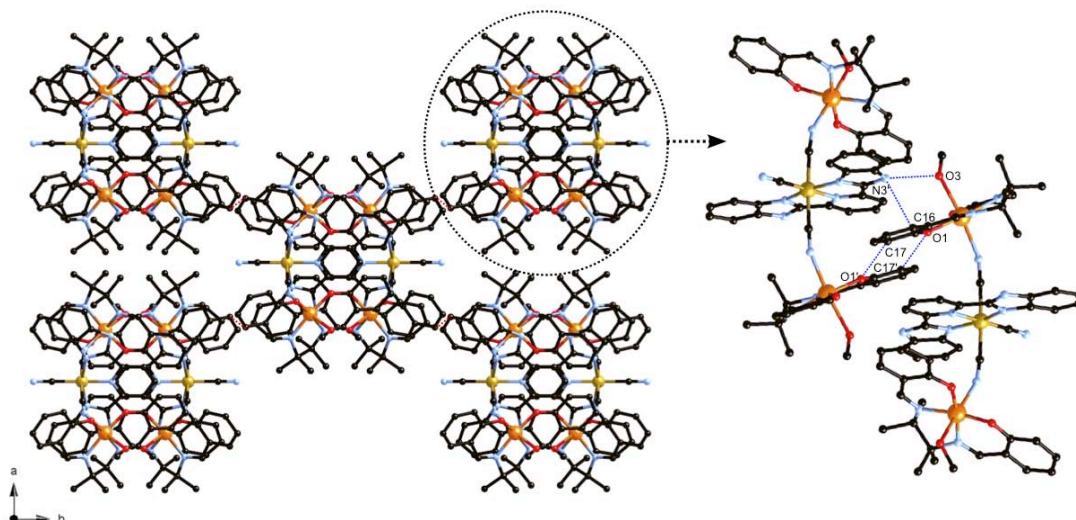


Figure IV.22 View of the crystal packing for **10** in *ab* plane (left), highlighting the intermolecular short contacts described in the main text (right).

IV.2.3 Magnetic properties

The static magnetic properties of **10** was investigated over a temperature range of 270 to 1.8 K, and are shown in **Figure IV.23** (left) as the thermal dependence of the χT product (per {Fe^{III}Mn^{III}₂} unit). At 270 K, the χT product (6.86 cm³Kmol⁻¹) is slightly higher than the expected value (6.48 cm³Kmol⁻¹) for the non-interacting Fe^{III}_{LS} ($S = 1/2$ with $g = 2.26$ as determined on **6**) and Mn^{III}_{HS} ($S = 2$ with $g = 2.0$ as reported (Miyasaka et al. 2004)) ions in a 1:2 ratio. As the temperature is lowered, the value of the χT product is fairly constant down to 80 K, and then increases until 7 K with a maximum value of 8.02 cm³Kmol⁻¹. At lower temperatures, the χT value decreases to 6.9 cm³Kmol⁻¹ at 1.8 K. The observed behavior suggests the dominating ferromagnetic interactions between Fe^{III} and Mn^{III} ions in **10** with the probable small inter-molecular antiferromagnetic interactions. Moreover, additional evidence for ferromagnetic exchange interactions being dominant within **10** is found in the field-dependence of the magnetization data (**Figure IV.23**, right). At 1.8 K, the magnetization value monotonically increases upon applying the external dc fields, without showing S-shape curves that could be indicative for the presence of the antiferromagnetic interactions. At 70 kOe, the magnetization (8.2 μ_B) is still approaching the expected value (9.1 μ_B) for parallel arrangements of Fe and Mn ions, implying a significant magnetic anisotropy within **10**.

With the guidance of the structural description (see IV.2.2), the molar magnetic susceptibility was simulated using an isotropic Heisenberg trinuclear model with the following spin Hamiltonian being $H = -2J(S_{Mn1}S_{Fe} + S_{Mn2}S_{Fe})$. The equivalent exchange constants (J) between the central Fe^{III} and two external Mn^{III} ions were considered. An analytical expression of the magnetic susceptibility can be calculated in the weak field approximation by the van Vleck equation² as given below ($x = J/k_B T$):

$$\chi_{Mn_2Fe} T = \frac{Ng^2\mu_B^2}{4k_B} \left[\frac{(e^{-6x} + e^{-4x}) + 10(e^{-7x} + e^{-3x}) + 35(e^{-8x} + e^{-2x}) + 85(e^{-9x} + e^{-x}) + 165}{(e^{-6x} + e^{-4x}) + 2(e^{-7x} + e^{-3x}) + 3(e^{-8x} + e^{-2x}) + 4(e^{-9x} + e^{-x}) + 5} \right] \quad \text{Eq IV.19}$$

Since the significant short contacts between trinuclear moieties are present, the intercomplex interactions (zJ') were also considered in the frame of the mean-field approximation:

$$\chi = \frac{\chi_{Mn_2Fe}}{1 - \frac{2zJ'}{N\mu_B^2 g^2} \chi_{Mn_2Fe}} \quad \text{Eq IV.20}$$

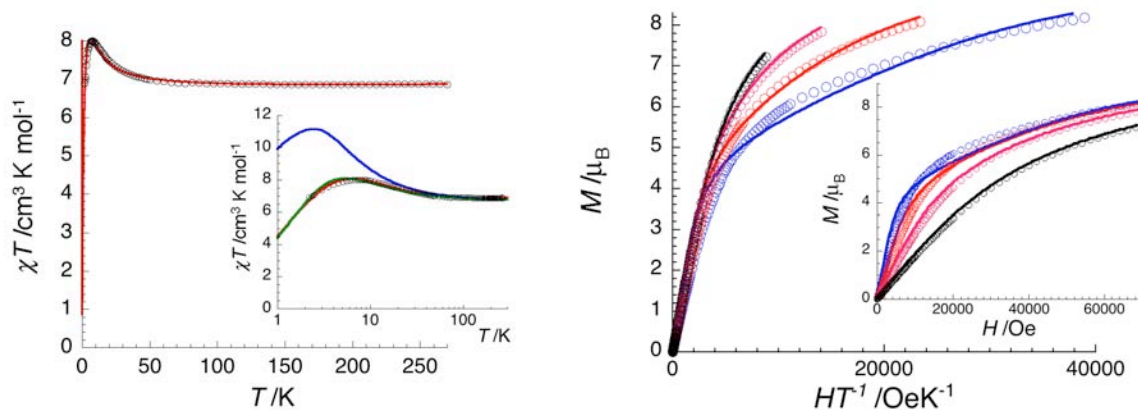


Figure IV.23 Temperature dependence of the χT product for **10** measured at $H_{dc} = 1000$ Oe. Inset: Expansion view of the main figure in semi-logarithmic plot. The solid lines are the best fits to models described in the text (left). M vs HT^{-1} (right) and M vs H (right, inset) curves for **10** at different temperatures; blue, 1.8 K; red, 3 K; purple, 5 K; black, 8 K; The solid lines are fitting results as described in the main text (right).

The best fitting result is shown in **Figure IV.23** (red line in left figure) with giving the following parameters: $g = 2.05$, $J/k_B = 3.2$ K, and $zJ'/k_B = -0.11$ K. The positive value of exchange coupling J through the cyanido bridges confirms that ferromagnetic interactions are operative between the high spin Mn^{III} and low spin Fe^{III} ions, leading to $S_T = 9/2$ spin ground state for **10**. For the Mn^{III} -NC- Fe^{III} systems in the literatures, the exchange coupling is quite sensitive to the bonding feature of Mn^{III} -N-C- Fe^{III} , showing both ferromagnetic and antiferromagnetic behaviors (Miyasaka et al. 2007). The correlation between the nature of magnetic interactions and structures (the Mn^{III} -N-C angle) cannot be simply summarized as many geometrical parameters govern the magnetic exchange. Nevertheless, the magnitude of the exchange coupling (J) within **10** is comparable to those seen in the complexes having the ferromagnetic interactions through CN bridges between Mn^{III} and Fe^{III} (Choi et al. 2004; Miyasaka et al. 1998; Ni et al. 2007). The negative value of zJ' suggests that weak antiferromagnetic interactions between trinuclear units are present. However, it is important to mention that these interactions could be overestimated in this model, as their estimation also contains the effects of the magnetic anisotropy brought by Mn^{III} ions. Therefore, an alternative model including the magnetic anisotropy parameters, D_{Mn} , has also been used with the following Hamiltonian: $H = -2J(S_{Mn1}S_{Fe} + S_{Mn2}S_{Fe}) + D_{Mn}(S_{z,Mn1}^2 + S_{z,Mn2}^2)$. The M vs H curves between 1.8 and 8 K have been numerically simulated using MAGPACK program (Borrás-Almenar et al. 2001) to compare with the experimental data (**Figure IV.23**, right), resulting in $g = 2.06$, $D_{Mn}/k_B = -4.1$ K, $J/k_B = 3.0$ K. The obtained D_{Mn} value is in agreement with ones found in similar Mn^{III} complexes (Miyasaka et al. 2004; Miyasaka et al. 2002). The reproduced χT vs T curve by MAGPACK program based on the above deduced parameters displays a large deviation from the experimental data at low temperature below 35 K, as shown in **Figure IV.23** (blue line in the inset of left figure). This implies that the magnetic model considering only the Mn^{III} anisotropy instead of the intercomplex magnetic interactions does not lead to an acceptable fit of the experimental data. The presence of the intercomplex magnetic interactions has negligible effect on M vs H curves compared to one on χT vs T curve. Therefore,

taking into account these intercomplex interactions using Eq IV.20 on the simulated MAGPACK χT product, we obtained the green curve in the inset of **Figure IV.23** with $zJ'/k_B = 0.10$ K. Even if the second approach seems more physically reasonable, the quality of the fits is not improved. Therefore, the obtained values for the D_{Mn}/k_B and zJ'/k_B parameters must be taken with caution as they produce similar effects on magnetic properties.

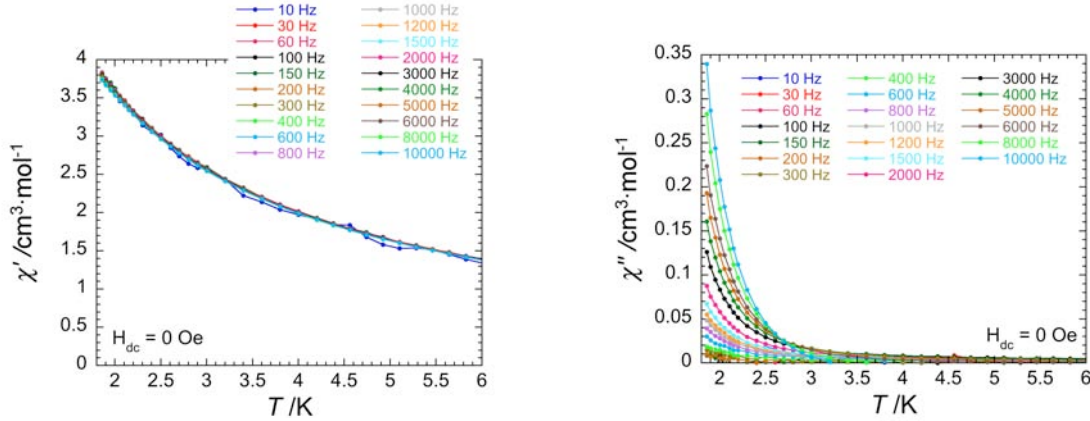


Figure IV.24 Temperature dependence of in-phase (left) and out-of-phase (right) components of the magnetic susceptibility for **10** at different frequencies. The solid lines are guide for eyes.

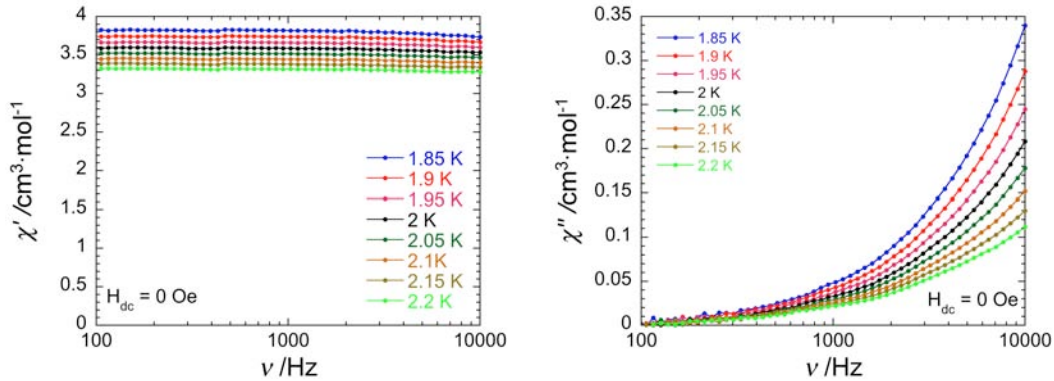


Figure IV.25 Frequency dependence of the real (χ' , left) and imaginary (χ'' , right) components of the ac susceptibility for **10** at different temperatures between 1.85 and 2.2 K under zero dc field.

The slow dynamics of the magnetization in **10** was studied by ac susceptibility measurements on a polycrystalline sample. Under zero dc field, the real (χ') and imaginary (χ'') components of the ac susceptibility have been measured as a function of the temperature above 1.85 K and a function of the ac field frequency from 100 to 10000 Hz (**Figure IV.24** and **Figure IV.25**). The frequency dependent out-of-phase signal was detected suggesting the slow relaxation of the magnetization, and therefore, SMM-like behavior. However the characteristic relaxation time (τ) of the system could not be followed in the available ranges of ac frequency and temperature with our experiment. In other words, the relaxation time of the system in zero dc-field is too fast for our ac technique to be studied accurately in temperature. This result can be explained by the presence of QTM that “short-cut” the thermal energy barrier: in zero field, the energy of the $\pm m_S$ states have the same energy and QTM between these pairs of levels is possible. When a magnetic field is applied, the $m_S < 0$ and $m_S > 0$ levels decrease and increase respectively, preventing quantum tunneling between the $\pm m_S$ states (see section I.1.2 in Chapter I).

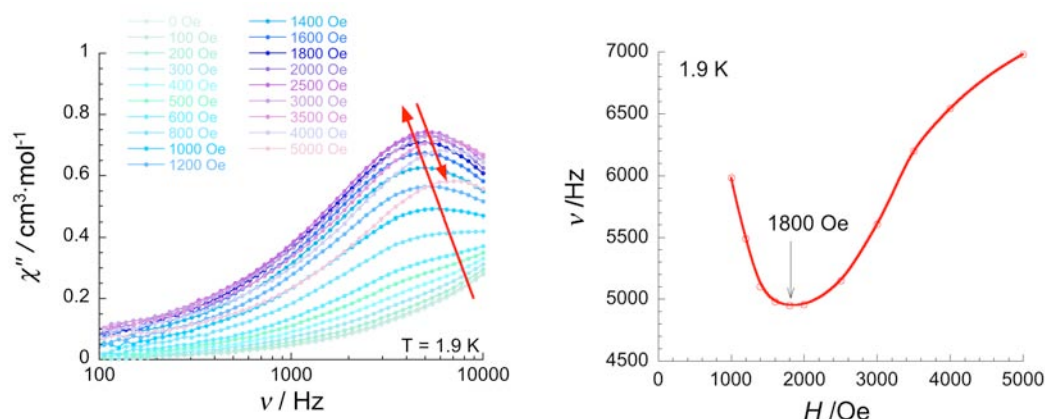


Figure IV.26 χ'' vs ν plot at 1.9 K under various applied H_{dc} for **10** (left). Field-dependence of the characteristic frequency (maximum of the χ'' vs ν plot) at 1.9 K (right).

Therefore, to reduce the possible fast zero-field relaxation usually induced by QTM and consequently to investigate the dynamics of **10**, we performed ac susceptibility measurements under several applied dc magnetic fields (**Figure IV.26**, left). At 1.9 K, the characteristic frequency (maximum of the χ'' vs ν plot) decreases from 6000 Hz at 0 Oe to 4950 Hz in an optimum dc field of about 1800 Oe (**Figure IV.26**, right) confirming the presence of fast relaxation at zero-field.

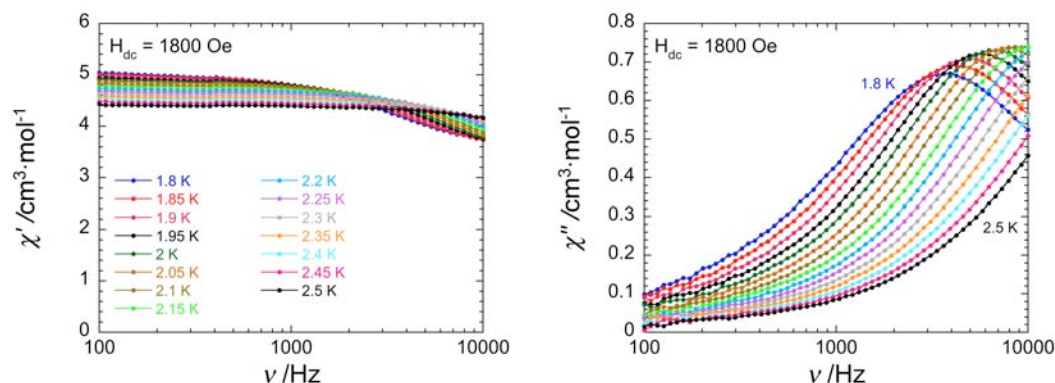


Figure IV.27 Frequency dependence of the real (χ' , left) and imaginary (χ'' , right) components of the ac susceptibility for **10** at different temperatures between 1.85 and 2.2 K under $H_{dc} = 1800$ Oe.

Hence to estimate the temperature dependence of the relaxation time, ac data were collected at 1800 Oe (**Figure IV.27**). Under 1800 Oe, a clear maximum is now detected on the χ'' vs ν plots allowing the determination of the relaxation time of **10** in a relatively large temperature domain. As expected for SMMs, the deduced relaxation time follows a thermally activated behavior (**Figure IV.28**) with $\tau_0 = 4.6 \times 10^{-8}$ s and an energy gap $\Delta_{eff}/k_B = 12.4$ K. It is worth noting that this energy gap allows for an estimation of the uniaxial anisotropy at $D_T/k_B = -0.62$ K, for the trinuclear $S_T = 9/2$ $[\text{Mn}_2\text{Fe}]$ unit. This value is smaller than the one estimated for previously reported $[\text{Mn}_2\text{Fe}]$ SMM ($D_T/k_B = -1.25$ K) (Ferbinteanu et al. 2005). The explanation can be found in the orientation of two JT axes in the $[\text{Mn}_2\text{Fe}]$ complexes: the previously reported $[\text{Mn}_2\text{Fe}]$ SMM is almost linear leading two JT axes on Mn^{III} ions being almost parallel, while compound **10** is bent with Mn-N-C angle being $154.2(3)^\circ$ that induce a separation angle between two JT axes as *ca.* 70° . Therefore, the total anisotropy of **10** is reduced compared to the linear complex.

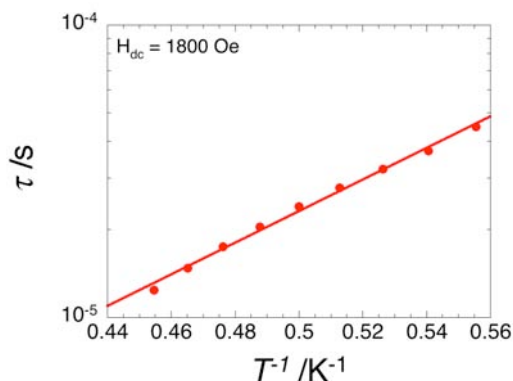


Figure IV.28 τ vs T^{-1} plot at $H_{\text{dc}} = 1800$ Oe. The solid line represents an Arrhenius fit of the data.

IV.2.4 Concluding remark

We have described the syntheses, structures, and magnetic properties of a new cyanido-bridged trinuclear $[\text{Mn}^{\text{III}}_2\text{Fe}^{\text{III}}]$ complex **10**. The trinuclear complex has a bent structure, giving one cyanido ligand left uncoordinated on the Fe^{III} ion with an enough accessible space for an additional complexation, for example with compound **7**. Consequently, JT axes on Mn^{III} ions are not parallel showing a separation angle of *ca.* 70° . Magnetic studies undoubtedly reveal an overall ferromagnetic interaction between Mn^{III} and Fe^{III} centers bridged by cyanido group. This ferromagnetic coupling within the trinuclear unit and the magnetic anisotropy brought by Mn^{III} ions give rise to slow relaxation of the magnetization in complex **10**. Although the estimation of the relaxation time was difficult at zero-field, ac susceptibility measurements in a non-zero dc field indicate that **10** is a SMM.

IV.3 Conclusion and perspectives

In Chapter IV, two heterometallic molecular compounds, based on a *mer*-tricyanidoiron(III) building block (**6**), are investigated in terms of syntheses, structural characterization, and magnetic properties. Compound **8** is a dinuclear $[\text{Co}^{\text{II}}\text{Fe}^{\text{III}}]$ complex and compound **10** is a trinuclear $[\text{Mn}^{\text{III}}_2\text{Fe}^{\text{III}}]$ system. Keeping in mind the concluding remarks for both complexes at the sections IV.1.6 and IV.2.4, let us now summarize here the initial inspiration of this project, and therefore the following perspectives.

Compound **8** displays a thermal spin crossover on Co^{II} ion in solid state and a protonation triggered metal-to-metal electron transfer in solution. Therefore, **8** acts as the fascinating molecular switches between two states. Considering that our objective concerns the design of a dinuclear $[\text{FeCo}]$ complex as a photomagnetic switch in coordination compounds or networks, we need a complex possessing well defined photoswitching properties on the metal ion that will be further coordinated to metal complexes or SMMs.

Although compound **8** shows a spin crossover in solid state, photo-induced electron transfer has not yet been observed with this complex. Nevertheless, we observed that the protonation of bbp ligand belonging to Fe center significantly modified its redox potential in solution, and consequently the reduced ΔE resulted in the occurrence of an intramolecular metal-to-metal electron transfer. Knowing this result, next step would be crystallization of this di-protonated $[\text{FeCo}]$ species. Since the

di-protonated Fe precursor (**9**) has been isolated in its solid state, building-block approach would be performed with the Co precursor (**7**).

Furthermore, we do not know yet a coordination effect of two free cyanide groups on the [FeCo] dinuclear complex (**8**) to other metal centers. The further coordination of **8** to other metal complexes would eventually modify of redox potential of Fe site, leading to an intramolecular electron transfer in [FeCo] unit. Therefore, it is worth enough trying to assembly compound **8** with [Mn(SB)]⁺ complex or SMMs, although this dinuclear unit itself does not behave as a photomagnetic linker.

We can also suggest the future direction of this project to obtain new electron transfer dinuclear systems, based on the present compound **8**. Keeping in mind the obtained results, the next challenge will be to modify the redox potential of Co and/or Fe building blocks in order to decrease ΔE . The electron donating groups (eg. $-\text{NH}_2$, $-\text{NR}_2$) and/or electron withdrawing groups (eg. $-\text{X}$, $-\text{CX}_3$ with X being halogens) can be respectively introduced on the ligands of Co and Fe building blocks. The functionalization of ligands is in progress in the frame of the thesis project of S. Calancea (PhD thesis, 2010 – 2013) and D. Mitcov (PhD thesis, 2010 – 2013).

On the other hand, a new trinuclear [Mn₂Fe] system, compound **10**, shows slow relaxation of the magnetization and behaves as a SMM in a non-zero dc field. Therefore, **10** can be one of the interesting candidates to coordinate a suitable Co^{II} complex to one available cyanido present on the middle Fe^{III} ion. During this thesis, we have performed preliminary tries with compound **7**, but compound **10** in solution was dissociated leading to the [FeCo] dinuclear complex **8**.

IV.4 Preliminary results

IV.4.1 Dinuclear [(bbp)Fe(CN)₃Co(PY5R₂)] systems (R = Me, H, OH)

Synthetic approach. As mentioned in the main text, structurally similar [FeCo] dinuclear complexes with compound **8** are obtained by performing the reaction in different mixture of solvents and also by changing the methyl substituents on PY5 ligands. Compared to the synthesis of **8** that was done in a mixture of methanol and acetonitrile, we have carried out same reaction to assemble the Fe and Co precursors (compounds **6** and **7**) but (i) in the mixture of acetonitrile and dichloromethane and (ii) only in acetonitrile. They respectively afforded dinuclear [FeCo] complexes containing the same building [FeCo] unit with different composition of interstitial solvent molecules: [(bbp)Fe(CN)₃Co(PY5Me₂)]·1.5(CH₂Cl₂)·0.5H₂O (**11**) and [(bbp)Fe(CN)₃Co(PY5Me₂)]·2.5(CH₃CN)·0.5H₂O (**12**). We have also performed the syntheses with Co building units possessing different derivatives of PY5 ligands (Scheme IV.3), while keeping the same Fe precursor (**6**) in the mixture of methanol and acetonitrile. The introduction of PY5H₂ (2,6-*bis*(1,1-*bis*(2-pyridyl)methyl)pyridine) and PY5OH₂ (2,6-*bis*(1,1-*bis*(2-pyridyl)hydroxymethyl)pyridine) ligands on Co^{II} ions respectively resulted in [(bbp)Fe(CN)₃Co(PY5H₂)]·5(CH₃OH) (**13**) and [(bbp)Fe(CN)₃Co(PY5OH₂)]·5(CH₃OH) (**14**) (see supporting information for synthesis details).

The stretching bands for the cyanide are seen in the infrared spectrum for compounds **11** – **14**. The bridging cyanide band is observed at *ca.* 2161 – 2163 cm⁻¹ with a small intensity for all compounds, as seen in compound **8** (Figure IV.29). The terminal cyanides are observed in lower energy *ca.* 2124 cm⁻¹ without significant further splitting. For compound **14**, however, the absorption for cyanides in another energy was also observed in addition to the aforementioned one: a weak absorption at 2090 cm⁻¹ and a more intense one at 2066 cm⁻¹ (Figure IV.29). Moreover, these bands are observed in both wet sample just taken from the crystallization tube and dry sample after the SQUID measurements. It is worth mentioning that these energies in the range for the bridging CN⁻ in Fe^{II}_{LS}Co^{II}_{HS} or Fe^{II}_{LS}Co^{III}_{LS} systems (Berlinguette et al. 2005; Li et al. 2008). This probably implies the mixture of different oxidation states of {FeCo} units in **14**.

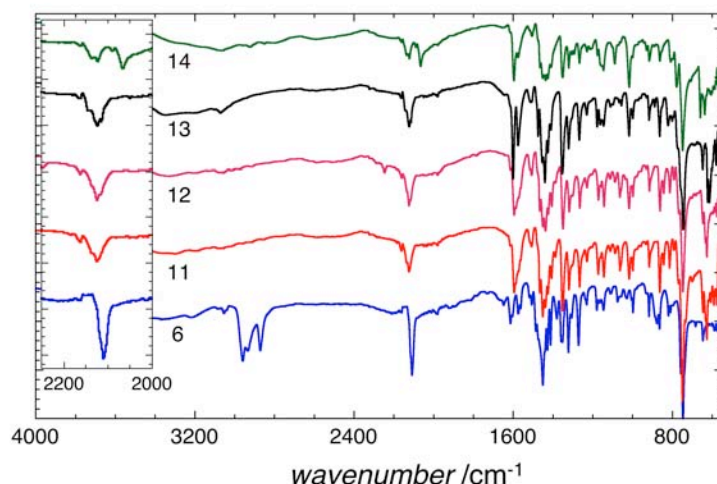


Figure IV.29 FT-IR spectra of compounds **6** and **11** – **14** at 298 K, highlighting cyanide stretching in inset.

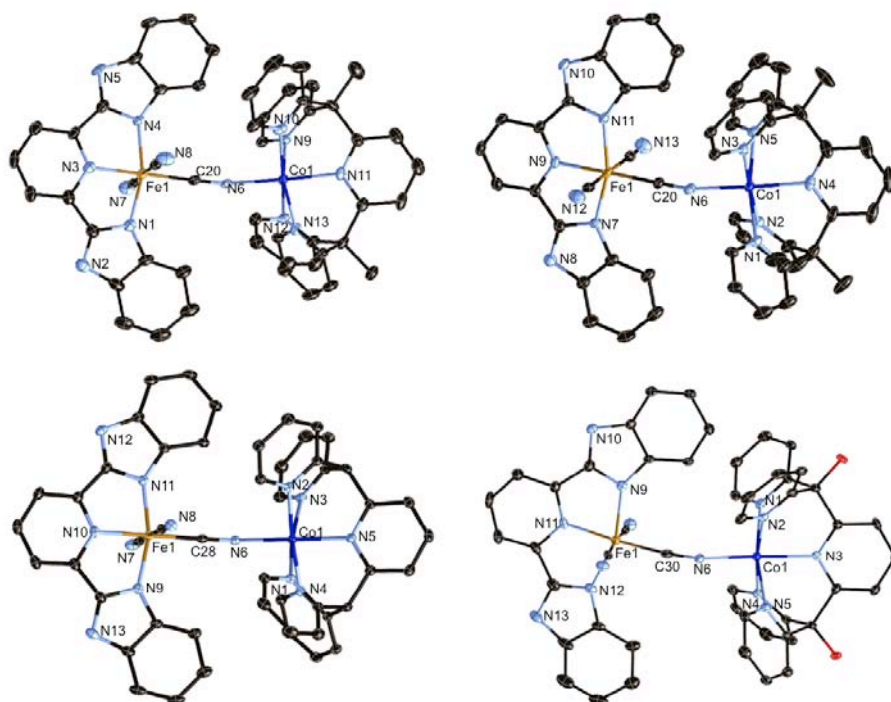


Figure IV.30 ORTEP-type view of molecular structures of compounds **11** (left, top), **12** (right, top), **13** (left, bottom), and **14** (right, bottom) with thermal ellipsoids at 40 % level. Yellow, Fe; blue, Co; skyblue, N; black, C; red, O. Lattice solvents and hydrogen atoms are omitted for clarity.

Structural description. The crystallographic data for compounds **11** – **14** are summarized in **Table IV.8**. All four complexes contain neutral dinuclear units (**Figure IV.30**), as seen in compound **8**. The coordination sphere of cobalt center in all four complexes (**11** – **14**) exhibits an octahedral geometry, without the significant distortion. The average Co-N_{py} bond lengths in **11** and **12** compare almost perfectly with those observed in the mononuclear Co precursor (**7**) (**Table IV.2**), implying the presence of high spin cobalt(II) ions. The average Co-N_{py} bond lengths in **13** and **14** also fall in the range of those found for [Co^{II}(PY5R₂)]²⁺ complexes with Co^{II}_{HS} (Klein Gebbink et al. 2002; Sun et al. 2011; Wasylenko et al. 2011). For the coordination environment of the Fe center in **11** – **13** is in a good agreement with the one observed in Fe precursor (**6**) and the dinuclear compound **8**. For compound **14**, however, the average Fe-N bond distance is longer than the one observed for other compounds (**8**, **11** – **13**) (**Table IV.9**), showing the longest one being 2.004(4) Å for Fe1-N12. These bond distances longer than a iron(III) site seen in compounds **6** and **9**, but shorter than iron(II) with bbp-derivative ligands (2.111(3) – 2.168(3) Å) (Wang et al. 2003). It is also important noting that a weak electron density in the difference Fourier maps was observed around N13 and the ellipsoids on this half of the bbp ligand (defining the middle with the N11-Fe1-C30 axis, the side containing N13) are obviously elongated compared to those at the other side. Furthermore, we could not observe any counter ions. These features with those observed in infrared probably suggest the statistical mixture of [(bbp)Fe^{III}_{LS}-Co^{II}_{HS}] and [(Hbbp)Fe^{II}_{LS}-Co^{II}_{HS}] moieties. This hypothesis should be studied and verified with further characterization techniques including structural characterization at different temperatures.

Table IV.8 Crystallographic data of compounds **11** – **14**.

	11 (120 K)	12 (100 K)	13 (90 K)	14 (100 K)
Empirical formula	C ₁₀₅ H ₈₀ Cl ₆ Co ₂ Fe ₂ N ₂₆ O	C ₅₆ H _{44.5} CoFeN _{15.5} O _{0.5}	C ₅₄ H ₅₂ CoFeN ₁₃ O ₅	C ₅₄ H ₅₂ CoFeN ₁₃ O ₇
Formula weight, g	2164.21	998.76	1077.87	1109.87
Crystal system	Monoclinic	Monoclinic	Monoclinic	Monoclinic
Space group	<i>P</i> 2 ₁ / <i>c</i>	<i>P</i> 2 ₁ / <i>c</i>	<i>P</i> 2 ₁ / <i>c</i>	<i>P</i> 2 ₁ / <i>c</i>
Wavelength, Å	0.71073	0.71073	0.71069	0.71073
<i>a</i> , Å	13.984(4)	13.903(4)	14.285(5)	13.328(5)
<i>b</i> , Å	13.266(4)	13.337(2)	13.646(5)	13.819(3)
<i>c</i> , Å	25.865(7)	25.670(6)	26.810(5)	29.636(10)
β , °	94.21(14)	93.32(1)	102.078(5)	109.21(1)
<i>V</i> , Å ³	4785.2(2)	4752.0(2)	5110.0(3)	5154.3(3)
<i>Z</i>	2	4	4	4
ρ_{calcd} , Mg m ⁻³	1.533	1.478	1.401	1.430
μ , mm ⁻¹	0.851	0.715	0.671	0.670
^a <i>R</i> ₁ (<i>I</i> > 2 σ (<i>I</i>))	0.0752	0.0696	0.0434	0.0630
^b <i>wR</i> ₂ (all)	0.2297	0.2118	0.1230	0.2164
GoF ^a	1.018	1.018	1.077	1.083

$$^a R_1 = \sum ||F_o| - |F_c|| / \sum |F_o|, \text{ and } ^b wR_2 = [\sum w(F_o^2 - F_c^2)^2 / \sum w(F_o^2)^2]^{1/2}.$$

Table IV.9 Selected bond lengths [Å] and angles [°] for **11** – **14**.

	11 (120 K)	12 (100 K)	13 (90 K)	14 (100 K)
av(Fe-N)	1.936(4)	1.933(4)	1.928(2)	1.977(5)
av(Fe-C)	1.957(6)	1.944(5)	1.944(2)	1.925(6)
av(Co-N _{py})	2.130(4)	2.130(4)	2.155(2)	2.150(4)
Co-N-C ^a	161.8(4)	161.6(4)	164.2(2)	165.4(5)
Fe-C-N ^a	178.5(4)	178.5(4)	176.7(2)	173.7(5)

^aThese angles are through the bridging cyanido ligand.

Magnetic properties. As shown in **Figure IV.31**, temperature dependence of the magnetic susceptibilities for compounds **11** – **14** were measured at an external dc field of 1000 Oe. The χT product at room temperature for all compounds is *ca.* 3.1 cm³Kmol⁻¹, that agrees well with the room temperature value for compound **8**. This implies the presence of a {Fe^{III}_{LS}Co^{II}_{HS}} unit. With decreasing temperatures, the χT product for compounds **11**, **12**, and **14** remains roughly constant down to 100 K, and then decreases due to the spin-orbit coupling of the high spin Co^{II} ion (Kahn 1993), as observed in the mononuclear Co compound **7**. Whereas, compound **13** displays a gradual decrease of the χT product from the room temperature down to 8 K to reach 1.86 cm³Kmol⁻¹. Then, further abrupt decrease below 8 K is like those also observed for other compounds in that temperature region, which should be associated with spin-orbit coupling of the Co^{II}_{HS}. Supposing the partial spin crossover on Co^{II} ion for compound **13**, we have collected structure at both 270 and 90 K, to compare. However, no significant difference was observed between two data. As discussed previously, the distorted coordination of Co^{II} site at low temperature, that is the hallmark for the low spin Co^{II}, was not seen, and all Co-N bond distances also exclude the low spin Co^{III}.

These preliminary studies allow us to give some remarks. Given the fact that compounds **11** and **12** contains same ligands around Co and Fe centers like in compound **8**, the observed spin crossover behavior in **8** is strongly influenced by the interstitial solvents that are the only differences with **11** and **12**. Furthermore, the modification in the surroundings of Co in **13** and **14** were not enough to induce a solid state electron transfer in these dinuclear complexes.

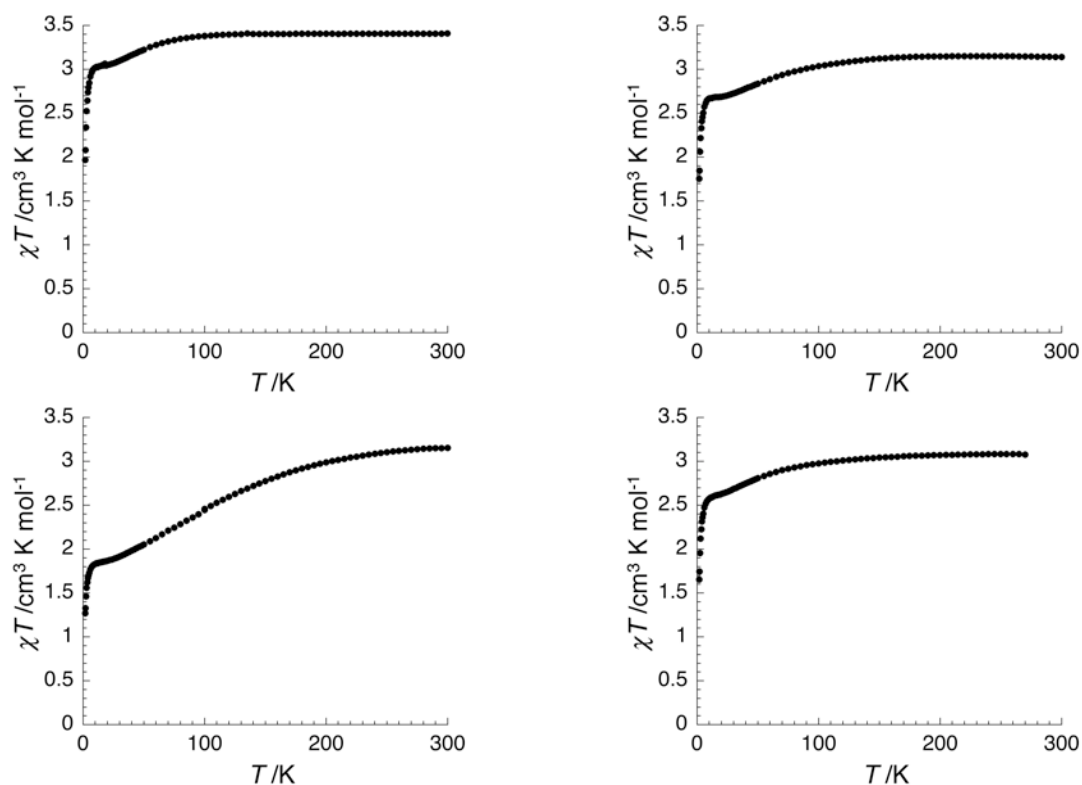


Figure IV.31 Temperature dependence of the χT product for compounds **11** (left, top), **12** (right, top), **13** (left, bottom), and **14** (right, bottom) measured at 1000 Oe.

IV.4.2 Dinuclear $[(\text{Tp})\text{Fe}(\text{CN})_3\text{Co}(\text{PY5Me}_2)]^+$ system

Syntheses. In collaboration with Prof. Li (Central China Normal University and visiting professor at CRPP in 2010), we have also obtained an other dinuclear complex, $[(\text{Tp})\text{Fe}(\text{CN})_3\text{Co}(\text{PY5Me}_2)]\cdot\text{OTf}\cdot\text{DMF}\cdot 2\text{H}_2\text{O}$ (**15**) (Tp: trispyrazolylborate, OTf: trifluoromethanesulfonate, DMF: dimethylformamide). Instead of using bbb ligand, Tp ligand was exploited for the iron precursor, while keeping the PY5Me₂ ligand for cobalt building unit. Compound **15** was prepared from the a DMF solution containing PY5Me₂ ligand, Co(OTf)₂, and the pre-formed Fe precursor, (NBu₄)[Fe(Tp)(CN)₃]. The vapor diffusion of the diethylether to the reaction solution afforded dark orange colored crystals suitable for the single crystal diffraction with a needle-like shape. The magnetic and optical properties of this compound **15** are different upon the removal of interstitial solvent molecules. So we performed the experiments with as-prepared samples (**15**) and the ones after drying (**15a**). The compound **15a** was prepared by drying in the vacuum at 40 °C for 24 h. FT-IR confirmed no presence of water (3400 cm⁻¹) and DMF (1675 cm⁻¹) molecules after the drying treatment. The stretching bands for cyanido ligands are observed in 2160, 2121, 2080, and 2058 cm⁻¹, without a significant difference between **15** and **15a** (Figure IV.32).

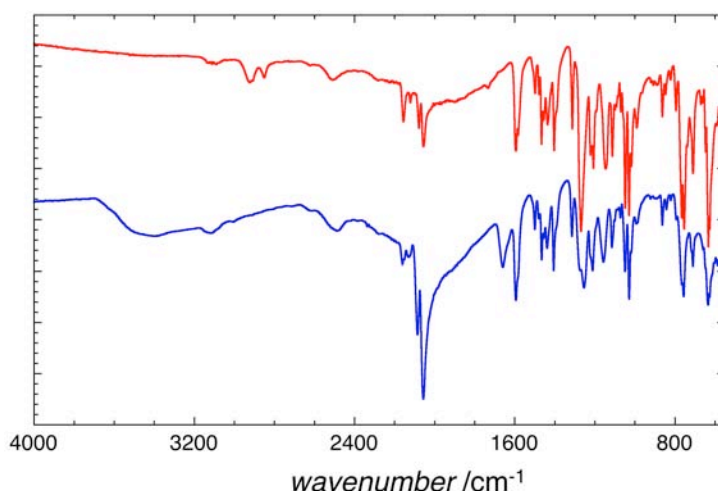


Figure IV.32 FT-IR spectra of compounds **15** (blue) and **15a** (red) at 298 K.

Magnetic properties. DC susceptibility measurements on compound **15** (filtered polycrystalline sample) and **15a** were carried out between 1.8 and 300 K at 5 K/min with $H = 10000$ Oe (**Figure IV.33** and **Figure IV.34**). For **15**, the χT product at 300 K is $3.57 \text{ cm}^3\text{Kmol}^{-1}$ corresponding to one low-spin $S = 1/2$ iron(III) and one high-spin $S = 3/2$ cobalt(II) spin. Then, there are three decreases of the χT product with decreasing temperature at ca. 250, 205, and 180 K, successively. On the other hand, compound **15a** displays one step of sharp transition at ca. 170 K with a hysteresis of ca. 4 K at 5 K/min. The χT product at 300 K is $3.19 \text{ cm}^3\text{Kmol}^{-1}$ and slightly increases up to $3.28 \text{ cm}^3\text{Kmol}^{-1}$ at 180 K before the transition. For both compounds **15** and **15a**, the χT product below 145 K is fairly constant at $0.007 \text{ cm}^3\text{Kmol}^{-1}$ highlighting the stabilization of the diamagnetic state. The foregoing results indicate that a partial loss of solvents in compound **15** has led to different environment of [CoFe] pair in the crystal field, and therefore temperatures in which an electron transfer occurs are changed. Further studies should be done in solution. Compound **15a** was also rapidly introduced into the magnetometer at 10 K in order to quench the high temperature state. But diamagnetic state was detected due to the thermal equilibrium in the magnetometer was stabilized at ca. 40 K right after the introduction of the compound. At this temperature, the paramagnetic state relaxes to the diamagnetic state as shown in the reflectivity measurements (see the following).

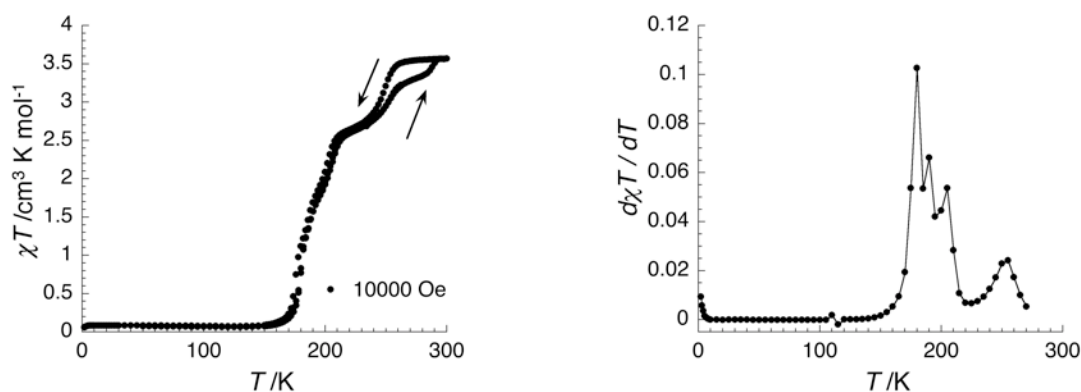


Figure IV.33 χT vs T (left) and $d\chi T/dT$ vs T (right) plots of compound **15** at 10000 Oe at 5 K/min (with χ being the molar magnetic susceptibility defined as M/H per dinuclear complex).

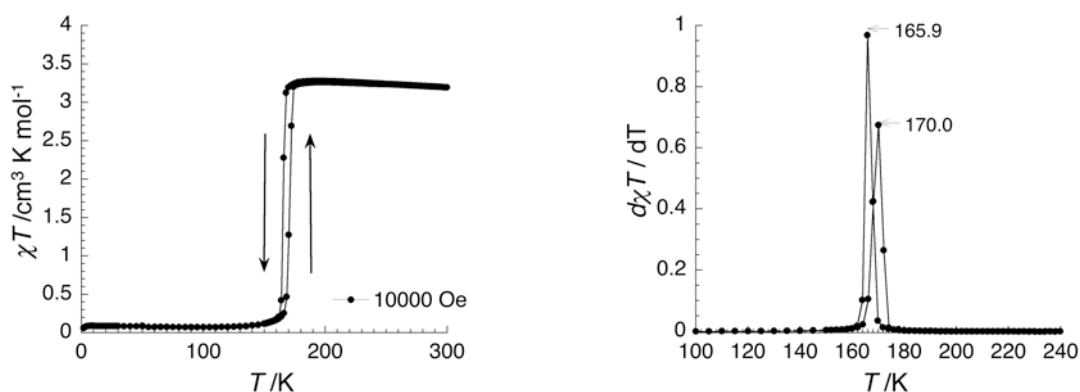


Figure IV.34 χT vs T (left) and $d\chi T/dT$ vs T (right) plots of compound **15a** at 10000 Oe at 5 K/min (with χ being the molar magnetic susceptibility defined as M/H per dinuclear complex).

Differential scanning calorimetry. The behavior observed for **15a** by magnetic measurements was confirmed by DSC analysis (**Figure IV.35**). As shown by the magnetic measurements, phase transition is observed in the DSC traces when the sample is cooled down and heated up at ca. 165 and 173 K, respectively. This endothermic peak agrees with the phase transition of the diamagnetic $[\text{Fe}^{\text{II}}_{\text{LS}}\text{Co}^{\text{III}}_{\text{LS}}]$ units into the paramagnetic $[\text{Fe}^{\text{III}}_{\text{LS}}\text{Co}^{\text{II}}_{\text{HS}}]$ state. Integrations of the DSC peaks lead to an estimation of the transition enthalpy equal to ca. 9.35 kJ/mol probably associated with this structural and magnetic phase transition. The DSC measurement is in good agreement with magnetic study.

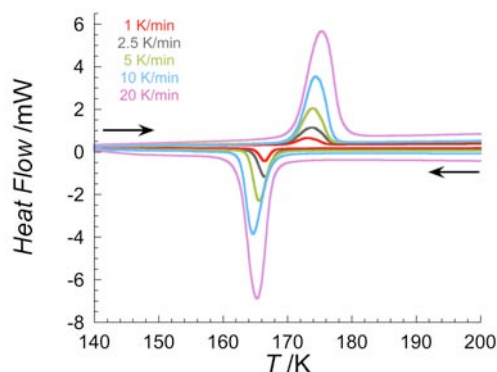


Figure IV.35 DSC thermograms of **15a** at different scan rate. Endothermic peaks are pointing up.

Table IV.10 Transition temperatures and corresponding enthalpies of **15a** on DSC measurement of heating and cooling.

	1 K/min	2.5 K/min	5 K/min	10 K/min	20 K/min
T_{heating} (K)	172.9	173.7	173.9	174.3	175.3
$\Delta H_{\text{heating}}$ (kJ/mol)	9.24	9.31	9.38	9.42	9.37
T_{cooling} (K)	166.3	166.4	165.6	164.5	165.1
$\Delta H_{\text{cooling}}$ (kJ/mol)	8.73	9.72	9.33	9.52	9.37

Reflectivity measurements. Optical measurements have been investigated with the reflectivity set-up on both compounds **15** and **15a**. This set-up uses a white light source, and collects the light reflected by the sample (that is the sum of direct and diffuse reflected light). Several irradiation protocols have been used to test the photosensitivity of the compound. The first set of measurements consists in studying the thermal dependence of the reflectivity spectra. To limit photoexcitation effects, the power of the white light is fixed at 0.08 mW, and the light is only switched on for 1 s to

record at one temperature the reflectivity spectrum, and then the light is switched off during the next temperature step. The spectra in these conditions are shown in **Figure IV.37** during cooling and heating modes.

Figure IV.36 presents the reflectivity spectra of the compound **15** between 300 K and 10 K on cooling (left) and then on heating (right) modes with a sweeping temperature rate of 4 K/min. At room temperature, **15** presents an absorption band with a maximum at 860 nm. The other strong absorption at higher energy (< 600 nm) was also detected. When the temperature is decreasing down to 100 K, **15** becomes more and more absorbent above 650 nm as a signature of the electron transfer occurring between Co(II) and Fe(III): $\text{Co}^{\text{II}}_{\text{HS}}\text{Fe}^{\text{III}}_{\text{LS}}$ convert into diamagnetic $\text{Co}^{\text{III}}_{\text{LS}}\text{Fe}^{\text{II}}_{\text{LS}}$. Upon further cooling, the spectra are only slightly modified. Once the compound is re-heated, the same variation of the spectra is observed suggesting a reversible change from the diamagnetic state to the paramagnetic state. An alternative way to visualize the change of spectra as function of temperature is presented in **Figure IV.37** in the form of the thermal dependence of the reflectivity at 735 ± 5 nm (noted R_{735}). Upon cooling from 300 K, R_{735} decreases from 0.43 down to 0.14 at 150 K as a signature of thermal-induced electron transfer phenomenon. However, there are three different steps as already observed by magnetic properties. In the heating mode from 10 K to 150 K, R_{735} stays at constant value of 0.14 and R_{735} starts to increase displaying the hysteresis effect. The spectrum at 300 K is similar to the one obtained before the thermal cycle suggesting that the compound almost recovers its high temperature $\text{Co}^{\text{II}}_{\text{HS}}\text{Fe}^{\text{III}}_{\text{LS}}$ phase.

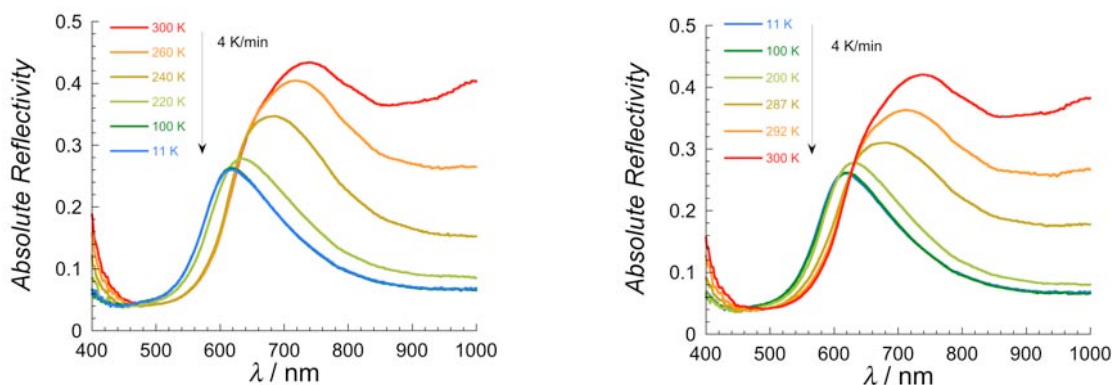


Figure IV.36 Selected reflectivity spectra of **15** as function of temperature: between 300 and 11 K (left); between 11 and 300 K (right).

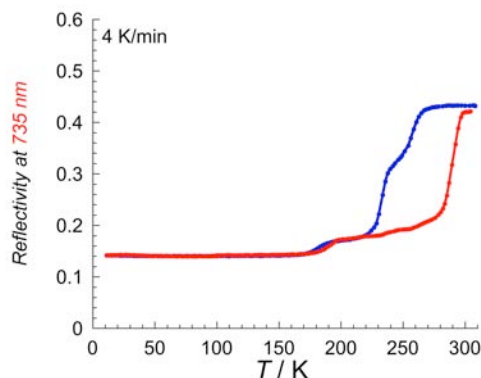


Figure IV.37 Thermal evolution of reflectivity signal recorded at $\lambda = 735 \pm 5$ nm (R_{735}) in cooling mode (310 K– 10 K: blue), and in heating mode (10 K - 310 K: red) with the sweeping rate 4 K/min for compound **15**.

The second set of measurements is similar to the first set except the white light irradiation is switched on during the complete thermal cycles. The obtained spectra are displayed in **Figure IV.38** and **Figure IV.39**.

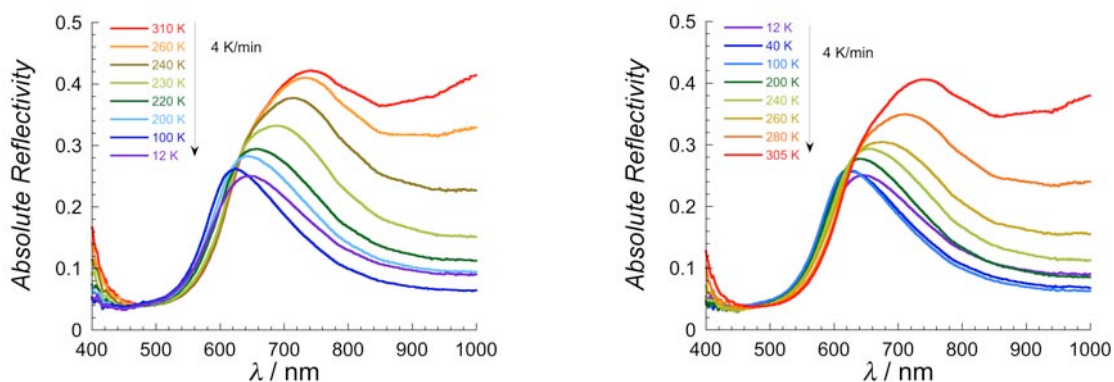


Figure IV.38 Selected reflectivity spectra of **15** as function of temperature: (top) between 310 and 10 K; (bottom) between 10 and 305 K.

The important changes are observed between the two experiments, with and without light irradiation during the ramping. As exemplified by the **Figure IV.39**, when the temperature is decreased, R_{735} decreases from 0.42 to 0.15 with only two steps. Below 50 K, there is a small increase of R_{735} and it decreases with a hysteresis upon heating. Above 50 K, R_{735} is first nearly constant up to 190 K and starts to increase with a hysteresis larger compared to the first experiments. Further heating induces several steps also with hysteresis effect. The difference between two experiments can be raised by the photo-sensitivity of the sample and by the evolution of sample in time (solvent loss during the experiment). In order to probe the photo-induced state, we performed an additional experiment: the compound is cooled to 10 K in the dark, and when the temperature is stable, the white light irradiation starts with a light intensity of 0.08 mW. **Figure IV.40** (left) shows the time evolution of the reflectivity, R_{735} , at 10 K during irradiation. At the beginning of the irradiation, the compound is in a state with $R_{735} = 0.16$, then R_{735} increases to reach a value of 0.38 after 90 mins. As shown by **Figure IV.40** (right), the spectra at 10 K before and after this white light excitation are very different. Moreover, the spectrum after irradiation is close to the spectrum at room temperature suggesting that the same $\text{Co}^{\text{II}}_{\text{HS}}\text{Fe}^{\text{III}}_{\text{LS}}$ state is involved. Finally, the thermal evolution of R_{735} after this photoexcitation is shown in **Figure IV.41**. R_{735} is nearly constant until 30 K, and then shows a decrease from this temperature to reach 0.17 at 50 K. This decrease corresponds to the thermal-activated relaxation from the photo-excited state. Above 170 K, only one step of high-temperature transition was observed different from the previously mentioned other measurements. Considering the dried sample (**15a**) has one-step transition at similar temperature in magnetic susceptibility measurement, the compound **15** is supposed to lose interstitial solvents during the reflectivity experiments. Thus, we have performed the same reflectivity experiments with **15a**.

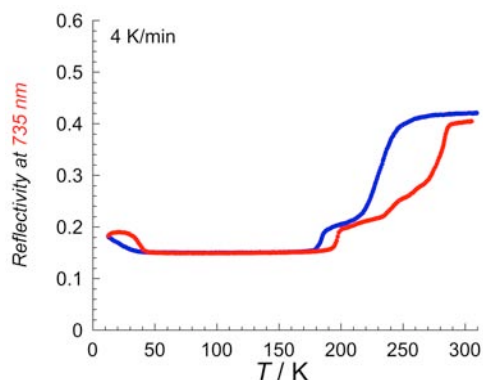


Figure IV.39 Thermal evolution of reflectivity signal recorded at $\lambda = 735 \pm 5$ nm (R_{735}) in cooling mode (300 K– 10 K: blue), and in heating mode (10 K - 270 K: red) with the sweeping rate 4 K/min for compound **15**.

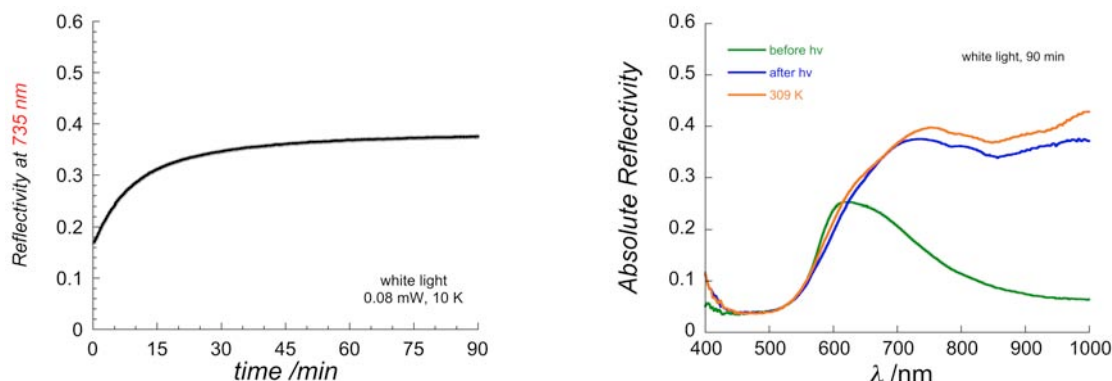


Figure IV.40 Time evolution at 10 K of reflectivity signal recorded at $\lambda = 735 \pm 5$ nm (R_{735}) under white light irradiation (0.08 mW) for compound **15** (left). Spectra obtained before irradiation and after 90 mins of white light irradiation, and at 309 K (right).

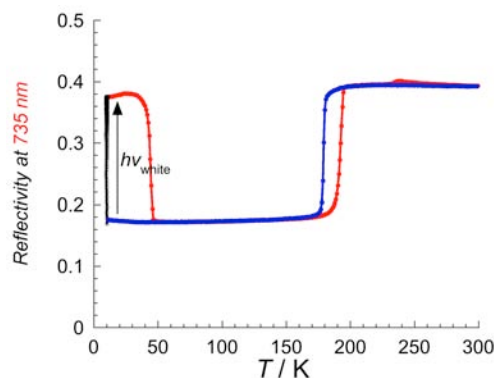


Figure IV.41 Thermal evolution of reflectivity signal of **15** recorded at $\lambda = 735 \pm 5$ nm (R_{735}) under white light (0.08 mW) during 90 mins at 10 K (dark points), in heating mode (red points) and cooling mode (blue points).

Figure IV.42 presents the reflectivity spectra of the compound **15a** between 300 K and 10 K on cooling (left) and then on heating (right) modes with a sweeping temperature rate of 4 K/min. At room temperature, **15a** presents an absorption band with a maximum at 860 nm similar to the one of compound **15**. When the temperature is decreasing down to 100 K, **15** becomes more and more absorbent above 650 nm as a signature of the electron transfer occurring between Co(II) and Fe(III): $\text{Co}^{\text{II}}_{\text{HS}}\text{Fe}^{\text{III}}_{\text{LS}}$ convert into diamagnetic $\text{Co}^{\text{III}}_{\text{LS}}\text{Fe}^{\text{II}}_{\text{LS}}$. Upon further cooling, the spectra are only slightly modified. Once the compound is re-heated, the same variation of the spectra is observed suggesting a reversible change from the diamagnetic state to the paramagnetic state. An alternative way to visualize the change of spectra as function of temperature is presented in **Figure IV.43** (left) in the form of the thermal dependence of the reflectivity at 735 ± 5 nm (noted R_{735}). Upon cooling from 300 K, R_{735}

slightly increases from 0.52 up to 0.56 at 195 K before decreasing progressively down to 0.18 below 166 K as a signature of thermal-induced electron transfer phenomenon. In this case, there is only one step as already observed by magnetic properties of compound **15a**. In the heating mode from 10 K to 172 K, R_{735} stays at constant value of 0.18 and R_{735} starts to increase displaying the hysteresis effect of ca. 5 K. The spectrum at 300 K is similar to the one obtained before the thermal cycle suggesting that the compound almost recovers its high temperature $\text{Co}^{\text{II}}_{\text{HS}}\text{Fe}^{\text{III}}_{\text{LS}}$ phase. The second set of measurements is similar to the first set except the white light irradiation is switched on during the complete thermal cycles. The obtained spectra are displayed in **Figure IV.43** (right). Upon cooling from 300 K, the evolution of R_{735} is basically identical, except for the photo-induced effect at low temperature. In order to probe the photo-induced state, we performed an additional experiment: the compound is cooled to 10 K in the dark, and when the temperature is stable, the white light irradiation starts with a light intensity of 0.08 mW. **Figure IV.44** (left) shows the time evolution of the reflectivity, R_{735} , at 10 K during irradiation. At the beginning of the irradiation, the compound is in a state with $R_{735} = 0.18$, then R_{735} increases to reach a value of 0.62 after 700 mins with a saturation. As shown by **Figure IV.44** (right), the spectra at 10 K before and after this white light excitation are very different. Moreover, the spectrum after irradiation is close to the spectrum at 310 K suggesting that the same $\text{Co}^{\text{II}}_{\text{HS}}\text{Fe}^{\text{III}}_{\text{LS}}$ state is involved. Finally, the thermal evolution of R_{735} after this photoexcitation is shown in **Figure IV.45**. R_{735} is nearly constant until 30 K, and then shows a decrease from this temperature to reach 0.18 at 50 K. This decrease corresponds to the thermal-activated relaxation from the photo-excited state. Above 173 K, only one step of high-temperature transition was observed like the previously mentioned other measurements for compound **15a**.

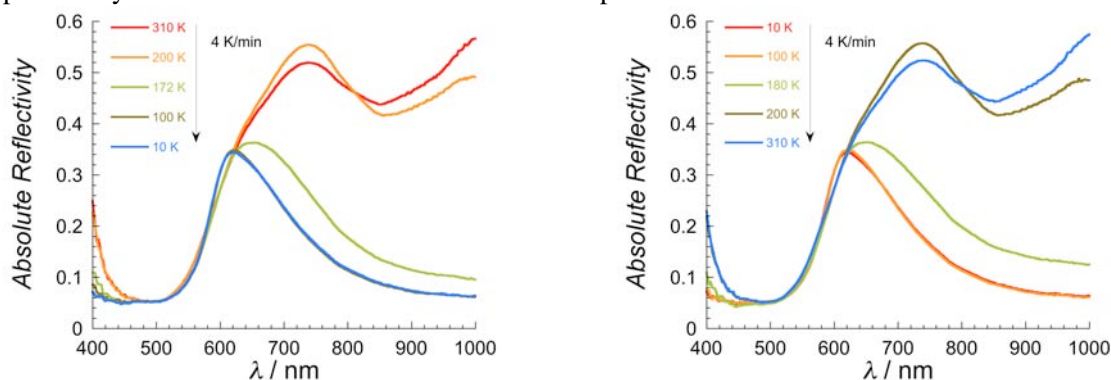


Figure IV.42 Selected reflectivity spectra of **15a** as function of temperature: (top) between 310 and 10 K; (bottom) between 10 and 310 K.

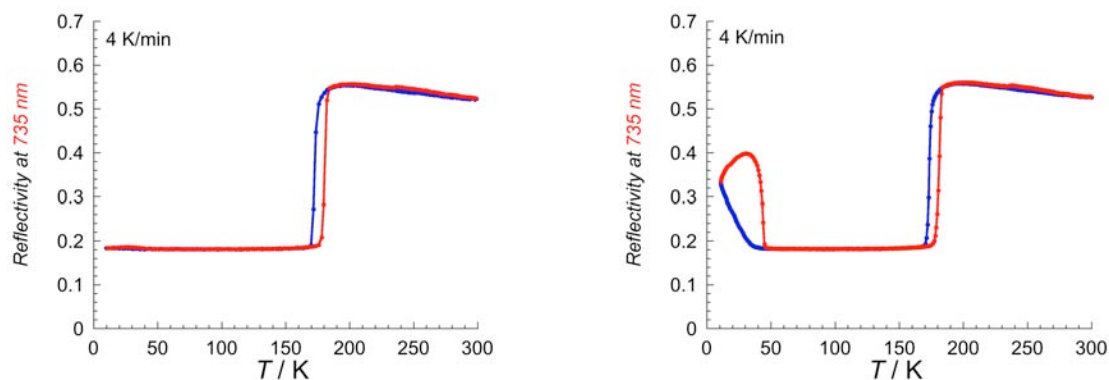


Figure IV.43 Thermal evolution of R_{735} in cooling mode (blue), and in heating mode (red) with the sweeping rate 4 K/min for compound **15a**, without (left) and with (right) light irradiation during the ramping.

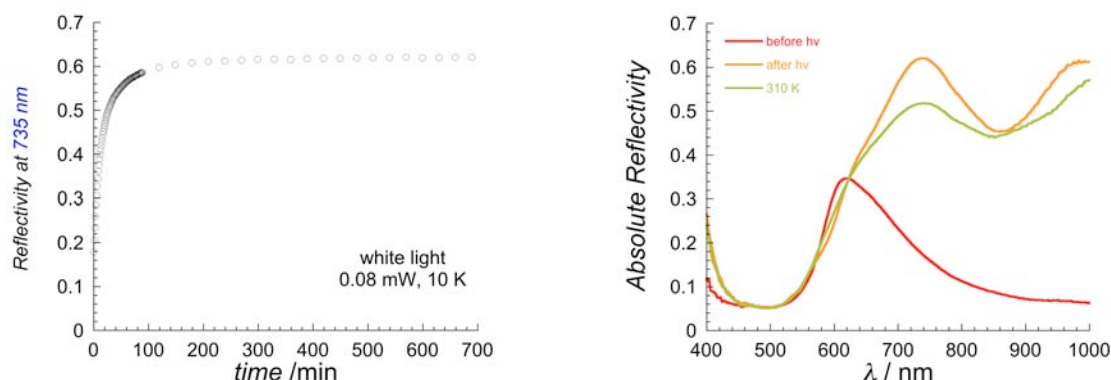


Figure IV.44 Time evolution of R_{735} at 10 K recorded under white light irradiation (0.08 mW) for compound **15a** (left). Spectra obtained before irradiation and after 700 mins of white light irradiation, and at 309 K (right).

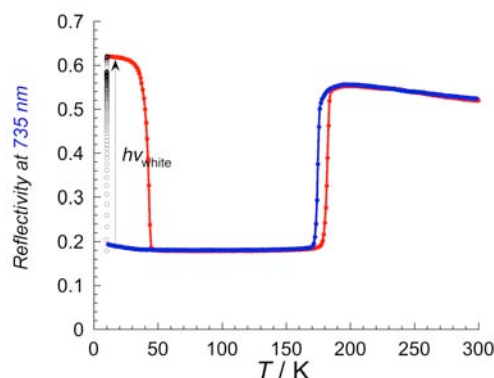
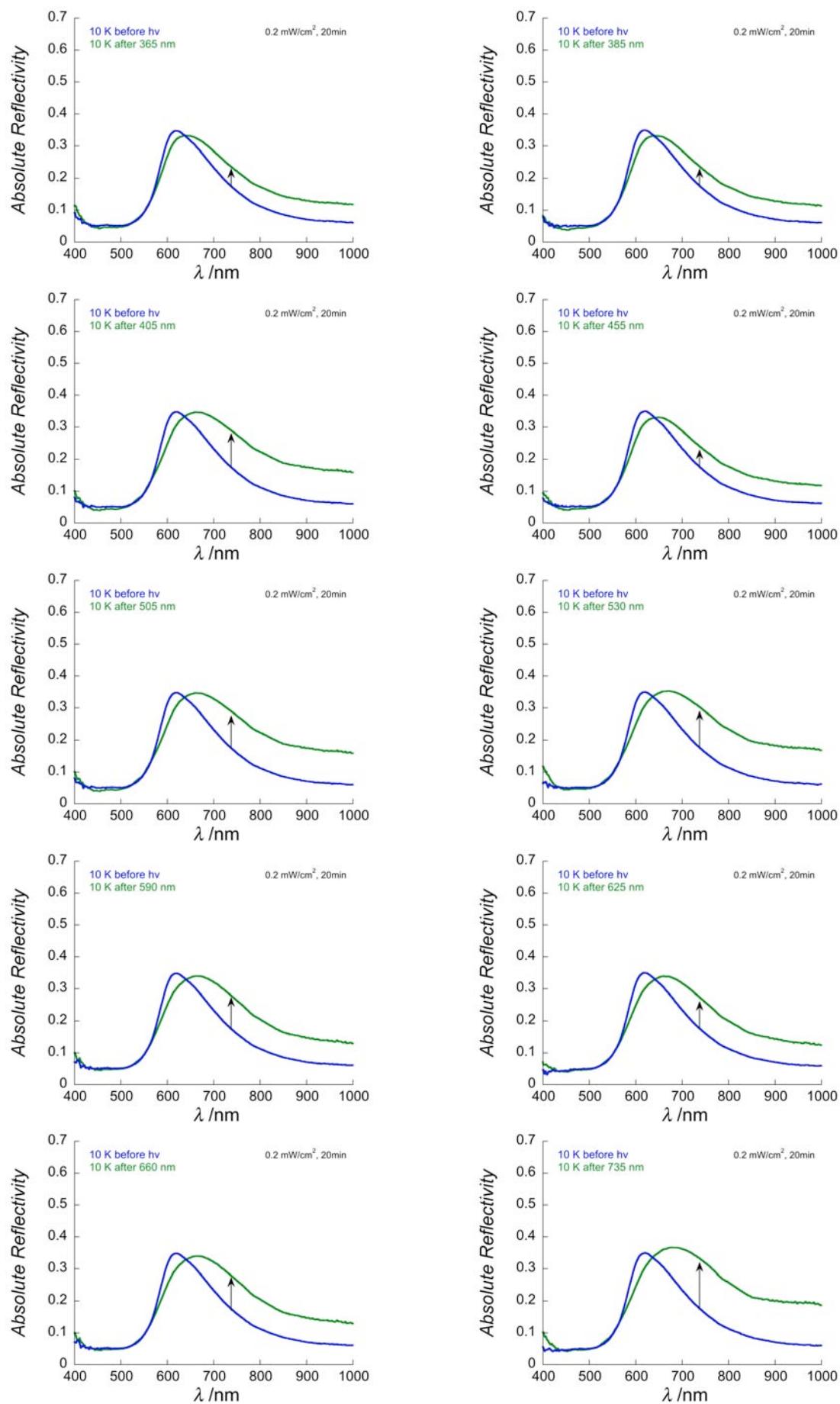


Figure IV.45 Thermal evolution of R_{735} for **15a** under white light (0.08 mW) during 700 mins at 10 K (dark points), in heating mode (red points) and cooling mode (blue points).

In conclusion of these reflectivity studies obtained with white light for compounds **15a**, the electron transfer in this compound is accompanied by a clear change of the color of the compound (thermochromic effect). This electron transfer can be also photo-induced at the surface below 50 K with a white light irradiation (photochromic effect).

We have further investigated the reflectivity properties of the compound **15a** using specific wavelengths for photo-excitation experiments. Compared to the above optical measurements, the white light is still used for spectroscopy, and a set-up of 14 different LEDs are used for irradiations. Several measurements have been performed in order (i) to find the most efficient wavelength for irradiation, (ii) at this optimum wavelength, to study the effect of power under a fixed irradiation time.

To test the different LEDs, we have used the following protocol: the compound is placed at 10 K in its LS state after a cooling at 10 K/min in the dark, and a spectrum is first collected (named *before hv*). Then the compound is irradiated with one LED for 20 mins with a power of 0.2 mW. A new spectrum is recorded (named *after λ nm*). Then, to recover the LS state, the compound is reheated at 300 K, and then placed again at 10 K in the dark at 10 K/min, and finally it is irradiated with an other LED. This procedure is repeated for each LED. The results for the different LEDs are shown in **Figure IV.46**. The most important changes in the spectra before and after 20 mins of irradiation are observed with the 1050 and 940 nm LEDs.



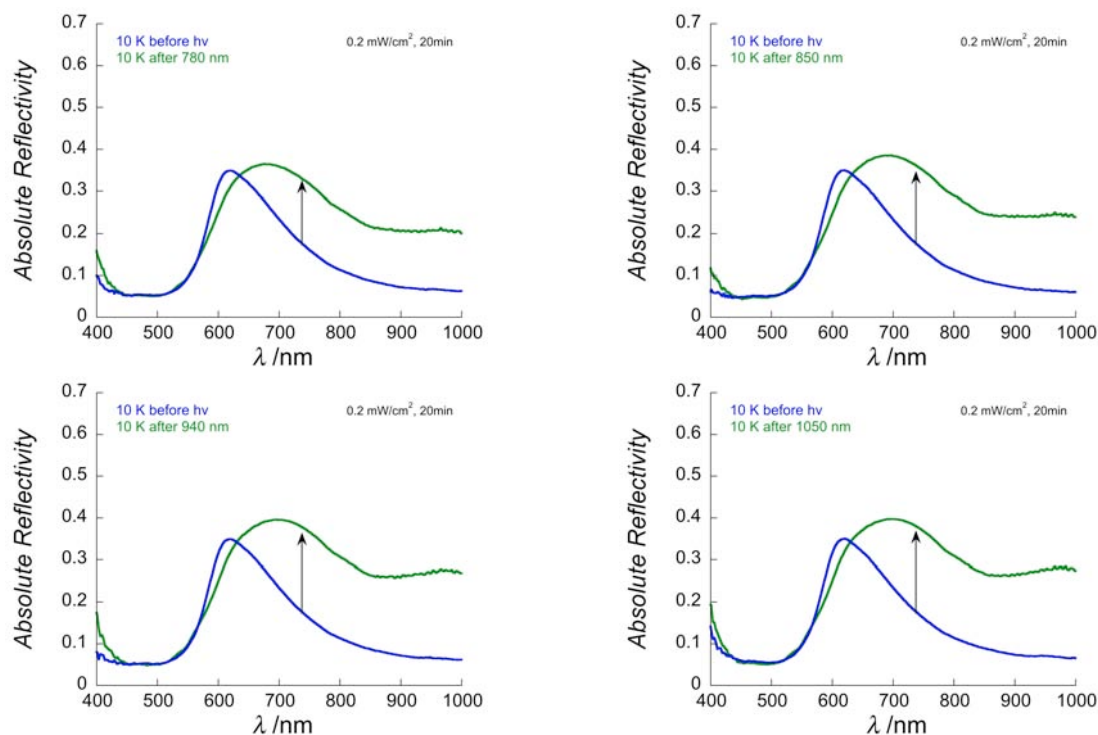


Figure IV.46 Spectra of **15a** obtained before irradiation and after 20 mins of irradiation at different wavelengths delivered by LEDs.

An alternative way to visualize the changes induced by the LED irradiations is to plot the difference of absolute reflectivity (ΔAR) at selected wavelengths as shown in **Figure IV.47**. These plots show clearly than the most efficient irradiations for **15a** lie in the 850-1050 nm range.

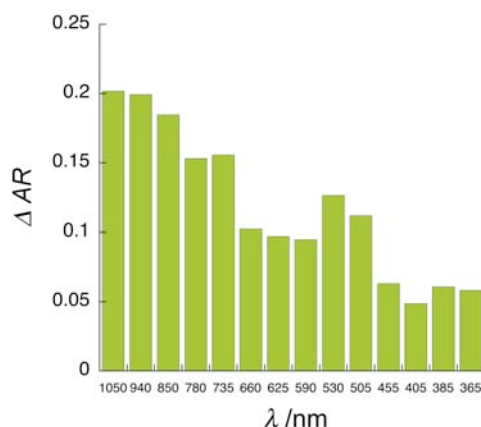


Figure IV.47 Difference in absolute reflectivity (ΔAR) obtained before irradiation and after 20 mins of irradiation with the different LEDs ($P = 0.2$ mW).

Then, the influence of the power of the light has been studied with the use of the 1050 nm LED. We have used the following protocol: the compound is placed at 10 K in its LS state after a cooling at 10 K/min in the dark, and a spectrum is first collected (named *before hv*). Then the compound is irradiated with the 1050 nm LED for 60 min with a selected power. Spectra are recorded each minute, the LED being switched off. Then, when the irradiation is finished, the compound is reheated at 300 K, and then placed again at 10 K at 10 K/min, and finally irradiated with the same LED with a different power. The **Figure IV.48** shows the result of this experiment as the time evolution of R_{735} during the successive irradiations. The different curves have similar shapes and reach

a saturation value. When the power is increased, the saturation value is higher and also is reached faster. This can be interpreted as a better light penetration at the surface of the compound when the power is increased. We can note also that the spectrum obtained after the 1050 nm irradiation clearly shows a band appearing around 860 nm, that is also observed in the spectrum at 310 K (**Figure IV.48**, right).

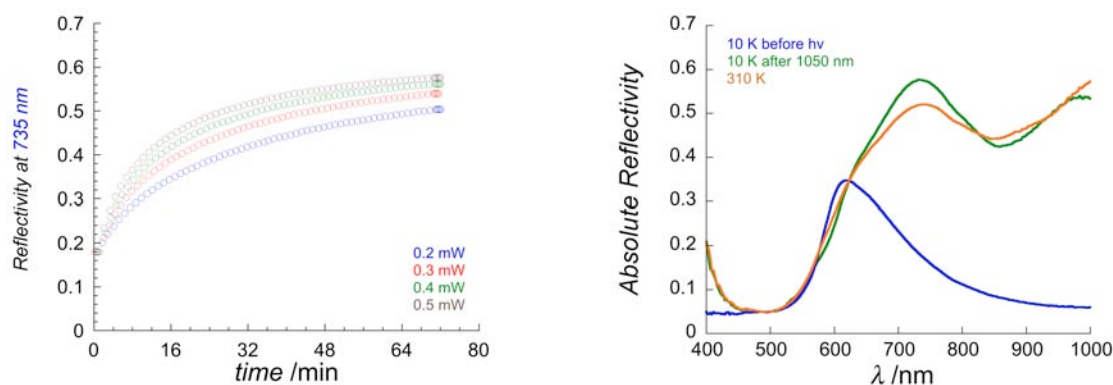


Figure IV.48 Time evolution of R_{735} during successive irradiations at 1050 nm with different power irradiances between 0.2 mW and 0.5 mW (left). Spectra obtained before 1050 nm irradiation and after 70 mins of 1050 nm irradiation, and at 310 K (right).

Finally, the thermal evolution of R_{735} after the photoexcitation with the 1050 nm LED at 0.5 mW is shown in **Figure IV.49**. R_{735} is nearly constant until 30 K, and shows a decrease from this temperature to reach 0.18 at 50 K. This decrease corresponds to the thermal-activated relaxation from the photo-excited state. Above 173 K, the same behavior for R_{735} than the other measurements is observed. This shows again the good reversibility of the photo-induced electron transfer in the sample.

To finish this reflectivity study with the LED, we have tested the eventual photoreversibility at 10 K by doing cycles of photo-excitation with 1050 nm (20 min with a power at 0.5 mW) and photo-deexcitations with an other LED (each irradiation for 10 min with a power at 0.5 mW). We have selected four LEDs (365 nm, 385 nm, 405 nm, 455 nm) for the de-excitation. As shown by **Figure IV.50**, no photoreversibility has been observed for this compound.

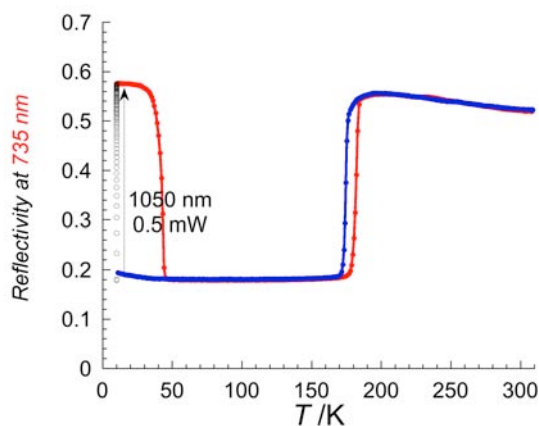


Figure IV.49 Thermal evolution of R_{735} in cooling mode (310 K – 10 K, blue points), under 1050 nm (0.5 mW) during 70 min at 10 K (dark points) and in heating mode (10 K – 310 K, red points)

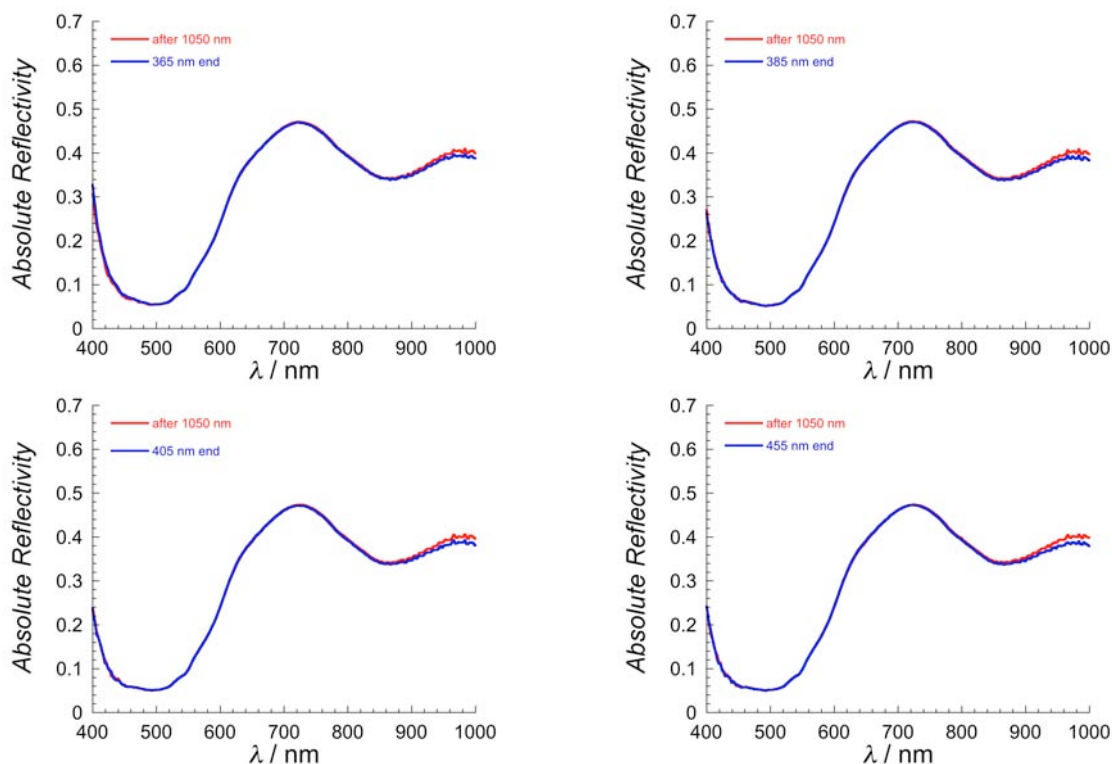


Figure IV.50 Spectra obtained after irradiation at 1050 nm (0.5mW, 20 min, in red) and after irradiation at 365 nm, 385 nm, 405 nm and 455 nm (0.5mW, 10 min, in blue).

Structural description. On the basis of the magnetic data and optical data above, the x-ray crystal structure of compound **15** should be collected at three different temperatures: 298, 225, and 120 K. At the moment, we have the data only at 298 K. The crystallographic data and selected bond distances/angles are respectively summarized in **Table IV.11** and **Table IV.12**.

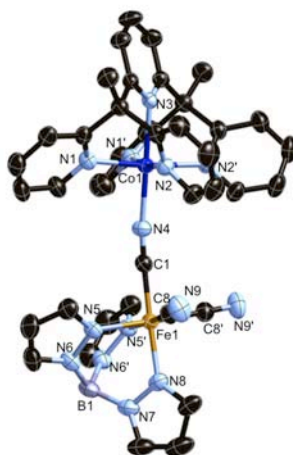


Figure IV.51 ORTEP-type view of molecular structures of compounds **15** at 298 K with thermal ellipsoids at 40 % level. Yellow, Fe; blue, Co; skyblue, N; black, C. Lattice solvents and hydrogen atoms are omitted for clarity.

As shown in **Figure IV.51**, the $[\text{Co}(\text{PY5Me}_2)]^{2+}$ unit was formed in-situ during the reaction, and its axial position is occupied by one of cyanido ligands from the Fe-building block. Two terminal cyanides are left uncoordinated, and OTf⁻ counter anion and interstitial solvent molecules occupy the void space in the crystal packing. The coordination sphere of Co corresponds to one observed in the

mononuclear Co precursor (**7**) (**Table IV.2**), implying the presence of high spin cobalt(II) ions. Thus, the Fe center is assigned as trivalent based on the charge balance consideration. Also, Fe-C and Fe-N average bond lengths around Fe are in agreement with those found in $[\text{Fe}(\text{Tp})(\text{CN})_3]^-$ precursor (Lescou  zec et al. 2002).

Table IV.11 Crystallographic data of compounds **15**.

	15 (298 K)
Empirical formula	$\text{C}_{45}\text{H}_{44}\text{BCoF}_3\text{FeN}_{15}\text{O}_5\text{S}$
Formula weight, g mol^{-1}	1089.6
Crystal system	Orthorhombic
Space group	$Pnma$
Wavelength, \AA	0.71073
a , \AA	18.865(3)
b , \AA	15.383(2)
c , \AA	18.003(3)
V , \AA^3	5224.5(14)
Z	4
ρ_{calcd} , Mg m^{-3}	1.385
μ , mm^{-1}	0.704
$^a R_1$ ($I > 2\sigma(I)$)	0.0700
$^b wR_2$ (all)	0.2326
GoF ^a	1.025

^a $R_1 = \sum ||F_o| - |F_c|| / \sum |F_o|$, and ^b $wR_2 = [\sum w(F_o^2 - F_c^2)^2 / \sum w(F_o^2)^2]^{1/2}$.

Table IV.12 Selected bond lengths [\AA] and angles [$^\circ$] for **15**.

	15 (298 K)
av(Fe-N)	1.984(4)
av(Fe-C)	1.912(5)
av(Co-N _{py})	2.138(3)
av(N-Co-N) ^a	84.87(12)
av(N-Co-N) ^b	99.46(18)
Co-N-C ^c	172.6(5)
Fe-C-N ^c	176.7(5)

^aThese N atoms belong to pyridyl rings attached to the same methine carbon. ^bThese N atoms belong to pyridyl rings attached to different methine carbons. ^cThese angles are through the bridging cyanido ligand.

Remarks. In the magnetic and the optical properties, we clearly see the inter-conversion between two different states, which might be attributed to the one between $[\text{Fe}^{\text{III}}_{\text{LS}}\text{Co}^{\text{II}}_{\text{HS}}]$ and $[\text{Fe}^{\text{II}}_{\text{LS}}\text{Co}^{\text{III}}_{\text{LS}}]$ states. On the basis of the results, we need to know the structure at low temperatures, before and after drying of the compound. It is also worth noting that the observed cyanide band stretching of **15** and **15a** suggests likely the two different states of iron center: the IR band values agree with Fe^{III} and Fe^{II} , based on the previously reported systems. Nevertheless, the value of the χT product at room temperature for both **15** and **15a** correspond well to the one for $[\text{Fe}^{\text{III}}_{\text{LS}}\text{Co}^{\text{II}}_{\text{HS}}]$. This work needs further experiments to be fully understood.

IV.4.3 Heterometallic [MnFe] systems

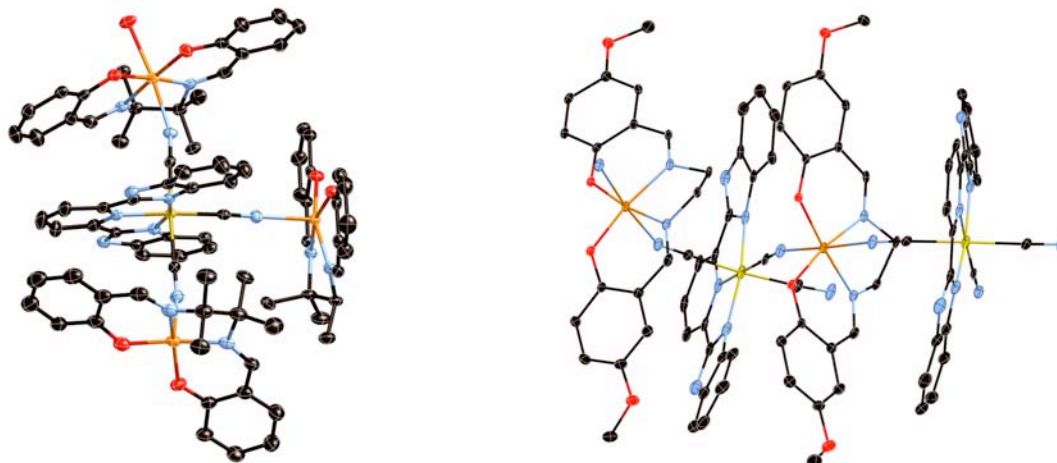


Figure IV.52 ORTEP-type view of molecular structures of compounds **16** at 150 K (left) and compound **17** at 100 K (right) with thermal ellipsoids at 40 % level. Mn, Fe, C, N, O atoms are in orange, yellow, black, blue, red. The solvent molecules, counter ions, and hydrogen atoms are omitted for clarity.

Table IV.13 Crystallographic data of compounds **16** and **17**.

	16 (150 K)	17 (100 K)
Empirical formula	C ₉₀ H ₉₁ ClFeMn ₃ N ₁₈ O ₁₁	C ₆₀ H _{59.5} FeMn ₂ N ₁₂ O _{12.5}
Formula weight, g mol ⁻¹	1856.93	1314.43
Crystal system	Monoclinic	Orthorhombic
Space group	<i>P</i> 2 ₁ / <i>c</i>	<i>P</i> bcn
Wavelength, Å	0.71069	0.71073
<i>a</i> , Å	21.161(5)	32.630(2)
<i>b</i> , Å	20.426(5)	12.9224(9)
<i>c</i> , Å	19.562(5)	27.867(2)
β , °	8335(4)	-
<i>V</i> , Å ³	8335(4)	11750.3(14)
<i>Z</i>	4	8
ρ_{calcd} , Mg m ⁻³	1.480	1.486
μ , mm ⁻¹	0.721	0.742
^a <i>R</i> ₁ (<i>I</i> > 2 σ (<i>I</i>))	0.0578	0.0461
^b <i>wR</i> ₂ (all)	0.1966	0.1032
GoF ^a	1.031	1.013

^a*R*₁ = $\Sigma||F_o| - |F_c||/\Sigma|F_o|$, and ^b*wR*₂ = $[\Sigma w(F_o^2 - F_c^2)^2/\Sigma w(F_o^2)^2]^{1/2}$.

The similar condition for the reaction of compound **10** was also applied to the reactions with different manganese precursors. In compound **10**, we observed methanol molecules occupy two axial positions of trinuclear unit to stabilize the isolated molecular unit. In order to extend this trinuclear units to a chain, less coordinating dichloromethane and acetonitrile were used for a reaction of **16**, with using compound **6** and [Mn₂(saltmen)₂(H₂O)₂] \cdot 2ClO₄ as precursors. However, this reaction afforded tetranuclear compound, {[Mn(saltmen)(H₂O)][Mn(saltmen)]₂[Fe(bbp)(CN)₃]} \cdot (ClO₄) \cdot 4CH₃CN (**16**), in which three cyanido ligands on the iron center were coordinated to [Mn(saltmen)]⁺ units (**Figure IV.52**). The perchlorate anion compensate the charge of the tetranuclear complex. On the other hand, we have also used [Mn(5-MeO-salen)(H₂O)] \cdot PF₆ (5-MeO-salen²⁻ = N,N'-ethylenebis(5-methoxy-

salicylideneimine)) as a Mn precursor, since it was shown to form a chain structure containing hexacyanidoferrate(III) linked with the out-of-plane dinuclear $[\text{Mn}_2]$ unit (Ferbinteanu et al. 2005). The obtained compound is, however, a zigzag shaped chain in which $[\text{Mn}(5\text{-MeO-salen})]^+$ units are coordinated to Fe building unit in a *cis*-geometry: $\{[\text{Mn}(5\text{-MeO-salen})]_2[\text{Fe}(\text{bbp})(\text{CN})_3]_2\} \cdot [\text{Mn}_2(5\text{-MeO-salen})_2(\text{H}_2\text{O})_2]$ (**17**) (**Figure IV.52**). The charge is balanced by the isolated out-of-plane dinuclear $[\text{Mn}_2(5\text{-MeO-salen})_2(\text{H}_2\text{O})_2]^{2+}$ complex. The crystallographic data is summarized in **Table IV.13**.

IV.5 Supporting information

IV.5.1 Experimental section

Materials. The starting ligands H₂BBP and PY5R₂ (R = CH₃, H, OH) and the starting precursors [Mn₂(saltmen)₂(ReO₄)₂], (NBu₄)[Fe(Tp)(CN)₃], [Mn₂(saltmen)₂(H₂O)₂]ClO₄, and [Mn(5-MeO-salen)(H₂O)]PF₆ were prepared as reported previously (Addison and Burke 1981; Bechlars et al. 2010; Kim et al. 2004; Miyasaka et al. 2004; Miyasaka et al. 2002). The starting Fe precursor for **17**, Na₂[Fe(bbp)(CN)₃], is obtained as described for the synthesis of compound **6**, but without adding [NBu₄]Br. The reactions for **7**, **8**, **11** – **15** were performed under an argon atmosphere using standard Schlenck and drybox techniques. Solvents for these reactions were degassed using freeze-pump-thaw method and kept under nitrogen.

Synthesis of (NBu₄)₂[Fe(bbp)(CN)₃]·6H₂O (6**).** Addition of bbp (3.13 g, 10.0 mmol) diluted in methanol (20 mL) to a methanol solution (60 mL) of FeCl₃·6H₂O (2.70 g, 10.0 mmol) afforded a red solution that was refluxed for 1 h. An aqueous solution (40 mL) of NaCN (2.94 g, 60.0 mmol) was then added to the reaction. After an additional 8 h reflux, the solution became dark blue and the mixture was subsequently filtered. The filtrate was concentrated via rotary evaporation to ca. 30 mL volume. Solid [NBu₄]Br (3.22 g, 10.0 mmol) was added to the filtrate and a blue crystalline solid precipitated. The blue microcrystals were isolated via suction filtration, washed with water (2 × 10 mL), and dried under vacuum at room temperature for 12 h. Dark blue crystals suitable for single crystal X-ray analysis were obtained via slow evaporation of a methanol solution containing **6** at room temperature within one week. Yield: 8.74 g (89 %); FT-IR (ATR, cm⁻¹): 3368 (br), 2959 (m), 2872 (m), 2109 (s), 1648 (w), 1614 (w), 1574 (w), 1451 (m), 1352 (m), 1323 (m), 1271 (m), 1146 (w), 1075 (w), 1029 (w), 998 (w), 917 (w), 865 (w), 747 (s), 646 (w); elemental analysis calc for C₅₄H₉₁FeN₁₀O₄ (**6** – 2 H₂O): C 64.8, H 9.2, N 14.0; found: C 64.2, H 8.6, N 14.8.

Synthesis of [Co(PY5Me₂)(H₂O)](BF₄)₂ (7**).** To an acetonitrile solution (5 mL) of ligand PY5Me₂ (200 mg, 0.45 mmol) was added a methanol solution (5 mL) of Co(BF₄)₂·6H₂O (150 mg, 0.45 mmol). The pale orange colored solution was stirred for 3 h, and then filtrated. The slow diffusion of ether vapor afforded yellow crystals in 2 days. Yield 0.27 g (86 %); FT-IR (ATR, cm⁻¹): 3406 (m), 1644 (w), 1594 (s), 1470 (w), 1466 (m), 1454 (m), 1440 (m), 1411 (w), 1389 (w), 1067 (s), 1016 (s), 995 (s), 865 (w), 843 (w), 762 (m), 628 (m), 576 (w); elemental analysis calc for C₂₉H₂₇B₂CoF₈N₅O: C 50.2, H 3.9, N 10.1; found: C 50.2, H 4.2, N 10.3.

Synthesis of [Co(PY5Me₂)(NCCH₃)](BF₄)₂ (7a**).** To an acetonitrile solution (10 mL) of ligand PY5Me₂ (200 mg, 0.45 mmol) was added Co(BF₄)₂ (105 mg, 0.45 mmol). The pale orange colored solution was stirred for 3 h, and then filtrated. The slow diffusion of ether vapor afforded yellow crystals in 2 days. Yield 0.25 g (77 %); FT-IR (ATR, cm⁻¹): 1953 (m), 1484 (w), 1469 (m), 1454 (m), 1439 (m), 1411 (w), 1394 (w), 1287 (w), 1174 (w), 1036 (s), 866 (m), 847 (m), 772 (m), 757 (s), 651 (m), 628 (s), 583 (m).

Synthesis of [(bbp)Fe(CN)₃Co(PY5Me₂)]·2.5CH₃OH (8**).** A methanol solution (5 mL) of **6** (71 mg, 0.065 mmol) was layered with an acetonitrile solution (5 mL) of **7** (47 mg, 0.065 mmol) in a tube of 2 × 12 cm, to afford single crystals in 1 week. Yield 51 mg (75.1 %); FT-IR (ATR, cm⁻¹): 3337 (br), 2161 (w), 2137 (m), 2118 (m), 1642 (w), 1592 (m), 1507 (w), 1451 (m), 1439 (m), 1348 (m),

1320 (m), 1265 (m), 1057 (m), 1022 (s), 916 (m), 861 (m), 817 (m), 745 (s), 646 (m); elemental analysis calc for $C_{52}H_{44}CoFeN_{13}O_3$ (**8** - 1.5CH₃OH + 2H₂O): C 62.6, H 4.5, N 17.8; found: C 61.5, H 4.4, N 17.8.

Synthesis of [Fe(H₂bbp)Fe(CN)₃]·2H₂O (9**).** To a methanol solution (5 mL) of **6** (100 mg, 0.095 mmol) was added 2 eq. of trifluoroacetic acid (1.46×10^{-2} mL, 0.19 mmol). The solution was slowly evaporated to give dark violet crystals. More than 2 eq. of acid up to 10 eq. of acid afforded identical crystals. Yield 38 mg (86 %); FT-IR (ATR, cm⁻¹): 2119 (w), 1783 (s), 1592 (w), 1468 (w), 1387 (m), 1352 (m), 1178 (m), 1117 (m), 1047 (m), 845 (m), 775 (m), 755 (m), 710 (m) 571 (w), 561 (w); elemental analysis calc for C₂₂H₁₅FeN₈O: C 57.0, H 3.3, N 24.2; found: C 56.8, H 3.0, N 23.9.

Synthesis of {[Mn(saltmen)(MeOH)]₂[Fe(bbp)(CN)₃]}·4CH₃OH (10**).** A methanol solution (3 mL) of **6** (49.1 mg, 0.05 mmol) was added to a methanol solution (5 mL) of [Mn₂(saltmen)₂](ReO₄)₂ (62.8 mg, 0.05 mmol). The dark green color solution was stirred at room temperature for 1 h, and then filtered. The slow diffusion of ether vapor afforded brown crystals in 1 week. Yield 35.3 mg (51 %); FT-IR (ATR, cm⁻¹): 3503 (w), 2980 (w), 2936 (w), 2128 (m), 2105 (m), 1596 (s), 1536 (s), 1462 (m), 1436 (s), 1392 (s), 1357 (m), 1305 (s), 1272 (m), 1203 (w), 1141 (m), 1124 (m), 1030 (w), 960 (w), 907 (m) 848 (m) 799 (m), 737 (s), 624 (m) 591 (w), 570 (w); elemental analysis calc for C₆₈H₇₃FeMn₂N₁₂O₁₀: C 59.0, H 5.3, N 12.1; found: C 59.6, H 4.9, N 12.3.

Synthesis of [(bbp)Fe(CN)₃Co(PY5Me₂)]·1.5CH₂Cl₂·0.5H₂O (11**).** A dichloromethane solution (5 mL) of **6** (71 mg, 0.065 mmol) was layered with an acetonitrile solution (5 mL) of **7** (47 mg, 0.065 mmol) in a tube of 2 × 12 cm, to afford single crystals in 1 week. Yield 42 mg (59 %); FT-IR (ATR, cm⁻¹): 3297 (br), 2161 (w), 2124 (m), 1596 (m), 1507 (w), 1452 (m), 1439 (m), 1351 (m), 1320 (m), 1267 (m), 1173 (w), 1144 (w), 1063 (m), 1017 (w), 999 (w), 916 (m), 863 (m), 843 (w), 749 (s), 627 (m).

Synthesis of [(bbp)Fe(CN)₃Co(PY5Me₂)]·2.5CH₃CN (12**).** An acetonitrile solution (5 mL) of **6** (71 mg, 0.065 mmol) was layered with an acetonitrile solution (5 mL) of **7** (47 mg, 0.065 mmol) in a tube of 2 × 12 cm, to afford single crystals in 1 week. Yield 47 mg (72 %); FT-IR (ATR, cm⁻¹): 3329 (br), 2161 (w), 2124 (m), 1596 (m), 1507 (w), 1452 (m), 1438 (m), 1350 (m), 1319 (m), 1265 (m), 1172 (w), 1144 (w), 1064 (m), 1018 (w), 998 (w), 916 (m), 862 (m), 843 (w), 748 (s), 627 (m).

Synthesis of [(bbp)Fe(CN)₃Co(PY5H₂)]·5CH₃OH (13**).** To an acetonitrile solution (5 mL) of ligand PY5H₂ (200 mg, 0.45 mmol) was added a methanol solution (5 mL) of Co(ClO₄)₆·6H₂O (176 mg, 0.45 mmol). The yellow colored solution was stirred for 3 h, and then filtrated. The addition of ether afforded yellow microcrystalline products. Then, an acetonitrile solution (5 mL) of this yellow crude product (47 mg, 0.065 mmol) was layered with an acetonitrile solution (5 mL) of **6** (71 mg, 0.065 mmol) in a tube of 2 × 12 cm, to afford single crystals in 1 week. Yield based on **6**: 48 mg (64 %); FT-IR (ATR, cm⁻¹): 3341 (br), 2163 (w), 2123 (m), 1600 (s), 1576 (m), 1512 (w), 1454 (m), 1440 (s), 1354 (s), 1322 (m), 1268 (m), 1179 (w), 1146 (w), 1017 (m), 999 (w), 917 (w), 864 (m), 822 (w), 746 (s), 627 (m), 614 (m).

Synthesis of [(bbp)Fe(CN)₃Co(PY5OH₂)]·5CH₃OH (14**).** To an acetonitrile solution (5 mL) of ligand PY5OH₂ (200 mg, 0.48 mmol) was added a methanol solution (5 mL) of Co(ClO₄)₆·6H₂O (163 mg, 0.48 mmol). The yellow colored solution was stirred for 3 h, and then filtrated. The addition of ether afforded yellow microcrystalline products. Then, an acetonitrile solution (5 mL) of this yellow crude product (45 mg, 0.065 mmol) was layered with an acetonitrile solution (5 mL) of **6** (71 mg, 0.065 mmol) in a tube of 2 × 12 cm, to afford single crystals in 1 week. Yield based on **6**: 45 mg

(64 %); FT-IR (ATR, cm^{-1}): 3058 (br), 2161 (w), 2124 (m), 2089 (w), 2066(m), 1597 (m), 1506 (w), 1453 (m), 1437 (m), 1352 (m), 1321 (m), 1267 (m), 1177 (w), 1147 (m), 1090 (m), 1017 (m), 1000 (w), 917 (m), 864 (m), 843 (w), 749 (s), 659 (m), 638 (m).

Synthesis of $[(\text{Tp})\text{Fe}(\text{CN})_3\text{Co}(\text{PY5Me}_2)]\cdot\text{OTf}\cdot\text{DMF}\cdot 2\text{H}_2\text{O}$ (15). Ligand PY5Me₂ (15 mg, 0.034 mmol) and $\text{Co}(\text{OTf})_2$ (12 mg, 0.034 mmol) were dissolved in 2 mL of dimethylformamide and stirred for 2 hours. To this yellow colored solution was added $(\text{NBu}_4)[\text{Fe}(\text{Tp})(\text{CN})_3]$ (20 mg, 0.034 mmol). The dark orange colored solution was stirred for 5 h, and then filtrated. The slow diffusion of ether vapor afforded dark orange, needle-like crystals. Yield: 13 mg (36 %); FT-IR (ATR, cm^{-1}): 3095 (w), 2924 (w), 2513 (w), 2155 (m) 2120 (w), 2079 (w), 2055 (m), 1675 (s), 1595 (m), 1499 (w), 1479 (m), 1404 (m), 1313 (m), 1269 (s), 1208 (m), 1146 (m), 1114 (m), 1049 (m), 1030 (m), 988 (w), 909 (w), 864(w), 754 (m), 710 (m), 634 (m), 573 (w).

Synthesis of $\{[\text{Mn}(\text{saltmen})(\text{H}_2\text{O})][\text{Mn}(\text{saltmen})]_2[\text{Fe}(\text{bbp})(\text{CN})_3]\}\cdot(\text{ClO}_4)\cdot 4\text{CH}_3\text{CN}$ (16). An acetonitrile solution (1.5 mL) of **6** (49.1 mg, 0.05 mmol) was added to a mixture of acetonitrile (2 mL) and dichloromethane (2.5 mL) solution of $[\text{Mn}_2(\text{saltmen})_2(\text{H}_2\text{O})_2](\text{ClO}_4)_2$ (49.5 mg, 0.05 mmol). The dark green color solution was stirred at room temperature for 1 h, and then filtered. The slow diffusion of ether vapor afforded brown crystals in 1 week. Yield: 49 mg (53 %); FT-IR (KBr, cm^{-1}): 3432 (w), 2970 (m), 2120 (m), 1600 (s), 1540 (s), 1462 (s), 1388 (s), 1357 (m), 1293 (m), 1228 (m), 1200 (w), 1169 (m), 1144 (m), 1043 (m), 907 (s), 823 (m), 755 (m), 677 (w), 652 (w) 578 (w), 536 (w).

Synthesis of $\{[\text{Mn}(\text{5-MeO-salen})]_2[\text{Fe}(\text{bbp})(\text{CN})_3]_2\}\cdot[\text{Mn}_2(\text{5-MeO-salen})_2(\text{H}_2\text{O})_2]$ (17). A water solution (1.5 mL) of $\text{Na}_2[\text{Fe}(\text{bbp})(\text{CN})_3]$ (15.0 mg, 0.025 mmol) was added to an acetonitrile solution (2.5 mL) of $[\text{Mn}(\text{5-MeO-salen})(\text{H}_2\text{O})](\text{PF}_6)$ (27.1 mg, 0.05 mmol). The dark brown color solution was stirred at room temperature for 1 h, and then filtered. The slow evaporation of the solution at room temperature afforded brown crystals in 1 week. Yield based on Fe: 18 m (55 %); FT-IR (KBr, cm^{-1}): 3736 (w), 3435 (br), 2925 (s), 2851 (m), 2150 (w), 2125 (m), 1619 (m), 1599 (s), 1539 (m), 1462 (s), 1386 (m), 1302 (m), 1223 (m), 1140 (m), 1085 (m), 957 (w), 888 (w), 821 (m), 739 (w), 570 (w), 535 (w).

Physical Methods. Elemental analysis for C, H and N were performed following the classical Pregl-Dumas technique on a ThermoFischer Flash EA1112. FT-IR spectra were recorded in the range 400-4000 cm^{-1} on a Thermal Scientific Nicolet™ 6700 ATR (attenuated total reflection) spectrometer equipped with a smart iTR diamond window, and as KBr pellets on a Nicolet 750 Magma-IR™ spectrometer. The magnetic susceptibility measurements were obtained with the use of MPMS-XL Quantum Design SQUID magnetometer and PPMS-9 susceptometer. These magnetometer and susceptometer work between 1.8 and 400 K for dc applied fields ranging from -70 kOe to 70 kOe (MPMS-XL). An M vs H measurement was performed at 100 K to confirm the absence of ferromagnetic impurities. Experimental data were corrected for the sample holder and for the diamagnetic contribution of the sample. ac susceptibility measurements were measured with an oscillating ac field of 1 Oe with frequency between 10 to 10000 Hz (PPMS). Mössbauer measurements were performed using a constant acceleration HALDER-type spectrometer with a room temperature $^{57}\text{Co}/\text{Rh}$ source in transmission geometry. The polycrystalline absorber containing about 10 mg cm^{-2} of iron was used to avoid experimental broadening of the peaks. The spectra were recorded at 293 and 4.2 K using a variable temperature cryostat. The velocity was calibrated using pure iron metal as the standard material. The refinement of Mössbauer spectra has been done

assuming a distribution of hyperfine fields. The thermogravimetric analysis (TGA) was carried out between 298 and 900 K at 5 K min⁻¹ in a nitrogen atmosphere using a thermogravimetric analyzer Setaram TAG 16. Powder X-ray diffraction patterns were recorded at 298 K on a PANalytical X'pert MPD Bragg-Brentano θ - θ geometry diffractometer equipped with a secondary monochromator over an angular range of $2\theta = 8 - 30^\circ$. The CuK α radiation was generated at 40 KV and 40 mA. The samples were put on sample holders made of silicon and flattened with a piece of glass. UV-vis spectra were collected between 400 and 900 nm using a Spectrophotometer UNICAM UV4-100. NMR spectra were obtained by JEOL JMN-ECS 400. Cyclic voltammetry measurements were carried out in a standard one-compartment cell under N₂, equipped with platinum wires for counter/reference electrodes and silver wire for the working electrode using potentiostat CHI 760c. The measurements were performed in dimethylsulfoxide (for **6** and **8**) and in acetonitrile (for **7**) with 0.1 M tetrabutylammonium hexafluorophosphate (Bu₄N⁺PF₆⁻) as the supporting electrolyte.

Crystallography. Single crystal X-ray diffraction data for **7a**, **10**, **11**, **12**, and **14** were collected on a Nonius Kappa CCD diffractometer using monochromatized Mo-K α radiation. DENZO-SMN (Otwinowski et al. 1997) was used for data integration and SCALEPACK (Otwinowski et al. 1997) corrected data for Lorentz-polarisation effects. The crystallographic data for **6** – **9**, **13**, **15** – **17** were collected with a Bruker APEX II diffractometer, equipped with a graphite monochromator centered on the path of MoK α . The program SAINT was used to integrate the data, which was thereafter corrected for absorption using SADABS (Sheldrick 2000). All structures were solved by the direct method and refined by a full-matrix least-squares method on F² using the SHELXL97 crystallographic software package (Sheldrick 1997). Hydrogen atoms were placed at calculated positions using suitable riding models, except those belonging to the coordinated water molecule in compound **7** and those connected to the nitrogen atoms in compound **9**. The latter were found in the difference Fourier maps, and refined using DFIX constraints in compound **9**. All hydrogen atoms were refined using isotropic displacement parameters derived from their parent atoms. Non-hydrogen atoms were refined with anisotropic displacement parameters.

IV.5.2 Supporting figures

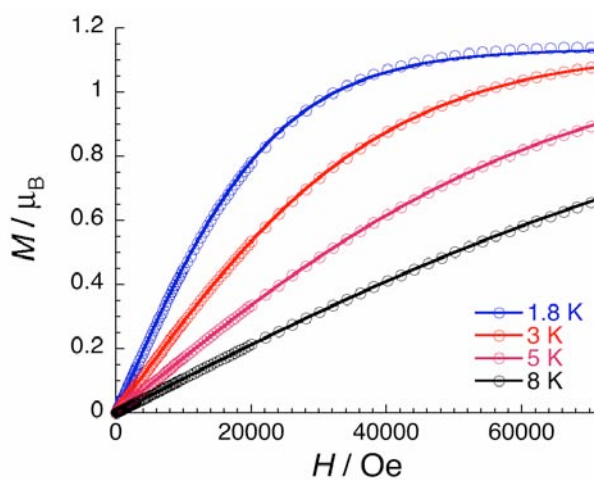


Figure SIV.1 M vs H curves of **6** at different temperatures. Solid lines are fitting results with Brillouin function.

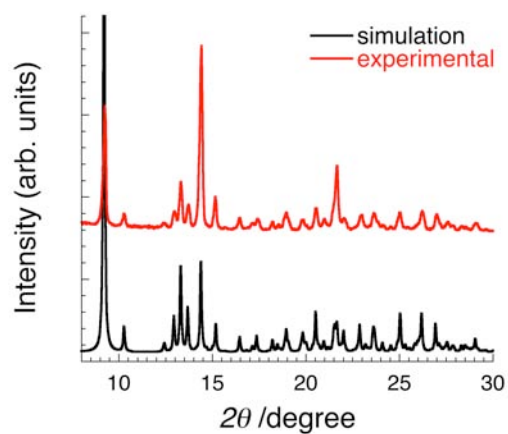


Figure SIV.2 Powder X-ray diffraction patterns of **8** (red, at 298 K) compared with the simulation (black) obtained from the single crystal data at 270 K.

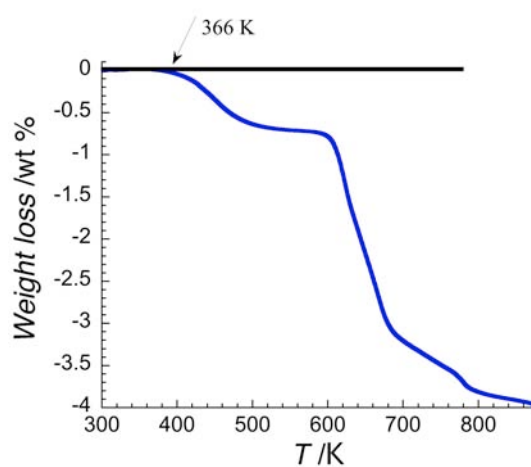


Figure SIV.3 Thermogravimetric analysis of **8**.

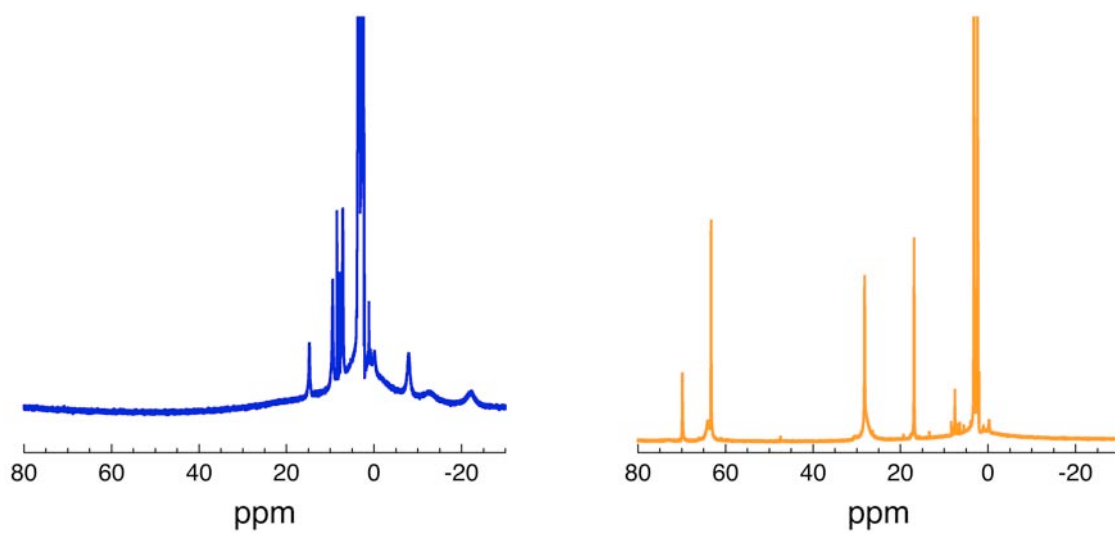


Figure SIV.4 ^1H NMR spectra of **6** (left) and **7** (right).

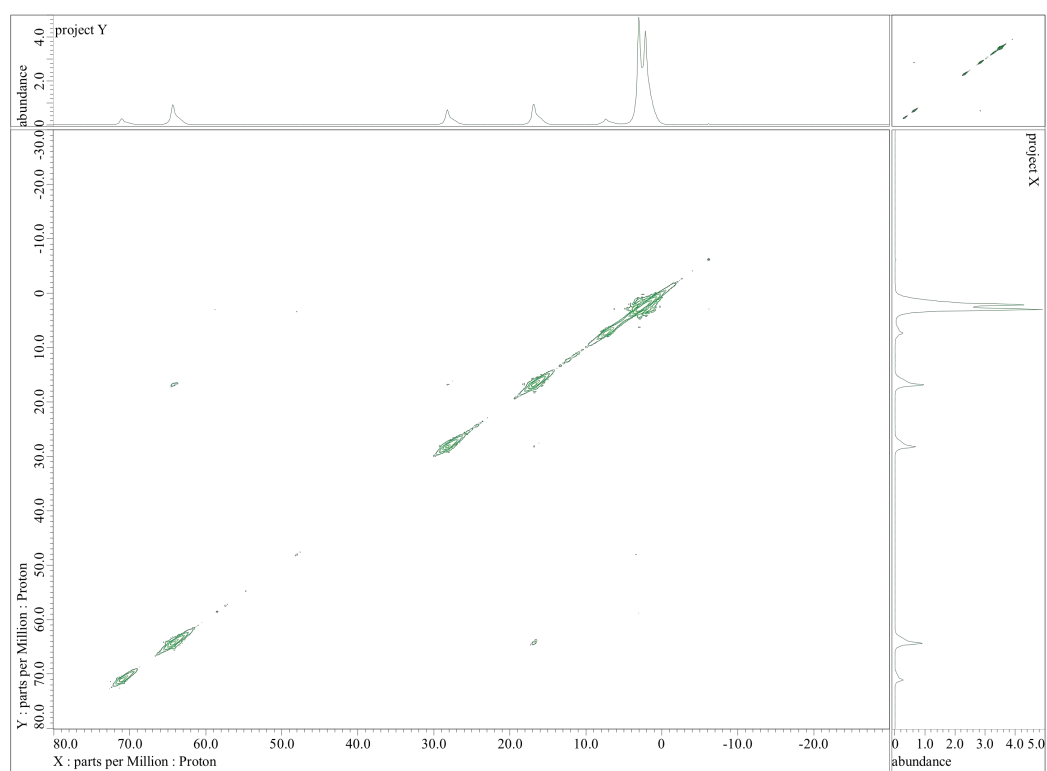


Figure SIV.5 ^1H - ^1H COSY spectrum of **7**.

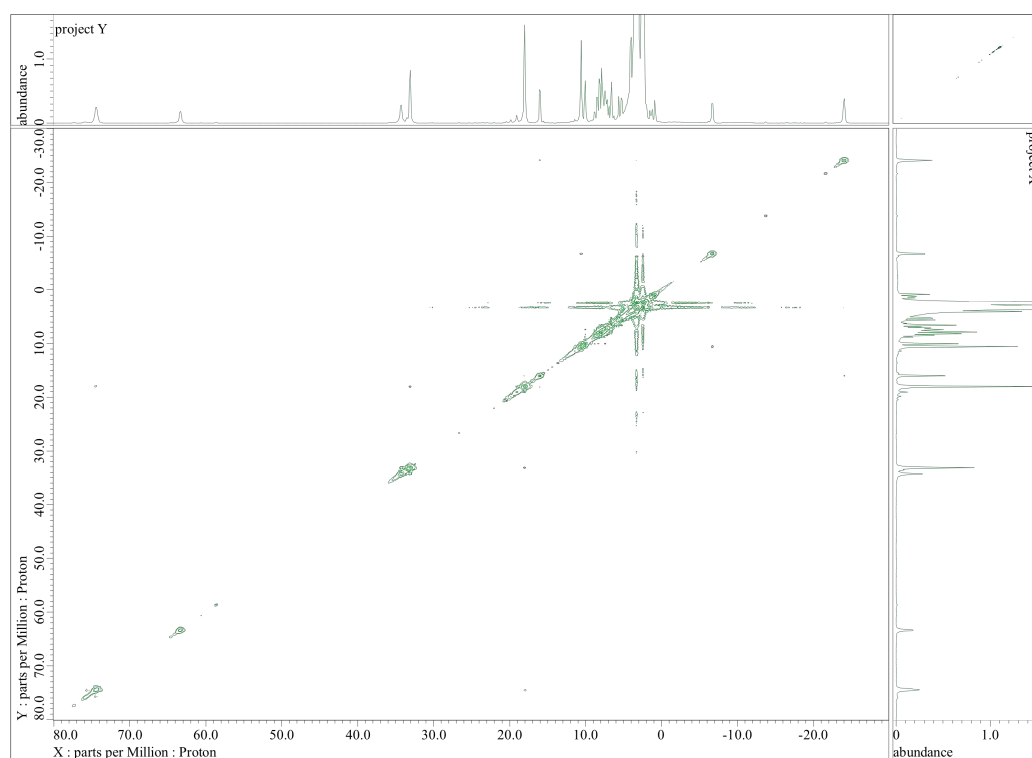


Figure SIV.6 ^1H - ^1H COSY spectrum of **8**.

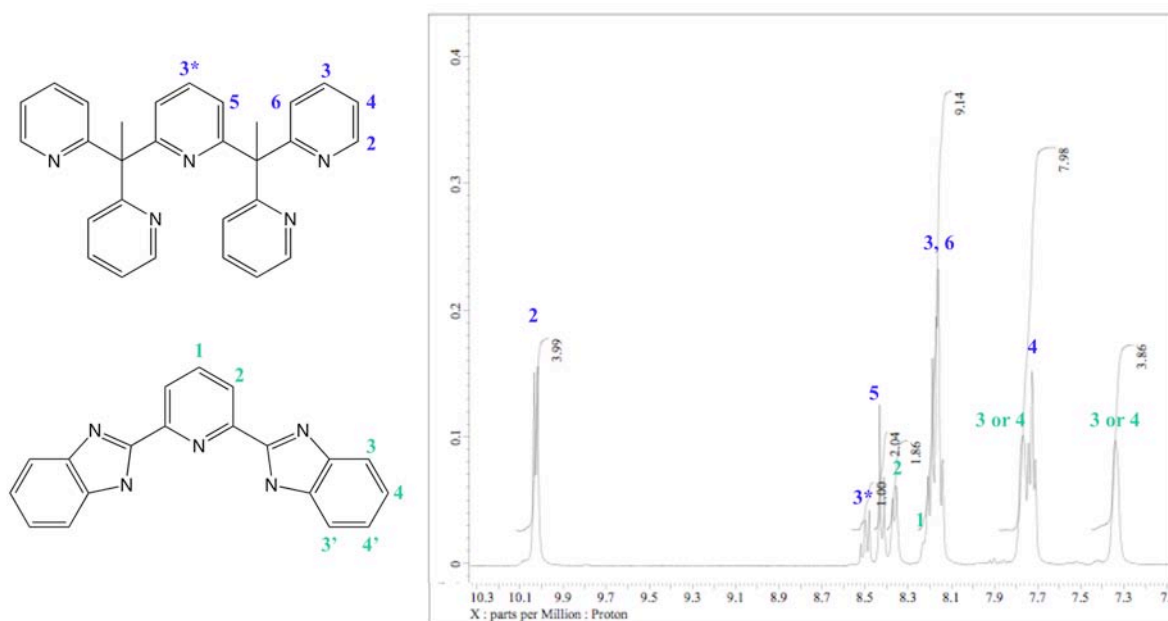


Figure SIV.7 ^1H NMR spectrum of protonated **8**, ($[\text{H}_2\text{FeCo}]$). The resonance peaks are attributed to each ligand

References

- Addison AW, Burke PJ (1981) *J. Heterocycl. Chem.* 18, 803.
- Bechlars B, D'Alessandro DM, Jenkins DM, Iavarone AT, Glover SD, Kubiak CP, Long JR (2010) *Nature Chem.* 2, 362.
- Beltran LMC, Long JR (2005) *Acc. Chem. Res.* 38, 325.
- Berlinguette CP, Dragulescu-Andrasi A, Sieber A, Güdel H-U, Achim C, Dunbar KR (2005) *J. Am. Chem. Soc.* 127, 6766.
- Bernhardt PV, Bozoglian F, Macpherson BP, Martinez M (2004) *Dalton Trans.* 2582.
- Bordwell FG (1988) *Acc. Chem. Res.* 21, 456.
- Borrás-Almenar JJ, Clemente-Juan JM, Coronado, E, Tsukerblat BS (2001) *J. Comput. Chem.* 22, 985.
- Choi HJ, Sokol JJ, Long JR (2004) *Inorg. Chem.* 43, 1606.
- Ferbinteanu M, Miyasaka H, Wernsdorfer W, Nakata K, Sugiura K-i, Yamashita M, Coulon C, Clérac R (2005) *J. Am. Chem. Soc.* 127, 3090.
- Fultz B (2011) *Mössbauer Spectrometry in « Characterization of Materials »*, John Wiley & Sons, New York.
- Goodwin HA (2004) *Top. Curr. Chem.* 234, 23.
- Greenwood NN, Gibb TC (1971), *Mössbauer Spectroscopy*, Chapman and Hall Ltd, London.
- Hayami S, Komatsu Y, Shimizu T, Kamihata H, Lee YH (2011) *Coord. Chem. Rev.* 255, 1981.
- Jeżowski A, Litwicki Z, Sumarokov VV, Stachowiak P (2006) *Low Temp. Phys.* 32, 1082.
- Kahn O (1993) *Molecular Magnetism*, VCH Publishers
- Kim JI, Han S, Cho I-K, Choi KY, Heu M, Yoon S, Suh B (2004) *Polyhedron* 23, 1333.
- Kim JI, Kwak HY, Yoon JH, Ryu DW, Yoo IY, Yang N, Cho BK, Park J-G, Lee H, Hong CS (2009) *Inorg. Chem.* 48, 2956.
- Kim JI, Yoo HS, Koh EK, Kim HC, Hong CS (2007a) *Inorg. Chem.* 46, 8481.
- Kim JI, Yoo HS, Koh EK, Hong CS (2007b) *Inorg. Chem.* 46, 10461.
- Klein Gebbink RJM, Jonas RT, Goldsmith CR, Stack TDP (2002) *Inorg. Chem.* 41, 4633.
- Krivokapic I, Zerara M, Daku ML, Vargas A, Enachescu C, Ambrus C, Tregenna-Piggott P, Amstutz N, Krausz E, Hauser A (2007) *Coord. Chem. Rev.* 251, 364.
- Lescouëzec R, Vaissermann J, Lloret F, Julve M, Verdaguer M (2002) *Inorg. Chem.* 41, 5933.
- Lescouëzec R, Vaissermann J, Toma LM, Carrasco R, Lloret F, Julve M (2004) *Inorg. Chem.* 43, 2234.
- Li D, Clérac R, Roubeau O, Harté E, Mathonière C, Le Bris R, Holmes SM (2008) *J. Am. Chem. Soc.* 130, 252.
- Liu T, Dong D, Kanegawa S, Kang S, Sato O, Shiota Y, Yoshizawa K, Hayami S, Wu S, He C, Duan C-Y (2012) *Angew. Chem. Int. Ed.* 51, 4367.
- Miyasaka H, Clérac R, Ishii T, Chang H-C, Yamashita M (2002) *Dalton Trans.* 1528.
- Miyasaka H, Clérac R, Wernsdorfer W, Lecren L, Bonhomme C, Sugiura K-i, Yamashita M (2004) *Angew. Chem. Int. Ed.* 43, 2801.
- Miyasaka H, Ieda H, Chimica D, Perugia I, Crescenzi R, Floriani C, Meoh S (1998) *Inorg. Chem.* 37, 255.
- Miyasaka H, Madanbashi T, Saitoh A, Motokawa N, Ishikawa R, Yamashita M, Bahr S, Wernsdorfer W, Clérac R (2012) *Chem. –Eur. J.* 18, 3942.
- Miyasaka H, Nezu T, Sugimoto K, Sugiura K-i, Yamashita M, Clérac R (2005) *Chem. –Eur. J.* 11, 1592.
- Miyasaka H, Saitoh A, Abe S (2007) *Coord. Chem. Rev.* 251, 2622.
- Ni W-W, Ni Z-H, Cui A, Liang X, Kou H-Z (2007) *Inorg. Chem.* 46, 22.
- Ni Z-H, Kou H-Z, Zhang L-F, Ni W-W, Jiang Y-B, Cui A-L, Ribas J, Sato O (2005) *Inorg. Chem.* 44, 9631.
- Nihei M, Okamoto Y, Sekine Y, Hoshino N, Shiga T, Liu IP-C, Oshio H (2012) *Angew. Chem. Int. Ed.* 51, 6361.
- Nihei M, Sekine Y, Suganami N, Nakazawa K, Nakao A, Nakao H, Murakami Y, Oshio H (2011) *J. Am. Chem. Soc.* 133, 3592.
- Otwinowski Z, Minor W (1997) *Macromolecular Crystallography Part A*, 276, 307.
- Panja A, Guionneau P, Jeon I-R, Holmes SM, Clérac R, Mathonière C (2012) *submitted*
- Ratera I, Sporer C, Ruiz-Molina D, Ventosa N, Baggerman J, Brouwer AM, Rovira C, Veciana J (2007) *J. Am. Chem. Soc.* 129, 6117.
- Sato O, Einaga Y, Fujishima A, Hashimoto K (1999) *Inorg. Chem.* 38, 4405.
- Senapati T, Pichon C, Ababei R, Mathonière C, Clérac R (2012) *Inorg. Chem.* 51, 3796.
- Shatruk M, Avendano C, Dunbar KR (2009) *Cyanide-Bridged Complexes of Transition Metals: A Molecular Magnetism Perspective*, John Wiley & Sons, Inc.
- Sheldrick GM (2000) *SADABS, Version 2.03; Bruker Analytical X-Ray Systems*. Madison.
- Sheldrick GM (1997) *SHELXL97, Program for Crystal Structure Refinement*. University of Göttingen.

- Siretanu D, Li D, Buisson L, Bassani DM, Holmes SM, Mathonière C, Clérac R (2011) *Chem. –Eur. J.* 17, 11704.
- Sun Y, Bigi JP, Piro NA, Tang MLLong JR, Chang CJ (2011) *J. Am. Chem. Soc.* 133, 9212.
- Wang X, Wang S, Li L, Sundberg EB, Gacho GP (2003) *Inorg. Chem.* 42, 7799.
- Wasylenko DJ, Ganesamoorthy C, Borau-Garcia J, Berlinguette CP (2011) *Chem. Commun.* 47, 4249.
- Zadrozny JM, Freedman DE, Jenkins DM, Harris TD, Iavarone AT, Mathonière C, Clérac R, Long JR (2010) *Inorg. Chem.* 49, 8886.
- Zhang Y, Li D, Clérac R, Kalisz M, Mathonière C, Holmes SM (2010) *Angew. Chem. Int. Ed.* 49, 3752.

General conclusion and perspectives

In the field of molecule-based magnetism, organization of single-molecule magnets (SMMs) has become critical to progress our research towards future applications. Our strategic approach in this thesis is to organize these molecules into coordination networks of different dimensionalities using carefully chosen bridging units. We herein summarize the principal results obtained during this thesis work and future perspectives.

In Chapter I, we discussed the general theoretical aspects of the four important classes of magnetic coordination complexes considering SMMs, single-chain magnets (SCMs), spin crossover (SC), and electron transfer (ET) systems. This theoretical background offers the readers an opportunity to understand easily the following Chapters II – IV, and furthermore gives chemists an idea to design new molecules with enhanced magnetic properties. Especially, some theoretical calculations, which are not fully described in most of recent scientific publications, were detailed in the supporting information at the end of Chapter I.

In Chapter II, literature examples of SMM-based coordination networks and photoactive cyanido-based bimetallic complexes were thoroughly reviewed. We illustrated the interest of coordination chemistry to design the magnetic materials that could accomplish the fundamental and technological demands. Based on this general overview, we emphasized the next challenges in the field of molecule-based magnetic materials, followed by the motivation of this thesis project. We presented two different strategies to answer some of the questions facing in the group during the past research, and in the field of molecular magnetism: (i) the first one was to utilize magnetic linkers that may favor strong magnetic interactions and an effective ferromagnetic coupling between the SMM units, finally to enhance the characteristics and the performance of these SMM-based coordination systems; (ii) the second one was to develop new photo-responsive linkers with an ultimate goal of assembling them with SMM, to realize finally photo-switchable magnet.

On the basis of our strategy (i), Chapter III presents five coordination networks based on $[\text{Mn}_4]$ SMMs.

In the first part of Chapter III, two coordination chains of $[\text{Mn}_4]$ SMMs linked by diamagnetic mono- and di-chlorido bridges (**1** and **2**) have been prepared and carefully studied. On the basis of structural characterization and magnetic measurements, **1** and **2** can be viewed as chains of antiferromagnetically coupled $S_T = 9$ $[\text{Mn}_4]$ anisotropic spins. Especially for compound **2**, the detailed crystallographic analyses and the heat capacity studies showed a single-crystal-to-single-crystal second order phase transition. In both compounds **1** and **2**, hydrogen bonds, short contacts, and weak $\pi \cdots \pi$ interactions cause the formation of 3D supramolecular architectures at low temperature, that indeed result in a canted antiferromagnetic and an antiferromagnetic ground states, respectively for **1** and **2**. Nevertheless, slow dynamics in **1** and **2** were detected, confirming a magnet behavior. This behavior is induced by magnetic moments that are not compensated in antiferromagnetic arrangement due to the presence of spin canting. Slow dynamics corresponding to 1D magnetic chains was observed with an energy barrier that is much more enhanced compared to the one of the isolated $[\text{Mn}_4]$ SMMs.

In the second part of Chapter III, we have discussed two chains (**3** and **4**) and one 2D framework (**5**) consisting of $[\text{Mn}_4]$ SMMs and paramagnetic metal centers (Ni^{II} , Mn^{II} , and Cu^{II}). For compounds **3** and **4**, $[\text{Mn}_4]$ units and metal ions (Ni^{II} and Mn^{II}) are antiferromagnetically coupled along the chain, while $[\text{Mn}_4]$ units and Cu^{II} ions are ferromagnetically coupled through the 2D network of **5**. The presence of isotropic Mn^{II} ions in **4** between anisotropic $[\text{Mn}_4]$ units along the chain resulted in the unprecedented magnetic behavior that is significantly different from Ising chain behavior. Therefore, we developed a new chain model that indeed compares with the experimental data. Compound **4** showed 3D antiferromagnetic order at low temperature. When the interchain interactions are overcome with the applied dc field (250 Oe), the chains are likely decoupled and consequently slow dynamics corresponding to the chain was observed.

The aforementioned compounds **1** – **5** represent an important impact to the nascent field of coordination assemblies based on SMMs. Our results highlight that the approach to organize SMMs in 1D geometry by diamagnetic linkers is indeed an efficient way to design molecule-based magnets, even though these chains are not completely isolated in both structural and magnetic point of view. Furthermore, an introduction of paramagnetic linkers to a network of $[\text{Mn}_4]$ SMMs has been realized in a rational way for the first time. The extensive physical characterization and theoretical studies for compounds **1** – **5** were performed during this thesis, demonstrating a significant modulation in the magnetic properties of $[\text{Mn}_4]$ SMMs by the exchange interactions through the coordination and the supramolecular networks. However, the magnetic exchange interactions through diamagnetic and paramagnetic linkers were found to be antiferromagnetic except for compound **5**. In addition, the chosen paramagnetic metal complexes did not mediate stronger magnetic interactions compared to the diamagnetic ones. Therefore, we need to seek coordinating linkers, such as metal cyanides or radical ions to enhance magnetic interactions for future direction of the project. On the other hand, although the developed model for a chain consisting anisotropic and isotropic units reproduce well the phase diagram resulting in reasonable values of exchange interaction parameters, it could not simulate perfectly the magnetic susceptibility behavior mainly due to the overlap of two regimes: 3D AF order and thermal population of excited states of $[\text{Mn}_4]$ SMMs. In order to avoid this overlap, design of chains with bigger anions may allow a better separation of chains and consequently the stabilization of AF order at lower temperature. In the mean time, new SMMs with large intra-molecular magnetic interactions to induce a large energy difference between the ground state and the first excited state of the complex need to be sought.

Considering the strategy (ii), we had choices between SC and ET complexes for photo-responsive switching linkers. Since SMM networks connected by SC linkers had been studied during the thesis of R. Ababei (2007 – 2010), we have oriented our work to design of new ET complexes. Chapter IV was dedicated to the newly synthesized heterometallic $[\text{FeCo}]$ (**8**) and $[\text{Mn}_2\text{Fe}]$ (**10**) complexes based on a *mer*-tricyanidoiron(III) precursor, using a building block approach. Among a series of dinuclear $[\text{FeCo}]$ compounds that we have obtained, compound **8** unambiguously revealed the presence of a cobalt(II) spin crossover induced by temperature in solid-state and an intramolecular electron transfer assisted by controlled protonation in solution. Both phenomena were accompanied by magnetic and/or optical changes in the material. Therefore, **8** shows two distinct switching processes depending on its physical state and external stimuli. This new dinuclear complex is the smallest possible molecule that mimics the physical properties found in the well-known 3D Fe/Co

photomagnetic Prussian blues and recent polynuclear Fe/Co complexes. On the other hand, compound **10** represents a new trinuclear $[\text{Mn}_2\text{Fe}] S_T = 9/2$ SMM. Extensive magnetic characterization demonstrates a large anisotropy on Mn^{III} ions and a ferromagnetic exchange interaction between Mn^{III} and Fe^{III} . Slow dynamics observed at zero field was significantly slow down under an external dc field (1800 Oe).

As future perspectives for the development of dinuclear [FeCo] photomagnetic linkers, we would like to emphasize a critical importance in the redox potential of metal building blocks as seen in the solution studies of compound **8**. Although a fascinating multifunctionality has been observed in compound **8**, photo-induced electron transfer in solid state is still a challenge for $[(\text{bbp})\text{Fe}(\text{CN})_3\text{Co}(\text{PY5R}_2)]$ systems. Nevertheless, we have seen that the protonation on the ligand belonging to Fe center of **8** played an important role to induce a positive shift of redox potential on the Fe site, and consequently trigger an intramolecular electron transfer in solution. Therefore, it would be interesting to try to crystallize this protonated [FeCo] dinuclear unit through building-block approach using Co-precursor (**7**) and protonated Fe-precursor (**9**). In addition, it is also worth trying to connect compound **8** with SMMs, since metal coordination to two free cyanides of **8** might also tune the redox potential of Fe site in this compound. Thus, depending on the degree of the potential shift, we may have a photoswitchable magnet. Furthermore, since the rational assemblies of the two Fe and Co precursors are well established during this work, the next step is to play with the functionalization of bbp and PY5 ligands in order to optimize the redox potential difference between two metal building blocks toward an occurrence of intramolecular electron transfer. In the mean time, compound **10** could be one of the interesting candidates to coordinate a suitable Co^{II} complex to one available cyanido present on the middle Fe^{III} ion, with an ultimate goal to realize a photo-switchable SMM.

As summarized in the previous paragraphs, the organization of SMMs into coordination networks by dia- and para-magnetic bridges has been well achieved and offered an opportunity to observe original magnetic behaviors. Now one of the greatest challenges will be an incorporation of photomagnetic electron transfer linkers with SMMs to realize a next generation of SMM-based magnetic materials. Given the fact that only a few examples of photo-switchable SMMs and SCMs exist in the literature, the foregoing research would give a valuable contribution in the field.

Abbreviations and physical constants

Abbreviations

1D	one-dimensional
2D	two-dimensional
3D	three-dimensional
1-CH ₃ im	1-methylimidazole
3,5-Brsalen	<i>N,N'</i> -ethylene-bis(3,5-dibromosalicylideneimine)
ac	alternating current
AF	antiferromagnetic
bpy	2,2'-bipyridine
bpy ^{Me}	4,4'-methyl-2,2'-bipyridine
bpym	2,2'-bipyrimidine
CV	cyclic voltammetry
dc	direct current
dcn ⁻	dicyanamide
DSC	differential scanning calorimetry
dtbbpy	4,4'-di-tert-butyl-2,2'-bipyridine
eiao	1-ethylimidazole-2-aldoximate
ET	electron transfer
FT-IR	Fourier transform infrared
H ₂ bbp	2,6-bis(benzimidazo-2-yl)pyridine
H ₂ Brppz	3-(5-bromine-2-phenolate)pyrazolate
H ₂ btda	bithiophenedicarboxylic acid
H ₂ dae	1,2-bis(5-carboxyl-2-methyl-3-thienyl)perfluorocyclopentene
H ₂ hmi	(2-hydroxy-3-methoxyphenyl)methylene(isonicotino)hydrazine
H ₂ Meppz	3-(2-hydroxy-5-methylphenyl)pyrazole
H ₂ pdm	pyridine-2,6-dimethanol
H ₂ ppz	3-(2-hydroxyphenyl)pyrazole
H ₂ sao	salicyl-aldoxime
Hhmp	2-hydroxymethylpyridine
Hmpko	methyl 2-pyridyl ketone oxime
Hpic	picolinic acid
HS	high-spin
JT	Jahn-Teller
LED	light emitting diode
LS	low-spin
Me-bbp	2,6-bis(N-methylbenzimidazo-2-yl)pyridine
Meim	methylimidazole
miao	1-methylimidazole-2-aldoximate
MMCT	metal-to-metal charge transfer

naphtmen ²⁻	<i>N,N'</i> -(1,1,2,2-tetra-methylethylene)bis(naphthylideneiminato) dianion
NMR	nuclear magnetic resonance
pao	pyridine-2-aldoxime
pdH ₂	1,3-propanediol
pn	1,3-diaminopropane
PY5H ₂	2,6- <i>bis</i> (1,1- <i>bis</i> (2-pyridyl)methyl)pyridine
PY5Me ₂	2,6- <i>bis</i> (1,1- <i>bis</i> (2-pyridyl)ethyl)pyridine
PY5OH ₂	2,6- <i>bis</i> (1,1- <i>bis</i> (2-pyridyl)hydroxymethane)pyridine
QTM	quantum tunneling of the magnetization
salen	<i>N,N'</i> -ethylene-bis(salicylideneiminate)
salmen	<i>rac-N,N'</i> -(1-methylethylene)-bis(salicylideneiminate)
salpn	<i>N,N'</i> -propane-bis(salicylideneiminate)
saltmen	<i>N,N'</i> -(1,1,2,2-tetramethylene)bis(salicylideneiminate)
SC	spin crossover
SCM	single-chain magnet
SMM	single-molecule magnet
SQUID	superconducting quantum interference device
TFA	trifluoroacetic acid
TfOH/HOTf	trifluoromethanesulfonic acid
tfa ²⁻	terephthalate dianions
TGA	thermogravimetric analysis
thd	tetramethylheptanedionato
tpa	tris(2-pyridylmethyl)amine
Tp	trispyrazoylborate
Tp [*]	tris(3,5-dimethyl)pyrazoyl borate
valpn	1,3-propanediyl-bis(2-iminomethylene-6-methoxy-phenol)

Physical constants

	Symbol	Value	SI	CGS
Avogadro number	N_A	6.02217	10^{23} mol^{-1}	
Boltzmann constant	k_B	1.38062	$10^{-23} \text{ J}\cdot\text{K}^{-1}$	$10^{-21} \text{ erg}\cdot\text{G}^{-1}$
Bohr magneton	μ_B	9.27410	$10^{-24} \text{ J}\cdot\text{T}^{-1}$	$10^{-16} \text{ erg}\cdot\text{K}^{-1}$
1 electron volt	eV	1.60219	10^{-19} J	10^{-11} erg
Vacuum permeability	μ_0		$4\pi 10^{-7} \text{ N}\cdot\text{A}^{-2}$	1
Molar gas constant	R	8.31446	$\text{J}\cdot\text{mol}^{-1}\cdot\text{K}^{-1}$	$10^7 \text{ erg}\cdot\text{mol}^{-1}\cdot\text{K}^{-1}$

List of publications

- 1 I-R. Jeon, R. Ababei, L. Lecren, Y-G. Li, W. Wernsdorfer, O. Roubeau, C. Mathonière, R. Clérac, Two-dimensional assembly of $[\text{Mn}^{\text{II}}_2\text{Mn}^{\text{III}}_2]$ Single-Molecule Magnets and $[\text{Cu}(\text{pic})_2]$ linking units, *Dalton Trans.*, **2010**, 39, 4744.
- 2 M. Hołyńska, D. Premužić, I-R. Jeon, R. Clérac, S. Dehnen, $[\text{Mn}^{\text{III}}_6\text{O}_3\text{Ln}_2]$ Single-Molecule Magnets: Increasing the Energy Barrier above 100 K, *Chem. Eur. J.*, **2011**, 17, 9605.
- 3 P. Sarkar, I-R Jeon, F. Durola, H. Bock, Tetraazarenes by the ceramidone, *New. J. Chem.*, **2012**, 36, 570.
- 4 J. Wu, D. J. MacDonald, R. Clérac, I-R. Jeon, M. Jennings, A. J. Lough, J. Britten, C. Robertson, P. A. Dube, K. E. Preuss, Metal Complexes of Bridging Neutral Radical Ligands, *Inorg. Chem.*, **2012**, 51, 3827.
- 5 I. Bhowmick, T. D. Harris, P. Dechambenoit, E. A. Hillard, C. Pichon, I-R. Jeon, R. Clérac, Cyanido-Bridged One-Dimensional Systems Assembled from $[\text{Re}^{\text{IV}}\text{Cl}_4(\text{CN})_2]^{2-}$ and $[\text{M}^{\text{II}}(\text{cyclam})]^{2+}$ (M = Ni, Cu) Precursors, *Science China Chemistry*, **2012**, 55, 1004.
- 6 I-R. Jeon, R. Clérac, Controlled Association of Single-Molecule Magnets (SMMs): Toward New Generation of Magnetic Materials, *Dalton Trans.*, *Perspective article*, **2012**, 41, 9569.
- 7 D. Visinescu, I-R. Jeon, A. M. Madalan, M-G. Alexandru, B. Jurca, C. Mathonière, R. Clérac, M. Andruh, *Dalton Trans.*, **2012**, 41, 13578.
- 8 A. Panja, P. Guionneau, I-R. Jeon, S. Holmes, R. Clérac, C. Mathonière, Syntheses, structures and magnetic properties of a novel *mer*- $[(\text{L})\text{Fe}^{\text{III}}(\text{CN})_3]^{2-}$ building block and its related heterobimetallic Fe(III)-Ni(II) complexes, *Inorg. Chem.*, **2012**, 51, 12350.
- 9 I-R. Jeon, S. Calancea, A. Panja, D. Piñero Cruz, P. Dechambenoit, C. Coulon, A. Wattiaux, P. Rosa, C. Mathonière, R. Clérac, Spin Crossover or Intra-Molecular Electron Transfer in a Cyanido-Bridged Fe/Co Dinuclear Dumbbell: A Matter of State, *Submitted*.

Résumé

Organisation par chimie de coordination de molécules-aimants : vers une nouvelle génération de matériaux magnétiques et photomagnétiques

Octobre -2009 – Septembre 2012, Université de Bordeaux 1

Centre de Recherche Paul Pascal (CRPP) & Institut de Chimie de la Matière Condensée (ICMCB)

Introduction. La conception rationnelle des matériaux basés sur les molécules est actuellement un sujet d'activités de recherche dans le monde entier, principalement tirée par le développement rapide de la technologie moderne qui nécessite une meilleure performance des matériaux présents.¹⁻³ Cet axe de recherche est extrêmement actif grâce au développement de la chimie de coordination, qui offre une approche moléculaire pour sélectionner les propriétés des précurseurs et des connecteurs pour obtenir des matériaux avec des architectures et des propriétés physiques souhaitées.⁴⁻⁶ Ce champ en pleine croissance offre également différentes alternatives pour produire des matériaux magnétiques qui sont indispensables dans notre vie présente. Les aimants classiques, tels que le fer, le cobalt, l'oxyde de chrome ou des alliages de métaux des terres rares sont rigides et nécessitent pour leur préparation des méthodes métallurgiques à haute température très coûteuses en énergie.^{7,8} Ces caractéristiques ont incité les chercheurs à développer de nouveaux types d'aimants qui sont des matériaux magnétiques conçus et construits en utilisant une approche moléculaire.^{9,10} En général, ces aimants peuvent être préparés à température ambiante et permettent des modifications au niveau moléculaire comparables à des synthèses organiques. Ainsi, les matériaux magnétiques ayant une solubilité dans des solvants organiques, une transparence, et une faible densité peuvent être obtenus.

Dans le domaine des matériaux à base de molécules, un effort de recherche considérable a été consacré à la synthèse de systèmes à l'échelle nanométrique afin de réduire la taille des unités magnétiques pour le stockage d'information, et donc la taille des appareils. Différentes approches ont été utilisées pour obtenir des mono-domaines de particules magnétiques, mais le début des années 90 a été marquée par la découverte des molécules-aimants.¹¹⁻¹³ Ces composés paramagnétiques ont suscité de grands espoirs pour coder les informations sur des molécules uniques et donc de réduire considérablement la taille des unités de stockage magnétiques. Ainsi, l'organisation de ces molécules afin de réaliser des dispositifs pour d'éventuelles applications est devenue un enjeu important de notre recherche. Actuellement plusieurs groupes dans le monde ont placé cette stratégie de recherche en priorité. Une des voies possibles est d'utiliser les molécules-aimants comme des précurseurs moléculaires et les assembler à l'aide de la chimie de coordination.¹⁴ Cette stratégie présente un défi puisque les propriétés magnétiques intrinsèques des molécules-aimants de départ peuvent être modifiées, et fournit aussi une occasion unique d'enquêter sur les nouveaux comportements à la frontière entre les molécules-aimants et les aimants classiques. En outre, la conception de systèmes avec des propriétés de molécules-aimants «améliorées» ou le comportement d'aimants est théoriquement possible en choisissant des connecteurs coordinants qui pourraient favoriser un arrangement ferromagnétique des SMM.

Projet. Dans ce contexte, mon projet de thèse porte sur l'organisation des molécules-aimants dans les

réseaux de coordination vers une nouvelle génération de matériaux magnétiques. Comme SMM, nous avons choisi un composé tétranucléaire $[\text{Mn}_4]$ contenant l'unité $[\text{Mn}^{\text{II}}_2\text{Mn}^{\text{III}}_2(\text{hmp})_6]^{4+}$ ($\text{hmpH} = 2$ -hydroxyméthylpyridine),^{15,16} qui a été intensivement étudiée dans le groupe M^3 au Centre de Recherche Paul Pascal (CRPP). Dans ce composé moléculaire polynucléaire, les ions Mn^{II} ($S = 5/2$) et Mn^{III} ($S = 2$) sont couplés ferromagnétiquement pour donner un état fondamental de spin (S_T) égal à 9. En raison des propriétés moléculaires intrinsèques (état fondamental de spin élevé (S_T) et forte anisotropie uniaxiale), une barrière d'énergie est créée, ce qui induit la présence de cycles d'hystérésis magnétiques analogue à ce qui est observé pour les aimants classiques. Dans le même temps, nous avons envisagé trois types de liens pour connecter les molécules-aimants $[\text{Mn}_4]$: (i) des groupements simples diamagnétiques, (ii) des composés paramagnétiques contenant des ions de métaux de transition et, (iii) des composés photomagnétiques que peuvent basculer entre deux états magnétiques en fonction d'un stimulus lumineux. Ce dernier type de connecteur est particulièrement attrayant car il pourrait permettre un contrôle par la lumière sur les propriétés magnétiques des matériaux finaux à base de molécules-aimants.

Dans le cadre de la première stratégie (i), les molécules-aimants $[\text{Mn}_4]$ ont été assemblées avec des liens mono- et di-chlorido pour former des systèmes unidimensionnels, $[\text{Mn}_4(\text{hmp})_6(\text{H}_2\text{O})_2\text{Cl}](\text{ClO}_4)_3 \cdot 1.5\text{CH}_3\text{CN}$ (**1**) et $[\text{Mn}_4(\text{hmp})_6\text{Cl}_2](\text{ClO}_4)_2$ (**2**). Les analyses structurales montrent que les deux composés **1** et **2** sont constitués d'unités $[\text{Mn}_4]$ le long de chaînes avec deux orientations différentes placées alternativement. Surtout pour le composé **2**, les analyses cristallographiques détaillées et les études de chaleurs spécifiques ont montré une transition de phase du deuxième ordre à 219 K. Dans les deux composés **1** et **2**, des liaisons hydrogènes, des contacts courts et faibles liées à des interactions $\pi \cdots \pi$ génèrent la formation d'architectures supramoléculaires 3D à basse température, qui conduisent à un état fondamental antiferromagnétique pour **1** et **2**. Sur la base des mesures magnétiques détaillées, **1** et **2** peuvent être considérés comme des chaînes de spins anisotropes $S_T = 9$ couplés de manière antiferromagnétique avec un arrangement canté. Les deux liens mono- et di-chlorés conduisent à des interactions antiferromagnétiques entre les unités $[\text{Mn}_4]$. Néanmoins, la dynamique lente de **1** et **2** a été détectée, ce qui confirme leur comportement d'aimant. Cette propriété est induite par le moment magnétique non compensé à cause de la présence des axes d'anisotropie non parallèles le long des arrangements 1D de molécules-aimants $[\text{Mn}_4]$ couplées antiferromagnétiquement. Les résultats précédents soulignent que notre approche d'organiser des molécules-aimants en géométrie 1D par des liens diamagnétiques est un moyen efficace pour concevoir des aimants à base moléculaire, même si ces chaînes ne sont pas complètement isolées d'un point de vue structurale et magnétique. En particulier, la barrière d'énergie pour inverser l'aimantation de ces matériaux est augmentée par rapport à celles observées dans les molécules-aimants $[\text{Mn}_4]$ isolées, en raison de leur organisation 1D.

En parallèle, des réseaux uniques 1D et 2D de molécules-aimants $[\text{Mn}_4]$ ont été obtenus avec des liens paramagnétiques préformés (des composés de Mn^{II} , Ni^{II} , Cu^{II}) pour réaliser la deuxième stratégie (ii): $[\text{Mn}_4(\text{hmp})_6(\text{H}_2\text{O})_2][\text{Ni}(\text{pic})_2(\text{H}_2\text{O})_2](\text{ClO}_4)_4 \cdot 3\text{CH}_3\text{CN}$ (**3**) ($\text{picH} =$ acide picolinique) et $[\text{Mn}_4(\text{hmp})_6(\text{H}_2\text{O})_2][\text{Mn}(\text{pic})_2(\text{H}_2\text{O})_2](\text{ClO}_4)_4 \cdot 3\text{CH}_3\text{CN} \cdot 2\text{H}_2\text{O}$ (**4**) sont des chaînes d'un point de vue structural et $[\text{Mn}_4(\text{hmp})_6\{\text{Cu}(\text{pic})_2(\text{ClO}_4)_2\}_2] \cdot 2\text{CH}_3\text{CN}$ (**5**)¹⁷ forme un réseau 2D. Pour les composés **3** et **4**, les unités

[Mn₄] et des ions métalliques (Ni^{II} et Mn^{II}) sont couplés de manière antiferromagnétique le long des chaînes, tandis que les unités [Mn₄] et les ions Cu^{II} sont couplés ferromagnétiquement par l'intermédiaire du réseau 2D dans **5** conduisant à un comportement d'aimant. En particulier, la présence d'ions isotropes Mn^{II} dans **4** entre les unités anisotropes [Mn₄] le long de la chaîne conduit à un comportement magnétique original qui est sensiblement différent d'un comportement de type Ising pour les chaînes. Ce fait nous a motivés à développer un nouveau modèle de chaîne qui reproduit bien les données expérimentales. Le composé **4** montre un ordre 3D antiferromagnétique. Néanmoins, lorsque les interactions interchaînes sont surmontées avec un champ appliqué (250 Oe), les chaînes sont susceptibles d'être découplées et par conséquent, la dynamique lente, correspondant à la chaîne individuelle a été observée. La barrière énergétique obtenue est renforcée par rapport aux molécules-aimants [Mn₄] isolées en raison de l'interaction magnétique entre les molécules-aimants [Mn₄] et les ions paramagnétiques Mn^{II} le long de la chaîne.

La dernière partie de mon travail de thèse est dédiée la conception de nouveaux complexes à transfert d'électrons dans le but ultime de les assembler avec des molécules-aimants pour réaliser un aimant photo-commutable (stratégie (iii)). Sur la base de la littérature, les analogues de bleu de Prusse 3D contenant le motif {Fe(μ -CN)Co} sont connus pour présenter un transfert d'électrons métal-métal réversible entre des unités diamagnétiques {Fe^{II}_{BS}(μ -CN)Co^{III}_{BS}} (Fe^{II}_{BS}, $S = 0$; Co^{III}_{BS}, $S = 0$) et des unités paramagnétiques {Fe^{III}_{BS}(μ -CN)Co^{II}_{HS}} (Fe^{III}_{BS}, $S = 1/2$; Co^{II}_{HS}, $S = 3/2$) (BS: bas spin, HS: haut spin). Compte tenu du fait que nous avons besoin d'un complexe à transfert d'électrons qui pourrait être un lien entre des molécules-aimants, nous avons préparé un composé binucléaire de Fe et Co pour provoquer la propriété de transfert d'électrons. Avec un choix judicieux de ligands pour les précurseurs moléculaires du fer et du cobalt, nous avons préparé un composé binucléaire de Fe et Co pontés par un groupement cyanido: [(BBP)Fe(CN)₃Co(PY5Me₂)]·2.5CH₃OH (H₂BBP = 2,6-bis(benzimidazole-2-yl) pyridine, PY5Me₂ = 2,6-bis(1,1-bis(2-pyridyl)éthyl) pyridine).¹⁸ A l'état solide, des mesures de susceptibilité magnétique ont montré une conversion de spin induite par la température autour de l'ion cobalt entre les espèces [Fe^{III}_{BS}-CN-Co^{II}_{BS}] et [Fe^{II}_{BS}-CN-Co^{III}_{HS}]. Le processus de transfert d'électrons éventuel a pu être écarté par des études cristallographiques à différentes températures, des mesures magnétiques et de spectrométrie Mössbauer de ⁵⁷Fe. A notre connaissance, ce composé est le seul exemple d'un complexe hétérobimétallique présentant une conversion de spin sur un ion cobalt. De manière remarquable, nos études en solution ont révélé d'importants changements optiques et magnétiques induits par un transfert d'électron métal-métal intramoléculaire modulé par protonation. Pour la première fois, ce nouveau complexe montre deux processus de commutation distincts selon son état physique et le stimulus externe utilisé: présence d'une conversion de spin induite par la température dans l'état solide, et un transfert d'électron intramoléculaire assisté par protonation en solution.

Conclusion. Dans ce travail de thèse, nous avons obtenu l'organisation contrôlée de molécules-aimants [Mn₄] via des liens diamagnétiques et paramagnétiques pour construire des réseaux 1D et 2D. Diverses mesures physiques, y compris la cristallographie, la chaleur spécifique et les propriétés magnétiques ainsi que des modèles théoriques ont confirmé les comportements magnétiques de ces matériaux qui sont modulés et renforcés par rapport à celles des molécules-aimants [Mn₄] isolées. Par conséquent, ces résultats prouvent que l'association de SMM dans les réseaux de coordination est un moyen

efficace pour concevoir de nouveaux matériaux moléculaires magnétiques. En parallèle, le premier complexe binucléaire qui imite les propriétés de commutation dans les bleus de Prusse a été synthétisé par une approche « building-block ». L'étude des propriétés physiques a mis en évidence une conversion de spin à l'état solide, et un transfert d'électron intramoléculaire en solution. Cette dualité dans les propriétés physiques est unique pour un même composé et représente une contribution précieuse aux composés moléculaires multifonctionnels.

References

- (1) Bruce, D. W.; O'Hare, D.; Walton, R. *Molecular Materials*; John Wiley & Sons, 2010; p. 378.
- (2) Bradshaw, D.; Claridge, J. B.; Cussen, E. J.; Prior, T. J.; Rosseinsky, M. J. *Accounts of Chemical Research* **2005**, *38*, 273–282.
- (3) Yen, Y.-S.; Chou, H.-H.; Chen, Y.-C.; Hsu, C.-Y.; Lin, J. T. *J. Mat. Chem.* **2012**, *22*, 8734.
- (4) Lehn, J.-M. *Supramolecular Chemistry: Concepts and Perspectives*; VCH, 1995; p. 286.
- (5) Dinolfo, P. H.; Hupp, J. T. *Chem. Mater.* **2001**, *13*, 3113–3125.
- (6) Öhrström, L.; Larsson, K. *Molecule-based materials*; Elsevier Science: Amsterdam, 2005.
- (7) Robinson, A. L. *Science* **1984**, *223*, 920–922.
- (8) Buschow, K. H. J. *Materials Science Reports* **1986**, *1*, 1–63.
- (9) Miller, J. S.; Drillon, M. *Magnetism: Molecules to Materials*; Wiley-VCH, 2001; p. 464.
- (10) Miller, J. S.; Gatteschi, D. *Chem. Soc. Rev.* **2011**, *40*, 3053–3368.
- (11) Boyd, P. D. W.; Li, Q.; Vincent, J. B.; Folting, K.; Chang, H. R.; Streib, W. E.; Huffman, J. C.; Christou, G.; Hendrickson, D. N. *J. Am. Chem. Soc.* **1988**, *110*, 8537–8539.
- (12) Caneschi, A.; Gatteschi, D.; Sessoli, R.; Barra, A. L.; Brunel, L. C.; Guillot, M. *J. Am. Chem. Soc.* **1991**, *113*, 5873–5874.
- (13) Sessoli, R.; Tsai, H. L.; Schake, A. R.; Wang, S.; Vincent, J. B.; Folting, K.; Gatteschi, D.; Christou, G.; Hendrickson, D. N. *J. Am. Chem. Soc.* **1993**, *115*, 1804–1816.
- (14) Jeon, I.-R.; Clérac, R. *Dalton Trans.* **2012**, 9569–9586.
- (15) Lecren, L.; Wernsdorfer, W.; Li, Y.; Roubeau, O.; Miyasaka, H.; Clérac, R. *J. Am. Chem. Soc.* **2005**, *9*, 11311–11317.
- (16) Lecren, L.; Li, Y.-G.; Wernsdorfer, W.; Roubeau, O.; Miyasaka, H.; Clérac, R. *Inorg. Chem. Commun.* **2005**, *8*, 626–630.
- (17) Jeon, I.-R.; Ababei, R.; Lecren, L.; Li, Y.-G.; Wernsdorfer, W.; Roubeau, O.; Mathonière, C.; Clérac, R. *Dalton Trans.* **2010**, *39*, 4744–4746.
- (18) Jeon, I.-R.; Calancea, S.; Panja, A.; Piñero Cruz, D.; Dechambenoit, P.; Coulon, C.; Wattiaux, A.; Rosa, P.; Mathonière, C.; Clérac, R. Soumis.